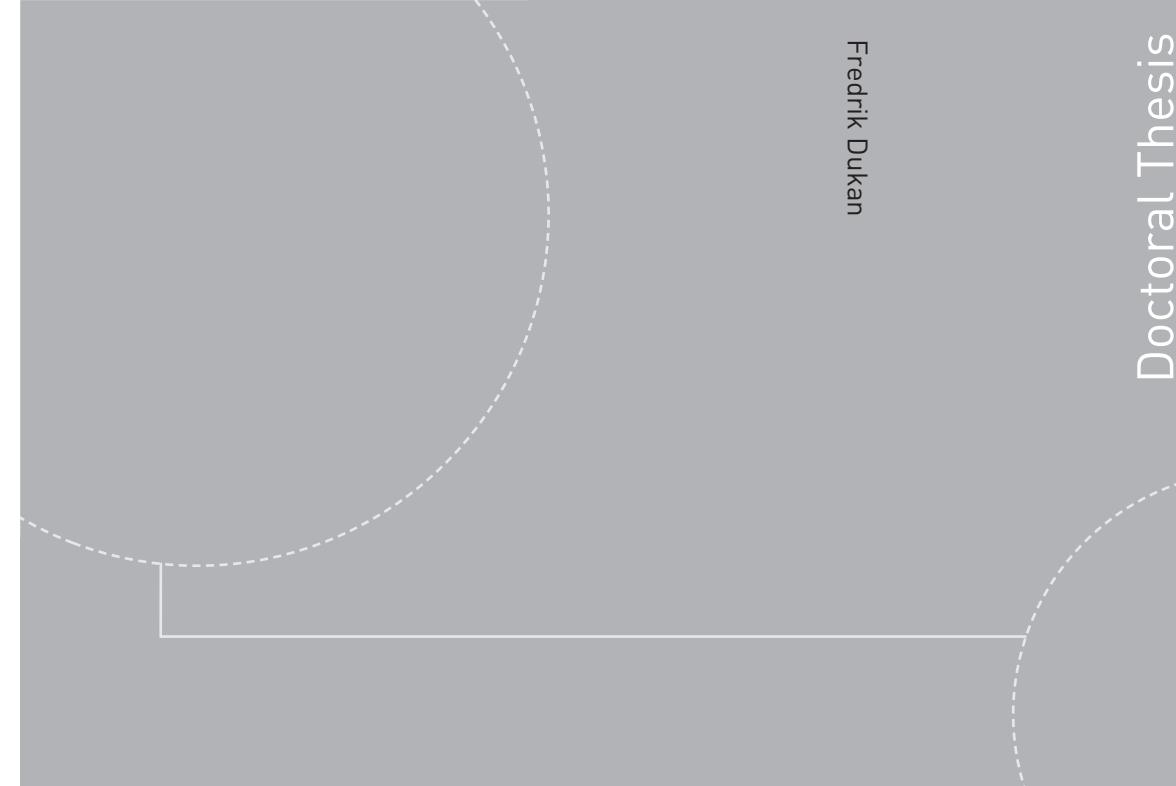


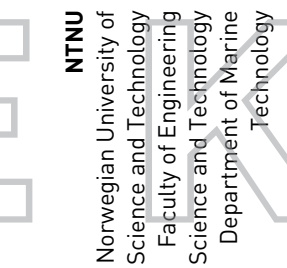
ISBN 978-82-326-0502-6 (printed version)  
ISBN 978-82-326-0503-3 (electronic version)  
ISSN 1503-8181



**NTNU – Trondheim**  
Norwegian University of  
Science and Technology



© NTNU



**NTNU – Trondheim**  
Norwegian University of  
Science and Technology

Doctoral theses at NTNU, 2014:295

Fredrik Dukan

## ROV Motion Control Systems

K O R R  
DOKTUR

Fredrik Dukan

# ROV Motion Control Systems

Thesis for the degree of Philosophiae Doctor

K O R R E K T U R  
Trondheim, October 2014

Norwegian University of Science and Technology  
Faculty of Engineering  
Science and Technology  
Department of Marine  
Technology



**NTNU – Trondheim**  
Norwegian University of  
Science and Technology

**NTNU**

Norwegian University of Science and Technology

Thesis for the degree of Philosophiae Doctor

Faculty of Engineering  
Science and Technology  
Department of Marine  
Technology

© Fredrik Dukan

ISBN 978-82-326-0502-6 (printed version)

ISBN 978-82-326-0503-3 (electronic version)

ISSN 1503-8181

K O R R E K T U R

Doctoral theses at NTNU, 2014:295



Printed by Skipnes Kommunikasjon as

# Abstract

This thesis is about automatic motion control systems for remotely operated vehicles (ROV). The work has focused on topics within guidance and navigation. In addition, a motion control system has been developed, implemented, tested and used on two ROVs in sea trials.

The main motivation for the work has been the need to automate ROV tasks in order to make the ROV a more efficient tool for exploring the ocean space. Many parts of a motion control system for a ROV is similar to that of surface vessels and ships. However, there are many differences as well which require special solutions. This thesis proposes solutions to some of these challenges.

Underwater navigation is one of the main challenges of developing a motion control system as no global positioning system (GPS) is available below the surface. The work here contains contributions in both model-based and sensor-based state estimation methods. Model-based Kalman filters, both linearized and extended, have been developed and tested successfully on ROVs in sea trials. However, the need for an observer that works during manipulation work, and other cases with uncertain and rapid varying disturbances and dynamics, inspired the research on sensor-based state estimation. Specifically, a new type of attitude estimator known as an explicit complementary filter has been adopted and modified for ROV use. This attitude estimator is also used in an integration filter to estimate the translational positions. The main contribution here is a new method to include velocity measurements from a Doppler velocity log (DVL), or velocity estimates, to approximate the proper acceleration of the vehicle. This is used to improve the attitude estimation for accelerated vehicles, and hence the estimated positions when used in cascade with an integration filter.

Guidance of the ROV is needed to perform automatic tasks such as trajectory tracking and terrain following. The guidance modes require different levels of operator interaction. The thesis contains contributions on joystick in closed-loop control, reference models for A to B moves and path tracking, and altitude control and terrain following.

Joystick in closed-loop control compensates for dynamical and environmental forces in order for the pilot to easily guide the ROV. This work uses a filter-based reference model to generate desired trajectories based in the joystick commands. These trajectories are tracked by a closed-loop controller. The reference model is modified to reduce pilot induced oscillations. The human-in-the-loop is a special case where the interaction between the operator and the controller determines the overall performance of the ROV operation.

A simple and intuitive reference model for A to B moves and path tracking is a useful

tool for surveys of the sea floor. This thesis proposes a constant jerk reference model. The idea is to generate feasible desired velocities and positions from integration of a constant jerk (time derivative of acceleration) that is on or off. Some benefits over filter-based reference models are that the maximum velocity is low and acceleration and deceleration stages are short. This gives a predictable behavior of the ROV for the pilot who is monitoring the operation.

In order to perform video surveys or photomosaicking of the sea floor, the ROV must be able to follow the terrain automatically. A new method for sea floor geometry approximation and altitude control based on DVL range measurements is proposed. The method has also been implemented in the developed motion control system and has been successfully used on two ROVs. The main contributions here are the sea floor geometry approximation method and a new guidance law for desired depth corresponding to the reference altitude. Thus, altitude control is obtained by using the depth controller. The main new contribution in the guidance law is a feed forward term that assures proper heave velocity.

As part of the work with the thesis, a motion control system, including software and hardware, has been developed in collaboration with other PhD candidates and MSc students, where the author has had the responsibility of putting every thing together under the supervision of postdoc Martin Ludvigsen and prof. Asgeir J. Sørensen. This motion control system has been implemented on two ROVs and it has been used in cruises for ocean sciences and pipeline inspection.

# Acknowledgements

This thesis is submitted to the Norwegian University of Science and Technology (NTNU) for partial fulfillment of the requirements for the degree of philosophiae doctor. The thesis work has been conducted in the period from January 2010 to April 2014.

This doctoral work has been performed at the Department of Marine Technology, NTNU, Trondheim, with Asgeir J. Sørensen as the main supervisor and with co-supervisor Harald Ellingsen.

From 2010 to 2012 I have been affiliated with Centre for Ships and Ocean Structures (CeSOS), and from 2013 with Centre for Autonomous Marine Operations and Systems (AMOS). The Norwegian Research Council is acknowledged as the main sponsor of CeSOS and AMOS.

I would like to thank my supervisor Asgeir J. Sørensen for motivation, feedback and discussions on several topics within guidance, navigation and control. This has been very valuable in the work with the thesis. I would also like to thank him for advices in other aspects of life.

Thank you Martin Ludvigsen for all the help with the tinkering and implementation on the ROV Minerva and ROV 30k. This thanks goes also to Robert Staven and Frode Volden who have put a lot of time and effort into getting the ROV systems ready for cruises.

The cruises, and hence progress with the motion control system and testing and validation of proposed theories, would not have been possible without the crew of RV Gunnerus. Thank you very much Capt. Arve Knudsen, Svenn Ove Linde, Kjell Vestnes, Mats Remme Reppe and Elias G. Selliseth. You have been very helpful and skilled in executing the ROV operations. Thank you Mats for all the delicious food you have been serving us onboard RV Gunnerus.

Special thanks go to Mauro Candeloro and Daniel de Almeida Fernandes who have been working with their PhDs on topics within ROV motion control systems as well. The collaboration with the development of the motion control system and technical discussions have been great fun and very useful. I would also like to thank all the MSc students that have contributed to the ROV DP project. Especially Marianne Kirkeby, Carl Christopher Lysdahl, Steffen Kørte, Phat Truong, Viktor Berg and Espen Tolpinrud who spent lots of effort and late nights on the motion control project for ROVs.

The cruises and collaboration with ocean science researchers in marine biology and archeology have been of great value. Both for learning about new topics, far away from engineering and control theory, and in order to understand the needs of those who use underwater technology as a tool. It has been great to learn about marine biology and primary

productivity in the Arctic from the very enthusiastic Geir Johnsen, and to collaborate with the marine biology group. Thank you Ingrid Myrnes Hansen and Stefan Ekehaug for being so interested in using new ROV technology in marine biology studies. It is inspiring to work with control engineering theory and applications when it is appreciated by others who can make use of it.

Oslo, April 2014

Fredrik Dukan

# Contents

<b>Abstract</b>	<b>i</b>
<b>Acknowledgements</b>	<b>iii</b>
<b>Contents</b>	<b>viii</b>
<b>1 Introduction</b>	<b>1</b>
1.1 Motivation . . . . .	1
1.2 Background . . . . .	2
1.2.1 What is a ROV? . . . . .	2
1.2.2 Short History of ROVs . . . . .	3
1.2.3 Evolution of ROV Motion Control Systems . . . . .	10
1.3 Problem Outline . . . . .	11
1.4 List of Publications . . . . .	12
1.5 Contributions . . . . .	13
1.6 Thesis Structure . . . . .	13
<b>2 Modeling and Hydrodynamics of ROVs</b>	<b>15</b>
2.1 Notations . . . . .	15
2.1.1 Generalized Coordinates . . . . .	16
2.1.2 Notation Norms . . . . .	16
2.2 Kinematics . . . . .	17
2.2.1 Fossen's Robot-Like Vectorial Model . . . . .	17
2.2.2 Reference Frames . . . . .	17
2.2.3 Vector Notations . . . . .	18
2.2.4 Transformations . . . . .	19
2.2.5 Earth's Rotation and Gravity . . . . .	20
2.3 Equations of Motion . . . . .	21
2.3.1 Process Plant Model . . . . .	21
2.3.2 Control Plant Model . . . . .	26
2.4 Generalized Forces . . . . .	27
2.4.1 Ocean Current Forces . . . . .	28
2.4.2 Propulsion Forces . . . . .	28
2.5 Sensors . . . . .	32

2.5.1	Sensor Description . . . . .	32
2.5.2	Setup . . . . .	35
2.5.3	Measurements . . . . .	36
<b>3</b>	<b>Development of a ROV Motion Control System</b>	<b>39</b>
3.1	Introduction . . . . .	39
3.1.1	Objectives . . . . .	39
3.1.2	Work Process & Methods . . . . .	41
3.2	Motion Control System Architecture . . . . .	43
3.2.1	ROV Operation Modes and Functions . . . . .	44
3.2.2	Modules . . . . .	45
3.2.3	Signal Flow . . . . .	46
3.2.4	Levels of Autonomy . . . . .	47
3.3	Software Development . . . . .	49
3.3.1	Specifications, Tasks & Functionality . . . . .	50
3.3.2	Software & Hardware Platforms . . . . .	50
3.3.3	Object-Oriented Programming . . . . .	51
3.3.4	Software Product . . . . .	52
3.4	Hardware-in-the-Loop Testing . . . . .	53
<b>4</b>	<b>Underwater Navigation</b>	<b>55</b>
4.1	Requirements for ROV Navigation . . . . .	56
4.1.1	Closed-loop Control . . . . .	57
4.1.2	Measurements vs. Models . . . . .	57
4.1.3	Observer Design & State Estimation . . . . .	57
4.2	Model-Based Observers . . . . .	58
4.2.1	Sector Kalman Filters . . . . .	58
4.2.2	Extended Kalman Filters . . . . .	60
4.3	Sensor-Based Observers . . . . .	62
4.3.1	Background . . . . .	62
4.3.2	Modeling . . . . .	64
4.3.3	Attitude Estimation . . . . .	65
4.3.4	Integration Filters . . . . .	68
4.3.5	Measurements and Output . . . . .	69
4.3.6	Simulation and Effect of Observer Interconnections . . . . .	70
4.3.7	Simulation vs. Experiments . . . . .	74
4.4	Conclusions and Future Work on Underwater Navigation . . . . .	83
<b>5</b>	<b>Guidance of ROVs</b>	<b>85</b>
5.1	Constant Jerk Reference Models . . . . .	85
5.1.1	Constant Jerk Equations . . . . .	86
5.1.2	Constant Jerk vs. Filter-based Reference Models . . . . .	88
5.1.3	Implementation and Considerations . . . . .	89
5.2	LOS for Fully Actuated ROV . . . . .	91

5.2.1	2-D LOS . . . . .	92
5.2.2	3-D LOS . . . . .	96
5.3	Joystick in Closed-loop Control . . . . .	99
5.3.1	The Joystick and ROV . . . . .	99
5.3.2	Human-in-the-Loop . . . . .	103
5.3.3	Joystick Reference Models and Control . . . . .	104
5.3.4	Joystick Experimental Results . . . . .	107
<b>6</b>	<b>Altitude Control and Terrain Following</b>	<b>111</b>
6.1	Altitude and the Sea floor Gradient . . . . .	112
6.1.1	Altitude . . . . .	113
6.1.2	Altitude Rate of Change . . . . .	113
6.2	DVL Measurements . . . . .	114
6.2.1	DVL Beams and Kinematics . . . . .	115
6.2.2	Transformation of Beams . . . . .	115
6.3	Sea Floor Approximation by Use of a DVL . . . . .	116
6.3.1	Basic Linear Approximation . . . . .	116
6.3.2	Least Squares Approximation . . . . .	117
6.3.3	Combination Methods for Sea Floor Approximation . . . . .	118
6.3.4	Higher Order Methods for Sea Floor Approximation . . . . .	118
6.4	Sea Floor Roughness and Approximation Validity . . . . .	118
6.4.1	Errors and Norms for Validation of the Sea Floor Approximation Method . . . . .	119
6.4.2	Approximation Modes . . . . .	121
6.5	Altitude Estimation . . . . .	122
6.6	Guidance Laws for Altitude Control . . . . .	125
6.6.1	Control Objectives for Altitude Control . . . . .	125
6.6.2	Guidance Law for Altitude Control . . . . .	125
6.6.3	Sea Floor Collision Avoidance . . . . .	128
6.6.4	Speed Reduction, Contouring and Platforming . . . . .	129
6.7	Experimental Results with Altitude Control . . . . .	132
6.8	Conclusion and Further Work on Terrain Following . . . . .	136
<b>7</b>	<b>Ocean Science Research Campaigns</b>	<b>137</b>
7.1	The Value of Experimental Testing . . . . .	137
7.1.1	Research Motivated by Sea Trials . . . . .	137
7.1.2	Lessons Learned . . . . .	138
7.2	AUR-Lab Cruises with RV Gunnerus . . . . .	139
7.2.1	Lawn Mower Pattern with Altitude Control . . . . .	139
7.2.2	Falstad Cruise and Search for Wreck . . . . .	142
7.2.3	Ormen Lange . . . . .	143
7.2.4	Video Survey of a Coral Reef at Tautra . . . . .	144
7.2.5	Barge Wreck Survey at Munkholmen . . . . .	145
7.2.6	Photomosaic . . . . .	147

<b>8 Conclusion and Future Work</b>	<b>149</b>
8.1 Concluding Remarks . . . . .	149
8.2 Future Work . . . . .	150
<b>Bibliography</b>	<b>161</b>
<b>A NTNU Vehicles</b>	<b>163</b>
A.1 ROVs . . . . .	163
A.1.1 Specifications . . . . .	163
A.1.2 Mathematical Properties . . . . .	163
A.2 Research Vessel Gunnerus . . . . .	166
<b>B Position &amp; Velocity Control</b>	<b>169</b>
<b>C Mathematical Toolbox</b>	<b>171</b>
C.1 Rotation Matrix . . . . .	171
C.2 Quaternions . . . . .	171
<b>D Altitude Control Dynamics and Stability</b>	<b>173</b>

# Chapter 1

## Introduction

This thesis is about automatic motion control of remotely operated vehicles (ROV). New scientific contributions on terrain following, state estimation and guidance are given. However, the thesis has a strong focus on practical aspects of both implementation, testing and use of automatic motion control systems for underwater vehicles. An automatic motion control system for NTNU's ROVs has been developed in collaboration with other PhD candidates and MSc students as part of the work with the thesis. The motion control system has been tested and used on several cruises with RV Gunnerus, which has been the surface vessel for the ROV Minerva and ROV 30k. The experimental results presented in the thesis come from tests performed at these cruises where the in-house developed motion control system has served as a platform for testing new algorithms related to guidance, navigation and control of ROVs.

The scientific methods and contributions are listed in Section 1.3. Briefly, the most important work has been done in areas of vehicle state estimation (navigation), guidance strategies and terrain following. The topics for the scientific work has been selected partially from needs discovered during real ROV operations with end users from marine biology and marine archeology.

An overview on ROVs and associated motion control systems is given in the following.

### 1.1 Motivation

ROVs are used in a variety of subsea work tasks. From small hand deployable ROVs to large work class ROVs for heavy intervention work at subsea offshore installations to full ocean depth research ROVs. Common for all types is that many applications instead of being manually controlled could have been performed with higher accuracy and faster with an automatic positioning control system. Most industrial ROVs are equipped with automatic heading and depth control only [19]. A pilot controls the thrust, from a command console with joystick, to move the ROV. Industrial manufacturers that deliver ROVs for the oil & gas industry are starting to implement automatic positioning systems with basic functions such as station keeping and moves from A to B. However, more research

is needed before the full potential of automatically controlled ROVs can be utilized. Compared to the advances and wide spread use of dynamic positioning (DP) of surface ships in the recent decades, DP for underwater vehicles is still in its infancy. However, commercial systems with station keeping and tracking ability have entered the market in the last decade. Examples of companies are Schilling Robotics<sup>1</sup> and Seebyte<sup>2</sup> who deliver automated motion control systems for a variety of ROVs. But there are still good opportunities for making important contributions to the field for the early movers.

DP control modes such as maintaining position and tracking should be automated. Then the pilot can focus on monitoring and planning of operations that demand human intervention or decision making. The degree of pilot interaction can depend on the control mode. A list with way-points could be the input to the tracking control system for e.g. mapping of the sea floor. A fully autonomous mode may also be implemented where the motion control system plan and re-plan the desired trajectory based on e.g. concentration level sensors during search for a leakage or certain characteristics in the sea such as salinity, temperature, oxygen levels etc. A properly designed motion control system must be in place in order to develop increased level of autonomy.

Position and orientation feedback is needed to make a closed-loop DP control system for an ROV. For most practical subsea navigation tasks this means that an acoustic positioning reference system is needed. Slow update rates and inaccuracies in position measurements due to varying conditions in the water column motivates the use of velocity sensors and inertial measurement units (IMU) as well for enhanced state estimation. The increasing accuracy and drop in price and size of micro electromechanical (MEMS) IMUs can make these especially suitable for smaller vehicles such as ROVs. However, integration of MEMS IMUs in an inertial navigation system (INS) guided by an acoustic positioning system (APS) requires more research including testing and verification of performance and robustness.

Many challenges need to be solved in several fields, such as guidance, navigation and control, in order to make a complete automated motion control system for ROVs. The challenges and the opportunity of making important contributions are motivating factors for the selection of topics for this thesis.

## 1.2 Background

The ROV system, a brief history of ROVs and evolution of ROV motion control systems are presented in the following.

### 1.2.1 What is a ROV?

A ROV is a remotely operated vehicle, here a remotely operated underwater vehicle. An example of a complete ROV system is seen in Figure 1.1, which shows a drawing of the SAAB Cougar XT ROV. A ROV consists of a frame with buoyancy elements, thrusters,

---

<sup>1</sup><http://www.fmctechnologies.com/en/SchillingRobotics>

<sup>2</sup><http://www.seebyte.com>

video cameras and manipulator arm(s). The ROV gets power and sends and receives signals via a tether that goes up the surface. The ROV pilot sits in a control room or container and uses a joystick or a computer to move the ROV. The ROV can be equipped with various instruments and tools in order to monitor or perform subsea work tasks.

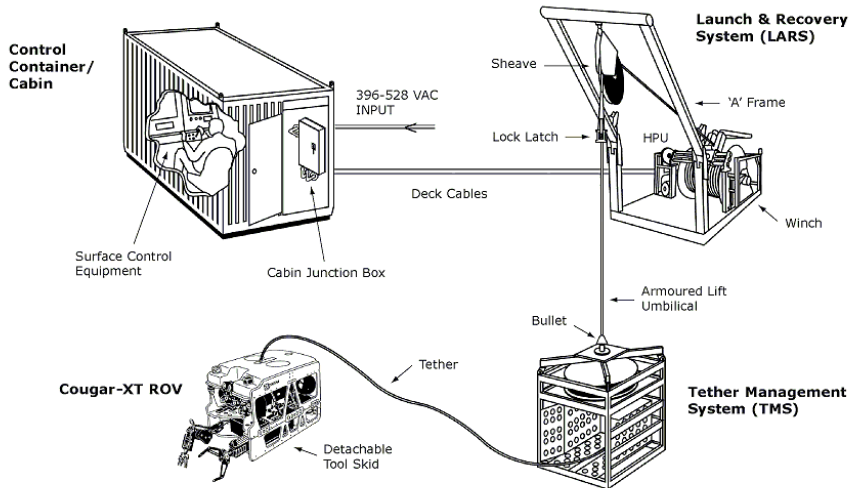


Figure 1.1: A ROV system including tether, winch and top side control container (Courtesy of SAAB).

ROVs are often used to replace a human divers as they are stronger and go deeper.

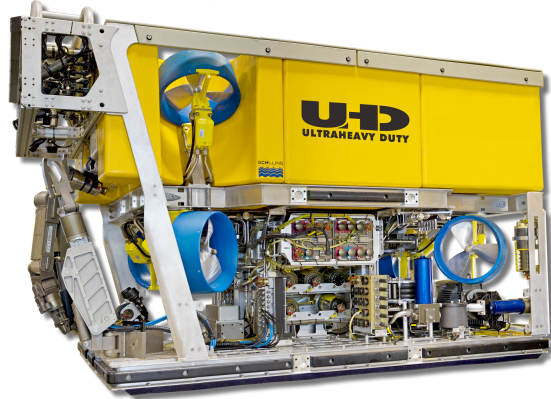
### 1.2.2 Short History of ROVs

It is uncertain who made the very first ROV, but early ROVs are seen from the beginning of the 1950s. The Royal Navy used their Cutlet ROV as seen in Figure 1.2a to recover practice torpedoes and mines from the sea floor in the 50s [71]. A state-of-the art ROV from 2012, the Schilling UHD is seen next to Cutlet in Figure 1.2b for comparison. Some have credited Dimitri Rebikoff with developing the first ROV. He made the POODLE in 1953, which was used for archeological research [18]. The US Navy developed a maneuverable underwater camera system called the XN-3, delivered in 1961, which was used for recovery of lost torpedoes. This design became the Cable-controlled Underwater Research Vehicle (CURV). The CURV ROVs made the international headlines twice. First, the CURV I, seen in Figure 1.3a, retrieved a lost atomic bomb off the coast of Palomares, Spain in 1966. The CURV III was used in a dramatic rescue operation South West off the coast of Ireland in 1973. The manned submersible Pisces III was stuck at 480 m, due to a leakage, with two men on-board. The CURV III connected lines to the wrecked submarine, as seen in Figure 1.3b, so it could be hoisted to the surface. After 85 hours in the submarine, the two men had only 12 minutes of oxygen left when the hatch was finally opened and the doomed crew could breathe fresh sea air again. Shortly after the rescue, one of the crew, Roger Chapman founded RUMIC which provides subsea

services and rescue submersibles. RUMIC was mobilized on behalf of the Royal Navy for the Kursk salvage operation in 2000.

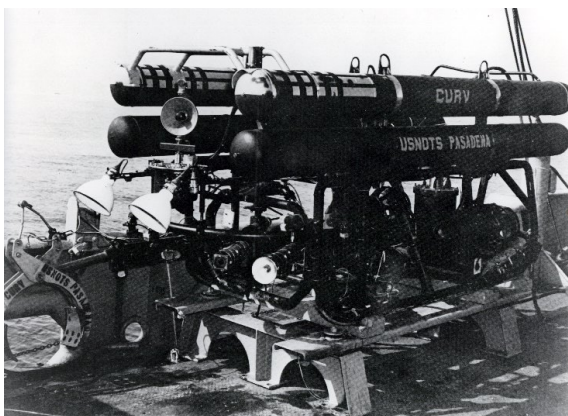


(a) Royal Navy's Cutlet ROV from the 50s. Used for recovery of torpedoes and mines.

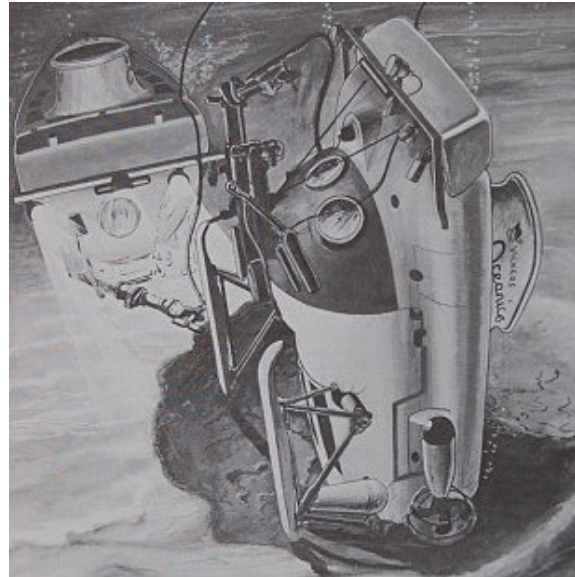


(b) Schilling UHD ROV from 2012. Used for subsea work in the oil & gas offshore industry.  
(Courtesy of FMC Schilling Robotics)

Figure 1.2: Examples of early and modern ROVs.



(a) CURV I ROV.

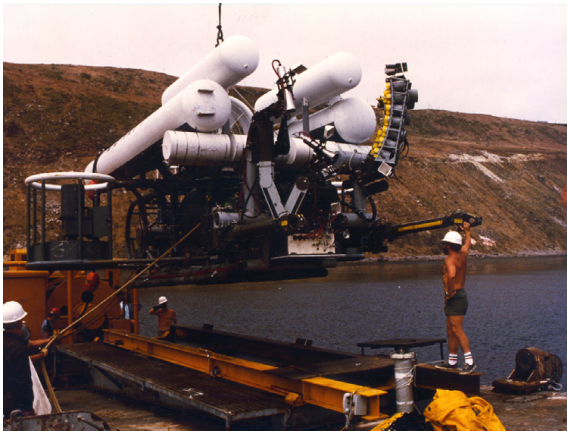


(b) An artist's impression of the rescue of the Pisces III submarine (Courtesy of the Dailymail).

Figure 1.3: Cable-Controlled Underwater Recovery Vehicle (CURV) ROVs. CURV I retrieved a lost atomic bomb off the coast of Palomares, Spain in 1966. CURV III helped in the rescue of the manned submarine Pisces III in 1973.

The US NAVY started developing more advanced vehicles after the success with the CURV designs. The large Pontoon Implacement Vehicle (PIV), seen in Figure 1.4a, was

made to aid in recovery of sunken submarines. The small-size SNOOPY was one of the first portable ROVs when launched in the 70s, see Figure 1.4b. It had two independently controlled hydraulic thrusters and automatic depth control [44].



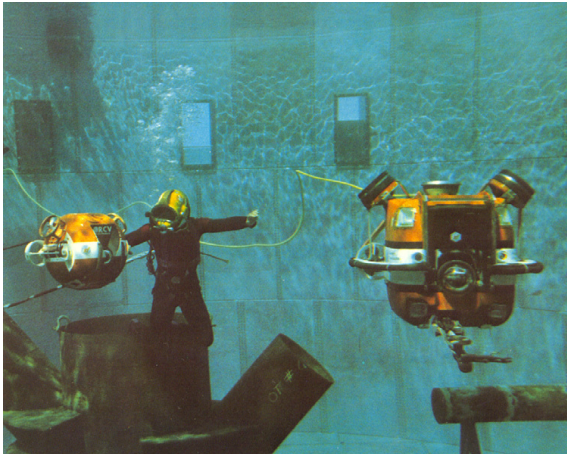
(a) Launch of the US Navy's Pontoon Implantation Vehicle (PIV).



(b) US Navy's Snoopy, the first portable ROV.

Figure 1.4: US Navy underwater vehicles (Courtesy of Wernli, Robert L.).

Hydro Products' line of Remotely Controllable Vehicles (RCV) were the first truly commercial ROVs. Their first vehicle, a RCV 225, was delivered to Stolt-Nielsen Seaway Diving in 1974 [17]. The larger RCV 150 followed up and both RCVs are seen in action in Figures 1.5a and 1.5b. However, the new vehicles had problems with entering the market dominated by manned submersibles and saturation divers at the time. It should take several years before the technology was fully accepted as replacement for divers.



(a) Hydro Products RCVs.



(b) Hydro Products RCV 225 and RCV 150 handing tools to diver.

Figure 1.5: First commercial ROVs from Hydro Products. An RCV 225 was delivered to Stolt-Nielsen Seaway Diving in 1974 (Courtesy of Hydro Products).

In 1974, only 20 vehicles were constructed and 17 of these were founded by gov-

ernments. Among these was the SNURRE ROV from 1973, which was developed and owned by the establishment of the Continental Shelf Division (NTNF-K) of the Royal Norwegian Council for Scientific Research [4]. The SNURRE ROV is seen in Figure 1.6a and the control room is shown in Figure 1.6b.



(a) NTNF-K's Snurre ROV.

(b) Control room for Snurre.

Figure 1.6: The first Norwegian made ROV. Snurre by NTNF-K (IKU) in 1980 (Courtesy of Norsk Oljemuseum).

In the period from 1974 to 1982 there was a large growth in the ROV market with about 500 vehicles by the end of 1982. The funding of ROV projects also changed in this period. From the beginning in 1953 to 1974, 85 % of ROVs were founded by governments but 96 % of the vehicles produced from 1974 to 1982 were made or owned by private industry [18].

The increasing reliability of the ROVs made them accepted by the offshore industry, which again caused a wave of new ROV developers and vehicles. In the period from 1982 to 1989, there was a rapid growth of the ROV industry. In 1970, there was only 1 commercial manufacturer of ROVs, and by 1984, the number had grown to 27. In the late 70s and early 80s, the market was dominated by North American companies, with Hydro products, AMETEK and Perry Offshore producing the majority of ROVs. Jim McFarlane, a Canadian, got into the business with a range of low-cost vehicles developed by International Submarine Engineering (ISE). However, as ROVs were accepted by the offshore oil & gas industry, the real money was in the North Sea. The low dollar to pound exchange rate in the mid 80s was bad for the American companies as it was cheaper to produce ROVs and equipment in the UK. So the European companies Slingsby Engineering, Sub Sea Offshore, and the OSEL Group cornered the North Sea market. The only North American survivors were Perry Offshore, who wisely teamed up with the competitors across the pond, and ISE due to their diverse product line and can-do attitude of their owner [18].

Technological advancements in the late 70s and 80s, especially within electronics and computers, made it possible to make smaller ROVs. While the established companies where fighting for contracts in the North Sea, new markets opened up to those who utilized the new technology to make smaller and cheaper ROVs. The low-cost ROV pioneer Chris Nicholson, owner of Deep Sea Systems International (DSSI), grasped the opportunity



(a) MiniRover ROV (1983).

(b) VideoRay ROV (1999).

(c) OpenROV (2012).

Figure 1.7: Evolution of mini &amp; micro ROVs.

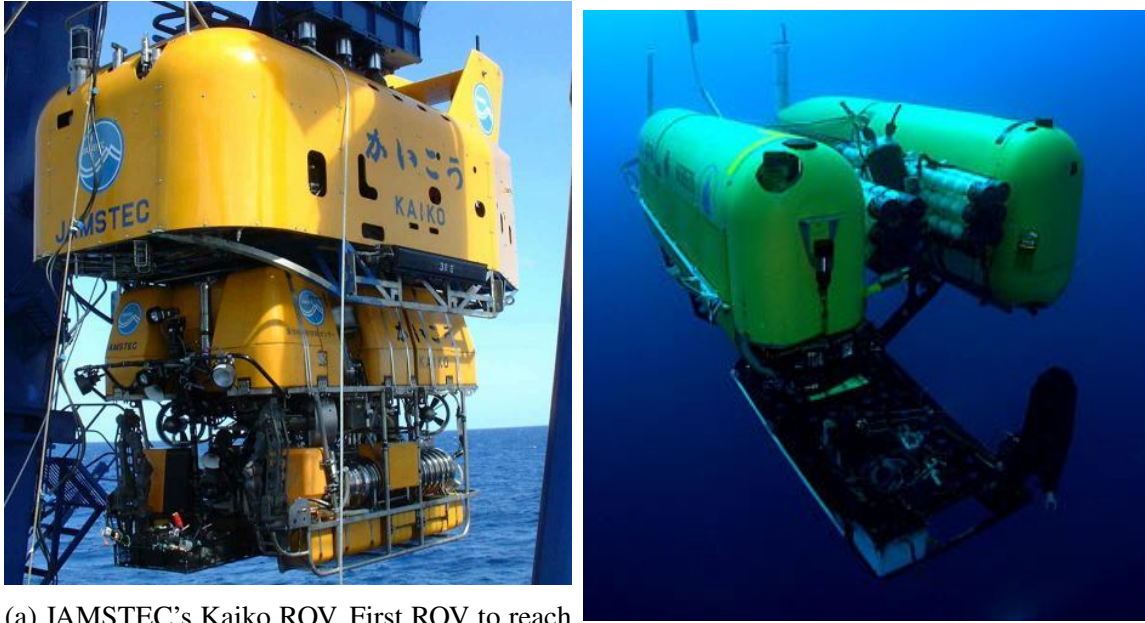
with his Mini Rover made in a garage in 1983. The Mini Rover, seen in Figure 1.7a, was priced at under \$30,000 when the cheapest competitor sold for more than \$100,000. This made ROVs affordable for civilian use. After Benthos picked up the Mini Rover line from DSSI in 1987, they and Deep Ocean Engineering (DOE) cornered the market for dam and tunnel inspection, police and security operations, fisheries, oceanography, nuclear plant inspection, and many other applications with the new affordable and portable mini ROVs [18].

In the 90s the ROV industry became more mature and diverse. It covered everything from light mini ROVs for civilian and scientific use to large and powerful work class ROVs for the offshore industry. New tools also increased the number of applications the ROV could be used for. The next challenge was to go deeper. The 20000 feet (6279 m) barrier was reached in 1990 by CURV III. However, the record was crushed by the Japanese JAMSTEC ROV Kaiko in 1995. Kaiko, seen in Figure 1.8a, placed a flag at the bottom of the Challenger Deep in the Mariana Trench, 10911 m below the surface. As it is impossible to go deeper, the record will stand.

For oil & gas exploration beyond the maximum depth for saturation divers, related subsea work tasks must be performed by ROVs. This forced a closer integration between the ROV industry and the oil & gas companies as all subsea structures and equipment must be designed so they can be installed, maintained and repaired by ROVs. This has led to a huge growth in the ROV tooling industry as well. The ROV serves a maneuverable platform where different tool modules can be mounted to perform specialized tasks.

In 1999 a new addition to the mini ROVs became very popular for inspection tasks. The VideoRay, seen in Figure 1.7b, weighs around 6 kg and comes with complete motion control system including video in a suitcase. Advances in various instrumentation technologies enables this micro ROV to be fitted with advanced sensors that used to require a much larger ROV and surface vessel for deployment. Thus the value to its users is enhanced over the first mini ROVs. This is reflected in sales, and VideoRay has sold more than 2500 ROV systems.

ROVs have also been used in various research projects for ocean science in areas such as oceanography, biology and archeology. One notable research ROV is the Nereus from Woods Hole Oceanographic Institution (WHOI), seen in Figure 1.8b. This is a hybrid ROV (HROV), which can operate with or without communication through a tether. That



(a) JAMSTEC's Kaiko ROV. First ROV to reach the bottom of the Challenger deep in the Mariana trench at 10911 m in 1995. (Courtesy of JAMSTEC)

(b) Woods Hole Oceanographic Institution's Nereus Hybrid ROV. Reached the Challenger deep in 2009. (Courtesy of WHOI)

Figure 1.8: Ultra deep sea ROVs.

is, it can work both as an ROV or as an autonomous underwater vehicle (AUV). The Nereus reached the Challenger Deep in 2009 and tied the record set by Kaiko almost 15 years earlier.

As of 2014 there were two Norwegian ROV manufacturers. Sperre AS in Notodden and Kystdesign AS in Haugesund. Sperre AS was founded by Tor Olav Sperre in 1988 after he had made a prototype of a small ROV for picking up wreck items. Sperre AS has delivered more than 80 ROV systems, and one of their ROVs, the SUB-fighter 15K is seen in Figure 1.9a. Kystdesign AS started in 1997 and produce work class ROVs for the offshore industry, with operators such as DOF and DeepOcean among the customers. Kystdesign deliver three ROV models; Supporter, Constructor and Installer. As of 2013 they had delivered 27 ROV systems. The Constructor work class ROV is seen in Figure 1.9b.

One of the most recent additions in the ROV industry is OpenROV, which started in a garage in Cupertino, CA in 2011. This US start-up is influenced by the open-source community. They make very affordable ROVs for teaching and exploration. The Open-ROV come as a kit, which the costumer can assemble themselves and modify the control software to their needs. The price tag of less than \$850 for the base version would have been unheard of in the 80s and 90s. This enables people all over to explore the oceans by themselves. The OpenROV is seen in Figure 1.7c.

In the late 90s there where over 100 ROV manufacturers and over 100 operators using around 3000 vehicles of different sizes according to [19]. It says in The World ROV



(a) Sperre AS SUB-Fighter 15k ROV. (Courtesy of Sperre AS)  
 (b) Kystdesign constructor work class ROV. (Courtesy of Kystdesign AS)

Figure 1.9: Modern Norwegian made ROVs.

Market Forecast 2011-2015 that there were 747 work class ROVs being operated by 21 major companies in 2011. The size of the total ROV market as of January 2014 is difficult to predict when including all smaller systems such as mini, micro an open source ROVs. Nonetheless, the growth in numbers of ROVs has been exponential since the start as seen in Figure 1.10 which shows numbers of produced ROVs and manufacturers from 1953.

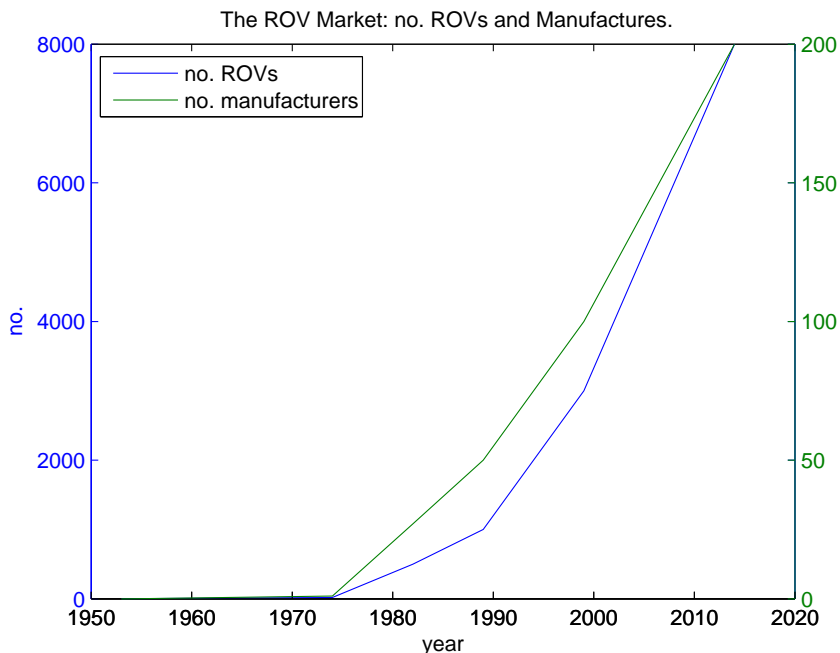


Figure 1.10: The evolution of the ROV market. Numbers of constructed ROVs and manufacturers since 1953.

### 1.2.3 Evolution of ROV Motion Control Systems

The early ROVs had rather primitive motion control systems. With independently controlled thrusters it took a skilled pilot a lot of effort to control it. Automatic depth control eased the operation of ROVs considerably as a ROV is rarely neutrally buoyant. With thruster allocation and an electronic compass (fluxgate compass), it was possible to include automatic heading control as well. Decoupled depth and heading control have been the standard automation functions for ROV positioning for decades and they still are. It is only in the recent years that other automated functions such as station keeping, velocity control and path tracking have gained popularity in commercial systems. The reason is most likely related to the underwater navigation problem. As there are no Global positioning systems (GPS) working under water, other means of finding an accurate position suitable for feedback to a position controller is needed. The standard solution has been to use acoustic positioning systems to get an absolute position fix. However, these can be inaccurate and "jumpy" and the update rate is slow. The alternative of INS, as used on submarines, have been too large and expensive for ROVs.

When the Doppler velocity log (DVL) came in the 80s, it was a revolutionary sensor for underwater vehicles and navigation as it could measure the velocity in the vehicle frame with high accuracy and update rates. However, the patent on the technology from 1996 led to a monopoly market with expensive DVLs. Nevertheless, the DVL became a very popular sensor for underwater vehicles. Although the sensors, needed in a DP system for ROVs, have been around for a while, it is strange that automated station keeping and tracking did not enter the commercial market until quite recently. Several Universities and research institutions, such as Woods Hole Oceanographic Institution (WHOI) and MBARI, have developed motion control systems with station keeping and tracking capabilities. Many papers from the 80s and 90s cover the topic, e.g. [106] from 1986, which is about a prototype supervisory control system for a ROV with experimental results.

Yet, the first commercial work class ROVs to use other automated functions than auto depth and heading did not come around until the beginning of the millennium. Schilling Robotics claims in [102] to be early pioneers in automated control of ROVs with their StationKeep introduced in 2001. StationKeep is an automated function for holding the ROV position. The improved StationKeep as of 2011 includes mid water station keeping ability when the DVL is out of range. These automated positioning functions are today implemented on the commercial Schilling UHD ROVs. The StationKeep is a result of a collaboration between C-innovation, CDL (Teledyne CDL<sup>3</sup>) and Schilling Robotics, where the INS system by CDL is the core enabling technology.

Oceaneering<sup>4</sup>, another ROV giant, teamed up with Sonardyne<sup>5</sup>, a major subsea navigation company, to deliver their automated ROV positioning solution; the Fly-by-wire system (FBW), which was demonstrated in the fall of 2012. In a press release from November 28, 2012, they claim the FBW to provide DP in all water depths with capabilities beyond current state-of-the-art, without affecting reliability or ease of use.

---

<sup>3</sup><http://www.teledyne-cdl.com>

<sup>4</sup><http://www.oceaneering.com>

<sup>5</sup><http://www.sonardyne.com>

As sensors and instruments are getting smaller and cheaper, automated positioning is now available for mini and micro ROVs. VideoRay<sup>6</sup> collaborated with Teledyne RDI, Teledyne BlueView and SeeByte to come up with their "click and go" positioning control system called the VideoRay CoPilot. In addition to station keeping, the CoPilot can track predefined survey patterns or use automatic target recognition, based on data from a BlueView multibeam sonar, to find and maintain a relative position to a target [100].

SeeByte has also delivered their SeeByte CoPilot positioning system to work class ROVs from SMD. The SeeByte CoPilot is an automatic positioning system software that can be retrofitted on any ROV fulfilling SeeByte's requirements on sensors specification and thruster configuration.

## 1.3 Problem Outline

The scientific goal of the thesis is to contribute with ideas and solutions that can enhance the operation of underwater vehicles and give them new applications. This is done by inventing or improving guidance and control functions and navigation solutions for ROVs. Developing a complete automated motion control system for a ROV requires knowledge in many aspects of control engineering, electronics, computer science, hydrodynamics, practical know-how and other skills. Thus, the contributions in this thesis are mainly limited to guidance, navigation and control. The work in these areas are covered in the following chapters. The following problems have been considered in more detail.

- Underwater navigation is the main problem to be solved in order to automate motion control of underwater vehicles. Thus, parts of the thesis consider the development of observers, model-based and sensor-based state estimators, that can estimate the ROVs position and velocity.
- The ROV must be guided in order to complete a mission. The guidance of ROVs can happen at several levels of human interaction. The thesis aims at providing solutions with guidance strategies for joystick in closed-loop control, A to B maneuvers and way-point tracking and management.
- Terrain following is a very useful feature during survey missions. The basic task in terrain following is to maintain a desired distance from the sea floor as the ROV moves over varying terrain. A proposed solution is covered in detail in the thesis with both theoretical contributions and experimental results and considerations.
- A ROV with an automated motion control system is needed in order to verify and test new theoretical contributions. Development, implementation and testing of an automated motion control system is done as part of the thesis work.

---

<sup>6</sup><http://www.videoray.com>

## 1.4 List of Publications

### Journal

1. F. Dukan and A.J. Sørensen. Sea Floor Geometry Approximation and Altitude Control of ROVs. *Control Engineering Practice*, 29:135–146, 2014
2. F. Dukan and A.J. Sørensen. Nonlinear Observer for Underwater Vehicles with IMU and Velocity Measurements in the Body Frame. *Submitted to IEEE Transactions on Control Systems Technology*, 2014
3. A.J. Sørensen, F. Dukan, M. Ludvigsen, D. de A. Fernandes, and M. Candeloro. Development of Dynamic Positioning and Tracking System for the ROV Minerva. In *Further Advances in Unmanned Marine Vehicles*. G. Roberts and B. Sutton, pages 113 –128, 2012
4. B. Zhao, R. Skjetne, M. Blanke, and F. Dukan. Particle Filter for Fault Diagnosis and Robust Navigation of Underwater Robot. *Control Systems Technology, IEEE Transactions on*, 1(1):1–16, 2014

### Conference

1. F. Dukan, M. Ludvigsen, and A.J. Sørensen. Dynamic Positioning System for a Small Size ROV with Experimental Results. In *OCEANS, 2011 IEEE - Spain*, pages 1 –10, june 2011
2. F. Dukan and A.J. Sørensen. Joystick in Closed-loop Control of ROVs with Experimental Results. In *Navigation, Guidance and Control of Underwater Vehicles*, volume 3, pages 293–300, 2012
3. F. Dukan and A.J. Sørensen. Altitude Estimation and Control of ROV by use of DVL. In *MCMC 2012, 9th IFAC Conference on Manoeuvring and Control of Marine Craft - Italy*, pages 1 –6, september 2012
4. F. Dukan and A.J. Sørensen. Integration Filter for APS, DVL, IMU and Pressure Gauge for Underwater Vehicles. In *CAMS 2013, The 9th IFAC Conference on Control Applications in Marine Systems 2013 - Japan*, pages 1 –6, september 2013
5. D. de A. Fernandes, F. Dukan, and A.J. Sørensen. Reference Model for High Performance and Low Energy Consumption Motions. In *Navigation, Guidance and Control of Underwater Vehicles*, volume 3, pages 217–222, 2012
6. Ø. Ødegård, M. Ludvigsen, G. Johnsen, A.J. Sørensen, S. Ekehaug, F. Dukan, and M. Moline. Managing Data from Multiple Sensors in an Interdisciplinary Research Cruise AUR-Lab Integrated Marine Environmental Monitoring and Mapping Cruise December 2011. In *Archaeology in the Digital Era. Papers from the 40th Annual Conference of Computer Applications and Quantitative Methods in Archaeology (CAA)*, volume 40. Amsterdam University Press, 2013

## 1.5 Contributions

The following scientific contributions are made in this work.

**Chapter 2:** Modeling and Hydrodynamics of ROVs. A process plant model for use in simulations and a control plant model for use in observers and controllers have been developed and implemented in both simulation and control software. The mathematical models of the ROVs build upon Fossen's robotic-like vectorial model.

**Chapter 3:** Development and Implementation of a ROV Motion Control System. A motion control system for automatic operation of ROVs has been developed, implemented and tested on the NTNU ROVs Minerva and 30k in the Trondheimsfjord.

**Chapter 4:** Underwater Navigation. i) A new method for fusing velocity measurements from a DVL with IMU data is proposed in order to improve the attitude, velocity and position estimation. The work has been presented in [28] and [30]. ii) An extended model-based Kalman filter is designed to provide another alternative for position and velocity estimation. This work was first published in [25].

**Chapter 5:** Guidance of ROVs. i) A guidance method for joystick in closed-loop control has been developed so the pilot does not need to compensate for environmental forces and ROV dynamics. The work has been presented in [27]. ii) A new type of reference model called "constant jerk" was developed for A to B maneuvers and way-point tracking. iii) A modified line-of-sight (LOS) guidance strategy for fully actuated vehicles is proposed.

**Chapter 6:** Altitude Control and Terrain Following. i) A new method for local sea floor geometry approximation from DVL measurements is proposed. ii) A new guidance law for depth needed in altitude control and terrain following is given. This work has been presented in [26] and [30].

**Chapter 7:** Ocean Science Research Campaigns. i) Several experimental results are obtained from cruises where the ROV motion control system has been implemented on the ROV Minerva and ROV 30k. This is a demonstration of the various contributions in the other Chapters working together.

## 1.6 Thesis Structure

The thesis is organized as

**Chapter 2:** Modeling and Hydrodynamics of ROVs. The notation style used in the thesis is introduced. Kinematics and mathematical models to describe the dynamics of ROVs are given. Forces acting on the ROV are explained. Sensors and their use in the motion control systems are presented.

**Chapter 3:** Development and Implementation of a ROV Motion Control System. The motion control system architecture, objectives and the development process are presented.

**Chapter 4:** Underwater Navigation. ROV navigation aspects are discussed and the contributions on vehicle state estimators are presented. Experimental results, showing the performance of the proposed observers, are shown.

**Chapter 5:** Guidance of ROVs. The different ROV modes of operation and corresponding guidance strategies are discussed. The proposed guidance methods and experimental results are presented.

**Chapter 6:** Terrain Following. Terrain following and altitude control are covered in detail. Contributions on sea floor geometry approximation methods and altitude control are presented and backed up by experimental results.

**Chapter 7:** Ocean Science Research Campaigns. The importance of doing experiments when working with ROV motion control systems is explained. Some important cruises and experiences are presented.

**Chapter 8:** Conclusions. The main results of the thesis are concluded and further work is suggested.

**Appendix A:** NTNU Vehicles. Specifications and dynamical properties of the NTNU ROVs Minerva and 30 k are given. The specifications of RV Gunnerus are presented.

**Appendix B:** Position & Velocity Control. The control laws for position and velocity control are given.

**Appendix C:** Mathematical Toolbox. Important definitions referred to in the main part are included.

**Appendix D:** Altitude Control Dynamics and Stability. Assessment of the dynamics and stability of the proposed closed-loop altitude control via depth control.

# Chapter 2

## Modeling and Hydrodynamics of ROVs

Mathematical models of the ROV and hydrodynamics are given in this section. Notations and the equations of motion are represented using Fossen's Robotic-like vectorial model. This is an efficient way of describing differential equations in 6 degrees of freedom with coupling effects in matrix form. A section describing sensors and their measurement equations are also included.

The chapter is mainly based on [40] where theory has been adapted to fit the ROV purpose. Theory from [36] and [87] are also included. The sensor section is derived as part of the thesis work, although the matrix notation is adopted from [40].

The main purpose of obtaining a hydrodynamical model is to be able to simulate the ROV motions and to exploit the knowledge of the ROV dynamics in the design of observers, controllers and thruster allocation.

### 2.1 Notations

The notation used in the thesis is adopted from the SNAME convention and Fossen's Robotic-like vectorial model. Motion, position and orientation of a vehicle are given by vectors and generalized coordinates.

The 6 degrees of freedom (DOF) of a vehicle and notations, according to the SNAME convention, are given in Table 2.1.

Table 2.1: Degrees of freedom.

no.	DOF	Forces & moments	mo-	Linear & angular velocities	Positions & Euler angles
1	Surge	X		$u$	$x$
2	Sway	Y		$v$	$y$
3	Heave	Z		$w$	$z$
4	Roll	K		$p$	$\phi$
5	Pitch	M		$q$	$\theta$
6	Yaw	N		$r$	$\psi$

### 2.1.1 Generalized Coordinates

The generalized position and velocity coordinates are given by (2.1) and (2.2), respectively.

$$\boldsymbol{\eta} = [x \ y \ z \ \phi \ \theta \ \psi]^T, \quad (2.1)$$

$$\boldsymbol{\nu} = [u \ v \ w \ p \ q \ r]^T. \quad (2.2)$$

The linear and angular position and velocity vectors are given by (2.3). These are sub-vectors of the generalized coordinates.

$$\boldsymbol{p} = \begin{bmatrix} x \\ y \\ z \end{bmatrix}, \quad \boldsymbol{v} = \begin{bmatrix} u \\ v \\ w \end{bmatrix}, \quad \boldsymbol{\Theta} = \begin{bmatrix} \phi \\ \theta \\ \psi \end{bmatrix}, \quad \boldsymbol{\omega} = \begin{bmatrix} p \\ q \\ r \end{bmatrix}, \quad (2.3)$$

where  $\boldsymbol{p} \in \mathbb{R}^{3 \times 1}$  is the linear position,  $\boldsymbol{v} \in \mathbb{R}^{3 \times 1}$  is the linear velocity,  $\boldsymbol{\Theta} \in \mathbb{R}^{3 \times 1}$  is the angular position, also referred to as attitude.  $\boldsymbol{p} \in \mathbb{R}^{3 \times 1}$  is the angular velocity, also called the turn rate vector or rotational velocity.

The force vector with elements corresponding to the 6 DOFs are given by (2.4).

$$\boldsymbol{\tau} = [X \ Y \ Z \ K \ M \ N]^T. \quad (2.4)$$

### 2.1.2 Notation Norms

All matrices are in boldface, upper case letters. All vectors are in boldface, lower case letters.

The estimate of a variable  $x$  is noted as  $\hat{x}$ , the time derivative is noted as  $\dot{x}$ , and the time derivative of the estimated variable is noted as  $\dot{\hat{x}}$ . Desired variables are noted with subscript as in  $x_d$ .

The cross product of vectors  $\boldsymbol{a} \in \mathbb{R}^3$  and  $\boldsymbol{b} \in \mathbb{R}^3$  can be calculated using the cross product operator  $\boldsymbol{S}$  as

$$\boldsymbol{a} \times \boldsymbol{b} = \boldsymbol{S}(\boldsymbol{a})\boldsymbol{b}, \quad (2.5)$$

where  $\boldsymbol{S}$  is defined as

$$\boldsymbol{S}(\boldsymbol{a}) = \begin{bmatrix} 0 & -a_3 & a_2 \\ a_3 & 0 & -a_1 \\ -a_2 & a_1 & 0 \end{bmatrix}, \quad \boldsymbol{a} = \begin{bmatrix} a_1 \\ a_2 \\ a_3 \end{bmatrix}. \quad (2.6)$$

$\boldsymbol{S}$  is a skew symmetric matrix, i.e.  $\boldsymbol{S} = -\boldsymbol{S}^T$ .

## 2.2 Kinematics

The most important background material for understanding the mathematical model of the ROV is provided in this section. A method for writing equations of motion in matrix form is presented and the reference frames used in the thesis are explained. Transformations and related notations are also described in this section.

### 2.2.1 Fossen's Robot-Like Vectorial Model

The equations of motion developed for the ROV are written in a vectorial setting adopted from [40]. An example of using the generalized coordinates and matrices to describe the 6 DOF differential equations of motion is seen in (2.7) and (2.8).

$$\dot{\boldsymbol{\eta}} = \mathbf{J}(\boldsymbol{\eta})\boldsymbol{\nu}, \quad (2.7)$$

$$\mathbf{M}\dot{\boldsymbol{\nu}} + \mathbf{C}(\boldsymbol{\nu})\boldsymbol{\nu} + \mathbf{D}(\boldsymbol{\nu})\boldsymbol{\nu} + \mathbf{g}(\boldsymbol{\eta}) = \boldsymbol{\tau}, \quad (2.8)$$

where  $\mathbf{J} \in \mathbb{R}^{6 \times 6}$  is the rotation matrix from the vehicle frame to the reference frame.  $\mathbf{M} \in \mathbb{R}^{6 \times 6}$  is the mass matrix,  $\mathbf{C} \in \mathbb{R}^{6 \times 6}$  is the Coriolis and centripetal force matrix and  $\mathbf{D} \in \mathbb{R}^{6 \times 6}$  is the damping matrix.  $\mathbf{g} \in \mathbb{R}^{6 \times 1}$  is a vector with restoring forces. Eq. (2.8) is Newton's second law expressed in a moving coordinate frame, hence the need to compensate for Coriolis and centripetal forces.

### 2.2.2 Reference Frames

Several reference frames are needed to describe the motion and to make use of various measurements. The reference frames that are used for navigation are

- ECI,  $\{i\}$ : The Earth-centered inertial frame with axes  $\{i\} = [x_i, y_i, z_i]$ ,
- ECEF,  $\{e\}$ : The Earth-centered Earth fixed frame with axes  $\{e\} = [x_e, y_e, z_e]$ ,
- NED,  $\{n\}$ : The North, East, Down frame with axes  $\{n\} = [x_n, y_n, z_n]$ ,

where the  $\{i\}$  frame is assumed to be an inertial frame when high accuracy is required. For even greater accuracy one could use a Sun-centered inertial frame, but this is usually not necessary. For slowly moving vehicles with restricted area of motion, the  $\{n\}$  frame can be assumed to be inertial for most applications. The  $\{e\}$  frame is useful for describing motion over longer distances where the flat Earth approximation of  $\{n\}$  is inaccurate. E.g. GPS coordinates are given in the  $\{e\}$  frame, but it is impractical to display attitude in this frame as zero roll and pitch usually means level. Figure 2.1 shows the reference frames and their relative positions and orientations.

The vehicle frame is fixed to the vehicle origin and rotates with the vehicle. This moving coordinate frame is also referred to as the body frame and is listed together with the measurement frame.

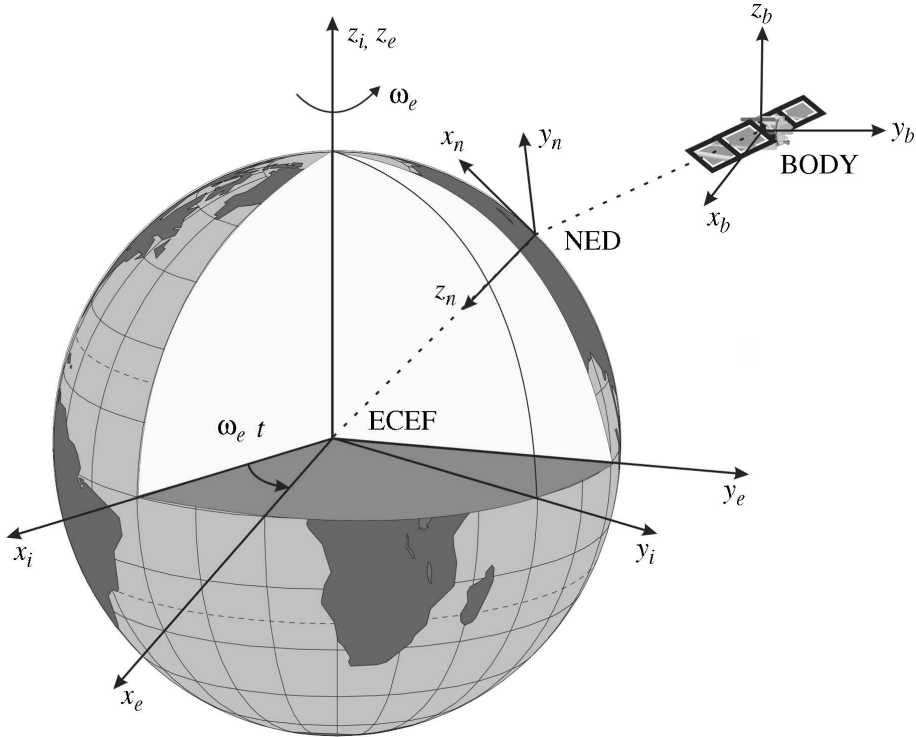


Figure 2.1: Reference and body frames (Courtesy of Wiley).

- BODY,  $\{b\}$ : The body frame with axes  $\{b\} = [x_b, y_b, z_b]$ ,
- MES,  $\{m\}$ : The measurement frame with axes  $\{m\} = [x_m, y_m, z_m]$ .

The measurement frame is also a moving frame, usually moving and rotating together with the body frame. Vector measurements, from an instrument that is mounted on a vehicle, are in the instrument's measurement frame and moving with the body frame. Other notations for the measurement frame are used when e.g. more than one instrument with vector measurements are mounted on a vehicle.

The body frame of a ROV is seen in Figure 2.2. The  $\{b\}$  axes define the surge, sway and heave directions and the rotational directions according to the right-hand rule.

### 2.2.3 Vector Notations

Super and subscripts on vectors are used to specify which reference frame the vector is decomposed in and where the vector starts and ends.

A vector decomposed in frame  $\{x\}$  can be expressed in  $\{y\}$  using the transformation matrix  $R_x^y(\Theta_{yx}) \in \mathbb{R}^{3 \times 3}$  as  $p^y = R_x^y p^x$ , where the argument of the rotation matrix was omitted for brevity. A vector superscript tells which frame it is decomposed in and the subscript has relative information about the vector. E.g.  $p_{x/y}^z$  is the position vector of the  $\{x\}$  frame relative to the  $\{y\}$  frame decomposed in the  $\{z\}$  frame.

The rotation of a coordinate system  $\{x\}$  w.r.t coordinate system  $\{y\}$  is given by the rotation vector  $\Theta_{yx} \in SO^3$ .

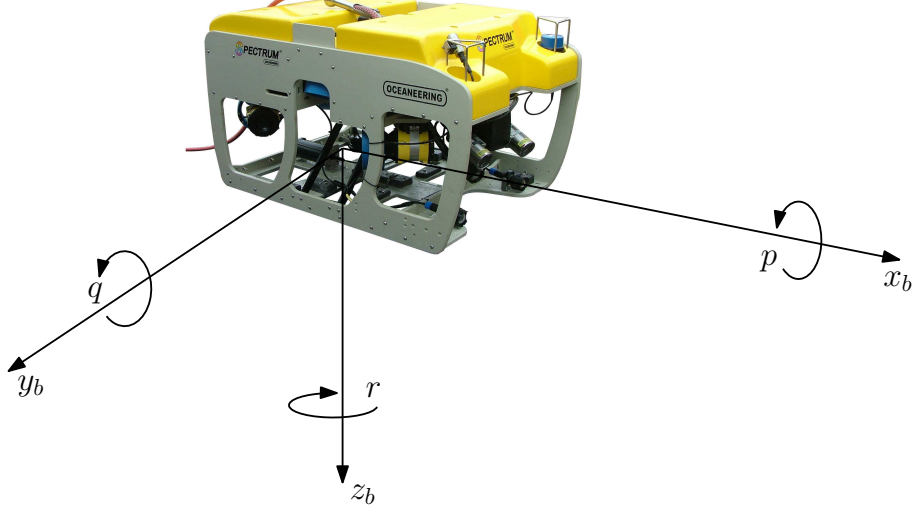


Figure 2.2: ROV body frame and rotations.

## 2.2.4 Transformations

### Translational Transformations

The rotation matrix from  $\{b\}$  to  $\{n\}$  is  $\mathbf{R}_b^n(\Theta_{nb}) \in SO(3)$  and is calculated as

$$\mathbf{R}_b^n(\Theta_{nb}) = \mathbf{R}_{z,\psi} \mathbf{R}_{y,\theta} \mathbf{R}_{x,\phi}, \quad (2.9)$$

where

$$\mathbf{R}_{x,\phi} = \begin{bmatrix} 1 & 0 & 0 \\ 0 & c\phi & -s\phi \\ 0 & s\phi & c\phi \end{bmatrix}, \quad \mathbf{R}_{y,\theta} = \begin{bmatrix} c\theta & 0 & s\theta \\ 0 & 1 & 0 \\ -s\theta & 0 & c\theta \end{bmatrix}, \quad \mathbf{R}_{z,\psi} = \begin{bmatrix} c\psi & -s\psi & 0 \\ s\psi & c\psi & 0 \\ 0 & 0 & 1 \end{bmatrix}, \quad (2.10)$$

are the rotations matrices from roll, pitch and yaw, respectively [40]. c and s are short for cosine and sine. Note that the order of rotation is important.

The inverse transformation is

$$\mathbf{R}_b^n(\Theta_{nb})^{-1} = \mathbf{R}_b^n(\Theta_{nb})^T = \mathbf{R}_n^b(\Theta_{nb}), \quad (2.11)$$

where it is noted that this Euler angle representation has a singularity at 90 degrees of pitch. It is recommended to use a quaternion representation of the attitude to avoid singularities and ease the computational footprint in implementations

### Rotational Velocity Transformations

The Euler rate vector  $\dot{\Theta}_{nb}$  can be obtained from the body fixed angular velocity vector  $\omega_{b/n}^b$  by a transformation given as

$$\dot{\Theta}_{nb} = \mathbf{T}_\Theta(\Theta_{nb})\omega_{b/n}^b, \quad (2.12)$$

where

$$\mathbf{T}_\Theta(\Theta_{nb}) = \begin{bmatrix} 1 & \sin \phi \tan \theta & \cos \phi \tan \theta \\ 0 & \cos \phi & -\sin \phi \\ 0 & \sin \phi / \cos \theta & \cos \phi / \cos \theta \end{bmatrix}, \quad (2.13)$$

and the derivation is shown in [40].

The transformation matrix for the generalized coordinates,  $\mathbf{J}(\boldsymbol{\eta})$ , as used in (2.7) can then be written as

$$\mathbf{J}(\boldsymbol{\eta}) = \begin{bmatrix} \mathbf{R}_b^n(\Theta_{nb}) & \mathbf{0}_{3 \times 3} \\ \mathbf{0}_{3 \times 3} & \mathbf{T}_\Theta(\Theta_{nb}) \end{bmatrix}. \quad (2.14)$$

More details on transformations between reference frames and moving coordinate systems are found in [40].

### Quaternion Representation of Rotation

A quaternion representation of the rotation is used to avoid singularities and ease the computational footprint. The quaternion vector representing the rotation of  $\{x\}$  w.r.t  $\{y\}$  is  $\mathbf{q}_x^y = [\eta \ \boldsymbol{\epsilon}^T]^T$ , where  $\eta$  is the real part and  $\boldsymbol{\epsilon}^T = [\epsilon_1 \ \epsilon_2 \ \epsilon_3]^T$  is a vector with three imaginary parts. The unit quaternion satisfies  $\mathbf{q}\mathbf{q}^T = 1$ . The set of unit quaternions is defined as  $Q := \{\mathbf{q} | \mathbf{q}^T \mathbf{q} = 1, \mathbf{q} = [\eta \ \boldsymbol{\epsilon}^T]^T, \ \boldsymbol{\epsilon} \in \mathbb{R}^3 \text{ and } \eta \in \mathbb{R}\}$  [40]. This representation is used in some of the methods proposed in the thesis and details on quaternions are found in Appendix C.

#### 2.2.5 Earth's Rotation and Gravity

It is sometimes useful to express the Earth's rotation in the  $\{n\}$  frame, such as when using high accuracy gyroscopes.  $\omega_{e/i}^n$  is the Earth's angular velocity decomposed in the  $\{n\}$  frame as seen in (2.15).

$$\omega_{e/i}^n = \mathbf{R}_e^n(\Theta_{en})\omega_{e/i}^e = \begin{bmatrix} \omega_e \cos(\mu) \\ 0 \\ -\omega_e \sin(\mu) \end{bmatrix}, \quad (2.15)$$

where  $\Theta_{en}$  is the orientation of the local  $\{n\}$  frame w.r.t  $\{e\}$ .  $\omega_e = 7.292115 \times 10^{-5}$  rad/s is the angular velocity of the Earth [40], and  $\mu$  is the latitude. As the in-bias gyro stability of MEMS IMUs are getting lower than the turn rate of the Earth,  $\omega_{e/i}^n$  should not be neglected in the the navigation system.

For a vehicle traveling large distance, its local  $\{n\}$  frame will rotate with a rate  $\omega_{n/e}^n$  as

$$\omega_{n/e}^n = \frac{1}{R_0 - z} \begin{bmatrix} 0 & 1 & 0 \\ -1 & 0 & 0 \\ 0 & -\tan(\mu) & 0 \end{bmatrix} \mathbf{R}_b^n \mathbf{v}_{b/e}^b, \quad (2.16)$$

where  $R_0$  is the Earth's radius, and  $z$  is the vertical coordinate in  $\{n\}$ . Note that  $\omega_{n/e}^n$  will be very small, in the order of  $10^{-8}$  to  $10^{-7}$  rads/s, for velocities typical for underwater vehicles. Thus,  $\omega_{n/e}^n$  can be neglected for practical applications.

$\mathbf{g}_l^n$  is the local gravity vector, or the "plumb bob" gravity vector, in  $\{n\}$ . This vector is the resultant of the gravity due to the mass of the Earth and the centripetal acceleration from the Earth's angular velocity. The components of  $\mathbf{g}_l^n$  are seen in (2.18) as

$$\mathbf{g}_l^n = \mathbf{g}^n - \omega_{e/i}^n \times \omega_{e/i}^n \times \mathbf{p}_{b/e}^n \quad (2.17)$$

$$= \mathbf{g}^n - \frac{1}{2}\omega_e^2(R_0 - z) \begin{bmatrix} \sin(2\mu) \\ 0 \\ 1 + \cos(2\mu) \end{bmatrix}, \quad (2.18)$$

where  $\mathbf{g}^n$  is the gravity due to the Earth's mass and will vary with location.  $\mathbf{g}_l^n$  is important in the gravity compensation used in INS, and in some of the methods proposed in the thesis.

## 2.3 Equations of Motion

The equations of motion for a ROV are presented in the following. A process plant model, which is a detailed mathematical model of the ROV dynamics, and control plant model, which is a simplified model [86]. The process plant model is used in simulations, and the control plant model is used in controller and observer design. There are no new contributions in this section other than adapting known models and hydrodynamic theory to obtain a mathematical model of the ROV dynamics.

The equations are expressed in the center of origin (CO), which can be placed anywhere, but most convenient on the center line or at intersections of symmetry planes. The vector from CO to the center of gravity (CG) is  $\mathbf{r}_g^b = [x_g \ y_g \ z_g]^T$ .

### 2.3.1 Process Plant Model

The process plant model given in (2.19) and (2.20) is the Newton-Euler equations of motion about CO. This model is based on Fossen's Robotic-like model as described in [40].

The Newtonian mechanics are expressed in the body frame in (2.20) and transformed to the NED frame in (2.19). The model contains rigid-body dynamics terms, hydrodynamical terms, a hydrostatic term, propulsion force and external forces.

$$\begin{aligned} \dot{\boldsymbol{\eta}} &= \mathbf{J}(\boldsymbol{\eta})\boldsymbol{\nu}, \quad (2.19) \\ \underbrace{\mathbf{M}_{RB}\dot{\boldsymbol{\nu}} + \mathbf{C}_{RB}(\boldsymbol{\nu})\boldsymbol{\nu}}_{\text{rigid-body terms}} + \underbrace{\mathbf{M}_A\dot{\boldsymbol{\nu}}_r + \mathbf{C}_A(\boldsymbol{\nu}_r)\boldsymbol{\nu}_r + \mathbf{D}(\boldsymbol{\nu}_r)\boldsymbol{\nu}_r + \mathbf{g}(\boldsymbol{\eta})}_{\text{hydrodynamic terms}} &= \boldsymbol{\tau} + \boldsymbol{\tau}_{ext}, \quad (2.20) \end{aligned}$$

where  $\mathbf{M}_{RB} \in \mathbb{R}^{6 \times 6}$  is the rigid-body mass matrix in CO and  $\mathbf{C}_{RB}(\boldsymbol{\nu}) \in \mathbb{R}^{6 \times 6}$  is the rigid-body Coriolis and centripetal matrix.  $\mathbf{M}_A \in \mathbb{R}^{6 \times 6}$  is the added mass matrix in CO,  $\mathbf{C}_A(\boldsymbol{\nu}_r) \in \mathbb{R}^{6 \times 6}$  is the added mass Coriolis and centripetal matrix and  $\mathbf{D}(\boldsymbol{\nu}_r) \in \mathbb{R}^{6 \times 6}$  is the damping matrix.  $\mathbf{g}(\boldsymbol{\eta}) \in \mathbb{R}^{6 \times 1}$  is the hydrostatic restoring force vector,  $\boldsymbol{\tau} \in \mathbb{R}^{6 \times 1}$  is the propulsion force vector, and  $\boldsymbol{\tau}_{ext} \in \mathbb{R}^{6 \times 1}$  is a vector with external forces, including the umbilical and manipulator forces. Each of the terms and matrices are explained in more detail in the following.

$\boldsymbol{\nu}_r \in \mathbb{R}^{6 \times 1}$  is the relative velocity vector with respect to the water and it is calculated as

$$\boldsymbol{\nu}_r = \boldsymbol{\nu} - \boldsymbol{\nu}_c, \quad (2.21)$$

where  $\boldsymbol{\nu}_c \in \mathbb{R}^{6 \times 1}$  is the ocean current velocity vector decomposed in the body frame. For irrotational ocean currents

$$\boldsymbol{\nu}_c = [u_c \ v_c \ w_c \ 0 \ 0 \ 0]^T, \quad (2.22)$$

where  $u_c$ ,  $v_c$  and  $w_c$  are the velocity components of the ocean current. The work in this thesis assumes irrotational ocean currents.

### Rigid-body Dynamics

The rigid-body mass matrix in CG is

$$\mathbf{M}_{RB}^{CG} = \begin{bmatrix} m\mathbf{I}_{3 \times 3} & \mathbf{0}_{3 \times 3} \\ \mathbf{0}_{3 \times 3} & \mathbf{I}_g \end{bmatrix}, \quad (2.23)$$

where  $m$  is the mass of the vehicle and  $\mathbf{I}_g \in \mathbb{R}^{3 \times 3}$  is the inertia matrix about CG given as

$$\mathbf{I}_g = \begin{bmatrix} \mathbf{I}_x & -\mathbf{I}_{xy} & -\mathbf{I}_{xz} \\ -\mathbf{I}_{yx} & \mathbf{I}_y & -\mathbf{I}_{yz} \\ -\mathbf{I}_{zx} & -\mathbf{I}_{zy} & \mathbf{I}_z \end{bmatrix}, \quad (2.24)$$

where  $\mathbf{I}_x$ ,  $\mathbf{I}_y$ ,  $\mathbf{I}_z$  are the moments of inertia about the  $\{b\}$  axes, and  $\mathbf{I}_{xy} = \mathbf{I}_{yx}$ ,  $\mathbf{I}_{xz} = \mathbf{I}_{zx}$  and  $\mathbf{I}_{yz} = \mathbf{I}_{zy}$  are the products of inertia. See [40] for more details. The inertia matrix  $\mathbf{I}_g$  is approximated as if the ROV is a box with evenly distributed mass.

The rigid-body Coriolis and centripetal matrix in CG is

$$\mathbf{C}_{RB}^{CG} = \begin{bmatrix} m\mathbf{S}(\omega_{b/n}^b) & \mathbf{0}_{3 \times 3} \\ \mathbf{0}_{3 \times 3} & -\mathbf{S}(\mathbf{I}_g \omega_{b/n}^b) \end{bmatrix}, \quad (2.25)$$

and is calculated directly from the mass, inertia matrix and the turn rate vector.

The mass and Coriolis matrices in CG must be transformed to CO before use in (2.19). The transformation is done using the matrix (2.26)

$$\mathbf{H}(\mathbf{r}_g^b) = \begin{bmatrix} \mathbf{I}_{3 \times 3} & \mathbf{S}^T(\mathbf{r}_g^b) \\ \mathbf{0}_{3 \times 3} & \mathbf{I}_{3 \times 3} \end{bmatrix}, \quad (2.26)$$

to get

$$\mathbf{M}_{RB} = \mathbf{H}^T(\mathbf{r}_g^b) \mathbf{M}_{RB}^{CG} \mathbf{H}(\mathbf{r}_g^b), \quad (2.27)$$

$$\mathbf{C}_{RB} = \mathbf{H}^T(\mathbf{r}_g^b) \mathbf{C}_{RB}^{CG} \mathbf{H}(\mathbf{r}_g^b), \quad (2.28)$$

which are the mass and Coriolis matrices in CO, respectively. A derivation is given in [40].

## Hydrodynamics

**Added mass:** The added mass of a body (vehicle) in a fluid is given by the added mass matrix  $\mathbf{M}_A$  with components as

$$\mathbf{M}_A = - \begin{bmatrix} X_{\dot{u}} & X_{\dot{v}} & X_{\dot{w}} & X_{\dot{p}} & X_{\dot{q}} & X_{\dot{r}} \\ Y_{\dot{u}} & Y_{\dot{v}} & Y_{\dot{w}} & Y_{\dot{p}} & Y_{\dot{q}} & Y_{\dot{r}} \\ Z_{\dot{u}} & Z_{\dot{v}} & Z_{\dot{w}} & Z_{\dot{p}} & Z_{\dot{q}} & Z_{\dot{r}} \\ K_{\dot{u}} & K_{\dot{v}} & K_{\dot{w}} & K_{\dot{p}} & K_{\dot{q}} & K_{\dot{r}} \\ M_{\dot{u}} & M_{\dot{v}} & M_{\dot{w}} & M_{\dot{p}} & M_{\dot{q}} & M_{\dot{r}} \\ N_{\dot{u}} & N_{\dot{v}} & N_{\dot{w}} & N_{\dot{p}} & N_{\dot{q}} & N_{\dot{r}} \end{bmatrix}, \quad (2.29)$$

where e.g. the hydrodynamical derivative  $X_{\dot{r}}$  is the added mass force coefficient in surge caused by acceleration in yaw. Note that  $\mathbf{M}_A$  is symmetrical,  $\mathbf{M}_A = \mathbf{M}_A^T$ . When a body is moving or oscillating in water, parts of the surrounding water mass will move as well. This means there is a pressure field in the water around the body. This pressure, not including the hydrostatic pressure, can be integrated over the surface of the body to find the added mass forces. Thus, added mass is not a specific amount of water moving with the body, but it should be understood in terms of hydrodynamic pressure [36].

The pressure field in the water, set up by the body motions, depends on the boundary conditions of the surrounding water, such as free surface and sea floor. Motions of a body in or close to the surface will generate waves, and the pressure field will be frequency dependent. For underwater vehicles, it is assumed that no waves are generated, and the added mass is constant.

An underwater vehicle has restoring forces only in roll and pitch, hence there are no natural frequencies for the other DOFs. The constant added mass is calculated as the zero frequency added mass for surge, sway, heave and yaw. For roll and pitch, the added mass corresponding to the natural frequency is used. The roll and pitch natural frequencies are calculated as

$$\omega_{roll} = \sqrt{\frac{C_{44}}{I_x + K_p(\omega_{roll})}}, \quad \omega_{pitch} = \sqrt{\frac{C_{55}}{I_y + M_q(\omega_{pitch})}}, \quad (2.30)$$

where  $C_{44}$  and  $C_{55}$  are the hydrostatic restoring forces to be defined later. Note that this is a recursive equation.

It can be difficult to find all 36 terms including the 30 off diagonal, cross coupling terms. Since  $\mathbf{M}_A$  is symmetrical, it suffices to find the 6 diagonal elements and the 15 elements above the diagonal. This can be reduced further by exploiting symmetry properties of the vehicle itself. To simplify, the ROV is assumed to have symmetry about the xz, yz, and xy planes (port/starboard, fore/aft, bottom/top). Thus, there are no cross coupling added mass terms and the added mass matrix is reduced to

$$\mathbf{M}_A = -\text{diag}\{X_{\dot{u}}(0), Y_{\dot{v}}(0), Z_{\dot{w}}(0), K_p(\omega_{roll}), M_q(\omega_{pitch}), N_r(0)\}, \quad (2.31)$$

where the values of each element is calculated from hydrodynamical tables. Alternatively, the full 36 element added mass matrix can be calculated by a computer program such as WADAM or WAMIT if CAD drawings are available. This has been done for the ROV 30k in [3].

**Coriolis and centripetal forces:** The hydrodynamical Coriolis and centripetal matrix  $\mathbf{C}_A$ , for a rigid body moving through an ideal fluid, can always be parametrized to be skew-symmetric so

$$\mathbf{C}_A(\boldsymbol{\nu}) = -\mathbf{C}_A^T(\boldsymbol{\nu}), \quad \forall \boldsymbol{\nu} \in \mathbb{R}^{6 \times 1} \quad (2.32)$$

$\mathbf{C}_A$  is calculated from the added mass matrix and the generalized velocity vector. The parametrization of  $\mathbf{C}_A$  used for the ROV is given in (2.33) as suggested by [40].

$$\mathbf{C}_A(\boldsymbol{\nu}) = - \begin{bmatrix} \mathbf{0}_{3 \times 3} & -\mathbf{S}(\mathbf{A}_{11}\mathbf{v} + \mathbf{A}_{12}\boldsymbol{\omega}) \\ -\mathbf{S}(\mathbf{A}_{11}\mathbf{v} + \mathbf{A}_{12}\boldsymbol{\omega}) & -\mathbf{S}(\mathbf{A}_{21}\mathbf{v} + \mathbf{A}_{22}\boldsymbol{\omega}) \end{bmatrix}, \quad (2.33)$$

where  $A_{ij} \in \mathbb{R}^{3 \times 3}$  is given by

$$\mathbf{M}_A = - \begin{bmatrix} A_{11} & A_{12} \\ A_{21} & A_{22} \end{bmatrix}. \quad (2.34)$$

**Damping:** For underwater vehicles, such as the ROV, the potential damping and other wave related damping effects are neglected. The damping of a ROV is mainly caused by vortex shedding and skin friction. The easiest way to determine damping properties of a ROV is to approximate its geometry as a box and use coefficients from hydrodynamical tables. However, the box approximation will result in an underestimation of the damping forces as the ROV has many cavities, exposed cables, manipulators and other appendages such as lights and instruments. It is difficult to calculate the damping of each of these appendages and asses the effects of flow interactions in the ROV frame caused by motion and jet from thrusters. To simplify, the damping is approximated with a linear and quadratic term given as

$$\mathbf{D}(\boldsymbol{\nu}_r) = \mathbf{D} + \mathbf{D}_n(\boldsymbol{\nu}_r), \quad (2.35)$$

where  $\mathbf{D}$  is the linear damping matrix due to skin friction and  $\mathbf{D}_n(\boldsymbol{\nu}_r)$  is the quadratic damping, mainly caused by vortex shedding. The damping matrix  $\mathbf{D}(\boldsymbol{\nu}_r)$  is strictly positive as energy is dissipated through damping.

An alternative damping model, especially suitable for low speeds, is given as

$$\mathbf{D}(\boldsymbol{\nu}_r) = \mathbf{D}e^{-\alpha||\boldsymbol{\nu}_r||} + \mathbf{D}_n(\boldsymbol{\nu}_r), \quad (2.36)$$

where  $\alpha$  is a tuning parameter for the exponential decaying linear damping with the vehicle speed,  $||\boldsymbol{\nu}_r||$ . This damping model was proposed by [87].

Diagonal damping matrices are used in the modeling of ROVs due to the difficulty of finding values for the non-diagonal damping terms, from calculation or experiments, and because the diagonal terms are dominant. The linear and nonlinear damping matrices are given as

$$\mathbf{D} = -\text{diag}\{X_u, Y_v, Z_w, K_p, M_q, N_r\}, \quad (2.37)$$

$$\mathbf{D}_n(\boldsymbol{\nu}_r) = -\text{diag}\{X_{|u|u}|u_r|, Y_{|v|v}|v_r|, Z_{|w|w}|w_r|, K_{|p|p}|p_r|, M_{|q|q}|q_r|, N_{|r|r}|r_r|\} \quad (2.38)$$

where the elements of  $\mathbf{D}$  and  $\mathbf{D}_n(\boldsymbol{\nu}_r)$  are determined from experiments. The damping coefficients can also be approximated analytically, assuming a box geometry, as in [36].

### Hydrostatics and Restoring Forces

The gravitational and buoyancy forces and the corresponding restoring moments are calculated in CG as

$$\mathbf{g}^{CG}(\boldsymbol{\eta}) = \begin{bmatrix} (W - B) \sin \theta \\ -(W - B) \cos \theta \sin \phi \\ -(W - B) \cos \theta \cos \phi \\ y_b B \cos \theta \cos \phi - z_b B \cos \theta \sin \phi \\ -z_b B \sin \theta - x_b B \cos \theta \cos \phi \\ x_b B \cos \theta \sin \phi + y_b B \sin \theta \end{bmatrix}, \quad (2.39)$$

where  $W$  is the vehicle weight and  $B$  is the buoyancy calculated as

$$W = mg, \quad B = \rho g \nabla, \quad (2.40)$$

where  $\rho$  is the water density,  $g$  is the acceleration of gravity and  $\nabla$  is the total volume (displacement) of the ROV. The vector from CG to the center of buoyancy (CB) is  $r^{CB} = [x_b, y_b, z_b]^T$ .  $\mathbf{g}^{CG}(\boldsymbol{\eta})$  is transformed to CO by

$$\mathbf{g}(\boldsymbol{\eta}) = \mathbf{H}^T(\mathbf{r}_g^b) \mathbf{g}^{CG}(\boldsymbol{\eta}), \quad (2.41)$$

before use in (2.20). Note that for most ROVs CB is straight above CG, i.e.  $r^{CB} = [0, 0, z_b]^T$ . Thus, the linearized spring coefficients for roll and pitch are  $C_{44} = C_{55} = z_b B$ , which is used in the calculation of the natural frequencies for roll and pitch.

Note that the equation of motion in (2.20) can be completely written in terms of the relative velocity as

$$\mathbf{M} \dot{\mathbf{v}}_r + \mathbf{C}(\boldsymbol{\nu}_r) \boldsymbol{\nu}_r + \mathbf{D}(\boldsymbol{\nu}_r) \boldsymbol{\nu}_r + \mathbf{g}(\boldsymbol{\eta}) = \boldsymbol{\tau} + \boldsymbol{\tau}_{ext}, \quad (2.42)$$

if the ocean current is irrotational,  $\boldsymbol{\nu}_c = [u_c \ v_c \ w_c \ 0 \ 0 \ 0]^T$  and the Coriolis and centripetal matrix is parameterized independent of linear velocity [40]. The effective mass,  $\mathbf{M} = \mathbf{M}_{RB} + \mathbf{M}_A$ , and Coriolis and centripetal,  $\mathbf{C}(\boldsymbol{\nu}_r) = \mathbf{C}_{RB}(\boldsymbol{\nu}_r) + \mathbf{C}_A(\boldsymbol{\nu}_r)$ , matrices are the sum of the respective rigid-body and hydrodynamical matrices.

The equations of motion in (2.19) and (2.20) have been implemented in a computer program to provide the simulation results presented in this thesis.

The propulsion thrust vector  $\boldsymbol{\tau}$  and external forces  $\boldsymbol{\tau}_{ext}$  are covered in Section 2.4.

### 2.3.2 Control Plant Model

The control plant model given by (2.43), (2.44) and (2.45) is used for analysis and in the design of observers and controllers. This is a simplified version of the process plant model. It is assumed that

- vehicle velocities are small, <1 m/s. Thus, the Coriolis and centripetal forces and nonlinear damping are neglected.

- ocean current velocities are constant or slowly varying. Thus, the equations are given in terms of the vehicle velocity,  $\nu$ , and additional forces from ocean currents are included in the bias estimate,  $b$ .
- roll and pitch motions are small, <10 degrees, and the ROV is neutrally buoyant with CB straight above CG. Thus, the restoring forces are linearized using  $G$ .

Although the control plant model a simplified model, it still captures the main dynamics of the ROV.

$$\dot{\eta} = J(\eta)\nu, \quad (2.43)$$

$$M\dot{\nu} + D\nu + G\eta = \tau + J^\top(\eta)b, \quad (2.44)$$

$$\dot{b} = -T_b^{-1}b + w_b, \quad (2.45)$$

where  $D \in \mathbb{R}^{6 \times 6}$  is the linear damping matrix.  $b \in \mathbb{R}^{6 \times 1}$  is the bias accounting for unmodelled dynamics and slowly varying loads, which is modeled as a 1<sup>st</sup> order Markov process.  $T_b \in \mathbb{R}^{6 \times 6}$  is a diagonal matrix with positive bias time constants.  $w_b \in \mathbb{R}^{6 \times 1}$  is a zero mean Gaussian white noise processes [87].  $G$  is a linearized restoring matrix given as

$$G^{CG} = \text{diag}\{0, 0, 0, -z_b B, -z_b B, 0\}, \quad (2.46)$$

$$G = H^T(r_g^b) G^{CG} H(r_g^b). \quad (2.47)$$

The bias estimation accounts for slowly varying forces, such as ocean currents, and errors in the modeling.

## 2.4 Generalized Forces

The generalized forces acting on the ROV are mainly from the ocean current, the umbilical, the manipulator and the thrusters. As seen in the process plant model in (2.20), the forces from the ocean current are included in the equations of motion through the relative velocity. Thus, only the model used for generating the ocean current velocity in a simulation is explained here. A model for the propulsion forces is given in this section as it is needed in the design of the control system.

The manipulator and umbilical forces can be dominating forces for some types of operation or for larger deep water ROVs. However, these are complex forces to model, and they are not included in the scope of the thesis. Previous work on ROV umbilical modeling and interaction with ROV and surface vessel motions is found in [60]. A control system for a thrust unit with cable is proposed in [79]. Modeling the ROV umbilical as lumped masses is suggested in [24] and experimental result are found in [72]. The presented models in the thesis are valid for a free swimming ROV where umbilical forces can be neglected. This is assumed to be valid for ROVs with relatively light tethers operating in shallow waters at low speeds.

### 2.4.1 Ocean Current Forces

The forces from the ocean current are included in the process plant model through the ocean current velocity in the body frame. In simulations, this is generated using a model of the ocean current speed and direction in the geographic reference frame, e.g. the NED frame.

The ocean current speed is  $V_c$  and it has vertical and horizontal direction  $\alpha_c$  and  $\beta_c$  in the  $\{n\}$  frame. The ocean current velocity vector in  $\{n\}$  is

$$\mathbf{v}_c^n = \mathbf{R}_{y,\alpha_c}^T \mathbf{R}_{z,-\beta_c}^T \begin{bmatrix} V_c \\ 0 \\ 0 \end{bmatrix}, \quad (2.48)$$

where the rotation matrices are found from (2.10) with  $\alpha_c$  and  $-\beta_c$  as arguments.

Dynamics for  $V_c$ ,  $\alpha_c$  and  $\beta_c$  can be added to obtain a slowly varying ocean current. A model suggested in [40] is to use a first order Gauss-Markov process as

$$\dot{V}_c + \mu V_c = w, \quad (2.49)$$

$$\dot{\alpha}_c + \mu_\alpha \alpha_c = w_\alpha, \quad (2.50)$$

$$\dot{\beta}_c + \mu_\beta \beta_c = w_\beta, \quad (2.51)$$

where  $\mu_i \geq 0$  is a constant and  $w_i$  is Gaussian white noise.

The ocean current is transformed to the body frame before use in the process plant model as

$$\boldsymbol{\nu}_c = \mathbf{J}^T(\boldsymbol{\eta}) \boldsymbol{\nu}_c^n, \quad (2.52)$$

where the elements of  $\boldsymbol{\nu}_c$  are given by (2.22).

### 2.4.2 Propulsion Forces

Most ROVs are fully actuated and can produce a force in any DOF by use of propellers. Each propulsion unit, with propeller and duct, is called a thruster. The thrusters used on the ROV Minerva are seen in Figure 2.3a and 2.3b which show the single and double side thrusters.

The forces produced by each thruster make up the total control force. However, the actual thrust is not easy to measure and must be estimated from a thruster model. The thruster dynamics are complex and errors in the thruster model affect the performance of higher level control as it is uncertain if the desired thrust vector  $\tau$  is produced. Thus, the actual control input is the revolution speed of the thrusters, and a mapping relating the revolution speed to thrust is needed. This section presents a model that relates the propeller revolution speed to thrust. However, the thrust also depends on flow velocity and conditions around the propeller. The performance of a single thruster in open water

is different from its performance when mounted on a vehicle. This is due to phenomena such as thruster-thruster interaction, flow patterns caused by the geometry of the ROV and equipment and other hydrodynamic effects. For details on thrust losses, see [84] and [78].

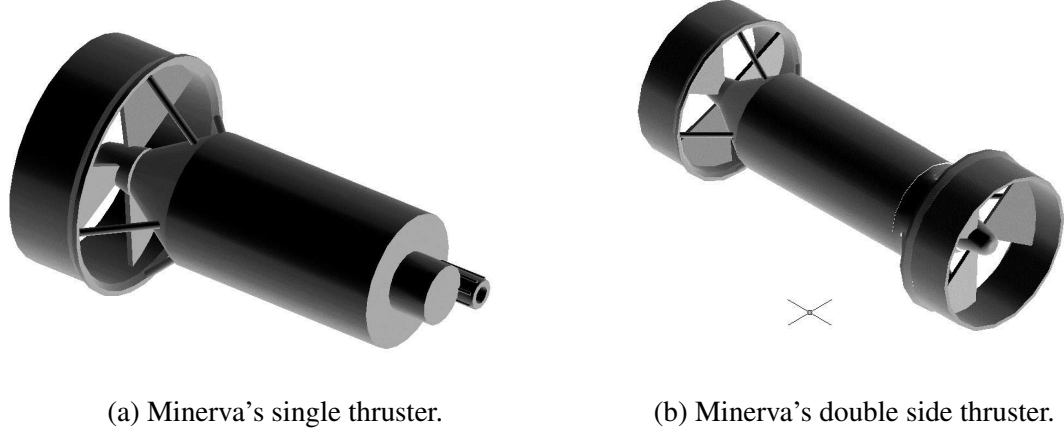


Figure 2.3: Thrusters on ROV Minerva.

A basic model of thrust production from a single thruster is given by (2.53) as

$$f = K_T(J)\rho D^4 n^2, \quad (2.53)$$

where  $f$  is the thrust,  $K_T(J)$  is the thrust coefficient,  $\rho$  is the water density,  $D$  is propeller diameter, and  $n$  is the propeller revolution speed in revolutions per second (r/s) [87].

The thrust coefficient depends on the advance number  $J$  which is given as

$$J = \frac{V_a}{nD}, \quad (2.54)$$

where  $V_a$  is the inflow water velocity to the propeller. The thrust coefficient can be given in a four quadrant diagram to show the thruster performance in all operation conditions [103]. An open water test was conducted in the cavitation tunnel at Marintek, Trondheim by Martin Ludvigsen in 2005 for a thruster used on the ROV Minerva. The results were reported in [64] and the polynomials in (2.55) and (2.56) were found from curve fitting of experimental data for the 1<sup>st</sup> and 3<sup>rd</sup> quadrant, respectively.

$$K_T(J)_1 = 0.5J^3 - 0.66J^2 - 0.25J + 0.24, \quad (2.55)$$

$$K_T(J)_3 = 0.025J^3 + 0.28J^2 - 0.17J - 0.15, \quad (2.56)$$

For no ocean current, 1<sup>st</sup> quadrant corresponds to forward thrust while going forward, and 3<sup>rd</sup> quadrant is reverse thrust while going forward (stop). 2<sup>nd</sup> quadrant is forward

thrust while going backwards, and 4<sup>th</sup> quadrant is reverse thrust while going backwards. The thrust coefficients for the 1<sup>st</sup> and 3<sup>rd</sup> quadrants are seen in the left plot in Figure 2.4. The right plot shows the produced thrust vs revolution speed for  $J = 0$ . That corresponds to a bollard pull case from maximum backwards thrust to maximum forward thrust. Note that the forward thrust is larger than the backward thrust.

The experimentally obtained thruster coefficients for the 2<sup>nd</sup> and 4<sup>th</sup> quadrant did not fit a nice polynomial. The water enters the propeller and duct first in these quadrants.

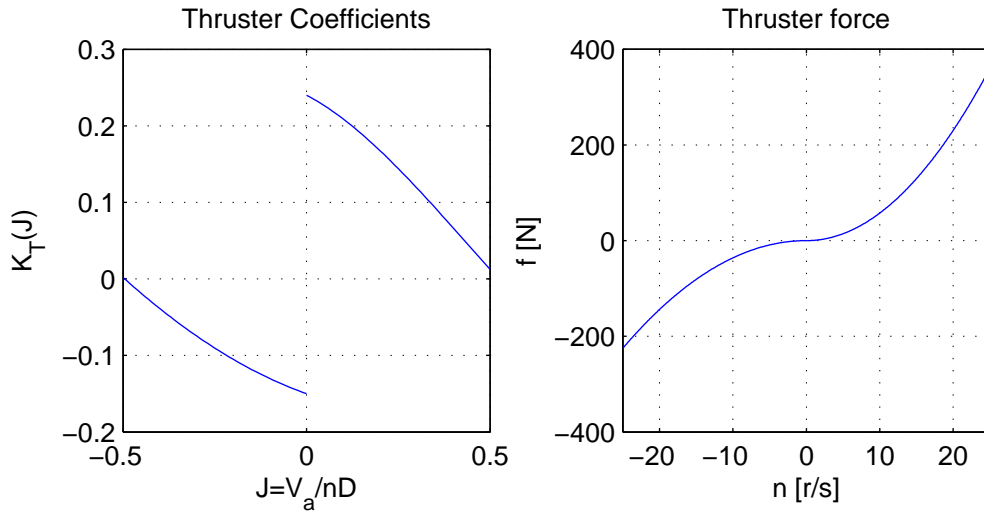


Figure 2.4: Thruster coefficients from open water tests.

It is difficult to asses the inflow velocity to each thruster as several thrusters are mounted on the ROV with different directions and flow interactions. As the ROV is a slowly moving vehicle, it is only the thruster coefficient for zero advance velocity,  $K_T(0)$  that is used in the in the thruster allocation. However, different values are used for forward and backward thrust to capture the most important thruster characteristics. That is the right plot in Figure 2.4 is a typical mapping for propeller revolution speed to force used in the thruster allocation in this thesis.

It is noted that this simplification can result in a large difference between commanded thrust and actual thrust for parts of the operation. This is seen from the left plot in Figure 2.4. E.g. if  $J = 0.5$ , the produced thrust is merely a fraction of what the control system believes it is providing. This can degrade the performance of the high level control and calls for very robust controllers. The uncertainty of the produced thrust is in general a problem for control of all vehicles using propellers for propulsion. However, it is believed that  $J \approx 0$  for most of ROV operations.

Other effects, such as reduced thrust due cross-flow and turbulence complicate the thrust mapping further. However, detailed thruster modeling is out of the scope for this thesis.

### The Thrust Vector

The thrust produced by thruster no.  $i$  is  $f_i$  and is given by (2.53). The vector with thrust for  $r$  thrusters is

$$\mathbf{f} = [f_1 \ f_2 \ \dots \ f_r]^T. \quad (2.57)$$

The total thruster force, in  $p$  DOFs, acting on the vehicle is

$$\boldsymbol{\tau} = \mathbf{T}\mathbf{f}, \quad (2.58)$$

where  $\mathbf{T} \in \mathbb{R}^{p \times r}$  is the thruster configuration matrix, which is a function of the thrusters position  $\mathbf{r}_{t_i/b}^b$  and azimuth and elevation angles,  $\alpha$  and  $\beta$ , respectively. All with respect to the vehicle frame. The thruster configuration matrix is

$$\mathbf{T} = [\mathbf{t}_1, \ \mathbf{t}_2 \ \dots, \ \mathbf{t}_r], \quad (2.59)$$

where the column vectors corresponding to thruster  $i$ , are calculated as

$$\mathbf{t}_i = \begin{bmatrix} \mathbf{I}_{3 \times 3} \\ -\mathbf{S}^T(\mathbf{r}_{t_i/b}^b) \end{bmatrix} \mathbf{R}(\alpha, \beta) \begin{bmatrix} 1 \\ 0 \\ 0 \end{bmatrix} f_i. \quad (2.60)$$

The rotation matrix from thruster axes to the vehicle frame is

$$\mathbf{R}(\alpha, \beta) = \mathbf{R}_{z,\alpha} \mathbf{R}_{y,\beta}, \quad (2.61)$$

where the rotation matrices from the elevation and azimuth angles are

$$\mathbf{R}_{y,\beta} = \begin{bmatrix} \cos \beta & 0 & \sin \beta \\ 0 & 1 & 0 \\ -\sin \beta & 0 & \cos \beta \end{bmatrix}, \quad \mathbf{R}_{z,\alpha} = \begin{bmatrix} \cos \alpha & -\sin \alpha & 0 \\ \sin \alpha & \cos \alpha & 0 \\ 0 & 0 & 1 \end{bmatrix}. \quad (2.62)$$

The azimuth and elevation angles are constant for fixed thrusters. This simplifies the thruster allocation problem as described next.

### Thrust Allocation

The thrust vector  $\boldsymbol{\tau}$ , as in (2.58), is commanded by the control system and must be distributed to the individual thrusters. More precisely, the input  $u_i$  to each thruster must be calculated. Here, the final input is the revolution speed of each thruster. Eq. (2.58) is rewritten as

$$\boldsymbol{\tau} = \mathbf{T} \mathbf{K} \mathbf{u}, \quad (2.63)$$

where  $\mathbf{K} \in \mathbb{R}^{r \times r}$  is a diagonal matrix with thruster coefficients.  $K_i = K_T(J)\rho D^4$  and the elements of  $\mathbf{u} \in \mathbb{R}^r$  is  $u_i = |n|n$ , where  $n$  is the propeller revolution speed.

The thruster allocation problem is to solve (2.63) for  $\mathbf{u}$  as

$$\mathbf{u} = \mathbf{K}^{-1} \mathbf{T}^{-1} \boldsymbol{\tau}. \quad (2.64)$$

However,  $\mathbf{T}$  may not be invertible. A common solution if  $r > p$  is to use the Moore-Penrose pseudo inverse as

$$\mathbf{T}^\dagger = \mathbf{T}^\top (\mathbf{T}\mathbf{T}^\top)^{-1}, \quad (2.65)$$

$$\mathbf{u} = \mathbf{K}^{-1} \mathbf{T}^\dagger \boldsymbol{\tau}, \quad (2.66)$$

where the revolution speed for each propeller is calculated from  $\mathbf{u}$  as

$$n_i = \text{sgn}(u_i) \sqrt{|u_i|}. \quad (2.67)$$

It should be noted that thruster saturation can cause problems. Thus, a thruster allocation method where DOFs can be prioritized is of interest. Heading is usually the most important DOF to control. Work on thruster allocation with DOF prioritization is found in [82]. A weighting function can be used in the allocation if certain thrusters should be prioritized, see [40]. Methods for thruster re-allocation are useful in case of thruster faults. However, this is not in the scope for this thesis.

## 2.5 Sensors

A ROV is a sensor platform for its navigation and payload instruments. A wide range of sensors can be mounted on a ROV. This section describes the most important sensors that are used for navigation. Measurements from these sensors are used in methods proposed later in this thesis.

### 2.5.1 Sensor Description

Four common ROV sensors are seen in Figure 2.5. These are a transponder, which is the vehicle mounted part of the acoustic positioning system (APS), a DVL, an inertial measurement unit (IMU) and a pressure gauge. A brief description and specifications of the sensors packages are given in the following.

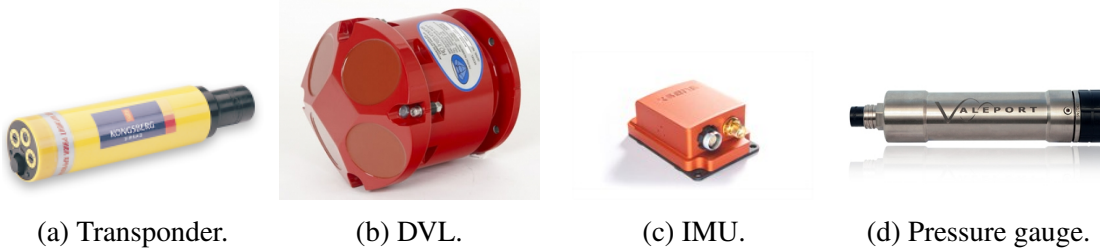


Figure 2.5: Typical ROV sensors.

### Transponder

The transponder sends and receives signals from an APS in order to determine the transponder position. Information about underwater acoustic positioning systems are found in [75] and [99]. The APS outputs the  $x$ ,  $y$  and  $z$  position coordinates of the transponder in  $\{n\}$ . The APS update rate is about 0.3-1 Hz, depending on water depth, in a typical ROV mission using a HiPAP system (SSBL).

The accuracy and range depend on the acoustic frequency of the system. Higher acoustic frequency gives better accuracy, but reduces the range as short sound waves are attenuated more in water. Thus, high frequency acoustic positioning systems with long range requires lots of power, which also means large and costly equipment.

The performance of the acoustic positioning system can be described in terms of accuracy, precision and repeatability. Systematic errors inherent in the system, such as incorrect sound velocity, baseline lengths or bending/refraction of acoustic beams, can be allowed for by careful calibration. A system with small systematic errors has high accuracy.

Random errors caused by frequently and unknown variations in the environment or equipment, such as tidal currents and ship noise, are difficult to predict as they can only be described in statistical terms. A system with small random errors has high precision.

A system that can return to a selected point with high level of confidence has high repeatability. Repeatability is the most important performance index for use in ROV control systems.

There are 3 main methods for underwater acoustic positioning; super short baseline (SSBL), short baseline (SBL) and long baseline (LBL).

SSBL uses range and angle (phase) measurements from a single multi element transducer in order to calculate the transponder position. Figure 2.6a shows the SSBL system with a hull mounted multi element transducer and a transponder at the sea floor. The Kongsberg HiPAP 500, used on RV Gunnerus, is a SSBL system with positioning accuracy of 0.2% of the range according to the manufacturer. The maximum range is 4000 m for this system.

SBL requires a minimum of 3 hull mounted transducers. A transponder is placed relative to the vessel, and range and angle measurements between the transducers and transponder is used to calculate the relative position of the transponder and vessel. Figure 2.6b shows the principle with baselines between the ship mounted transducers.

LBL is based on range measurements only. The ROV mounted transducer position

is calculated relative to a calibrated array of transponders. Figure 2.6c shows a semi-submersible positioned by a LBL system.

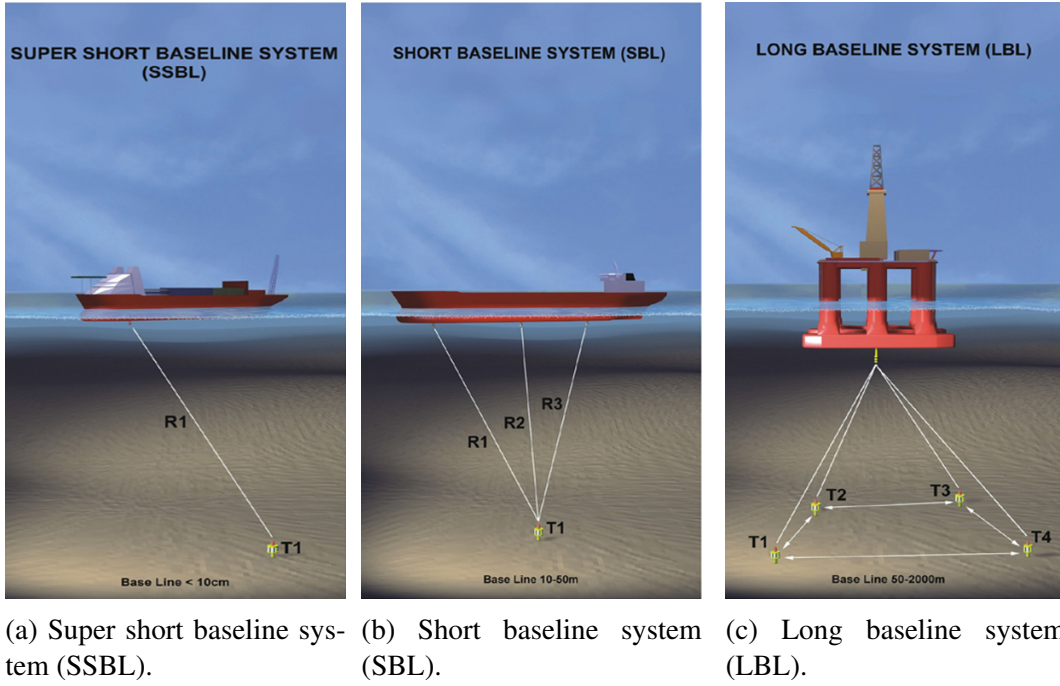


Figure 2.6: Underwater acoustic positioning methods: SSBL, SBL and LBL (Courtesy of Kongsberg Maritime).

The standard deviation of the position error can be in order of meters for deep waters. The APS should be calibrated for the sound velocity profile of the water column by conductivity, temperature and depth (CTD) or direct sound velocity measurements.

## DVL

The DVL uses the Doppler shift in the echo of the acoustic signal sent from the 4 transducer heads to calculate the velocity vector of the DVL w.r.t the sea floor or the water column. Principles of operation are found in [46]. The DVL outputs 3-DOF velocity measurements  $u, v, w$  in the DVL frame. A typical 600 kHz DVL has bottom track range from 0.7 m to 90 m with standard deviation of 0.3 cm/s at 1 m/s. Maximum ping rate is 7 Hz.

## IMU

A 9-DOF IMU has 3 accelerometers, 3 gyroscopes and 3 magnetometers. This is used to measure the 3-DOF accelerations, turn rates and the magnetic field components. Recent advances in MEMS technology have resulted in high accuracy, small and inexpensive IMU units. These are well suited for use in smaller vehicles. More accurate IMUs based on fiber optical gyroscopes (FOG) or ring laser gyroscopes (RLG) have north-seeking

capability and do not need magnetometers to find the heading. However, these IMUs are bigger and more expensive than MEMS based IMUs, which are used on the NTNU ROVs. A typical IMU has update rate of 100-1000 Hz, which is much faster than the APS and the DVL. Although the accuracy of the MEMS sensors is improving, there is still a challenge with gyroscope and accelerometer drift and noise. The magnetometers must be calibrated for soft and hard iron effects after the IMU is mounted on a vehicle. Some magnetometer calibration methods that require only magnetometer data are given in [74], [45], [42] and [98].

### Pressure Gauge

The pressure gauge is used to calculate the depth from a measured pressure. The accuracy of a high end sensor is typically 0.01% of full scale (FS) with resolution of 0.001% FS. Maximum update rate is around 8 Hz for most high end sensors. Note that the accuracy of the depth conversion also depends on the distribution of the density in the water column above the vehicle. The depth is also given by the acoustic positioning system, but the accuracy, resolution and update rate of the pressure gauge is superior to any APS.

#### 2.5.2 Setup

Figure 2.7 shows the ROV fixed coordinate system  $\{b\}$  and the outline of the ROV as a dashed box. The position of the sensor packages relative to the CO of the ROV fixed frame are given by the vectors  $\mathbf{r}_{tp/b}^b$ ,  $\mathbf{r}_{dvl/b}^b$ ,  $\mathbf{r}_{imu/b}^b$  and  $\mathbf{r}_{pg/b}^b$  for the transponder, DVL, IMU and pressure gauge, respectively. The DVL and IMU output vector measurements in their own sensor frames  $\{d\}$  and  $\{m\}$ . The orientation of  $\{d\}$  and  $\{m\}$  w.r.t  $\{b\}$  is  $\Theta_{bd}$  and  $\Theta_{bm}$ , respectively.

The orientation of  $\{d\}$  w.r.t  $\{m\}$  is  $\Theta_{md}$ , and this is constant after the DVL and IMU are mounted on the vehicle. However, it is difficult to measure the orientation  $\Theta_{md}$  exactly. The alignment errors of the DVL and IMU can be a source of error in the navigation system. A calibration should be done to obtain  $\Theta_{md}$  with sufficient accuracy. There are calibration methods that require additional position measurements, such as in [57], and others who need only IMU and DVL measurements with sufficient movement to obtain the orientation  $\Theta_{md}$ . See the calibration methods in [95] and [98]. In practice, it is also difficult to measure the positions of the sensor packages exactly. This is another error source that will affect the performance of the navigation system.

It is sometimes useful to express observer equations in the IMU frame. The position of the other sensors relative to the IMU, in  $\{m\}$ , are needed. These are noted  $\mathbf{r}_{tp/m}^m$ ,  $\mathbf{r}_{dvl/m}^m$  and  $\mathbf{r}_{pg/m}^m$  for the transponder, DVL, and pressure gauge, respectively, see (2.68), (2.69) and (2.70).

$$\mathbf{r}_{tp/m}^m = \mathbf{R}_b^m(\Theta_{bm})(\mathbf{r}_{tp/b}^b - \mathbf{r}_{imu/b}^b), \quad (2.68)$$

$$\mathbf{r}_{dvl/m}^m = \mathbf{R}_b^m(\Theta_{bm})(\mathbf{r}_{dvl/b}^b - \mathbf{r}_{imu/b}^b), \quad (2.69)$$

$$\mathbf{r}_{pg/m}^m = \mathbf{R}_b^m(\Theta_{bm})(\mathbf{r}_{pg/b}^b - \mathbf{r}_{imu/b}^b), \quad (2.70)$$

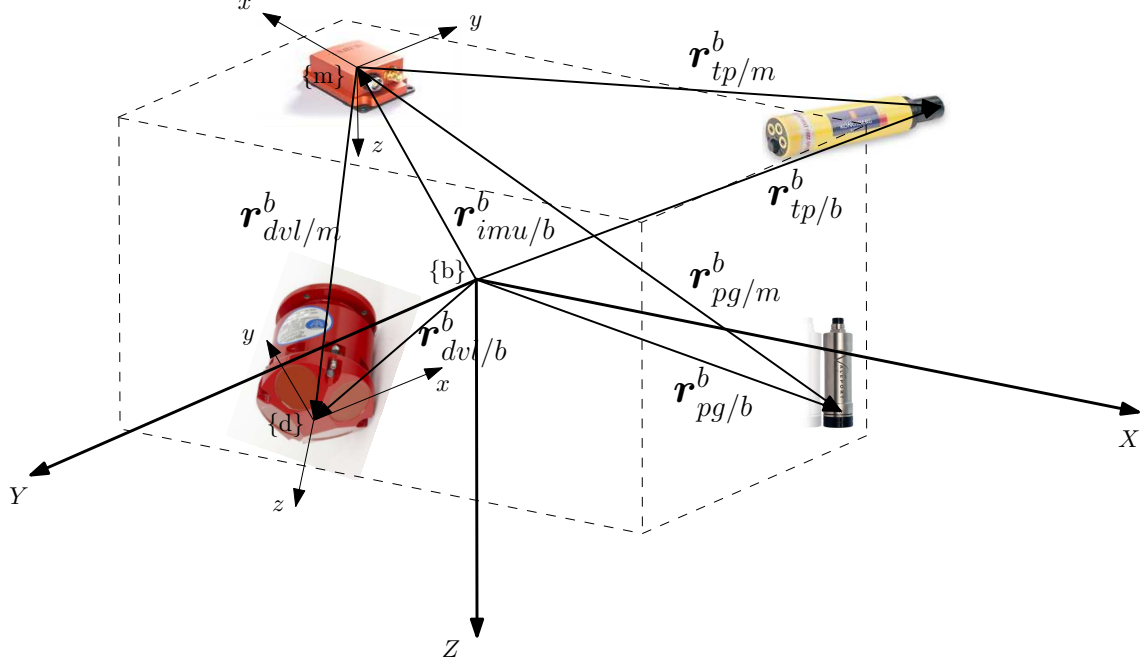


Figure 2.7: Sensors and positions on the ROV.

where  $\mathbf{R}_b^m(\Theta_{bm}) \in \mathbb{R}^{3 \times 3}$  is the rotation matrix from  $\{b\}$  to  $\{m\}$ .

### 2.5.3 Measurements

The sensors are placed and aligned in different positions on the ROV. Thus, all measurements must be transformed to the CO or another common origin of interest in order to provide complementary information. The equations describing these translations and transformations are given in the following. The measurement equations are also used to simulate sensor measurements in computer simulations.

#### IMU

The measurement equations for the IMU are given by (2.71), (2.72) and (2.73) for the accelerometers, gyroscopes and magnetometers, respectively. These equations are given in terms of states in the IMU frame.

$$\begin{aligned} \mathbf{a}_{imu}^m &= \dot{\mathbf{v}}_{m/e}^m + \omega_{m/i}^m \times \mathbf{v}_{m/e}^m + \mathbf{R}_n^m(\omega_{e/i}^n + \omega_{n/e}^n) \times \mathbf{v}_{m/e}^m - \mathbf{R}_n^m \mathbf{g}_l^n \\ &\quad + \mathbf{b}_{acc}^m + \mathbf{w}_{acc}^m, \end{aligned} \quad (2.71)$$

$$\omega_{imu}^m = \omega_{m/n}^m + \mathbf{R}_n^m(\omega_{e/i}^n + \omega_{n/e}^n) + \mathbf{b}_{gyro}^m + \mathbf{w}_{gyro}^m, \quad (2.72)$$

$$\mathbf{m}_{imu}^m = \mathbf{R}_n^m \mathbf{R}_e^m \mathbf{m}^e + \mathbf{b}_{mag}^m + \mathbf{w}_{mag}^m, \quad (2.73)$$

where  $\mathbf{a}_{imu}^m \in \mathbb{R}^3$  is the measured acceleration vector in  $\{m\}$ .  $\mathbf{b}_{acc}^m$  is the accelerometer bias vector, and  $\mathbf{w}_{acc}^m$  is the accelerometer noise vector.

$\omega_{imu}^m \in \mathbb{R}^3$  is the measured turn rate vector of the IMU,  $\mathbf{b}_{gyro}^m$  is the gyroscope bias vector and  $\mathbf{w}_{gyro}^m$  is the gyroscope noise vector.

$\mathbf{m}_{imu}^m \in \mathbb{R}^3$  is the measured magnetic field vector in  $\{m\}$ ,  $\mathbf{m}^e$  is the true magnetic field vector in  $\{e\}$ .  $\mathbf{b}_{mag}^m$  is the magnetometer bias vector and  $\mathbf{w}_{mag}^m$  is the magnetometer noise vector.

The IMU measurement equations in terms of states in the vehicle frame,  $\{b\}$  are given by (2.74), (2.75) and (2.76). This model is used to simulate IMU measurements from motions of the ROV in  $\{b\}$ .

$$\begin{aligned}\mathbf{a}_{imu}^m &= \mathbf{R}_b^m(\dot{\mathbf{v}}_{b/e}^b + \boldsymbol{\omega}_{b/e}^b \times \mathbf{v}_{b/e}^b + \dot{\boldsymbol{\omega}}_{b/e}^b \times \mathbf{r}_{imu/b}^b + \boldsymbol{\omega}_{b/n}^b \times (\boldsymbol{\omega}_{b/n}^b \times \mathbf{r}_{imu/b}^b) \\ &\quad + \mathbf{R}_n^b(\boldsymbol{\omega}_{e/i}^n + \boldsymbol{\omega}_{n/e}^n) \times \mathbf{v}_{b/e}^b - \mathbf{R}_n^b \mathbf{g}_l^n) + \mathbf{b}_{acc}^m + \mathbf{w}_{acc}^m,\end{aligned}\quad (2.74)$$

$$\omega_{imu}^m = \mathbf{R}_b^m(\boldsymbol{\omega}_{b/e}^b + \mathbf{R}_n^b(\boldsymbol{\omega}_{e/i}^n + \boldsymbol{\omega}_{n/e}^n)) + \mathbf{b}_{gyro}^m + \mathbf{w}_{gyro}^m, \quad (2.75)$$

$$\mathbf{m}_{imu}^m = \mathbf{R}_b^m \mathbf{R}_n^b \mathbf{m}^n + \mathbf{b}_{mag}^m + \mathbf{w}_{mag}^m, \quad (2.76)$$

where it is noted that different sampling rates are also included in the sensor models in simulations.

## DVL

The measurement equations for the DVL are given by (2.77) as

$$\mathbf{v}_{d/e}^d = \mathbf{R}_b^d(\Theta_{bd})(\mathbf{v}_{b/n}^b + \boldsymbol{\omega}_{b/n}^b \times \mathbf{r}_{dvl/b}^b) + \mathbf{w}_{dvl}^d. \quad (2.77)$$

$\mathbf{v}_{d/e}^d \in \mathbb{R}^3$  is the measured velocity in  $\{d\}$ , and  $\mathbf{w}_{dvl}^d$  is the DVL noise. Eq. (2.77) is used as is for sensor simulation and must be solved for  $\mathbf{v}_{b/n}^b$  for use in the control system.

## Transponder

The measurement equation for the transponder is given by (2.78) as

$$\mathbf{p}_{tp/n}^n = \mathbf{p}_{b/n}^n + \mathbf{R}_b^n(\Theta_{nb})\mathbf{r}_{tp/b}^b + \mathbf{w}_{tp}^n, \quad (2.78)$$

where  $\mathbf{p}_{tp/n}^n \in \mathbb{R}^3$  is the measured transponder position in  $\{n\}$ ,  $\mathbf{p}_{b/n}^n$  is the ROV position and  $\mathbf{w}_{tp}^n$  is the APS noise. Eq. (2.78) is used as is for sensor simulation and must be solved for  $\mathbf{p}_{b/n}^n$  for use in the control system.

## Pressure Gauge

The measurement equations for the pressure gauge are given by (2.79) and (2.80).

$$p_{pg} = p_{atm} + \rho g z_{pg/n}^n + w_{pg}, \quad (2.79)$$

$$z_{pg/n}^n = z_{b/n}^n + [0 \ 0 \ 1] \mathbf{R}_b^n(\Theta_{nb}) \mathbf{r}_{pg/b}^b, \quad (2.80)$$

where  $p_{pg} \in \mathbb{R}$  is the measured pressure,  $p_{atm}$  is the atmospheric pressure at the surface,  $\rho$  is the water density,  $g$  is the acceleration of gravity,  $z_{pg/n}^n$  is the depth of the pressure gauge, and  $w_{pg}$  is the PG noise.  $z_{b/n}^n$  is the depth of the ROV. Eq. (2.79) is only valid for constant water density throughout the water column. For real implementations, more refined measurement equations for converting pressure to depth should be used, e.g. the depth conversion formula in [39]. Eq. (2.80) is used as is for sensor simulation and must be solved for  $z_{b/n}^n$  for use in the control system.

# **Chapter 3**

## **Development of a ROV Motion Control System**

A motion control system for ROVs has been developed, implemented and tested as part of the work with this thesis. This work has been done in collaboration with other PhD candidates and MSc students as a vital part of the specialization in marine control systems and underwater technology at NTNU. The author has had the main responsibility, together with postdoc Martin Ludvigsen and by supervision of prof. Asgeir J. Sørensen, of putting everything together. This chapter presents the design of the motion control system architecture, software development and the motion control software.

### **3.1 Introduction**

The motion control system software has been tested regularly in the period from the spring of 2010 on cruises with the RV Gunnerus in the Trondheimsfjord, see Figure 3.1a. The control system has gone through an evolution where more advanced functions have been added and the user experience improved. This chapter does not go into every detail of the development, but it provides some insight to how the program is structured and what it can do.

Tremendous work has been done on developing the motion control system and software. This work includes logic, exception handling, drivers, GUI, communication, testing, de-bugging, etc. The implementation of the scientific contributions such as a certain controller or observer algorithm usually only takes a few lines of code. In addition to software development, lots of time has been spent on tinkering with the ROV and hardware itself, see Figure 3.1b.

#### **3.1.1 Objectives**

The main objectives for automation of station keeping and maneuvering functions of ROV operations are related to the keywords

- safety, performance, consistency, time and cost,

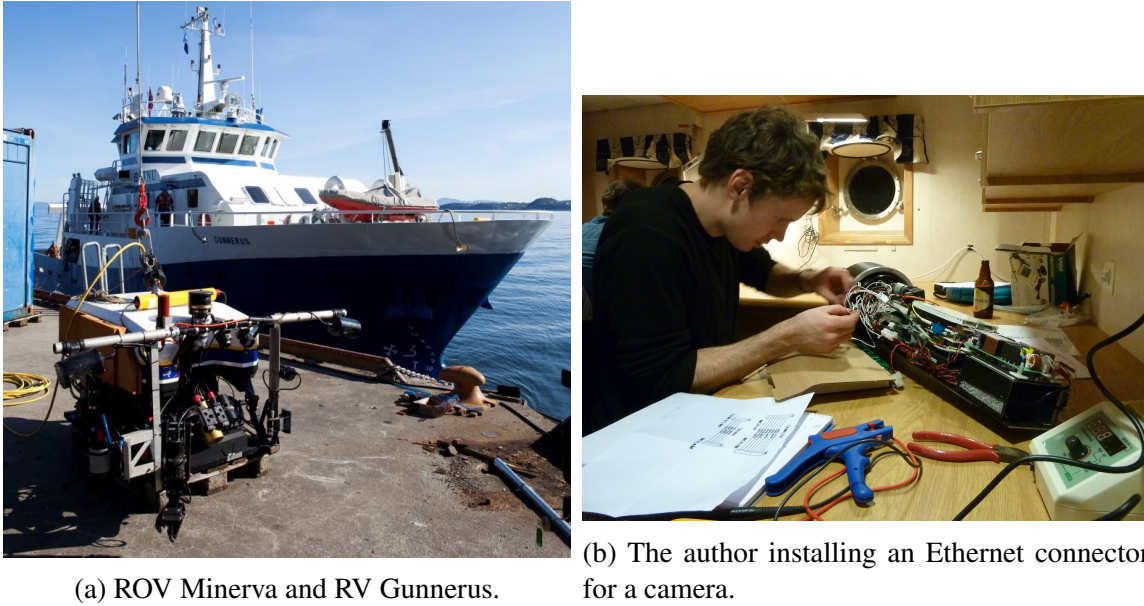


Figure 3.1: Development of the motion control system for ROVs.

where safety can be increased due to reduced human errors and higher precision motion control. A work task can be done with higher accuracy and increased performance. Tasks can be done over and over again with the same performance, they can be done faster than with a pilot, and the duration is the same every time so planning an operation is easy.

The more specific objectives for the motion control system presented here are given in the following.

### Testbed for control algorithms

For PhD candidates and MSc students the motion control system works as a test bed. That is, it should be easy to implement and test new algorithms in order to obtain experimental results verifying new controller designs. These results are used in publications and support the theory developed. The motion control system works as a frame work, and only a small module needs to be changed in order to get new experimental results demonstrating and verifying the performance of a specific theoretical contribution.

### Add value to ocean sciences

Ocean science research fields such as marine biology, archeology, oceanography and geology use ROVs as tools and sensor platforms to gather new knowledge in their respective areas. A goal is that researchers from interdisciplinary fields will also benefit from the functions provided by the motion control system. That is, due to the motion control system, new results can be discovered in other research fields as well. E.g. the ROV can track a given transect several times with high accuracy, year after year using automated functions. This gives accurate observations in both space and time which is useful for

mapping and monitoring environments such as coral reefs and kelp forests, and to learn about the life in these habitats.

### 3.1.2 Work Process & Methods

The start with development of the ROV motion control system at NTNU goes back to 2004, just after the ROV Minerva was acquired. The early work was mostly on modeling of hydrodynamics and thrusters for use in a future motion control system. Several test were conducted at the Marintek laboratories with both a small scale model of Minerva and open water tests of the thrusters. These tests were conducted by then MSc students Martin Ludvigsen and Øyvind Ødegård. Results are given in [61], [62], [64], [63], and [65].

A motion control system was designed as part of Svendby's MSc thesis in 2007. The goal was to make the ROV Minerva follow a predefined lawn mower pattern while maintaining constant distance to the sea floor. He reports in [91] that the simulation results were good, but the performance in the experiments was less satisfactory although the ROV reached the predefined way-points. The depth control showed the best performance, but it was not sufficient for use in maintaining a constant distance to the sea floor. However, with only two days of testing and challenges with measurements and technicalities, this was a good start.

The work of Svenby was continued by Kirkeby and Lysdahl in 2010 and results are presented in their MSc thesis [58], [66]. They improved the software made by Svendby in Matlab and were able to perform station keeping and short A to B moves for ROV Minerva in a sea trial in the spring of 2010. However, the motion control system had few functions besides station keeping in the beginning. Raw measurements were used in the controller and little could be changed by the user in real-time.

A push was done to develop the motion control system in the fall of 2010. The author was engaged as PhD with teaching assistance duties and took over the responsibility of development, implementation and testing. The hardware and software platforms for implementation were changed from PC and Matlab to compactRIO and LabVIEW. Several MSc students joined the team and contributed with code development and testing. From the fall of 2010 test cruises with RV Gunnerus and ROV Minerva became regular, almost two days every second month. The ROVs and team were included in AUR-Lab (Applied Underwater Robotics Laboratory) when it opened in 2011. The work related to developing the motion control system was most intensive in periods before cruises. A hardware-in-the-loop (HIL) simulator was made to enable testing and de-bugging before sea trial with an actual ROV.

The number of functions and options in the motion control system quickly expanded and controllers from [58] and guidance system from [59] became default functions in the system. It did not take long time and efforts before tracking of lawn mower patterns were possible.

The control software was restructured with object-oriented LabVIEW in 2012 in order to implement the motion control system on the ROV 30 k as well.

From 2011 the motion control system has been used as a tool for marine biologists

and archeologists. The motion control system has been used to systematically survey coral reefs, sea bed and ship wrecks while gathering data from cameras and other sensors. It has also been used to conduct surveys of pipelines for the oil & gas industry at Nyhamna. Not surprisingly, the lesson learned from using the motion control system in collaboration with biologists, and other non technical users, is that only well proven automated motion control functions should be used when the motion control system serves as a tool. That is, cruises for motion control system development and testing should be separated from cruises where the main objective is to gather information or samples for other research fields.

In the fall of 2013 an acoustic positioning system (LBL) network was installed outside Trondheim biological station where the ROVs are stored. This has enabled deployment of the ROVs from the quay with position feedback. Thus, testing can be done without the surface vessel and crew. This makes testing more available and will hopefully boost the development of the motion control system in the future.

A timeline showing the evolution of the motion control system is seen in Figure 3.2. The left plot with trajectories shows the first DP maneuvers with ROV Minerva in 2010. The ROV Minerva is seen under the opening of the AUR-Lab in 2011, when the Norwegian minister of trade, Trond Giske, opened the laboratory by cutting a subsea ribbon with the manipulator.

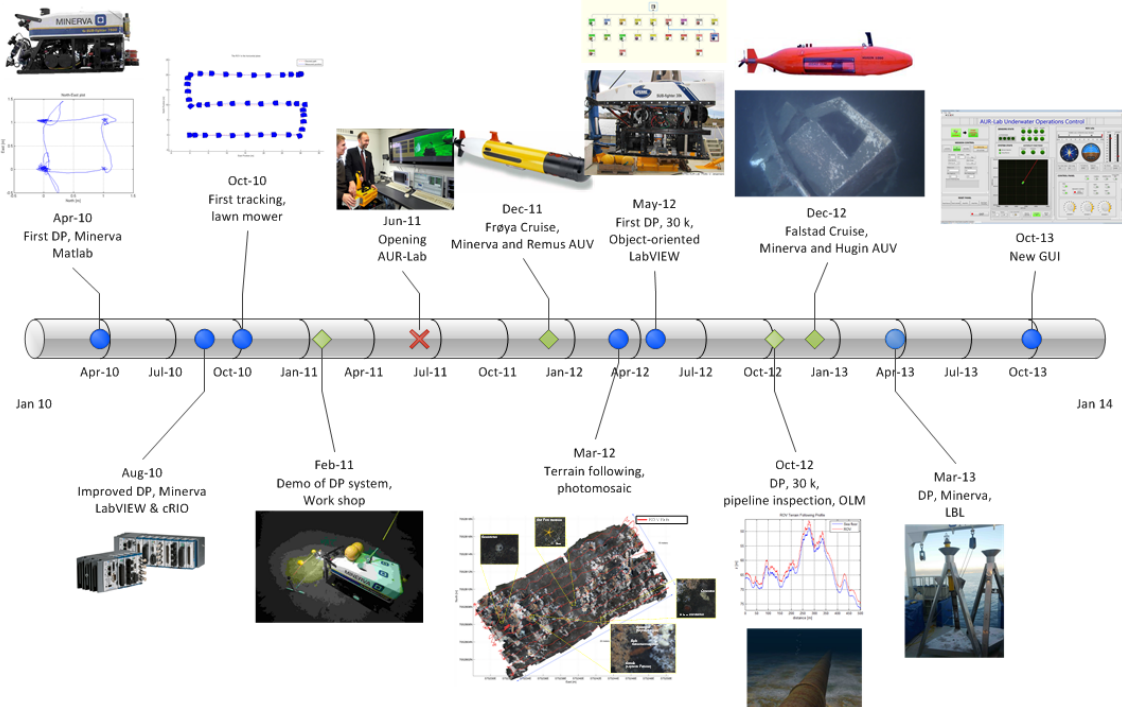


Figure 3.2: ROV motion control system timeline.

## 3.2 Motion Control System Architecture

The main architecture of the ROV motion control system is adopted from the architecture used by common DP systems for ships. The blocks and connections that make up the motion control system are seen in Figure 3.3. The motion control system gets input from sensors, commands from an operator, and outputs desired revolution speeds for each thruster. Each thruster has a low level controller that regulates the revolution speed correspondingly. Details about the motion control system blocks and signal flow are given in the following. An early version of the motion control system and functions is published in [25] and [88].

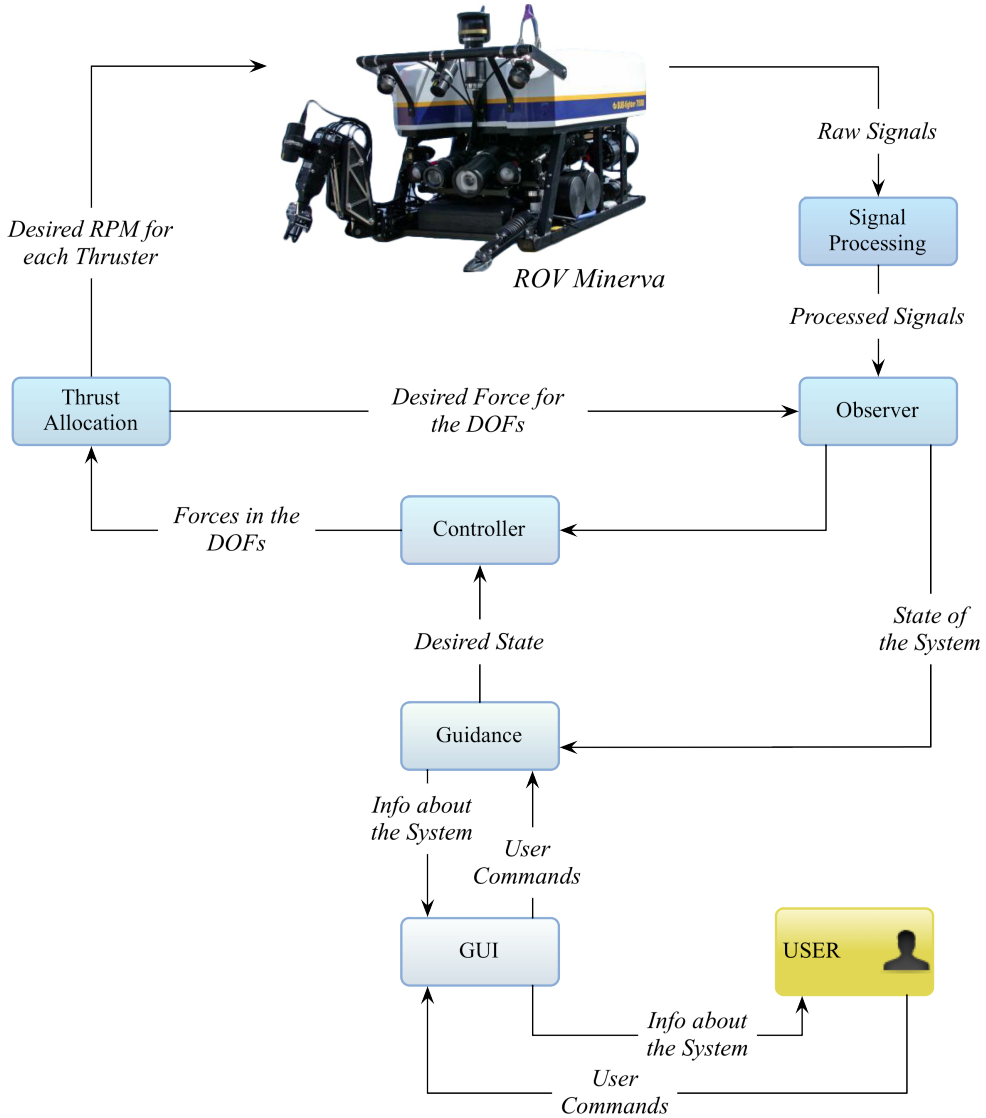


Figure 3.3: Control motion system architecture (Courtesy of Mauro Candeloro).

### 3.2.1 ROV Operation Modes and Functions

The automated motion control functions and modes that are implemented in the motion control system are described in the following.

#### Station Keeping

The most basic automated operation mode is station keeping. All 4 DOFs in the workspace are under set-point regulation to maintain a fixed position and heading. The guidance system outputs a constant reference state to the controller.

#### AtB

In maneuvers where the ROV goes from position A to position B (AtB), the guidance system must output a desired trajectory that can be tracked by the vehicle. Changes in heading is also considered as an AtB maneuver since heading is part of the generalized position  $\eta$ . The move is obtained with a reference model. The new position is an input to the reference model which calculates the desired path. A new reference model, that aim at being simple as possible, is proposed in Chapter 5.1. The constant "jerk" reference model is the default reference model for AtB moves. Other alternatives, such as filter based reference models, are also available in the developed motion control system.

#### Tracking

Trajectory tracking and path following of predefined paths are useful features. In trajectory tracking the desired positions have time constraints as well. These typically come from a set desired cruise speed before the operator starts the mission. Another mode, which has been tested, is path following with manual speed control. The ROV is controlled automatically to be on a desired path, but the surge speed is manually commanded by the operator.

The reference models in AtB moves can be used in tracking as well when a way-point management system automatically gives inputs to the reference models. Another alternative is Line-of-sight (LOS) for fully actuated vehicles, where the direction of the desired velocity is controlled so the ROV follows a path between way-points. For LOS, the output of the guidance system is a desired velocity and heading. The proposed LOS is found in Chapter 5.2.

#### Joystick in Closed-loop Control

In this mode, the guidance system produces desired trajectories, velocities or thrust based on the joystick commands. The closed-loop motion control system can be used to compensate for external forces and ROV dynamics. The guidance system interacts with the operator continuously. Quick reactions to commands are important as a human is in the feedback loop. Proposed methods for joystick in closed-loop control and experimental results are given in Chapter 5.3.

### Altitude Control/Terrain Following

In altitude control or terrain following, the guidance system produce a desired trajectory from sensor inputs. This is fundamentally different from the other modes where the path is either pre-defined or commanded by an operator. E.g. the desired depth generated as the ROV moves over varying terrain in altitude control is a function of sensor measurements reading the distance to the sea floor and slope. Altitude control is obtained without prior knowledge of the terrain. Thus, this mode is closer to autonomous operation than automated. Work and contributions on altitude control and terrain following is given in Chapter 6.

### 3.2.2 Modules

The main loop in the high level motion control system consists of signal processing, observer, controller and thruster allocation blocks. The controller action is decided by the guidance system, and the operator can select the modes in the guidance system via a graphical user interface (GUI) on a computer. Each of the blocks are explained in the following.

#### Signal Processing

The role of the signal processing block is to take in readings from all sensors and provide the observer with time stamped measurements in a common reference frame. In this process the quality and validity of the sensors must be checked so bad sensor readings are discarded. Filtering of signals may also be needed. Signal processing is a field on its own and it is out the scope of the thesis to provide new methods here. The signal processing implemented on the motion control system includes checking of wild points, signal range and variance. Change detection methods have been studied by other MSc students and tested in the motion control system, [89]. Improvements in dynamic settings of alarm limits, redundancy handling, diagnosis and change detection are topics for further research.

#### Observer

The task of the observer is to take in processed measurements and output smooth and accurate position and velocity (states) estimates to the controller. Even if the sensors have slow update rates, periods without measurements or the measurements are noisy, the observer must still provide state estimates with sufficient update rate and accuracy required for the dynamics of the vehicle to be controlled. Medium sized ROVs are fairly slow, so update rate to the controller of about 5-10 Hz is usually fast enough. However, the observer itself may run at a higher frequency if a model of the dynamics is used to predict the states or if some measurements are available at a faster rate.

Several types of observers have been tested in the motion control system. The default observer is a model-based Kalman filter. However, the attitude is estimated from the IMU measurements using an explicit complementary filter (ECF).

## Controller

The controller gets the desired states to be tracked from the guidance system. The state error is calculated as the difference between the estimated and desired states. The control output  $\tau$  is calculated based on the state error and feed forward from the desired states. A number of algorithms can be used to produce the final output  $\tau$ , and these are referred to as control laws. The default control law in the system is a type of proportional, integral derivative (PID) law with feedforward terms. Other laws, such as sliding mode, have also been tested.

## Thruster allocation

The control force  $\tau$  must be distributed to the thrusters. The process of calculating the needed thrust of each actuator in order to obtain a total control force  $\tau$  acting in the CO is called thruster allocation. However, the output of the thruster allocation here is the revolution speed of each propeller. The mapping method between revolution speed and thrust as described in Chapter 2.4.2 is used. Note that the NTNU ROVs, which the motion control system was designed for are fully actuated in their 4 DOF workspace and that all thrusters are fixed. Fixed thrusters simplifies the thruster allocation as the distribution of thrust is a geometrical task only. However, more advanced methods are needed in order to deal with thruster faults and saturation.

## Guidance

The guidance system produces desired states to the controller. A number of different algorithms can be run in the guidance block depending on the task given by the operator. Typical laws that run in the guidance block are reference models that produce smooth trajectories between way-points that the ROV is able to follow. Thus, the guidance system must consider the dynamic limitations of the vehicle to calculate feasible desired trajectories. However, it also uses feedback from the estimated states to automatically change the guidance commands if the ROV is unable to follow the desired path.

The guidance system is the highest level in the motion control system and interfaces the operator via a GUI.

### 3.2.3 Signal Flow

The signal flow from sensors on the ROV, and between different hardware in the motion control system are shown in Figure 3.4. Note that the absolute position of the ROV is given by the HiPAP (acoustic positioning system) which uses GPS and ship gyroscopes to calculate the position of the ROV transponder in the NED frame. The interface between the HiPAP system and the ROV motion control system can go via the commercial survey software NaviPac, as seen in Figure 3.4, or directly into the motion control system running on the compact RIO. The same goes for the other instruments, which can go through NaviPac as seen, or directly to the cRIO.

The NaviPac was used in the early stages of development to collect data from instruments and output a message to the motion control system on the cRIO. NaviPac provides drivers for typical instruments and part of the signal processing can be done here. In order to have more direct control of the sensors, drivers for instruments, such as the DVL and IMU, have been made for the cRIO.

The switch seen to the left in Figure 3.4 is used to select the commander in charge of the ROV. The ROV can be controlled with the original command console or with the developed motion control system on the cRIO. In addition to thrust, the commander in charge controls all signals to the ROV such as instrument power switches, lights, cameras, manipulators etc. However, this thesis focus on the motion control aspects. If something goes wrong in the motion control system, which can happen during development, it is easy and quick to switch back to the original manual mode of operation. Thus, there is little risk in trying new control solutions due to this safe fallback option.

The operator interfaces the motion control system via a host computer and joystick. Commands are given via the GUI, and tuning of controllers and observers can be done in real-time if needed. The GUI provides the operator with information about the ROV position and velocity, and the conditions of installed sensors and instruments.

### 3.2.4 Levels of Autonomy

The operator of a ROV with automated functions can use different levels of vehicle control. Some autonomy levels for the ROV motion control system are shown and described in Table 3.1. In general, the level of autonomy is set by the mission complexity, the environmental difficulty and human independence. A scale with autonomy levels from 1-10 for unmanned systems is given in [55]. Another qualitative scale with 4 levels of autonomy is given in [5]. However, it is difficult to make a single scale for levels of autonomy that suits every type of vehicle and operation.

In the most basic manual mode, the operator has direct control of each thruster. It is challenging to just to keep the ROV stationary in presence of ocean currents in this mode. Controlling 4 or more thrusters simultaneously while fighting external forces is not an easy job for a pilot. Using a joystick with thruster allocation, so the pilot controls each DOF instead of thrusters, will improve the performance considerably. However, the pilot must still compensate for external forces and vehicle dynamics, and station keeping requires constant focus and a skilled pilot.

The other extreme, regarding level of human interaction, is complete autonomy. In this mode of control the operator assigns a task and the vehicle performs it autonomously without further instructions from the pilot. E.g. the pilot shows a picture of a coral and tells the ROV to find it and bring it back home. The ROV starts the mission and performs the search and route planning on its own, finds the coral, picks it up and delivers it without any interaction from the operator. This is way beyond the current state of the motion control system presented here. However, there are several other automated functions at different levels of human interaction that can greatly enhance the efficiency of underwater operations as described in Section 3.2.1.

Way-point tracking with terrain following is an example of a mode that is included in

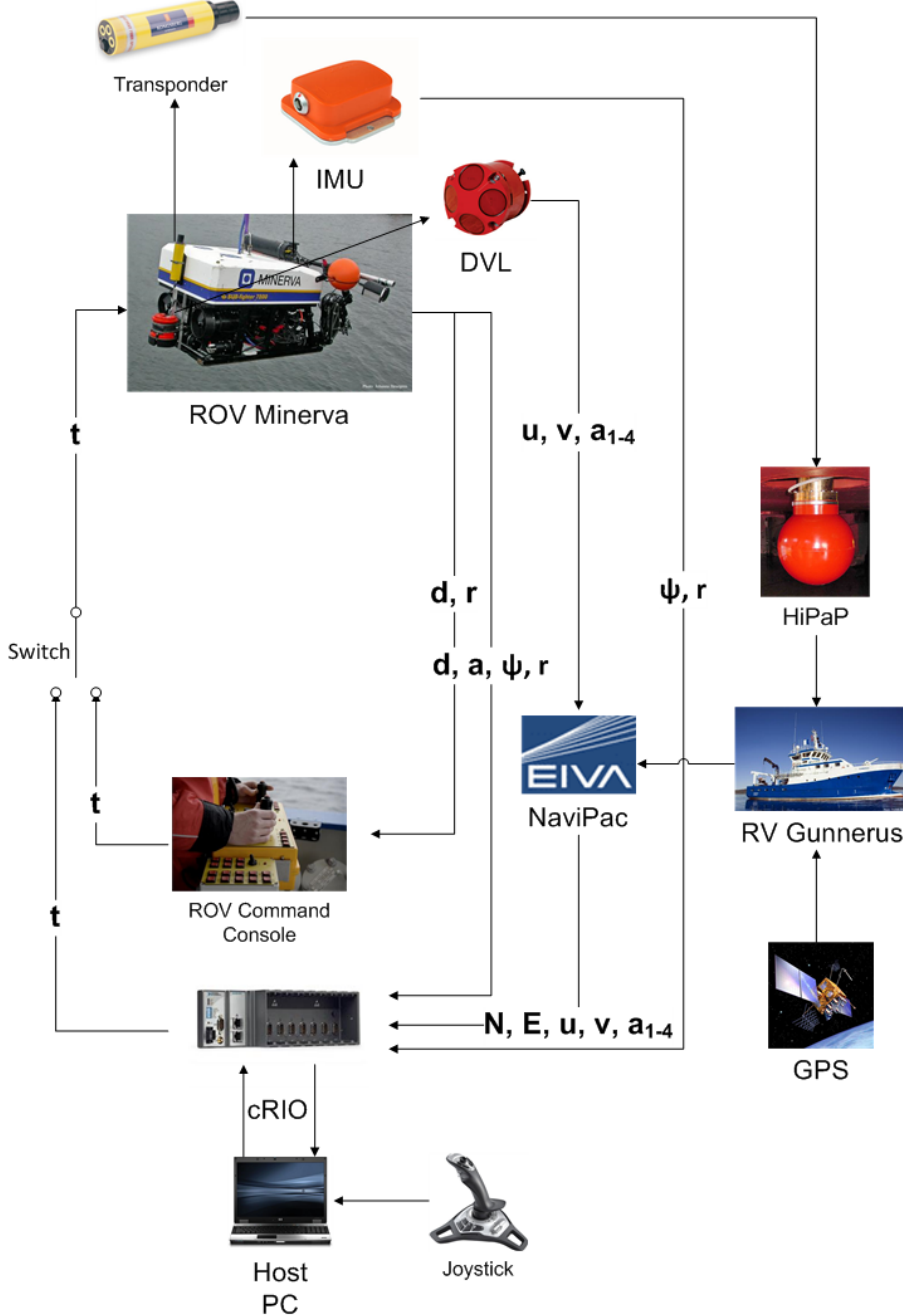


Figure 3.4: Signal flow in the motion control system.

the motion control system. The operator specifies a list of way-points, cruise speed and distance above the sea floor. Then the ROV moves automatically from way-point to way-point while maintaining the desired altitude despite ocean currents and unknown terrain geometry. The operator does not interact in the vehicle control, but monitors the data from cameras and sensors. If the operator sees something interesting or if the ROV gets into trouble, he must interact and give new instructions to the ROV. However, in this mode

Table 3.1: Autonomy levels of the ROV motion control system.

Level	Intervention time	Features
Remotely controlled	cont.	Direct thruster control or TA
		Pilot compensates for dynamics
		Pilot compensates for environmental forces
Operator guided	cont.	Ctrl system compensates for dynamics
		Ctrl system compensates for env. forces
		DP
Supervised	min-hrs	AtB
		Tracking
		Terrain following
Mission Control	hrs-days	Collision/obstacle avoidance
		Mission objective
		Artificial intelligence
Autonomous	days-yrs	

the operator is a supervisor rather than pilot. At this level, the operator's skills are not assessed based on his ability to maneuver the vehicle, but on what data and information he gets from the use of the ROV. Thus, this work can be regarded as a step towards autonomy.

### 3.3 Software Development

The software development for the ROV motion control system has been a learning by doing experience and many of the early solutions and implementations would have been unheard of today. Thus, there has been some progress. LabVIEW was selected as the software development environment as it is easy to learn and fast to implement new code. Students not too familiar with programming and software development can contribute with code to the project. The author had limited experience with software development before this project. However, much experience and skills have been gained in the process of making the motion control system.

The software was developed in a collaboration with other PhD candidates and MSc students. Each member was assigned a task such as writing a function with specified input and outputs. Then new code was included in the main software by the author and tested and de-bugged together with the contributor if needed. The tool for this was the hardware-in-the-loop (HIL) testing. If the code ran with sufficient performance in HIL tests, it was ready for use in sea trials.

Planning and structure suffered as more and more advanced functions were added by myself and other programmers whenever something seemed to be nice to have. Different programming styles and various levels of documentation resulted in a difficult to maintain, and impossible to improve software. This called for a change and a MSc student with computer background restructured the software as part of his thesis [94].

The new main software was object-oriented, it eliminated hard coding, and reduced

the complexity of logic from the previous solution. The main philosophy was to keep the software as modular as possible and it should be easy to adapt the motion control system to other ROVs with different sensors and actuators. The software builds on the motion control system architecture.

### **3.3.1 Specifications, Tasks & Functionality**

A detailed specification of the software is needed to avoid ad-hoc solutions, endless adding of "nice to have" functions and temporary quick-fixes becoming permanent solutions. However, some flexibility to incorporate new functionality in the future must be included in the design.

The way the software was designed was to start with identifying the tasks, then specify the needed functions and interactions. An example task could be to run the ROV in a lawn mower pattern from a way-point list. Another task could be to use a joystick in closed-loop control to operate the ROV. The interface to the user is different in these tasks, but lots of the same code run under the bonnet in both cases. Thus, for every task, it must be specified what parameters the user can change and what information will be presented. E.g. the lawn mower pattern is generated from a way-point list where the way-points are read for a file, added manually by clicking in a map or punching in coordinates, or generated from a function where the user enters parameters such as number, direction and length of lines. Nevertheless, all these top level functions results in a way-point list which is executed by the way-point management system which again calls the needed reference models.

The division of the software into several levels enables reuse of code and makes it easy to implement new top level functions, which gives added functionality of the ROV. The design process of the software system is about identifying these levels and the interaction between software modules. In this design it was a top down approach where the steps needed started from the ROV task and then specifying each underlying module.

### **3.3.2 Software & Hardware Platforms**

The software for GUI and control runs on the host computer and the compactRIO. The cRIO is a real-time controller with I/O modules. A cRIO is seen Figure 3.5b and LabVIEW, which is a graphical programming language, is illustrated in Figure 3.5a.

#### **LabVIEW**

LabVIEW is a graphical programming language, but Matlab code can be used for tasks that are not suited for graphical programming, such as lengthy algorithms. As most students are familiar with Matlab, this reduces the development time further. It is especially fast to develop custom GUIs. Also, LabVIEW is used to program the cRIO.



(a) LabVIEW graphical programming language.      (b) compact RIO real-time controller.

Figure 3.5: LabVIEW and cRIO.

## CompactRIO

The compactRIO is a reconfigurable embedded control and acquisition system. It consists of a real-time controller, a field programmable gate array (FPGA) and I/O modules. The I/O modules can be changed depending on the application. The ROV motion control system uses serial communication modules (RS-232) to get input from the sensors and to send control commands to the ROV. The cRIO communicates with a host PC via TCP/IP or UDP as it is connected to the PC or a network with an Ethernet cable. Messages on the network, such as position measurements from the acoustic positioning system, can be read via UDP.

### 3.3.3 Object-Oriented Programming

Object-oriented programming in LabVIEW is used in the motion control system software. One advantage of using object-oriented programming is reduced complexity in logic as polymorphic functions are used. E.g. switching between two observers is seamless as the observer is a polymorphic function which calls an instance of the observer class.

Programming in LabVIEW can easily result in spaghetti code where lines are going everywhere. This is considerably simplified using LabVIEW object-oriented programming where there is a main bus and the needed data is accessed with read and write functions.

A main feature using object-oriented programming is that the software architecture resembles the motion control system architecture seen in Figure 3.3 and 3.4.

## Supervisor

The software contains a supervisor class where the data members carry information about the system and properties. Communication between different modules and classes is done through the supervisor class which keeps track of everything that is going on in the system. It is also the interface to the GUI software, e.g. if new controller settings are entered in the

GUI, then it is the supervisor who brings the message to the controller or other modules that need the information.

## Classes

A class is constructed for each of the physical objects on the ROV, such as sensors and actuators. E.g. the DVL is an object in the sensor class. This makes the software modular by design, and adding or changing a sensor is easy. Classes are also made for each of the blocks in the motion control system architecture. E.g. the observer class contains several observer objects, such as implementations of a Kalman filter or an ECF.

### 3.3.4 Software Product

The main software product consists of two programs, the control software and the GUI software. Some features of these are described next.

#### Motion Control System

The motion control system is called Njord. It contains all blocks above the GUI block in Figure 3.3. The classes for sensors, actuators and vessels are also included here. When the motion control system is used on a new ROV, this is done by modifying the configuration file which contains information about the ROV parameters, sensors, thrusters, etc. The configuration file is read and the data members in the different classes are assigned the proper values. This works as long as the new ROV use the same type of sensors that are included in the sensor class. The same goes for thruster types and any other physical object that has a corresponding class in the motion control system. The motion control system can not be used directly on a ROV with azimuth thrusters as there is no object in the thruster allocation class that accounts for this in the current version. However, a ROV with different numbers of thrusters, mounting and direction is no problem as the respective thruster configuration matrices are made from the input in the configuration file.

Adding new sensors may require some more work if the corresponding driver is not available. However, the bank of available instruments increases as the motion control system is used with new sensors as the drivers are stored in the system and can be used again if included in the configuration file.

#### GUI

The GUI also got a major upgrade after converting to object-oriented programming. The GUI software is called Frigg. In the previous version lots of advanced settings, such as observer and controller tuning parameters, were directly available to the user and too much data was displayed. This made it difficult for a new user to separate the important data from advanced details. This was also true for the experienced developer if he had not been using the program for a while. Thus, the developers had to reconsider what information they actually needed and which functions they used the most. Based on this

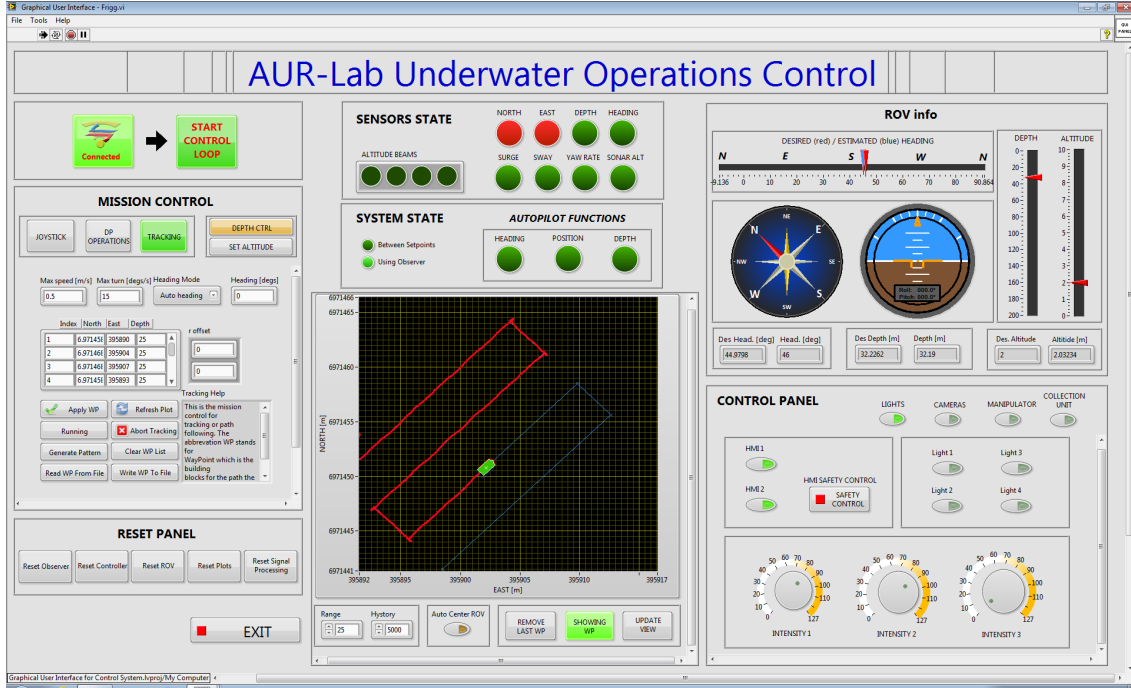


Figure 3.6: The motion control system graphical user interface (GUI).

reconsideration, the new GUI was designed with emphasis on being minimal and only data and options for the current mode should be available to the user.

An example of the GUI in tracking mode is seen in Figure 3.6. A map with the ROV is seen in the center where the red line is the trace and the blue line is the pattern to be tracked. Options related to the ROV motion is to the left, where the user can enter new way-points, change the speed, pause the ROV, etc. Alarms are given above the map and light, cameras and other tools are controlled via the control panel to the right. Advanced plots or options are accessed via the tool menu in the upper left corner. E.g. different terms in the control law can be shown in a separate plot, and the control law parameters can be set in a pop-up window.

### 3.4 Hardware-in-the-Loop Testing

The HIL testing has been very important in the development of the system. The idea with the HIL test is that every aspect of the motion control system should be the same as in actual sea trials. The only difference is that the motion control system sends and receives signals to a computer, running a mathematical model of the ROV as described in Chapter 2, instead of to a ROV. The signals are sent via serial communication or UDP from the cRIO as they are in the sea trials. Going from HIL test to sea trial is just a matter of unplugging the cables from the simulation computer and hook them up to the ROV.

All sensors are also simulated and their output protocols and formats are identical to the real sensors. Thus, HIL is also a test to check if all technicalities, such as instrument

drivers, work in the motion control system. Before a new instrument is to be deployed, the instrument with corresponding protocols and interface can be simulated based on the specifications given by the manufacturer. When the instrument arrives, it has already been tested in the motion control system (HIL) and time to sea trial readiness is reduced.

If the system runs fine in a HIL test, it is likely to succeed in sea trials. However, aspects that are not included in the simulation model can result in surprises during sea trials.

# Chapter 4

## Underwater Navigation

Underwater navigation may be the most important problem that needs to be solved in order to have more automated or autonomous underwater vehicles. Navigation, in this thesis, is the process of finding the position, velocity and attitude (PVA) of a vehicle in a given reference frame.

A major challenge is that there is no global positioning system that works under water. However, several other means of finding the position are available. Some submarines use INS which are based on large mechanical gyroscopes and accelerometers. The turn rate is integrated once to find the attitude. The acceleration, resolved in the reference frame, is integrated twice to find the position. This requires that the initial attitude and position are known, but after initialization, the INS is a self-contained system that does not rely on any external observations or measurements. However, the size and cost of these systems make them unsuitable for ROVs.

Gyroscopes and accelerometers based on other technologies, such as fiber optics and micro electromechanical systems, are much smaller and cheaper than their mechanical cousins. These are still less accurate than the mechanical solutions and the position estimates will drift-off. However, these systems can be strapped down to the vehicle. Hence, the name strapdown inertial navigation is used for systems relying on these sensors. To reduce the drift-off, such navigation systems must receive periodically position measurements from an external source. Some underwater vehicles can go to the surface to get a position fix from the GPS. This is used to correct or aid the navigation system. Hence, the name aided inertial navigation is used for such solutions.

If a velocity measurement is available, this can be resolved in the reference frame and integrated once to find the position. Determination of position without explicit position measurements, from integration of velocity or acceleration, is called dead-reckoning. Underwater vehicles use a DVL to measure the velocity relative to the sea floor or water. The DVL is widely used in underwater navigation systems, but the limited range to bottom is a challenge for mid-water navigation.

Instruments that can recognize features in the terrain, such as cameras and sonars, can be used in the navigation system close to the sea floor. These work similar to how you navigate, by determining your position from what you see around you. Simultaneous location and mapping (SLAM) is one type of terrain navigation where a map of an unknown

terrain is made as the vehicle moves around and makes observations. This map is used to find the vehicle position when features are recognized. If the map exists already, this can be given to the navigation system before the mission. The field of SLAM has been a very hot research topic in the last two decades. The solution to the problem is considered as the "Holy Grail" in the autonomous vehicle research community [23]. A tutorial on SLAM is found in [31] and [2]. An underwater case where vision-based SLAM is used in a survey of RMS Titanic is found in [35].

Knowledge about the vehicle dynamics can be used in navigation. If a perfect model of the vehicle was available and the actuator forces exactly known as well as the disturbances, then the positions could be obtained from the differential equations of motion and the initial conditions. Model-based navigation systems exploit knowledge of the vehicle dynamics to improve the accuracy and smoothness of the position estimates. However, measurements of acceleration, velocity or position is still needed in such navigation solutions. Nevertheless, good knowledge of the vehicle dynamics can compensate for noisy and low frequency measurements. Work on model-based control for ships is found in [85]. Model-based navigation for underwater vehicles is reported in [83], and a survey of underwater navigation methods is given in [56].

Any underwater navigation solution that drift-off must be corrected by position measurements. Acoustic positioning is the most used method to provide regular position fixes for underwater vehicles. There are several types of acoustic positioning systems. All are based on sending acoustic signals from known positions and use the time it takes to get a reply from the vehicle to tri-laterate its position. Acoustic positioning has limited range (only a few km), slow update rates and delays that vary with vehicle position. However, for ROVs, where the range is limited by the cable length, acoustic positioning is a good solution for most cases.

Some ROV positioning methods are using the cable to measure the position. It is easy to measure the cable length and starting point. When the curvature is also measured, this is used to calculate the ROV's position at the other end of the cable. Such techniques are not too common yet, but may take over for acoustic positioning of ROVs in the future. VideoRay has developed a smart tether as an alternative to acoustic positioning for their systems. Use of this is reported in [52].

The methods presented in this thesis are model based observers, with aiding from DVL and an acoustic positioning system, and aided strapdown inertial navigation. The contributions and experimental results are given in the following. This is mainly based on results reported previously in [25], [28] and [29].

## 4.1 Requirements for ROV Navigation

When a pilot is controlling the ROV manually, the requirements on the navigation system is less strict than when a closed-loop control system is used. A rough heading and depth indication in combination with visual feedback from cameras and some position fixes every now and then are sufficient for the pilot to complete typical work tasks. However, this is not sufficient for use in closed-loop control where more advanced and accurate

navigation methods are needed.

### 4.1.1 Closed-loop Control

The requirements to the navigation for automated ROV operations are much stricter for use in closed-loop control. The position feedback to the controller must be accurate and smooth. Jumps in the position measurements must not enter the controller as this leads to spikes in the commanded thrust. A ROV doing manipulation work must maintain a position within a decimeter or so, to be able to perform the task. The accuracy level of the navigation system must reflect this. The same goes for surveys of the sea floor with cameras or sensors with only a few meters swath width. If the navigation errors become too large, it is difficult to compare results from two repeated surveys.

It is also important that the navigation system is robust to different types of terrain, visibility or other water properties that can change from location to location. Preferably, the system should have the same accuracy everywhere, but it is difficult to obtain high accuracy navigation far off the sea floor when the DVL is out of range for bottom lock.

### 4.1.2 Measurements vs. Models

Strapdown INS that solely rely on sensor measurements, and especially accelerometers and gyroscopes, are sensitive to alignment and calibration errors. These solutions are also heavily affected by the accuracy of the attitude estimation. A small attitude error results in faulty resolved acceleration measurements which will cause the velocity and position to drift-off rapidly as this is used in the gravity compensation. Strapdown INS requires a good model of the gravity and centripetal acceleration from the Earth's rotation as well. However, when care is taken, and high accuracy sensors are used, these solutions can provide good position, velocity and attitude estimates. An advantage of strapdown INS is that all unknown forces acting on the vehicle are instantly felt by the accelerometers. The effect of the unknown forces on the vehicle's position is directly included in the INS. This is useful during manipulation work or for cases with dominating and hard to predict cable forces on the ROV.

Model-based navigation systems are very efficient at filtering noise and estimating states without causing phase lag. Although underwater vehicles with complex hydrodynamics are difficult to model, a simplified model capturing the main dynamics can improve the navigation solution considerably. Thus, knowledge of the vehicle dynamics, including the propulsion system, should be exploited in the navigation system. However, unmodelled dynamics and disturbances can result in errors in the position estimates.

### 4.1.3 Observer Design & State Estimation

Several observers have been tested on the NTNU ROVs, as taken from text books and other publications with modifications. The passive nonlinear observer from [41] was adopted for ROV use and has been tested. A particle filter was designed and tested on

ROV Minerva by Bo Zhao and results are presented in [107]. However, the main navigation workhorse has been the model-based Kalman filter.

The design and experimental results of the Kalman filters for ROV have been published in [25], and are presented in the Section 4.2.

The need to account for unknown dynamics and disturbances in the navigation system motivated the work done on attitude estimation and integration filters based on MEMS gyroscopes and accelerometers. This work has been published in [28] and [29], and is also presented in Section 4.3.

## 4.2 Model-Based Observers

Two versions of model-based Kalman filters for ROV navigation have been developed and tested. The first observer is a Kalman filter where the observer equations are linearized about 36 heading angles with sectors of  $10^\circ$  each. The second is an extended Kalman filter where nonlinearities are linearized about the estimated states. Both observers are based on Kalman filters for surface vessels in [40] and [87]. The presented Kalman filters are for the 4 DOF work space of the ROV; surge, sway, heave and yaw. The theoretical contribution is limited as this is a slight modification of known observers. However, sensor drop-outs and different sampling rates rates are dealt with in the measurement matrix  $\mathbf{H}$ , which depends on the available measurements. The observers have also been implemented and tuned on actual ROVs to get experimental results.

### 4.2.1 Sector Kalman Filters

The linearized Kalman filter, or the sector Kalman filter, is an observer for the ROV in the 4 DOF workspace. The control plant model in (2.43), (2.44) and (2.45) have been simplified accordingly to

$$\dot{\boldsymbol{\eta}} = \mathbf{R}_b^n(\psi)\boldsymbol{\nu}, \quad (4.1)$$

$$\mathbf{M}\dot{\boldsymbol{\nu}} + \mathbf{D}\boldsymbol{\nu} = \boldsymbol{\tau} + \mathbf{R}_n^b(\psi)\mathbf{b} + \mathbf{w}_m, \quad (4.2)$$

$$\dot{\mathbf{b}} = -\mathbf{T}_b^{-1}\mathbf{b} + \mathbf{w}_b, \quad (4.3)$$

where  $\mathbf{R}_b^n(\psi) \in \mathbb{R}^{4 \times 4}$  is the rotation matrix,  $\mathbf{M} \in \mathbb{R}^{4 \times 4}$  is the mass matrix including added mass, and  $\mathbf{D} \in \mathbb{R}^{4 \times 4}$  is the linear damping matrix.  $\mathbf{b} \in \mathbb{R}^{4 \times 1}$  is the bias which is modeled as a 1<sup>st</sup> order Markov process.  $\mathbf{T}_b \in \mathbb{R}^{4 \times 4}$  is a diagonal matrix with positive bias time constants.  $\mathbf{w}_m \in \mathbb{R}^{4 \times 1}$  and  $\mathbf{w}_b \in \mathbb{R}^{4 \times 1}$  are assumed to be the zero mean Gaussian white noise processes. Remember that the effect of umbilical, unmodelled dynamics and disturbance are accounted for by the bias model.

Eqs. (4.1), (4.2) and (4.3) are expressed in state space form as

$$\dot{\mathbf{x}} = \mathbf{A}\mathbf{x} + \mathbf{B}\mathbf{u} + \mathbf{E}\mathbf{w}, \quad (4.4)$$

$$\mathbf{y} = \mathbf{H}\mathbf{x} + \mathbf{v}, \quad (4.5)$$

where

$$\mathbf{x} = \begin{bmatrix} \boldsymbol{\eta} \\ \boldsymbol{\nu} \\ \mathbf{b} \end{bmatrix}, \quad \mathbf{u} = \boldsymbol{\tau}, \quad \mathbf{w} = \begin{bmatrix} \mathbf{0} \\ \mathbf{w}_m \\ \mathbf{w}_b \end{bmatrix},$$

and  $\mathbf{y} \in \mathbb{R}^{8 \times 1}$  is the measurement vector.  $\mathbf{H} \in \mathbb{R}^{8 \times 12}$  depends on available and accepted measurements from the signal processing block.  $\mathbf{v} \in \mathbb{R}^{8 \times 1}$  is a vector with sensor measurement noise.

$$\mathbf{A} = \begin{bmatrix} \mathbf{0} & \mathbf{R}_b^n(\psi) & \mathbf{0} \\ \mathbf{0} & -\mathbf{M}^{-1}\mathbf{D} & \mathbf{M}^{-1}\mathbf{R}_n^b(\psi) \\ \mathbf{0} & \mathbf{0} & -\mathbf{T}_b^{-1} \end{bmatrix}, \quad \mathbf{B} = \begin{bmatrix} \mathbf{0} \\ \mathbf{M}^{-1} \\ \mathbf{0} \end{bmatrix}, \quad \mathbf{E} = \begin{bmatrix} \mathbf{0} & \mathbf{0} & \mathbf{0} \\ \mathbf{0} & \mathbf{M}^{-1} & \mathbf{0} \\ \mathbf{0} & \mathbf{0} & \mathbf{I} \end{bmatrix},$$

where  $\mathbf{A} \in \mathbb{R}^{12 \times 12}$  is nonlinear due to the rotation matrix  $\mathbf{R}_b^n(\psi)$ .  $\mathbf{A}(\psi)$  is linearized about 36 heading angles  $\psi_i$ , where  $i$  is the sector number. Then  $\mathbf{A} = \mathbf{A}(\psi_i)$ , where each sector spans  $10^\circ$ . The measured heading from the compass together with a hysteresis function decides the sector number  $i$ . The hysteresis function is added to avoid chattering between sectors when the desired heading is close to the border of a sector.

The continuous time state space model in (4.4) and (4.5) is discretized as

$$\mathbf{x}(k+1) = \Phi(\psi_i)\mathbf{x}(k) + \Delta(\psi_i)\mathbf{u}(k) + \Gamma(\psi_i)\mathbf{w}(k), \quad (4.6)$$

$$\mathbf{y}(k) = \mathbf{H}(k)\mathbf{x}(k) + \mathbf{v}(k), \quad (4.7)$$

where

$$\Phi(\psi_i) = e^{\mathbf{A}(\psi_i)h} \simeq \mathbf{I} + \mathbf{A}(\psi_i)h, \quad (4.8)$$

$$\Delta(\psi_i) = \int_0^h e^{\mathbf{A}(\psi_i)s} ds \mathbf{B} \simeq \left( \mathbf{I}h + \frac{1}{2}\mathbf{A}(\psi_i)h^2 \right) \mathbf{B}, \quad (4.9)$$

$$\Gamma(\psi_i) = \int_0^h e^{\mathbf{A}(\psi_i)s} ds \mathbf{E} \simeq \left( \mathbf{I}h + \frac{1}{2}\mathbf{A}(\psi_i)h^2 \right) \mathbf{E}, \quad (4.10)$$

and  $k$  is the step number.  $h$  is the time step in seconds.

In the Kalman filter equations in (4.11) to (4.15),  $\mathbf{R} = \mathbf{R}^\top \in \mathbb{R}^{8 \times 8}$  and  $\mathbf{Q} = \mathbf{Q}^\top \in \mathbb{R}^{12 \times 12}$  are the covariance matrices.  $\mathbf{R}$  is a diagonal measurement covariance matrix.  $\mathbf{Q}$  is chosen to be a diagonal matrix where the elements are tuned to give satisfactory performance.

By copying the control plant model in (4.6) and (4.7), and adding injection terms, the following Kalman filter with corrector and predictor is proposed. The Kalman filter gain matrix  $\mathbf{K} \in \mathbb{R}^{12 \times 8}$  is

$$\mathbf{K}(k) = \bar{\mathbf{P}}(k)\mathbf{H}^\top(k)[\mathbf{H}(k)\bar{\mathbf{P}}(k)\mathbf{H}^\top(k) + \mathbf{R}(k)]^{-1}, \quad (4.11)$$

the corrector equations are

$$\hat{\mathbf{x}}(k) = \bar{\mathbf{x}}(k) + \mathbf{K}(k)[\mathbf{y}(k) - \mathbf{H}(k)\bar{\mathbf{x}}(k)], \quad (4.12)$$

$$\hat{\mathbf{P}}(k) = [\mathbf{I} - \mathbf{K}(k)\mathbf{H}(k)]\bar{\mathbf{P}}(k)[\mathbf{I} - \mathbf{K}(k)\mathbf{H}(k)]^\top + \mathbf{K}(k)\mathbf{R}(k)\mathbf{K}^\top(k), \quad (4.13)$$

and the predictor equations are

$$\bar{\mathbf{x}}(k+1) = \Phi(\psi_i)\hat{\mathbf{x}}(k) + \Delta(\psi_i)\mathbf{u}(k), \quad (4.14)$$

$$\bar{\mathbf{P}}(k+1) = \Phi(\psi_i)\hat{\mathbf{P}}(k)\Phi^\top(\psi_i) + \Gamma(\psi_i)\mathbf{Q}(k)\Gamma^\top(\psi_i), \quad (4.15)$$

where  $\hat{\mathbf{x}}$  is the estimated state vector which is input to the control block.

The Kalman filter runs at a fixed frequency. If a measurement is unavailable at the  $k^{th}$  iteration, the corresponding element in  $\mathbf{H}(k)$  is set to zero. It is only the predictor that runs for the state without measurements at every loop iteration.

### 4.2.2 Extended Kalman Filters

The dynamics of the ROV are highly nonlinear and coupled. This should be reflected in the observer in order to improve the state estimation. An extended 4 DOF Kalman filter that takes into account nonlinear damping, Coriolis and coupling forces are based on a modification of the process plant model in (2.42), and is given as

$$\dot{\boldsymbol{\eta}} = \mathbf{R}_b^n(\psi)\boldsymbol{\nu}, \quad (4.16)$$

$$\mathbf{M}\dot{\boldsymbol{\nu}} + \mathbf{C}(\boldsymbol{\nu})\boldsymbol{\nu} + \mathbf{D}(\boldsymbol{\nu})\boldsymbol{\nu} + \mathbf{g}(\boldsymbol{\eta}) = \boldsymbol{\tau} + \mathbf{R}_n^b(\psi)\mathbf{b} + \mathbf{w}_m, \quad (4.17)$$

$$\dot{\mathbf{b}} = -\mathbf{T}_b^{-1}\mathbf{b} + \mathbf{w}_b, \quad (4.18)$$

where  $\mathbf{C}(\boldsymbol{\nu}) \in \mathbb{R}^{4 \times 4}$  is the Coriolis and centripetal matrix, and  $\mathbf{D}(\boldsymbol{\nu}) \in \mathbb{R}^{4 \times 4}$  is the damping matrix where it is assumed that  $\boldsymbol{\nu}_r \simeq \boldsymbol{\nu}$ .

The enhanced control plant model in (4.16), (4.17) and (4.18) is written in state space form as

$$\dot{\mathbf{x}} = \mathbf{f}(\mathbf{x}) + \mathbf{B}\mathbf{u} + \mathbf{E}\mathbf{w}, \quad (4.19)$$

$$\mathbf{y} = \mathbf{H}\mathbf{x} + \mathbf{v}, \quad (4.20)$$

where  $\mathbf{B} \in \mathbb{R}^{12 \times 4}$ ,  $\mathbf{E} \in \mathbb{R}^{12 \times 12}$  and  $\mathbf{H} \in \mathbb{R}^{12 \times 12}$  are the same as for the sector heading Kalman filter in (4.4) and (4.5). All nonlinearities are put in the function

$$\mathbf{f}(\mathbf{x}) = \begin{bmatrix} \mathbf{R}_b^n(\psi)\boldsymbol{\nu} \\ -\mathbf{M}^{-1}(\mathbf{C}(\boldsymbol{\nu})\boldsymbol{\nu} + \mathbf{D}(\boldsymbol{\nu})\boldsymbol{\nu} + \mathbf{g}(\boldsymbol{\eta}) - \mathbf{R}_n^b(\psi)\mathbf{b}) \\ -\mathbf{T}_b^{-1}\mathbf{b} \end{bmatrix}, \quad (4.21)$$

which is linearized about the estimated states  $\hat{\mathbf{x}}$ . The discrete state space model has the same form as in the sector heading Kalman filter in (4.6), but  $\Phi(\psi_i) \rightarrow \Phi(k)$ ,  $\Delta(\psi_i) \rightarrow \Delta$  and  $\Gamma(\psi_i) \rightarrow \Gamma$ . The discrete state space matrices are calculated as

$$\Phi(k) = \mathbf{I} + h \frac{\partial \mathbf{f}(\mathbf{x}(k), \mathbf{u}(k))}{\partial \mathbf{x}(k)} \Big|_{\mathbf{x}(k)=\hat{\mathbf{x}}(k)}, \quad (4.22)$$

$$\Delta = h\mathbf{B}, \quad (4.23)$$

$$\Gamma = h\mathbf{E}. \quad (4.24)$$

The Kalman filter gain and corrector equations are the same as in the sector heading Kalman filter in (4.11),(4.12) and (4.13). However, the state vector in the predictor is changed as seen in (4.27). The corrector equations for the extended Kalman filter are given as

$$\hat{\mathbf{x}}(k) = \bar{\mathbf{x}}(k) + \mathbf{K}(k)[\mathbf{y}(k) - \mathbf{H}(k)\bar{\mathbf{x}}(k)], \quad (4.25)$$

$$\hat{\mathbf{P}}(k) = [\mathbf{I} - \mathbf{K}(k)\mathbf{H}(k)]\bar{\mathbf{P}}(k)[\mathbf{I} - \mathbf{K}(k)\mathbf{H}(k)]^\top + \mathbf{K}(k)\mathbf{R}(k)\mathbf{K}^\top(k), \quad (4.26)$$

and the predictor equations are

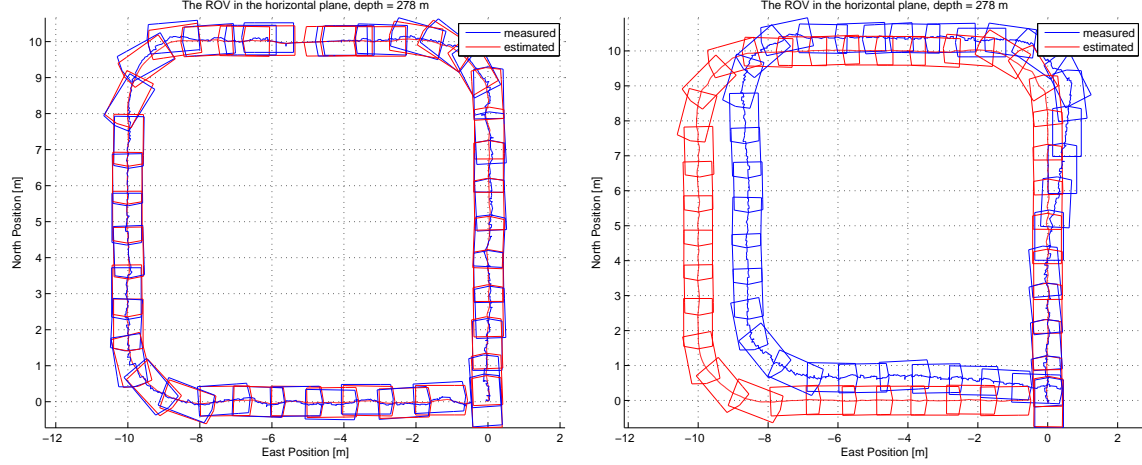
$$\bar{\mathbf{x}}(k+1) = \hat{\mathbf{x}}(k) + h\mathbf{f}(\hat{\mathbf{x}}(k)) + \Delta\mathbf{u}(k). \quad (4.27)$$

$$\bar{\mathbf{P}}(k+1) = \Phi(\psi_i)\hat{\mathbf{P}}(k)\Phi^\top(\psi_i) + \Gamma(\psi_i)\mathbf{Q}(k)\Gamma^\top(\psi_i). \quad (4.28)$$

It is the estimated state  $\hat{\mathbf{x}}(k)$  which is the input to the control block. Note that there is no proof of global asymptotic stability and convergence when the system is linearized.

The extended Kalman filter is more laborious to implement and to run than the sector Kalman filter. For slow ROVs the Coriolis force will be small. The extended Kalman filter can be useful for faster ROVs when the quadratic damping is important. However, it is the sector Kalman filter that is the default observer for the translational states in the developed motion control system.

Some experimental results with the ROV Minerva using the extended Kalman filter are seen in Figure 4.1. Figure 4.1a shows the trace and snapshots of the ROV outline for measured (blue) and estimated (red) positions while doing a square maneuver in closed-loop control with position measurements from the acoustic positioning system HiPAP 500 (SSBL). The dead-reckoning performance of the same maneuver is shown in Figure 4.1b. The estimated trajectory follows the squared path with rounded corners as given by the guidance system. However, the measured position, serving as the ground truth, differs from the estimated and indicates that dead-reckoning results in position errors. These errors can be due to small alignment and calibration inaccuracies of the DVL and heading sensor, bias estimation and modeling errors. A workhorse navigator DVL from Teledyne RDI and a motion reference unit, MRU5+, from Kongsberg Seatex was used in the experiment.



(a) ROV Minerva, extended Kalman filter with position measurements. (b) ROV Minerva, extended Kalman filter without position measurements.

Figure 4.1: Experimental results for the extended Kalman filter on ROV Minerva with position measurements and in dead-reckoning.

### 4.3 Sensor-Based Observers

Advances in sensor technology are resulting in smaller, lighter, cheaper and accurate sensor packages. This evolution is ideal for small underwater vehicles as they can use sensors previously only available to large vehicles at a great cost. The advances in MEMS based sensors are of special interest. This technology has enabled very small and inexpensive gyroscopes and accelerometers that can be mounted in sets of 3 mutually perpendicular sensors inside an IMU to measure rotation rates in roll, pitch and yaw and acceleration in surge, sway and heave. The MEMS based IMU with solid state magnetometers is the base sensor package for strapdown INS for ROVs in this thesis. It should be noted that the heading estimation is especially sensitive to magnetic disturbances when magnetometers are used in the navigation system.

The strapdown INS problem can be divided in two main parts, (i) attitude estimation and (ii) integration filter for estimation of the translational states; position and linear velocity. The INS can also have interconnections between (i) and (ii) to enhance the accuracy of the total navigation solution. A standard INS solution is shown in Figure 4.2 where the attitude estimator is mainly an integrator. This method requires very accurate sensors to estimate the attitude and positions and is not applicable for MEMS based IMUs. Other solutions are needed to use MEMS sensors in a strapdown INS. An alternative solution is proposed in the following.

#### 4.3.1 Background

MEMS based IMUs have improved greatly in performance in the recent years. However, due to gyroscope in-run bias stability errors, the attitude can not be obtained from pure

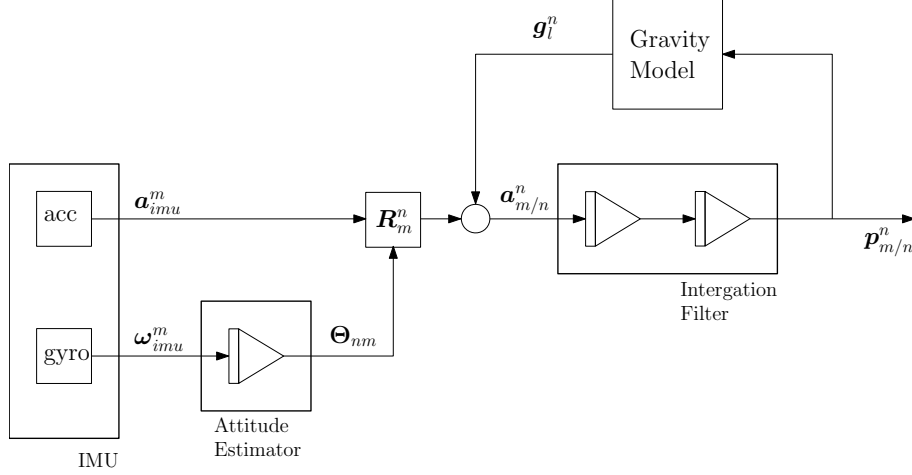


Figure 4.2: Strapdown INS.

integration only. The attitude estimation problem has been a research topic for several decades, and a large number of different approaches have been studied. A summary of some of these methods are given in [21], which is a survey on the subject. This survey concludes that the Kalman filter is still the workhorse of attitude estimation although other methods show promising results. It is noted that the nonlinear observers are especially interesting as global stability results can be obtained in many cases.

Since that survey, nonlinear observers have developed further. Some important work emerged from the research on ECFs presented first in [67] and [68]. The main idea of the ECF for attitude estimation is to compare the acceleration and magnetic measurement vectors to known reference vectors, and use this to correct the gyroscope measurements before integration. The method includes estimation and correction for gyroscope bias as well. The challenge with the method in [67] is that the acceleration reference vector, i.e. the specific force in the reference frame, is unknown and must be approximated. The acceleration reference vector in [67] was simply approximated as the gravity vector. This method showed fairly good performance for shorter periods of acceleration and zero mean acceleration. However, for longer periods of acceleration, the method would produce unacceptable errors. This work was taken further in [48] where global stability was proven also for varying reference vectors.

The limitation of the ECF in [67] to zero mean accelerations was addressed in [53], where it was proposed to use velocity measurements in the reference frame in order to estimate the specific force vector. This made attitude estimation possible for longer periods of acceleration, such as flying in circles. In practice, magnetic disturbances and natural variation in the Earth's magnetic field can cause large errors. To limit the effect of these errors to yaw, a method for decoupling roll and pitch from yaw estimation was proposed in [70] and adopted in [54]. Methods for estimating the unknown specific force vector in the reference frame was improved in [47] where integration of global navigation satellite systems (GNSS) and IMU measurements were used to estimate position and linear velocity in addition to attitude. The interconnection (acceleration feedback) between the estimation of linear velocity and position and attitude improved the estimation of all

states. The observer for GNSS aided inertial navigation in [49] was extended to account for the Earth's rate of rotation.

GNSS and INS integration for strapdown inertial navigation is a research field covered by several text books. [50] and [93] give an overview and introduction. Marine applications are found in [40]. Work on nonlinear observers for GNSS and INS integration has been studied since the 90's, see e.g. [76] and [101].

Although the new nonlinear observers for IMUs aided by GNSS measurements show promising results, GNSS is not available everywhere, e.g. indoors and underwater. For underwater applications, an acoustic positioning system can be used for aiding, but these measurements are not useful for estimation of the vehicle acceleration or velocity in the reference frame due to noise and slow update rates. However, a DVL provides accurate velocity measurements in the body frame of the vehicle. The method presented in this thesis is on attitude estimation for accelerated vehicles when the velocity measurements are available in the vehicle frame. The linear velocity and position are also estimated. In the work on ECFs mentioned above, the idea is to estimate the acceleration reference vector and compare this estimate with the IMU acceleration measurements. Here, the known gravity vector will be the reference vector and the IMU measurements are modified in order to approximate the gravity component. Thus, velocity measurements in the body frame can be used to improve the attitude estimation of underwater vehicles.

The main contributions in this section are

- A proposed modification to the ECF in order to use velocity measurements in the vehicle frame, or estimates, to improve the attitude estimation.
- Integration filter for velocities in the vehicle frame with the ECI frame assumed to be inertial.
- Simulation and experimental results.
- Sensitivity considerations.

The proposed method for using the DVL velocity measurements in order to improve the attitude estimation, was first proposed in a delivery for TK 8109 Advanced Topics in Guidance and Navigation, a class at NTNU in the spring of 2013. The method was later published in [28] and with experimental results in [29]. A very similar method was developed in parallel by [96]. That work uses the same main idea of using velocity measurements in the body frame to improve the attitude estimation and shows that dead-reckoning accuracy from integration of DVL velocities is improved by their enhanced attitude estimation. However, the DVL measurements are used directly in the attitude estimation in [96], and here it is the interconnection between the attitude observer and the integration filter that enhances the navigation solution.

### 4.3.2 Modeling

The equations for position, velocity and attitude are given by (4.29)-(4.31) when the ECI frame,  $\{i\}$ , is assumed to be inertial. Eq. (4.30) is given in  $\{m\}$ , because the velocity

measurements which are used in the observer are measured in the body frame of the velocity sensor,  $\{d\}$ . These equations are the basis for the observers.

$$\dot{\mathbf{p}}_{m/n}^n = \mathbf{R}_m^n \mathbf{v}_{m/e}^m, \quad (4.29)$$

$$\dot{\mathbf{v}}_{m/e}^m = \mathbf{a}_{m/i}^m - \boldsymbol{\omega}_{m/i}^m \times \mathbf{v}_{m/e}^m - \mathbf{R}_n^m (\boldsymbol{\omega}_{e/i}^n + \boldsymbol{\omega}_{n/e}^n) \times \mathbf{v}_{m/e}^m + \mathbf{R}_n^m \mathbf{g}_l^n, \quad (4.30)$$

$$\dot{\mathbf{R}}_m^n = \mathbf{R}_m^n \mathbf{S}(\boldsymbol{\omega}_{m/i}^m) - \mathbf{S}(\boldsymbol{\omega}_{e/i}^n) \mathbf{R}_m^n - \mathbf{S}(\boldsymbol{\omega}_{n/e}^n) \mathbf{R}_m^n, \quad (4.31)$$

where  $\mathbf{p}_{m/n}^n \in \mathbb{R}^{3 \times 1}$  is the position vector in  $\{n\}$  and  $\mathbf{v}_{m/e}^m \in \mathbb{R}^{3 \times 1}$  is the velocity vector in  $\{m\}$ .  $\boldsymbol{\omega}_{m/i}^m \in \mathbb{R}^{3 \times 1}$  is the gyroscope turn rate,  $\boldsymbol{\omega}_{e/i}^n \in \mathbb{R}^{3 \times 1}$  is the Earth's angular velocity and  $\boldsymbol{\omega}_{n/e}^n \in \mathbb{R}^{3 \times 1}$  is the turn rate of the local  $\{n\}$  frame. The two latter can be calculated according to (2.15) and (2.16).  $\mathbf{g}_l^n \in \mathbb{R}^{3 \times 1}$  is the local gravity vector, or the "plumb bob" gravity vector, in  $\{n\}$  and is calculated from (2.18) or a more advanced gravity model.

Note that  $\boldsymbol{\omega}_{n/e}^n$  will be very small, in the order of  $10^{-8}$  to  $10^{-7}$  rads/s, for velocities typical for underwater vehicles. Thus,  $\boldsymbol{\omega}_{n/e}^n$  can be neglected for practical applications. However, as the in-bias gyro stability of MEMS IMUs are getting lower than the turn rate of the Earth,  $\boldsymbol{\omega}_{e/i}^n$  should not be neglected in the observer equations.

It is seen from the last term in (4.30) that the estimation of velocity, and hence position, will drift off if the attitude  $\mathbf{R}_n^m$  or the gravity model  $\mathbf{g}_l^n$  is inaccurate. Thus, it is important to use the local gravity vector which includes the centripetal acceleration due to the Earth's rotation.

The differential equation for the attitude dynamics given in (4.31) is expressed in quaternions in (4.32) as

$$\begin{aligned} \dot{\mathbf{q}}_m^n &= \frac{1}{2} \left[ \begin{array}{c} -\boldsymbol{\epsilon}^T \\ \eta \mathbf{I} + \mathbf{S}(\boldsymbol{\epsilon}) \end{array} \right] \boldsymbol{\omega}_{m/i}^m - \frac{1}{2} \left[ \begin{array}{c} -\boldsymbol{\epsilon}^T \\ \eta \mathbf{I} - \mathbf{S}(\boldsymbol{\epsilon}) \end{array} \right] (\boldsymbol{\omega}_{e/i}^n + \boldsymbol{\omega}_{n/e}^n) \\ &= \mathbf{T}_q(\mathbf{q}_m^n) \boldsymbol{\omega}_{m/i}^m - \mathbf{\Omega}_q(\mathbf{q}_m^n) (\boldsymbol{\omega}_{e/i}^n + \boldsymbol{\omega}_{n/e}^n), \end{aligned} \quad (4.32)$$

where  $\mathbf{q}_m^n = [\eta \ \boldsymbol{\epsilon}^T]^T$  is the quaternion representation of the attitude. See Appendix C for details on quaternions. The matrices  $\mathbf{T}_q(\mathbf{q}_m^n) \in \mathbb{R}^{4 \times 4}$  and  $\mathbf{\Omega}_q(\mathbf{q}_m^n) \in \mathbb{R}^{4 \times 4}$  are introduced to simplify the notation of the differential equation.

Eq. (4.33) and (4.34) shows the relationship between turn rates. This was used in the derivation of the differential equations for motion in (4.29)-(4.31).

$$\boldsymbol{\omega}_{m/n}^m = \boldsymbol{\omega}_{m/i}^m - \mathbf{R}_n^m (\boldsymbol{\omega}_{e/i}^n + \boldsymbol{\omega}_{n/e}^n), \quad (4.33)$$

$$\boldsymbol{\omega}_{m/e}^m = \boldsymbol{\omega}_{m/i}^m - \mathbf{R}_n^m \boldsymbol{\omega}_{e/i}^n. \quad (4.34)$$

### 4.3.3 Attitude Estimation

The proposed attitude estimation here is a method based on the ECF in [67] and [28], where modifications from [54] and [47] have been adopted. The proposed method forms an interconnection between the attitude observer and the translational observer.

## Reference vectors

The reference vectors in  $\{n\}$  for the acceleration and magnetic field measurements are given by (4.35) as

$$\mathbf{r}_{01}^n = \frac{-\mathbf{g}_l^n}{\|\mathbf{g}_l^n\|}, \quad \mathbf{r}_{02}^n = \frac{\mathbf{m}^n}{\|\mathbf{m}^n\|}, \quad (4.35)$$

where  $\mathbf{r}_{01}^n$  is the normalized local gravity reference vector.  $\mathbf{r}_{01}^n = [0 \ 0 \ -1]^T$  if  $\{n\}$  is assumed to be an inertial frame.  $\mathbf{r}_{02}^n$  is the normalized Earth magnetic field reference vector. In order to decouple roll and pitch estimates from yaw, the second reference vector can be modified to

$$\mathbf{r}_{02}^n = \frac{\mathbf{r}_{01}^n \times \mathbf{m}^n}{\|\mathbf{r}_{01}^n \times \mathbf{m}^n\|}, \quad (4.36)$$

as proposed originally by [70].

## IMU vectors

The normalized acceleration and magnetic field vectors in  $\{m\}$  are given by (4.37) as,

$$\mathbf{r}_1^m = \frac{\bar{\mathbf{a}}_{imu}^m}{\|\bar{\mathbf{a}}_{imu}^m\|}, \quad \mathbf{r}_2^m = \frac{\mathbf{m}_{imu}^m}{\|\mathbf{m}_{imu}^m\|}. \quad (4.37)$$

where  $\bar{\mathbf{a}}_{imu}^m$ , given by (4.38), is the measured acceleration vector adjusted for centripetal and translational acceleration, Earth rotation, rotation of the local  $\{n\}$  frame and accelerometer bias as estimated in the translational observer.

$$\bar{\mathbf{a}}_{imu}^m = \mathbf{a}_{imu}^m - \hat{\omega}_{m/e}^m \times \hat{\mathbf{v}}_{m/e}^m - \mathbf{R}_n^m (\boldsymbol{\omega}_{e/i}^n + \boldsymbol{\omega}_{n/e}^n) \times \hat{\mathbf{v}}_{m/e}^m - \dot{\hat{\mathbf{v}}}_{m/e}^m - \hat{\mathbf{b}}_{acc}^m. \quad (4.38)$$

Ideally, the modified acceleration should be  $\bar{\mathbf{a}}_{imu}^m = -\mathbf{R}_n^m \mathbf{g}_l^n$ . The calibrated magnetometer measurement vector from the IMU is noted  $\mathbf{m}_{imu}^m$ . The components of  $\bar{\mathbf{a}}_{imu}^m$  for the case where  $\{n\}$  is inertial are shown in Figure 4.3 for the North-Down plane together with the gravity component ( $-\mathbf{R}_n^m \mathbf{g}^n$ ) and the reference vectors in (4.35).

If the second reference vector is modified to decouple roll and pitch from yaw, then the second IMU vector should be modified according to

$$\mathbf{r}_2^m = \frac{\bar{\mathbf{a}}_{imu}^m \times \mathbf{m}_{imu}^m}{\|\bar{\mathbf{a}}_{imu}^m \times \mathbf{m}_{imu}^m\|}. \quad (4.39)$$

The decoupling of roll and pitch from yaw is very useful in practical applications. Magnetic disturbances would otherwise produce roll and pitch errors in addition to heading errors. That can be a problem in this application due to the sensitivity to roll and pitch errors in the integration filter as explained earlier.

The reference vectors must be transformed to  $\{m\}$  in order to compare them with the IMU vectors. The transformation is given by (4.40) for the attitude expressed in quaternions. Note that  $\hat{\mathbf{q}} = \mathbf{q}$  when  $\hat{\mathbf{r}}_i^m = \mathbf{r}_i^m$ .

$$\hat{\mathbf{r}}_1^m = \mathbf{R}_n^m(\hat{\mathbf{q}})\mathbf{r}_{01}^n, \quad \hat{\mathbf{r}}_2^m = \mathbf{R}_n^m(\hat{\mathbf{q}})\mathbf{r}_{02}^n, \quad (4.40)$$

where  $\hat{\mathbf{q}}$  is estimated by the ECF as shown next.

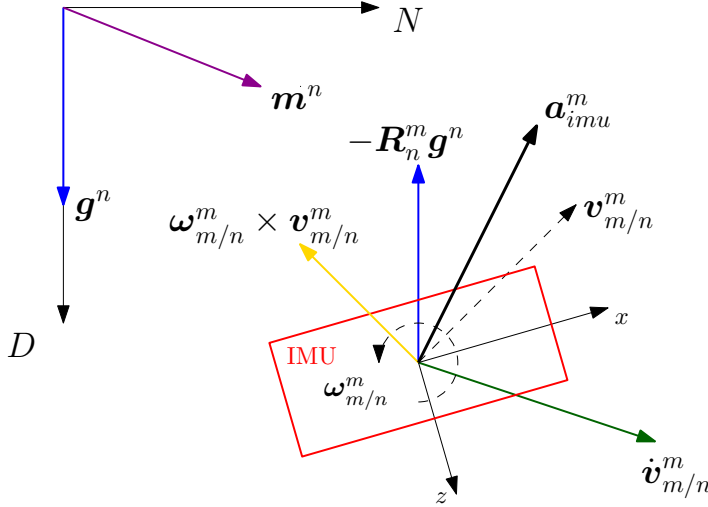


Figure 4.3: Reference and IMU vectors in North-Down plane (2-D).

### Explicit Complementary Filter

The explicit complementary filter equations given by (4.41), (4.42) and (4.43) are a combination and modification of the equations given in [40] and [54].

$$\boldsymbol{\sigma} = \sum_{i=1}^2 k_i \mathbf{r}_i^m \times \hat{\mathbf{r}}_i^m, \quad (4.41)$$

$$\dot{\hat{\mathbf{q}}}^n_m = \mathbf{T}_q(\hat{\mathbf{q}}^n_m) \left[ \boldsymbol{\omega}_{imu}^m - \hat{\mathbf{b}}_{gyro}^m + \mathbf{K}_p \boldsymbol{\sigma} \right] - \boldsymbol{\Omega}_q(\hat{\mathbf{q}}^n_m) (\boldsymbol{\omega}_{e/i}^n + \boldsymbol{\omega}_{n/e}^n), \quad (4.42)$$

$$\dot{\hat{\mathbf{b}}}_{gyro}^m = \mathbf{K}_b(sat_\Delta(\hat{\mathbf{b}}) - \hat{\mathbf{b}}) - \mathbf{K}_i \boldsymbol{\sigma}, \quad |\hat{\mathbf{b}}(0)| < \Delta \quad (4.43)$$

where  $\boldsymbol{\sigma} \in \mathbb{R}^3$  is the injection term.  $k_i$  is a gain to weight acceleration and magnetic field vectors.  $\mathbf{K}_p \in \mathbb{R}^{3 \times 3}$  is the observer gain matrix,  $\mathbf{K}_b \in \mathbb{R}^{3 \times 3}$  is the gain to control the gyro-bias rate of desaturation and  $\mathbf{K}_i \in \mathbb{R}^{3 \times 3}$  is the gyro-bias estimation gain matrix.  $\mathbf{K}_p$ ,  $\mathbf{K}_b$  and  $\mathbf{K}_i$  are set to be diagonal matrices.  $sat_\Delta(\cdot)$  is the classical saturation function with  $\Delta$  as the saturation limit. The  $\mathbf{K}_b$  term in (4.43) was proposed by [54] to ensure properties of stability and convergence, and to limit integral wind-up effects. The output of the ECF is the estimated attitude vector of the IMU,  $\hat{\mathbf{q}}_m^n$ .

A block diagram showing the attitude and translational observer with interconnections is seen in Figure 4.4. The diagram is drawn for the case where  $\{n\}$  is an inertial reference frame and the gyro-bias estimator is a pure integrator.

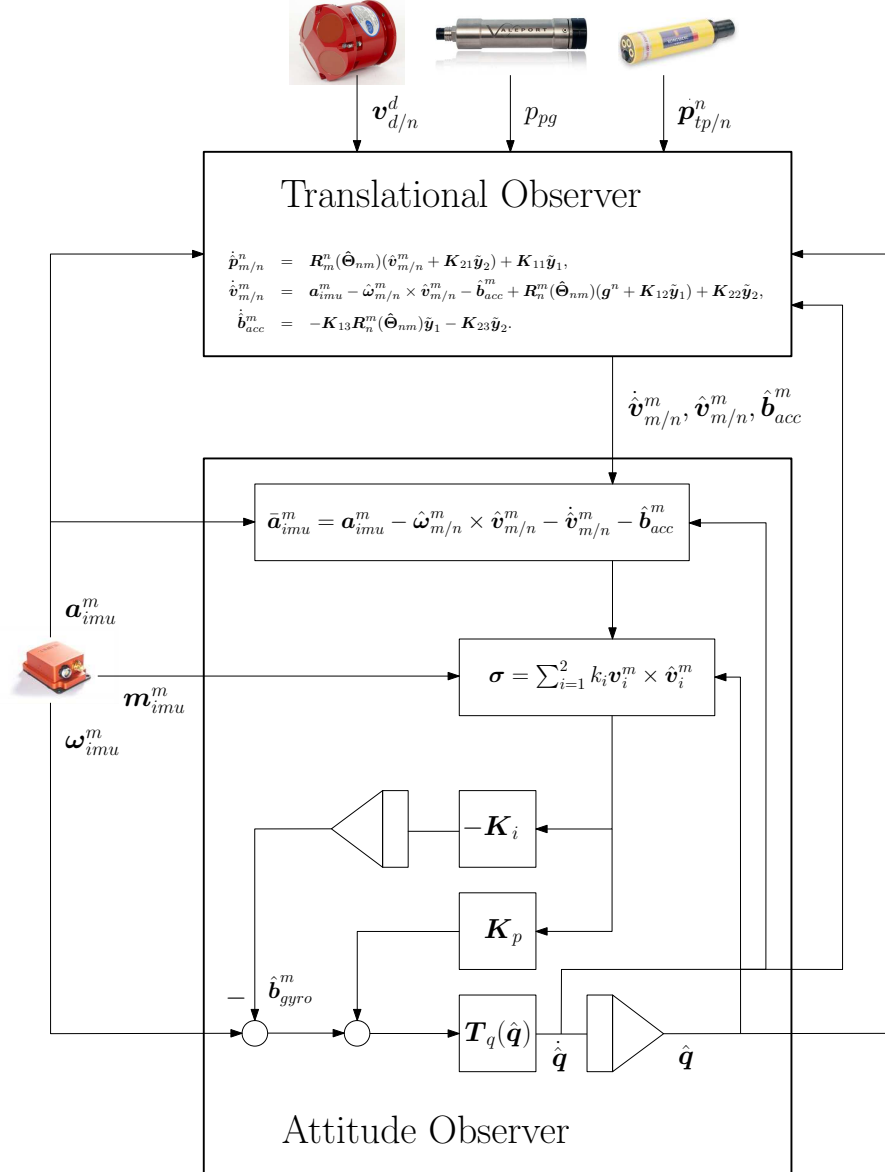


Figure 4.4: Block diagram, observer interconnections.

#### 4.3.4 Integration Filters

By copying (4.29) and (4.30) and adding injection terms and a bias estimator for the accelerometer, the following translational observer is proposed.

$$\dot{\hat{p}}_{m/e}^n = \hat{R}_m^n(\hat{v}_{m/e}^m + \mathbf{K}_{21}\tilde{y}_2) + \mathbf{K}_{11}\tilde{y}_1, \quad (4.44)$$

$$\begin{aligned} \dot{\hat{v}}_{m/e}^m &= \mathbf{a}_{imu}^m - \hat{\omega}_{m/i}^m \times \hat{v}_{m/e}^m - \hat{R}_n^m(\boldsymbol{\omega}_{e/i}^n + \boldsymbol{\omega}_{n/e}^n) \times \hat{v}_{m/e}^m - \hat{b}_{acc}^m \\ &\quad + \hat{R}_n^m(\mathbf{g}_l^n + \mathbf{K}_{12}\tilde{y}_1) + \mathbf{K}_{22}\tilde{y}_2, \end{aligned} \quad (4.45)$$

$$\dot{\hat{b}}_{acc}^m = -\mathbf{K}_{13}\hat{R}_n^m\tilde{y}_1 - \mathbf{K}_{23}\tilde{y}_2, \quad (4.46)$$

where  $\mathbf{K}_{11}$ ,  $\mathbf{K}_{21}$ ,  $\mathbf{K}_{12}$ ,  $\mathbf{K}_{22}$ ,  $\mathbf{K}_{13}$  and  $\mathbf{K}_{23} \in \mathbb{R}^{3 \times 3}$  are gain matrices. The estimation errors used in the injection terms are given by (4.47) and (4.48) for the translational position and velocity, respectively.

$$\tilde{y}_1 = p_{m/e}^n - \hat{p}_{m/e}^n, \quad (4.47)$$

$$\tilde{y}_2 = v_{m/e}^m - \hat{v}_{m/e}^m. \quad (4.48)$$

The observer gain matrices are chosen to have the structure in (4.49) as suggested in [40] for another similar integration filter.

$$\mathbf{K}_i = \text{diag}\{m_i, m_i, l_i\}, \quad i = 1, 2, 3. \quad (4.49)$$

where surge and sway have the same gains  $m_i > 0$  and heave is tuned by  $l_i > 0$ . Surge and sway use the same gain because an acoustic positioning system is used for the horizontal position measurements. A pressure gauge measures the depth.

Note that the velocity and position estimates in the translational observer can drift rapidly in case of drop-out of both velocity and position measurements. For periods without velocity or position feedback, the estimated velocity and position are based entirely on integration of IMU measurements. Hence, the dead-reckoning performance is very sensitive to the accelerometer accuracy and attitude estimation for gravity compensation. High accuracy and low noise accelerometers and gyros are needed if the velocity and/or position measurements have low update rates. If the velocity or position estimates drift off too quickly between velocity and position measurements, the estimated velocity will be choppy and not usable for closed-loop control.

### 4.3.5 Measurements and Output

Both the attitude observer and translational observer have origin in the  $\{m\}$  frame. Thus, the position and velocity measurements needed to calculate the estimation errors (4.47) and (4.48) must be given for  $\{m\}$ . General measurement equations for the ROV sensors and transformations are given in Chapter 2, and the needed measurements for the integration filter are given next followed by the transformation of the estimated states to  $\{b\}$ .

## Observer Inputs

The feedback used to calculate the estimation errors in the translational observer are calculated from the measurement equations as

$$\mathbf{p}_{m/n}^n = \mathbf{p}_{tp/n}^n - \mathbf{R}_m^n(\hat{\Theta}_{nm})\mathbf{r}_{tp/m}^m, \quad (4.50)$$

$$\mathbf{p}_{m/n}^n(3) = z_{pg/e}^n - [0 \ 0 \ 1]\mathbf{R}_m^n(\hat{\Theta}_{nm})\mathbf{r}_{pg/m}^m, \quad (4.51)$$

$$\mathbf{v}_{m/e}^m = \mathbf{R}_d^m(\Theta_{md})\mathbf{v}_{d/n}^d - \hat{\omega}_{m/e}^m \times \mathbf{r}_{dvl/m}^m, \quad (4.52)$$

where the vertical position is measured from the pressure gauge as this provides higher accuracy and update rate than the APS.

## Transformation to Vehicle Frame

Both the translational and attitude observers are expressed with origin in  $\{m\}$ . The estimated states must be transformed to the vehicle frame and CO before use in the motion control system. This transformation is given by (4.53)-(4.56).

$$\Theta_{nb} = \Theta_{nm} - \Theta_{bm}, \quad (4.53)$$

$$\mathbf{p}_{b/n}^n = \mathbf{p}_{m/n}^n - \mathbf{R}_b^n(\Theta_{nb})\mathbf{r}_{imu/b}^b, \quad (4.54)$$

$$\omega_{b/n}^b = \mathbf{R}_m^b(\Theta_{bm})\omega_{m/n}^m, \quad (4.55)$$

$$\mathbf{v}_{b/n}^b = \mathbf{R}_m^b(\Theta_{bm})\mathbf{v}_{m/e}^m - \omega_{b/n}^b \times \mathbf{r}_{imu/b}^b, \quad (4.56)$$

where  $\mathbf{p}_{b/n}^n$  is the position of the CO in  $\{n\}$ ,  $\Theta_{nb}$  is the vehicle attitude,  $\mathbf{v}_{b/n}^b$  is the vehicle velocity in  $\{b\}$  and  $\omega_{b/n}^b$  is the vehicle turn rate vector.

The final output of the attitude observer and integration filter is the estimated generalized coordinates  $\hat{\eta}$  and  $\hat{\nu}$  as seen in (4.57).

$$\hat{\eta} = \begin{bmatrix} \hat{\mathbf{p}}_{b/e}^n \\ \hat{\Theta}_{nb} \end{bmatrix}, \quad \hat{\nu} = \begin{bmatrix} \hat{\mathbf{v}}_{b/e}^b \\ \hat{\omega}_{b/n}^b \end{bmatrix}. \quad (4.57)$$

### 4.3.6 Simulation and Effect of Observer Interconnections

The presented simulation cases in this section, demonstrating the effects of the observer interconnections, contain two cases where the observer is run in different modes.

- case 0: the attitude estimator runs as a stand alone observer.
- case 1: the proposed interconnections between the attitude observer and integration filter are used.

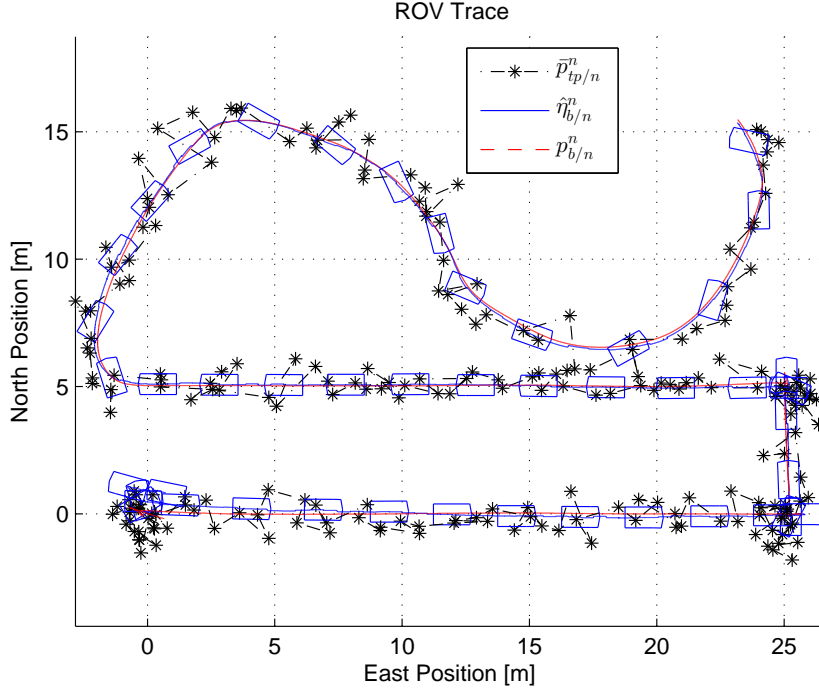


Figure 4.5: ROV trace and outline, case 1 (Simulated).

Both cases use the simulated run seen in Figure 4.5 where the ROV does a rectangular lawn mower pattern before going into a S maneuver in joystick mode. The cruise speed is 0.5 m/s. Figure 4.5 shows the ROV position in North and East coordinates. The red line shows the true positions, the black stars are position measurements of the simulated transponder, the blue line is the estimated trajectory with snapshots of the ROV outline, all for the case with interconnections, case 1.

The observer in the simulation cases use the simulated sensor measurements as described in Chapter 2. All simulations are based on the mathematical model of the ROV Minerva.

In this simulation the NED frame is assumed to be inertial, and the attitude observer is run with reference and IMU vectors as given by (4.35) and (4.37), respectively. That is the magnetometer is also used to estimate roll and pitch.

In the case with stand alone attitude observer,  $\bar{a}_{imu}^m = a_{imu}^m$ . With observer interconnections  $\bar{a}_{imu}^m$  is given as proposed in (4.38). The simulated sensors specifications and positions on the ROV are given by Table 4.1.

The observer gains for the translational observer are  $K_{11} = \text{diag}\{5, 5, 0.1\}$ ,  $K_{12} = 0.1I_{3 \times 3}$ ,  $K_{21} = 5I_{3 \times 3}$ ,  $K_{22} = 20I_{3 \times 3}$ ,  $K_{13} = 0_{3 \times 3}$  and  $K_{23} = 0_{3 \times 3}$  as the simulated accelerometers are bias free. The attitude observer gains are set to  $k_i = 1$ ,  $i = 1, 2$ ,  $K_p = \text{diag}\{1, 1, 10\}$  and  $K_i = 0.3I_{3 \times 3}$ . At each iteration, the attitude observer is run first to provide an estimated attitude for the translational observer.

The simulated IMU measurements are seen in Figure 4.6. Accelerations are in the top plot, gyroscope measurements in the middle and magnetometer data in the bottom plot.

Table 4.1: Sensor specifications and positions on ROV.

	Sensor specifications			Positions			
	noise [ $\sigma$ ]	bias	[Hz]	x [m]	y [m]	z [m]	
TP	$p_{tp/n}^n$	0.5 [m]	0	1	-0.75	0	-0.45
PG	$p_{pg}$	0.001 [m]	0	8	0	0	0.2
DVL	$v_{d/e}^d$	0.003 [m/s]	0	5	-0.75	0	0.25
	$a_{imu}^m$	0.007 [m/s <sup>2</sup> ]	0	100	0.79	-0.39	-0.35
IMU	$\omega_{imu}^m$	0.0012 [rad/s]	$\begin{bmatrix} -0.08 \\ 0.11 \\ 0.05 \end{bmatrix}$ [°/s]	100			
	$m_{imu}^m$	0.0035 [AU]	0	100			

Measurements in or about the x-axis are blue dashed, green dash dotted for y-axis, and red for z-axis measurements. E.g. the gyroscope yaw rate (red) of about -0.25 rads/s (15 deg/s) just after 100 s corresponds to the turn seen at 5 m North and 25 m East in Figure 4.5.

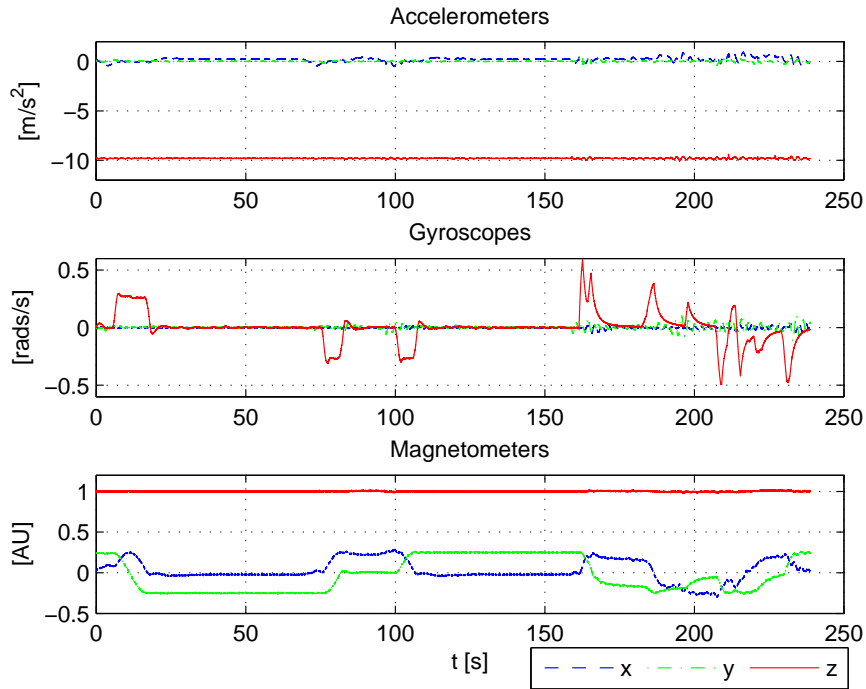


Figure 4.6: IMU simulated data output.

The interconnection enhances the performance of both observers as shown in Figure 4.7, 4.8a and 4.8b where case 0 is blue and case 1 is red.

Figure 4.7 shows the attitude estimation errors. Note the superior performance of case 1 during turns of the ROV. The IMU is mounted at a corner of the ROV so that it expe-

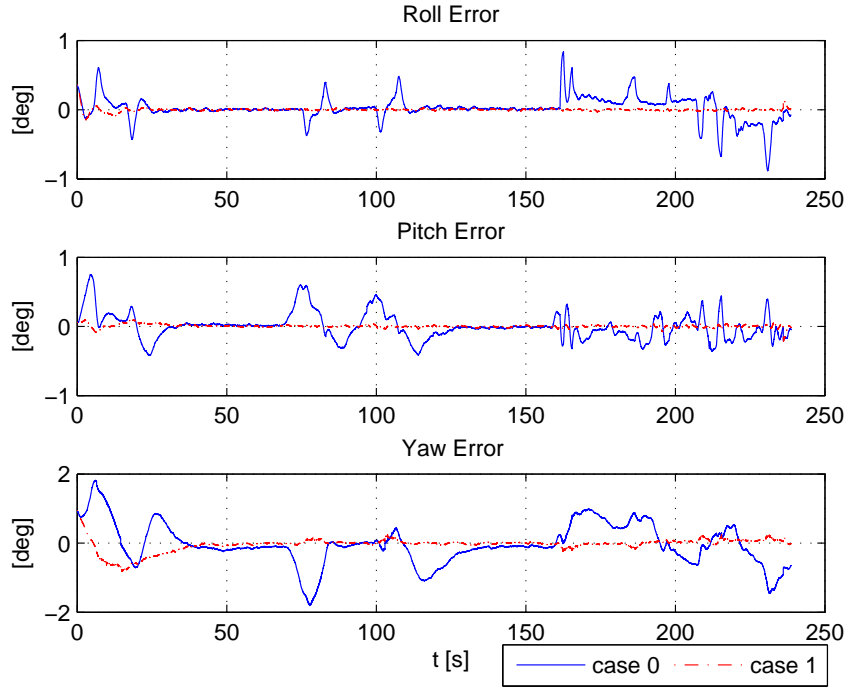
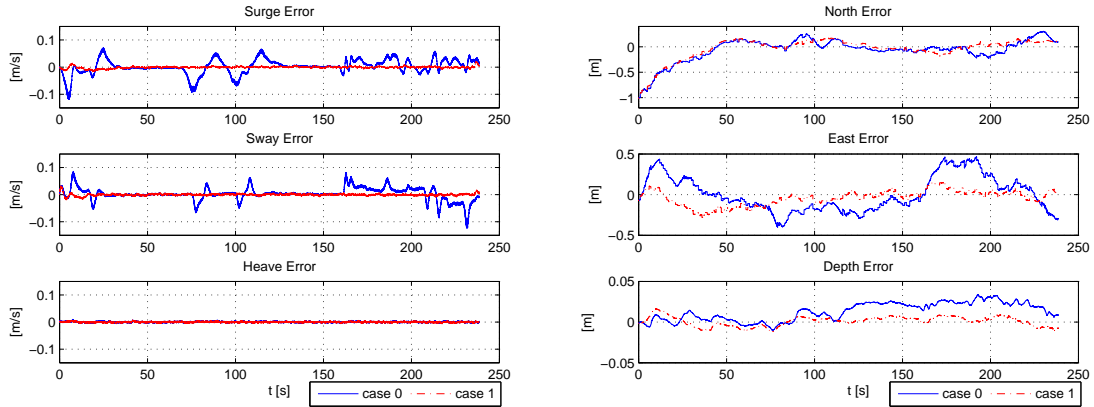


Figure 4.7: Attitude errors, case 0 (blue) and 1 (red).



(a) Velocity errors, case 0 (blue) and 1 (red).

(b) Position errors, case 0 (blue) and 1 (red).

Figure 4.8: Velocity and position estimation errors without (case 0) and with (case 1) observer interconnections.

riences centripetal accelerations also during pure turns of the ROV. Without the observer feedback, the attitude observer sees this as a roll and pitch motion as it can not separate the centripetal and translational acceleration from the acceleration of gravity. This causes an erroneous attitude which is used in the translational observer to compensate for gravity and to integrate the accelerometer measurements to obtain the estimated velocities. Hence, errors propagate to the estimated velocity and position as well in case 0.

Figure 4.8a shows the velocity estimation error  $\tilde{y}_2$  using the true value of  $v_{m/n}^m$ . The measured value of  $v_{m/n}^m$  is used in the observer. It is clear that the velocity error during periods of proper acceleration is affected by the attitude error in case 0.

Figure 4.8b shows the estimated position error  $\tilde{y}_1$ . Again, the plotted errors are calculated from the true values and the measured values are used in the observer. The observer is initialized at  $t=0$  with the measured position. Note that the estimation error is smallest for case 1 as the velocity errors from case 0 propagate to the estimated position. However, as the trajectory in this simulation has symmetrical turns, and about zero mean acceleration, the position errors are not too different for case 0 and 1. For a vehicle flying around in circles, the position error in case 0 would have had a steady state offset, and the difference between case 0 and 1 would have been more profound for the position estimation errors as well.

### 4.3.7 Simulation vs. Experiments

A comparison between simulation and experimental results that point out some important practical considerations is given in the following.

In order to test and verify the proposed observer a case study of star-patterns is defined. The ROV runs in a star-pattern inside a circle with 50 m diameter in the simulation and in an experiment with the ROV Minerva, seen in Figure 4.9. The ROV North-East trace is seen in Figure 4.10a and 4.10b for the simulation and experiment, respectively. The objective of the simulation and experiment is to see how the proposed observer works for a real implementation. In the simulation case, the sensors used on Minerva are simulated with noise properties as given by the manufacturers. The sensors have the same position and orientation in the simulation as on the ROV Minerva during the experiments. The ROV sensors are listed in Table 4.2. The simulation case is useful for comparison because the ground truth for position and attitude is not available in the experiments done here.

During the field trials, the ROV was run in closed-loop control using the control system described in Chapter 3. The experimental results are from post-processing of logged sensor data. However, it should be noted that the proposed ECF was used in the closed-loop control system during the sea trials as the attitude estimator. A model-based Kalman filter was used as the observer for the translational states.

In this simulation and experiment the ECI frame is assumed to be inertial, and the attitude observer is run with the second reference and IMU vectors as given by (4.36) and (4.39), respectively. That is yaw estimation is decoupled from roll and pitch. The attitude and translational observer are run with interconnections as given by (4.38).

### Sensors and Observer Specifications

The DVL and transponder are mounted on the center-line at the stern, and the IMU on the port bow. The DVL is oriented 45 degrees in yaw w.r.t the ROV and the IMU is aligned with the ROV. The sensor positions are given in Table 4.3.

The sensor properties for white noise, bias and update rate, used in the simulation and as found from the experimental data in post-processing, are given in Table 4.4. The

Table 4.2: ROV sensors.

Sensor	Manufacturer	Model	Technology/type
APS (TP)	Kongsberg Maritime	HiPAP 500	SSBL
PG	Valeport	MiniIPS	piezo-resistive
DVL	Teledyne RDI	Workhorse Navigator	Janus
IMU	Xsens	MTi-100	MEMS



Figure 4.9: The ROV Minerva with transponder (yellow cylinder) and DVL (red) mounted at the stern.

Table 4.3: Sensor positions on the ROV.

		x [m]	y [m]	z [m]
TP	$\mathbf{r}_{tp/b}^b$	-0.73	0	-0.86
PG	$\mathbf{r}_{pg/b}^b$	0.68	-0.38	-0.06
DVL	$\mathbf{r}_{dvl/b}^b$	-0.79	0	-0.10
IMU	$\mathbf{r}_{imu/b}^b$	0.68	-0.445	-0.60

properties from the experiments are found from a time series of 3 minutes where the ROV is sitting on the sea floor with constant thrust downwards. The performance of the APS, i.e. the position measurements of the TP, is very similar for simulation and experiment. The PG noise level is slightly higher in the experiments. This can be due to pressure fluctuations caused by the thruster jet or vibrations of the ROV. The actual sampling rate in the experiments is 5 Hz, although the PG sensor was set to output data at 8 Hz.

The noise levels of the DVL are not obtained as the DVL is out of range while sitting on the sea floor. The DVL update rate in the experiment is about 1 Hz, which is lower than specified. This is probably due to serial communication settings.

The noise levels of the IMU are considerably higher in the experiments for the accelerometers and gyroscopes. This is due to vibrations caused by the thrusters which is shaking the ROV and everything mounted on it. The IMU noise levels as measured on the ROV at rest, on shore, with thrusters off, are about the same as given in the IMU product sheet. The effect of the IMU noise is seen in the time series of the IMU measurements in

Table 4.4: Sensor specifications, simulation vs. experiments.

	Simulations			Experiments		
	noise [ $\sigma$ ]	bias	[Hz]	noise [ $\sigma$ ]	bias	[Hz]
$p_{tp/n}^n$	0.1 [m]	0	1	0.09 [m]	n/a	0.97
$p_{pg}$	0.001 [m]	0	8	0.0028 [m]	n/a	5
$v_{d/e}^d$	0.003 [m/s]	0	5	n/a	n/a	1
$a_{imu}^m$	0.0072 [m/s <sup>2</sup> ]	0	100	0.2079 [m/s <sup>2</sup> ]	n/a	100
$\omega_{imu}^m$	0.0014 [rad/s]	$\begin{bmatrix} -0.08 \\ 0.11 \\ 0.05 \end{bmatrix}$ [°/s]	100	0.0061 [rad/s]	$\begin{bmatrix} -0.15 \\ -0.10 \\ 0.00 \end{bmatrix}$	100
$m_{imu}^m$	0.0055 [AU]	0	100	0.0056 [AU]	n/a	100

Table 4.5: Observer gain selection, simulation vs. experiments.

	Simulations	Experiments
ECF	$k_i$ $K_p$ $K_i$ $K_b$ $\Delta$	$[1 \ 1]^T$ diag{0.1, 0.1, 0.1} diag{0.0001, 0.0001, 0.0001} diag{1, 1, 1} 0.03
	$K_{11}$	diag{5, 5, 10}
	$K_{21}$	diag{1, 1, 1}
	$K_{12}$	diag{1, 1, 1}
	$K_{22}$	diag{10, 10, 10}
Int	$K_{13}$	diag{0, 0, 0}
	$K_{23}$	diag{0, 0, 0}

Figure 4.11a and 4.11b.

The observer gains used for the ECF in simulations and experiments are given in the top part of Table 4.5. The integration filter gains are given in the lower part. The original idea was to use the same gains for simulation and experiment in both ECF and integration filter. However, the accuracy of the IMU measurements in the experiments was not good enough to produce decent position estimates with the "simulation gains" from the integration filter. More emphasis on the velocity and position measurements is needed in the experiments. The IMU acceleration measurements in the integration filter do more harm than good. However, it is noted that the attitude estimate from the ECF seems fairly good despite the high noise levels of the IMU.

The accelerometer bias estimation is canceled by setting  $K_{13}$  and  $K_{23}$  to  $0_{3 \times 3}$ . This is done as stable results for the accelerometer bias estimation were not achieved in the experiments. Thus, accelerometer bias estimation based on APS and DVL measurements require further work.

### Simulation and Experimental Results

Figure 4.10a and 4.10b show the trace of the ROV in the North, East plane while executing the star-pattern maneuver during simulation and experiment, respectively. The first way point in the pattern is at 25 m North, 0 m East. Then the ROV heads South to -25 m North, 0 m East before turning around and moving back to the first way point. From there it goes to the start of the next diameter line of the star-pattern, with bearing 30 degrees, and tracks this line back and forth as well. So the pattern continues until all 6 diameter lines are tracked back and forth.

Every measured transponder position,  $p_{tp/n}^n$ , is marked with a black mark with dash dotted lines connecting the marks. The blue trace and boxes show the estimated position, with boxes being snapshots of the outline of the ROV. The true position (ground truth) is given by the red dashed line in Figure 4.10a for the simulation case. Unfortunately, no ground truth is available for the experiments. However, the high accuracy measurements from the HiPAP 500 system combined with the chosen star-pattern gives a good indication of the true position.

When comparing Figure 4.10a and 4.10b, it is clear that the position estimates are more accurate and smoother in simulation than in the field trials. The position estimation seems to be especially poor at the North end of the line with bearing 330 degrees in the field trials. This happens because of a jump in the TP measurements, and since  $K_{11}$  is high, the performance of the estimated position suffers as well. With a more accurate and less noisy IMU, and higher update rate on the DVL,  $K_{11}$  can be reduced and a smoother estimated position will be achieved.

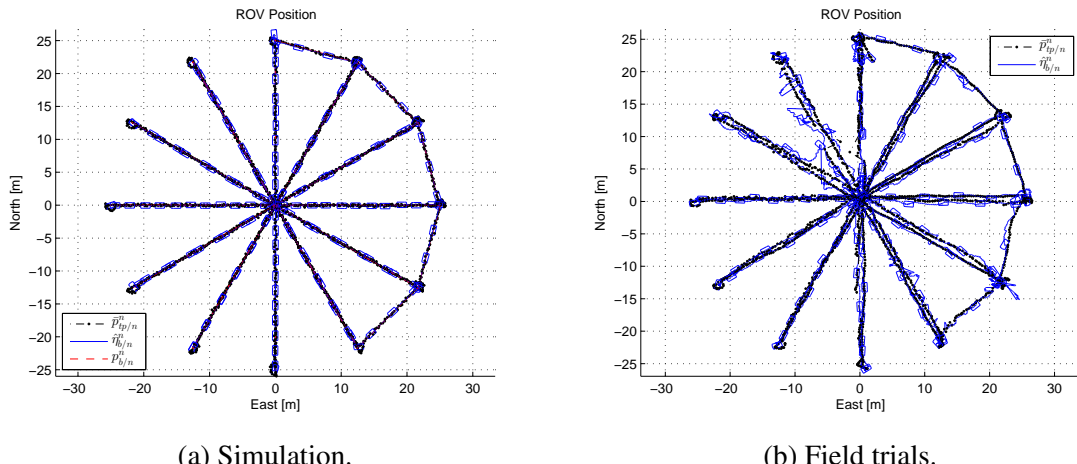


Figure 4.10: ROV measured and estimated positions during simulation and field trials.

The simulated and actual IMU measurements for the line from East to West, back and forth with one turn, are shown in Figure 4.11a and 4.11b. This segment of the star-pattern is noted the demo segment. The effect of the 180 degree clockwise turn at the far West way point is clearly seen in the yaw gyroscope (middle plot) and horizontal magnetometer components (lower plot), both in simulation and field trials. The high noise levels of the

accelerometers and gyroscopes in the field trial are seen in the upper and middle plot of Figure 4.11b.

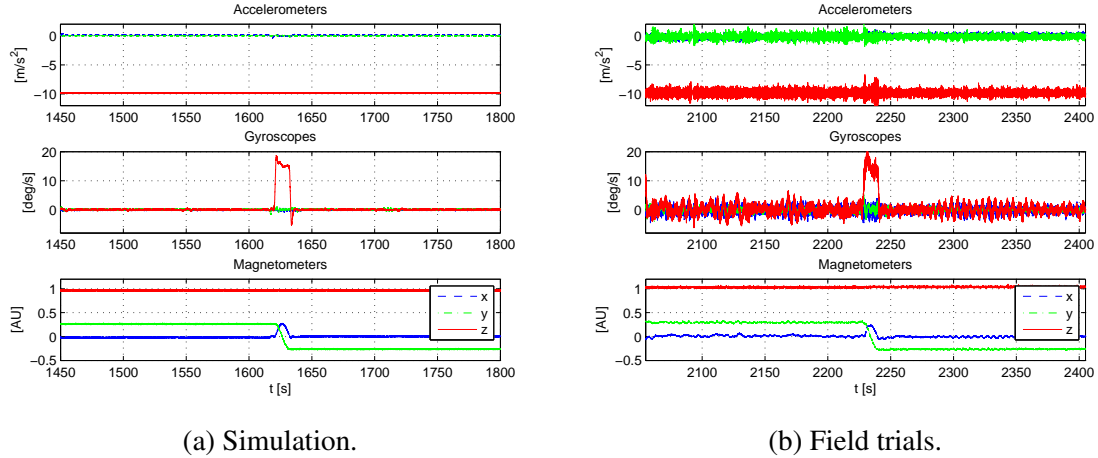


Figure 4.11: IMU measurements in simulation and field trials for the demo segments. Upper plot is accelerometer measurements, middle plot is gyroscope measurements and lower plot is magnetometer measurements. Dashed blue line is the sensor x component, dash-dotted green is the y component and red line is the z component.

The estimated attitude and algebraic measurements of attitude during the demo segments are shown in Figure 4.12a and 4.12b for the simulation and field trials, respectively. The red line is the true attitude in the simulation case. The algebraic measurements for roll and pitch are the angles between the accelerometer  $z$  and  $x, y$  components, and the heading is the magnetic heading. This is used as an approximate reference since a ground truth is unavailable in the field trials. The attitude estimation error for the simulation is seen in the lower plot of Figure 4.15a. The attitude estimation error is small, also during the 180 degree turn due to the proposed modified acceleration in (4.38). The effect of this term is demonstrated in Chapter 4.3.6. Although there is no ground truth to calculate the attitude errors from the field trials, Figure 4.12b shows how the noise is reduced in the ECF estimated attitude, compared to the algebraic measurements, while the phase lag is small. The higher roll and pitch amplitudes in the field trials are most likely real as there can be coupling effects not accounted for in the simulation model (unmodelled dynamics).

Figure 4.13a and 4.13b show the measured and estimated velocities of the IMU for the simulation and field trials, respectively. The measured velocity,  $v_{m/e}^m$ , is the DVL velocity measurements transformed to the IMU position by using the estimated attitude and turn rate as in (4.52). Both the measured and estimated velocity is smooth and accurate in simulation. The DVL is a high precision velocity sensor and the update rate is fairly high compared to the ROV dynamics. The velocity measurements in the field trials are also good although some noise is introduced through the transformation that relies on the estimated attitude and turn rate. However, the variance of the estimated velocity is higher than the measured, and the gain matrix  $K_{22}$  had to be high to even get the estimated

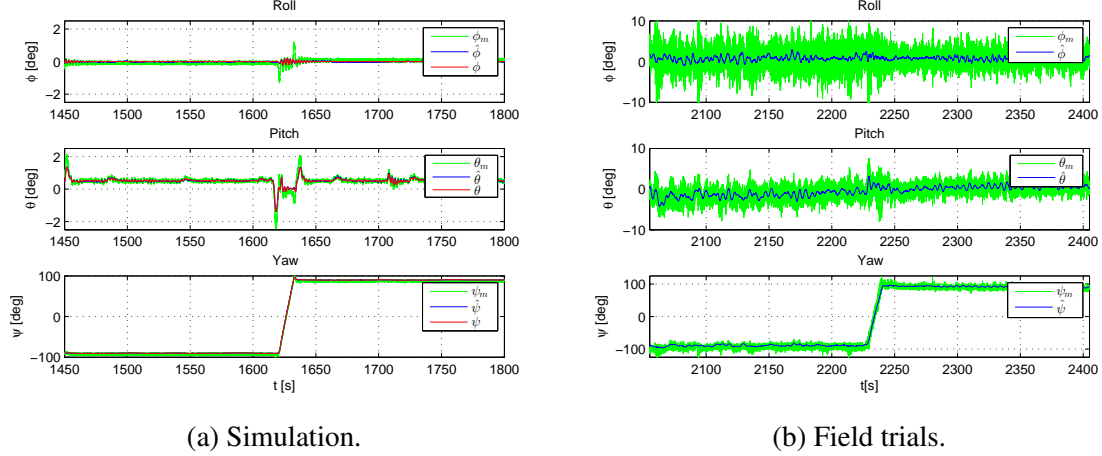


Figure 4.12: ECF estimated attitude and algebraic measured attitude in simulation and field trials for the demo segments.

velocity close to the measured. The reason is that the noisy accelerometers and small attitude estimation errors, that cause faulty gravity compensation, leads to an erroneous approximation of proper acceleration. As the proper acceleration is integrated to obtain estimated velocity, the estimated velocity is also error prone. This rises the question of how much accelerometer noise and attitude error can be tolerated before the accelerometer measurements makes more harm than good in the integration filter. This is discussed in Chapter 4.3.7.

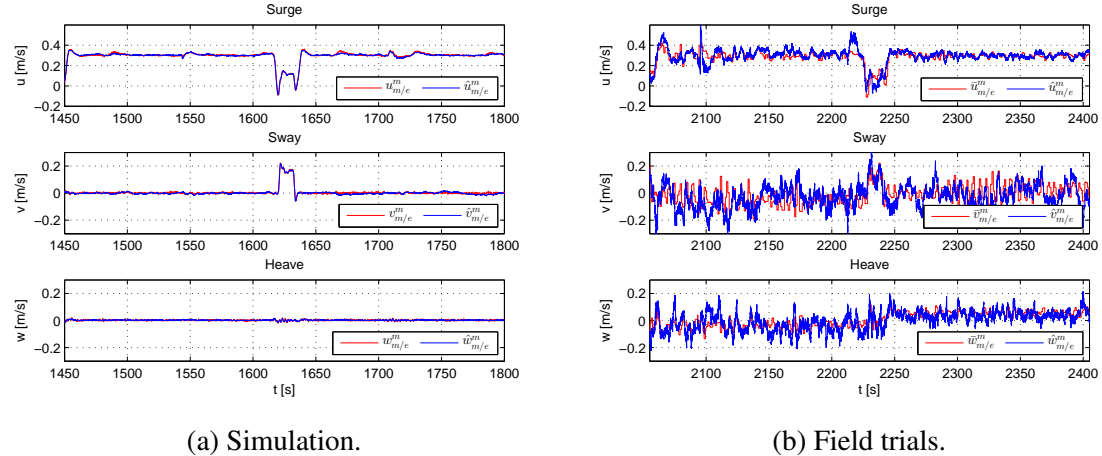


Figure 4.13: IMU velocity in simulation and field trials for the demo segments. Upper plot is surge, middle plot is sway and lower plot is heave. Red line is measured and blue line is estimated velocity.

The gyroscope bias estimation after initialization for simulation and field trials are seen in Figure 4.14a and 4.14b. Note that the initialization is done at the start of the demo segments, but the other Figures with the demo segments are with converged bias

estimation. Erroneous gyro bias estimation can lead to poor estimation performance of all DOFs. It is seen that the estimates converge to the true values within the duration of the demo segment in the simulation case. The convergence time after initialization is reduced by using an exponentially decaying bias gain,  $K_i$ , after start up. The bias estimations in the field trials are oscillating more, but converges eventually. Because the ROV is rolling, pitching and yawing more in the field trials than simulation, it takes longer to estimate the gyro bias. However, the bias estimation should converge while the vehicle is still at rest for practical use.

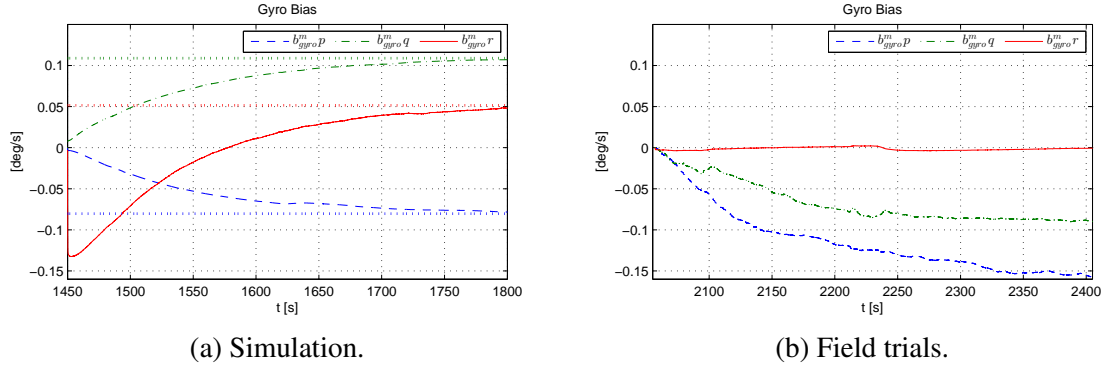


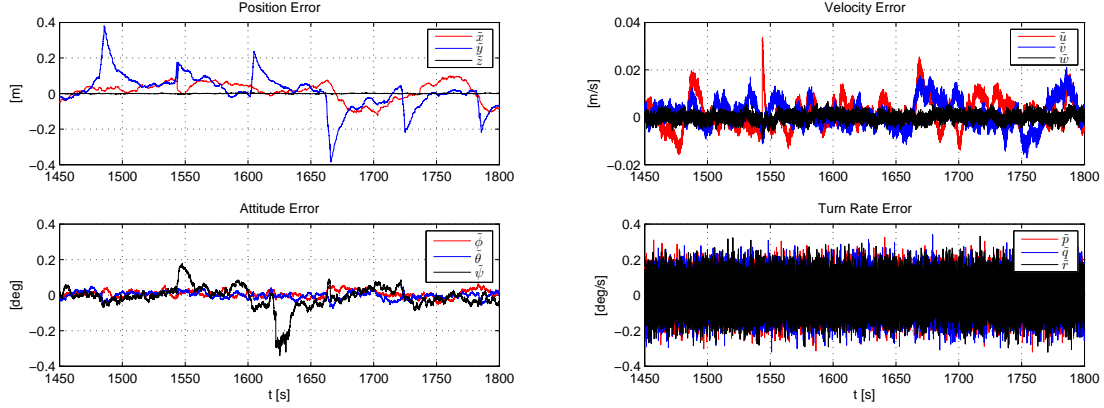
Figure 4.14: Gyroscope bias estimation in simulation and field trials after initialization at start of the demo segments. Blue dashed line is roll bias, green dash-dotted line is pitch bias and red line is yaw bias. The true bias is seen as dotted horizontal lines in the simulation plot.

The position, attitude and velocity errors for the demo segment of the simulation case are seen in Figure 4.15a and 4.15b. Note the spikes of almost 0.4 m in the position error due to the high gain matrix  $K_{11}$ . The roll and pitch errors are small,  $< 0.05$  degrees. The heading error is largest during the turn as expected. However, the heading error would have been greater without the interconnection between the ECF and translational observer obtained through the modified acceleration. This is due to the centripetal acceleration that makes it difficult to separate gravity from the measured acceleration.

The velocity errors are small, but since the ROV is a slow moving vehicle, the relative error is almost 10 % at the most. The challenge with the observer is to get velocity estimates that are smooth without phase lag. The same goes for the turn rate as the estimated turn rate is the measured turn rate corrected for bias. This should be filtered before use in a motion control system.

### Sensitivity Considerations

While the accuracy levels of MEMS accelerometers and gyroscopes are improving, the tested state-of-the-art MEMS IMU is not considered suitable for use in a stand alone INS. An IMU in such a strapdown INS system is seen in Figure 4.2. For this system to output accurate positions for longer time periods, the attitude error must be very small, the gravity model accurate and accelerometer and gyro bias and noise must be very limited.



(a) Position and attitude estimation errors in simulation.  
(b) Velocity and turn rate estimation errors in simulation.

Figure 4.15: Position, attitude and velocity estimation errors during the demo segment in simulation.

The proposed sensor-based observer does not claim to be an INS, but it relies on feedback from position and/or velocity measurements. For the translational observer, the accelerometer measurements are meant to enhance the estimated positions and velocity in between these measurements. However, if the estimated attitude is error prone, the accelerometer measurements noisy and the bias estimation poor, it is questionable if the accelerometer measurements provide useful data to the integration filter.

The proposed observer uses velocity measurements and estimates in the vehicle frame. This is seen in the block diagram in Figure 4.16, which is how the observer looks when stripped down to an INS. Thus, the effect of attitude error is slightly changed compared to the regular strapdown INS in Figure 4.2, as seen by the transformation  $R_m^n$ .

It is clear that the gyroscope and accelerometer bias will cause the INS velocity and position to drift. It is also clear that attitude estimation errors cause trouble, and the sensitivity to this is discussed in the following.

For any implementation where accelerometer measurements in the vehicle frame are used to produce position estimates in a reference frame, the attitude errors affect the results. The estimated attitude is used to calculate the proper acceleration,  $\mathbf{a}_{m/n}^n$  or  $\mathbf{a}_{m/n}^m$ , which is integrated to find the velocity and position. This is seen in Figure 4.2 and 4.16. The acceleration of gravity is roughly  $9.8 \text{ m/s}^2$  and the acceleration of underwater vehicles is small, thus the magnitude of the measured acceleration,  $\mathbf{a}_{imu}^m$  is in the order of  $10 \text{ m/s}^2$ . Assuming attitude estimation error,  $\tilde{\theta}$ , less than a few degrees and small roll and pitch angles,  $\sin \tilde{\theta} \approx \tilde{\theta}$  and  $\cos \tilde{\theta} \approx 1$ . Then the magnitude of the proper acceleration error, due to the attitude estimation error, is approximated as  $\tilde{a} \approx 10 \cdot \tilde{\theta}$ . E.g. an attitude estimation error of 1 degree will cause an error in the proper acceleration of  $0.02 \text{ m/s}^2$ . This yields a velocity error (drift) of  $0.2 \text{ m/s}$  after 10 s without velocity measurements, which is considerable as the typical speed range of ROVs is around  $0\text{-}1 \text{ m/s}$ . Even if velocity measurements are available at 1 Hz or faster, the rapid velocity drift-off caused

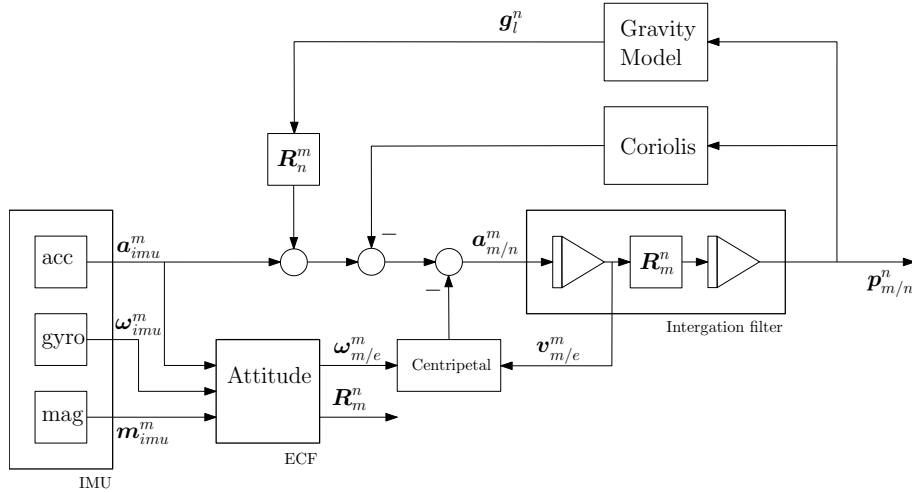


Figure 4.16: Strapdown INS with ECF and velocity in the vehicle frame.

by the accelerometer measurements makes the estimated velocity noisy as it must be corrected heavily by the velocity measurements at every update. Thus, simply neglecting the accelerometer, and integrate the velocity measurements directly to obtain position gives better performance for even small attitude errors (< 1 degree in roll and pitch). This is also true if the observer is used on a much faster vehicle, such as an airplane, but then, on the contrary, the velocity drift-off caused by the errors in the proper acceleration is small compared to the total speed.

If the attitude estimation error can not be guaranteed to be significantly less than 1 degree, it is better to use a model-based observer to estimate the translational states. Especially if the velocity measurements must be filtered. This leads to another question for comparing model-based observers against accelerometer based integration filters. What accuracy of the IMU measurements and performance of the attitude estimation is needed to outperform a model-based observer with given model and disturbances uncertainty. This is a consideration for further work, but it is noted that the performance of a model-based observer can not be directly compared to that of an integration filter. E.g. unknown and varying external forces are difficult to include in the model-based observer, but their effects are easily measured by accelerometers.

Errors in the accelerometer bias estimation (or neglect of) and inaccurate gravity model will also result in errors in the proper acceleration. However, velocity drift-off due to these errors are typically less than drift-off caused by attitude estimation errors. It is not concluded here on the accuracy required on attitude estimation for the accelerometer measurements to enhance the output of an integration filter. It also depends on the accuracy and update rate of the velocity and position measurements. However, as seen from the simulation results, the accelerometer measurements enhanced the estimation of velocity (and position) when the attitude errors were less than 0.05 degrees, and with noise properties as given for the tested IMU. In the experiments, the accelerometer measurements deteriorated the estimated velocity. It is likely that this is part due to small errors in the attitude estimation in addition to accelerometer noise, bias and inaccuracies

in the gravity model.

The violent shaking of the IMU due to the thrusters had negative effects on the test results. It is likely that better results can be obtained with the proposed observer, also in experiments, when mounted on a ROV with less vibrations. Thus, it is not concluded that the proposed observer will not be suitable for use in closed-loop control, but it is sensitive to noise, bias and attitude estimation. A hybrid solution, i.e. a mix between a model-based observer and accelerometer-based integration filter could also be considered. It should be noted that the ECF worked very well as a stand alone attitude estimator despite the vibrations from the thrusters. The main problem is concerned with attitude estimation and its effect on the gravity compensation in the integration filter.

Note that magnetometer data should not enter the estimation of roll and pitch (de-coupling of roll and pitch from yaw in ECF) when the estimated attitude is used in an integration filter with acceleration measurements as input. Small magnetic disturbances will then easily cause roll and pitch errors  $> 1$  degree, and the estimated velocity will drift-off quickly.

## 4.4 Conclusions and Future Work on Underwater Navigation

The work on underwater navigation in this thesis has focused on methods that are aided by, and depend on, external position measurements from an acoustic positioning system and velocity measurements from a DVL. The short term state estimation is based on either a dynamical model of the vehicle or inexpensive low grade inertial sensors.

Classical estimation and filtering techniques, such as the Kalman filter, have been adopted for use with sensors available for underwater vehicles, and tuned for ROV dynamics. In addition, new sensor-based estimation methods for attitude estimation and integration filters have been explored and tested. New variations and methods for ROVs have been proposed.

The model-based Kalman filter is still the observer of choice based on experience with practical implementations. It is very robust and performs well under most conditions. However, new sensor-based nonlinear observers look very promising, but need more development to provide robust estimation in real applications. An advantage is that the IMU based observers deal well with cases with unknown and rapid changing external forces. IMU based observers are also more generic and easy to implement on new vehicles as there is no need to perform thorough dynamical modeling, analysis and system identification for all new vehicles or modifications.

A hybrid solution between model and IMU based estimation methods may provide more robust and greater performance for more modes of operation. Also, including other solutions such as terrain navigation and cable monitoring should be investigated further.



# Chapter 5

## Guidance of ROVs

An example definition of guidance is given as "the process for guiding the path of an object towards a given point, which in general may be moving" [80]. Guidance is general and needed for all vehicles that are moving. There is a lot of information in the literature and especially in the missile community. Some of these theories are applicable to underwater vehicles as well. In terms of guidance, it is not important if the vehicle is in the air or beneath the surface. The most important is the actuation of the vehicle and the dimension of its work space. The ROVs covered in this thesis are fully actuated in their 4 DOF workspace; surge, sway, heave and yaw. Roll and pitch motion can occur, but the ROVs here are stable in these DOFs. Work on guidance systems for marine craft are found in [8], [9] and [40].

The guidance system presented here is made up by three main levels; reference models, way-point management and supervisor. The reference models are the algorithms that produce the desired states, the way-point management system gives input to the reference models, and a supervisor monitors the operation and take action if needed. E.g. if the desired position is too far off the actual position, the supervisor will make the reference model wait for the vehicle to catch up. The supervisor also selects the appropriate controller. Some modes requires position control and other velocity control.

Typical modes of operation for the ROV and the needed guidance strategies are discussed in this chapter. Three main contributions are presented;

- A constant jerk reference model.
- A modification to line-of-sight (LOS) guidance for fully actuated vehicles.
- Methods for joystick in closed-loop control with experimental results.

### 5.1 Constant Jerk Reference Models

A reference model is a function that creates a desired trajectory based on the reference position or velocity. The desired trajectory should start at the current position when the function is activated. The reference model should be simple and must produce a trajectory that is feasible for the vehicle and controller to track.

Objectives like minimizing energy consumption, thruster wear and tear or time to target may be of interest when designing reference models. However, a ROV operator only want to enter a new position coordinate and press go. If the ROV gets up to a decent cruising speed quickly and reaches the target, the operator is satisfied. More advanced inputs should be intuitive to the user, like changing the cruise speed or maximum acceleration instead of filter time constants.

Reference models based on low-pass filters and mass-damper-spring systems, with similar dynamics to the vehicle, are common simple implementations. However, the parameters must be set according to the distance between A and B and the maximum velocity is high with a correspondingly long deceleration period. A new method called the constant jerk reference model is proposed. The main concept is seen in Figure 5.1, which shows the desired velocity and position obtained by integration of a constant jerk that is on or off. The input to the reference model is the desired distance, cruise speed, maximum acceleration and constant jerk.

The work with constant jerk reference models is inspired from [38] where a reference model based on exponential functions are proposed. This is also an alternative to filter-based reference models.

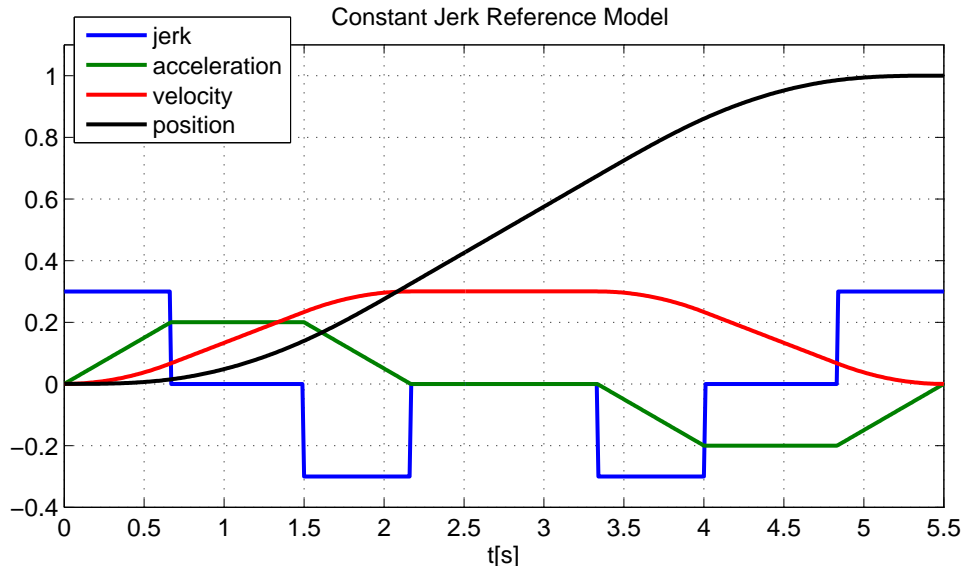


Figure 5.1: Constant jerk reference model states.

### 5.1.1 Constant Jerk Equations

The equations that produce the desired states in the constant jerk reference model are given in (5.1), (5.2), (5.3), and (5.4). Note that the analytical solution is given as this is used in the implementation directly. That is a benefit of keeping things simple.

$$j(t) = j_c \delta(t), \quad (5.1)$$

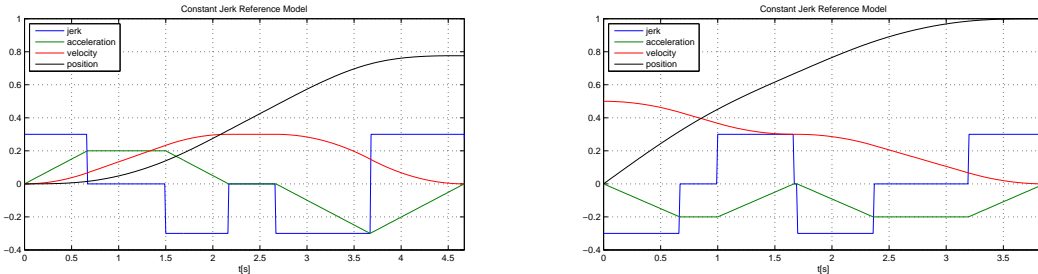
$$a(t) = \int_{t_0}^t j(\tau) d\tau + a_0 = jt + a_0, \quad (5.2)$$

$$v(t) = \int_{t_0}^t a(\tau) d\tau + v_0 = \frac{1}{2}jt^2 + a_0 t + v_0, \quad (5.3)$$

$$p(t) = \int_{t_0}^t v(\tau) d\tau + p_0 = \frac{1}{6}jt^3 + \frac{1}{2}a_0 t^2 + v_0 t + p_0, \quad (5.4)$$

where  $\delta(t) \in [-1, 0, 1]$  is the only parameter that forms the desired states when the constant jerk  $j_c$ , the maximum acceleration and cruise speed are given. It is recommended to use different values for the constant jerk depending of the direction of motion for vehicles with different dynamic characteristics and thrust forward and backwards.  $a_0, v_0$  and  $p_0$  are the initial acceleration, velocity and position, respectively. A move from A to B, as seen in Figure 5.1, consists of 3 main stages; the acceleration stage, the cruise stage and the deceleration stage. The acceleration stage is again made up of 3 segments; the positive jerk stage, the zero jerk stage and the negative jerk stage. The velocity is constant in the cruise stage. The deceleration stage can have 3 parts that are symmetrical to the acceleration stage. However, in a break maneuver, the zero jerk stage is avoided as seen in Figure 5.2a, to reduce the break distance. The corresponding acceleration must still be within the vehicle capabilities. The A to B maneuver with reference distance 1 m is aborted in the constant velocity stage and the final distance is less than 0.8 m.

The reference model must also deal with initial velocities and accelerations in case a new command is given while the previous is being executed. Figure 5.2b shows a case where the initial velocity is 0.5 m/s when the ROV is commanded to go 1 m further with cruise speed 0.3 m/s.



(a) Constant jerk reference model aborted during execution. (b) Constant jerk reference model from initial velocity.

Figure 5.2: Constant jerk reference models for brake maneuver and initial velocity.

For a A to B move the input to the reference model is a desired distance, cruise speed, maximum acceleration and the constant jerk magnitude. The function  $\delta(t)$  in (5.1) must

be specified in order to reach the cruise speed and to stop at the desired distance. For the case in Figure 5.1,

$$\delta(t) = \begin{cases} 1 & \text{if } t_0 < t < t_1, \\ 0 & \text{if } t_1 \leq t < t_2, \\ -1 & \text{if } t_2 \leq t < t_3, \\ 0 & \text{if } t_3 \leq t < t_4, \\ -1 & \text{if } t_4 \leq t < t_5, \\ 0 & \text{if } t_5 \leq t < t_6, \\ 1 & \text{if } t_6 \leq t, \end{cases} \quad (5.5)$$

where the duration of each stage, and hence switching times  $t_i$ , are calculated from analytical expressions obtained by solving for  $t$  in (5.2), (5.3) and (5.4) for the maximum acceleration, cruise speed and partial distances, respectively.

### 5.1.2 Constant Jerk vs. Filter-based Reference Models

Another alternative, in the class of simple and easy to implement reference models, is the filter-based model. Low-pass filtering of reference signals can be used to generate a desired trajectory. It is convenient to use reference models motivated by the dynamics of the vehicle, such as a mass-damper-spring system [40]. A transfer function representing the filter-based reference model from reference signal to desired state is given as

$$\frac{d_d}{d_{ref}}(s) = \frac{\omega_n^2}{s^2 + 2\zeta\omega_n s + \omega_n^2}, \quad (5.6)$$

where  $d$  is the distance,  $\omega_n$  is the natural frequency of the mass-damper-spring system, and  $\zeta$  is the relative damping. Note that the maximum velocity in response to a step input can be very high, and  $\omega_n$  must be tuned depending on the magnitude of the reference step in order to give satisfactory performance. A method to enhance the performance of filter-based reference model is to saturate the velocity.

A comparison of the response to a unit step input for the constant jerk and the filter-based reference model is seen in Figure 5.3. The filter parameters are set so the final position is reached in approximately the same time and for velocities within the vehicle capabilities. The constant jerk model is set with constant jerk magnitude of  $j_c = 0.3$  m/s<sup>3</sup>, maximum acceleration of  $a_m = 0.2$  m/s<sup>2</sup>, and cruise speed of  $v_m = 0.3$  m/s. The filter-based reference model from (5.6) is set with critical damping,  $\zeta = 1$  and  $\omega_n = 1.5$  in the original case and with  $\omega_n = 2$  in the case with velocity saturation of 0.3 m/s.

The top plot in Figure 5.3 shows the desired speeds in response to a step input in the position of 1 m. Note that the maximum velocity in the filter-based case is much higher than for constant jerk. Hence more energy is consumed due to the quadratic damping of the ROV. Although not shown in the plot, the maximum acceleration in the original filter-based case is 2.2 m/s<sup>2</sup>. This might be feasible, but it causes unnecessary wear and tear on the thrusters. The maximum jerk is 220 m/s<sup>3</sup> in the original filter case, about 1000 times greater than set in the constant jerk model. Adding velocity saturation to the

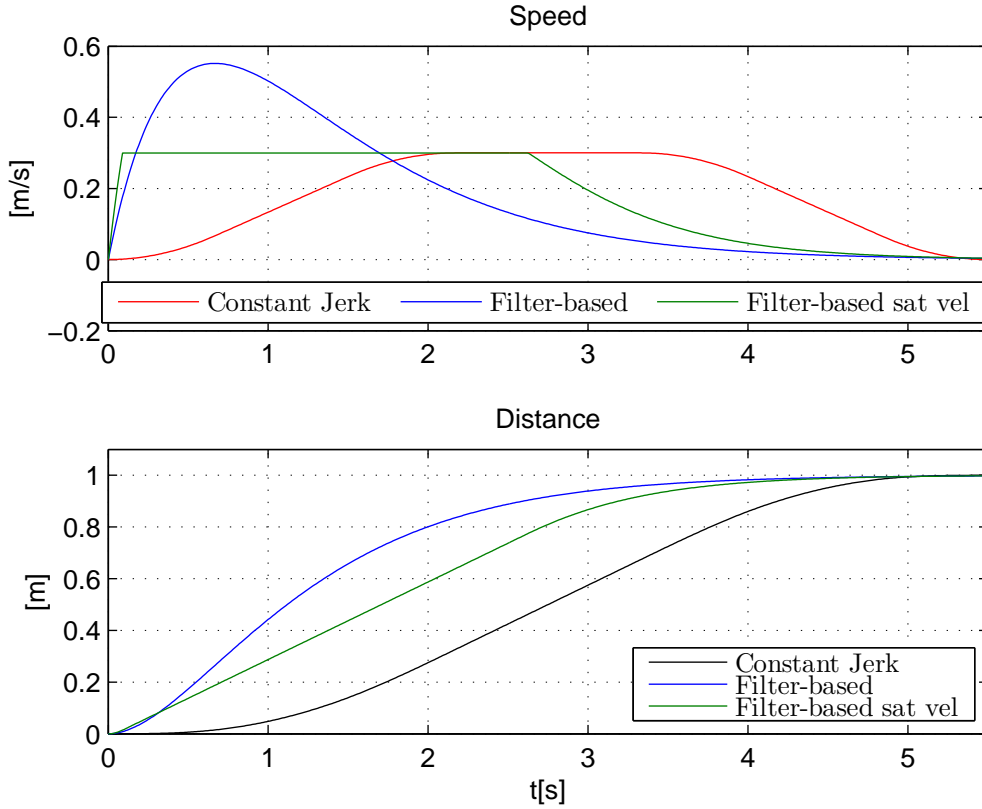


Figure 5.3: Response to step input: constant jerk vs. filter-based reference model with and without velocity saturation.

filter-based model improves the performance as the natural frequency can be increased to achieve a shorter deceleration stage without braking any speed limits of the vehicle. However, a basic saturation function causes the acceleration to be infinity when the saturation speed is reached. This is not feasible, and the kink in the desired speed profile can cause deteriorated performance when input to a closed-loop controller.

The bottom plot in Figure 5.3 shows the desired distances. The trajectory from the constant jerk reference model is the most sensible when the objective is to move from A to B. It has a steady pace that makes intuitive sense to the operator who is waiting for the ROV to reach the destination. The original filter-based model cover 90 % of the reference distance in the first half of the move duration. The last 10 % of the travel seems to take forever to an operator who thought the ROV was almost there. This is improved in the filter based model with velocity saturation, but the performance is still far behind the constant jerk reference model, which has the best performance.

### 5.1.3 Implementation and Considerations

The constant jerk reference model outputs a scalar desired state. Two scalar reference models are run in the implementation on a ROV with 4 or 6 DOF workspace. One for

the position vector  $\mathbf{p} \in \mathbb{R}^{3 \times 1}$  and one for the attitude vector  $\Theta$ . The process from the reference position vector to the desired position vector is seen in Figure 5.4. The first stage is to calculate the distance and bearing to the reference position. Second, the desired distance is calculated by the constant jerk scalar reference model. Last, the desired position vector is found from the bearing and desired distance. The content of the left and right boxes in Figure 5.4 are given in the following. For a ROV with 4 DOF workspace, the desired heading is produced using the scalar constant jerk reference model directly.

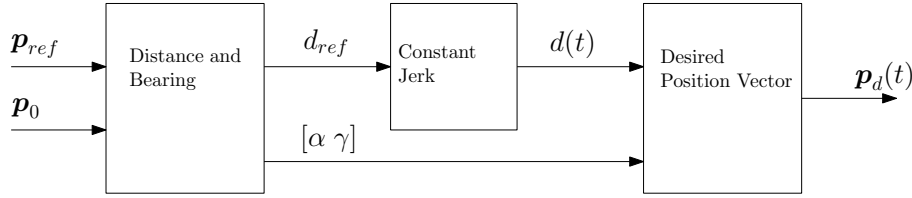


Figure 5.4: Implementation of constant jerk reference model for a position vector.

## Transformation

The transformation for A to B maneuvers along a straight line is given here. Other maneuvers, such as going in circles, can be obtained with other transformations of the output from the scalar constant jerk reference model. The distance between the current position and reference position is calculated as

$$d_{ref} = \sqrt{(x_{ref} - x_0)^2 + (y_{ref} - y_0)^2 + (z_{ref} - z_0)^2}, \quad (5.7)$$

and the horizontal and vertical bearing angles  $\alpha$  and  $\gamma$ , respectively are calculated as

$$\alpha = \text{atan2}(y_{ref} - y_0, x_{ref} - x_0), \quad (5.8)$$

$$\gamma = \arctan\left(\frac{-(z_{ref} - z_0)}{\sqrt{(x_{ref} - x_0)^2 + (y_{ref} - y_0)^2}}\right), \quad (5.9)$$

where  $\text{atan2}$  is the 4-quadrant version of  $\arctan$ .

The desired position vector is calculated from the desired distance and bearing as

$$\mathbf{p}_d(t) = \mathbf{R}_p \begin{bmatrix} 1 \\ 0 \\ 0 \end{bmatrix} d(t), \quad (5.10)$$

where  $\mathbf{R}_p$  is the rotation matrix from the path fixed frame to NED.  $\mathbf{R}_p$  is calculated from the bearing as

$$\mathbf{R}_p = \mathbf{R}_{p,z}(\alpha) \mathbf{R}_{p,y}(\gamma),$$

where

$$\mathbf{R}_{p,z}(\alpha) = \begin{bmatrix} \cos \alpha & -\sin \alpha & 0 \\ \sin \alpha & \cos \alpha & 0 \\ 0 & 0 & 1 \end{bmatrix}, \quad \mathbf{R}_{p,y}(\gamma) = \begin{bmatrix} \cos \gamma & 0 & \sin \gamma \\ 0 & 1 & 0 \\ -\sin \gamma & 0 & \cos \gamma \end{bmatrix}.$$

### Parameter Check

There are 4 parameters in the constant jerk reference model;  $j_c$ ,  $a_m$ ,  $v_m$ , and  $d_m$  which are the magnitudes of the constant jerk, maximum acceleration, cruise speed and travel distance, respectively. Not all combinations are valid. E.g. it is not possible to move 1 m with cruise speed of 5 m/s with maximum acceleration of only 0.2 m/s<sup>2</sup>. The reference distance is traveled before the cruise speed is reached.

This means the parameters must be checked and adjusted before the reference model is executed. This is done in an algorithm that runs whenever a new command is given. The cruise speed, in the example above, would have been reduced for short moves automatically.

### Discrete-time Implementations

The constant jerk reference model is implemented by analytical functions. That is there are no numerical integrations that can cause drift of the desired position. However, the implementation runs on a computer with finite time steps. The jerk switching times, and end time, may be in between time steps for given  $j_c$ ,  $a_m$ ,  $v_m$ , and  $d_m$ . A trick is done here where the solutions are also calculated for switching and end times that are in between time steps. This hybrid solution assures continuity and correctness of the desired state.

## 5.2 LOS for Fully Actuated ROV

A method to track lines between way-points is very useful in the overall guidance system for the ROV. The operator can plan the mission by setting way-points, desired speed and heading or control the latter two manually as the ROV goes from way-point to way-point automatically. As opposed to line-of-sight (LOS) for underactuated vessels, which is a steering law, the method for a fully actuated ROV outputs a desired velocity vector. Work on LOS with desired velocity vector can be found in [8]. The magnitude of the velocity vector (speed) can be controlled manually or by a reference model. The heading can be treated separately or it can be linked to the LOS algorithm in different ways as shown in this Chapter. A regular LOS algorithm for underactuated vessels is found in [40]. Work on optimal cross track control for underactuated underwater vehicles is found in [7] and [6]. The LOS algorithm is modified for underactuated underwater vehicles in [14] to compensate for ocean currents.

The main motivation for using a LOS scheme for ROVs is that the desired velocity vector can be tracked by a speed controller. This gives much smoother motions than when a position feedback controller is used to track a parameterized path.

The LOS scheme is given in a 2-D and 3-D version. The 3-D is more general as it includes depth. However, the 2-D version is useful when a separate altitude control is used or the depth needs to be manually controlled. This LOS scheme also provides a method for switching between way-points. The contributions are

- the modification of the classical LOS steering law to be applied on the velocity vector instead of heading.
- modes of complementary attitude and depth control for use with the proposed LOS guidance law.

### 5.2.1 2-D LOS

The guidance scheme for the fully actuated ROV is divided into the horizontal translational motions, depth and yaw. The LOS algorithm is used to produce a reference trajectory in the horizontal plane. The proposed LOS for fully actuated vehicles outputs a desired direction of the velocity vector. The vector magnitude, or speed, is treated separately.

#### The 2-D LOS algorithm

An ROV navigating between way-points  $p_k$  and  $p_{k+1}$  with the LOS algorithm is seen in Figure 5.5.

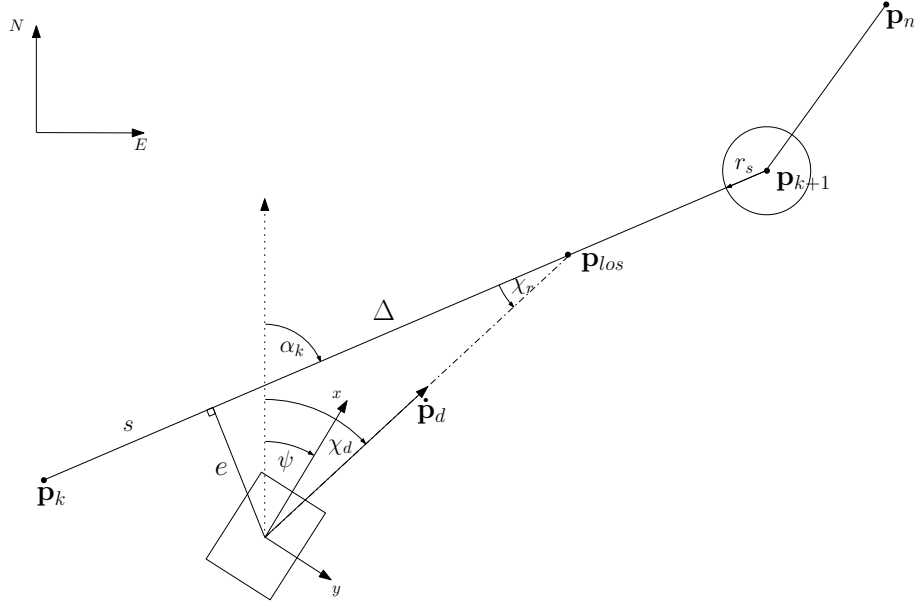


Figure 5.5: 2-D LOS parameters.

The bearing between two way-points  $p_k$  and  $p_{k+1}$  is given by  $\alpha_k$  as

$$\alpha_k = \text{atan2}(y_{k+1} - y_k, x_{k+1} - x_k), \quad (5.11)$$

where atan2 is the 4 quadrant version of arctan. The horizontal ROV position in the NED frame is  $\mathbf{p} = [x \ y]^T$ . The position in the path fixed frame between way-point  $\mathbf{p}_k$  and  $\mathbf{p}_{k+1}$  is given by (5.12) as

$$\boldsymbol{\varepsilon}(t) = \begin{bmatrix} s(t) \\ e(t) \end{bmatrix} = \mathbf{R}_{p,z}(\alpha_k)^T(\mathbf{p}(t) - \mathbf{p}_k), \quad (5.12)$$

where

$$\mathbf{R}_{p,z}(\alpha_k) = \begin{bmatrix} \cos \alpha_k & -\sin \alpha_k \\ \sin \alpha_k & \cos \alpha_k \end{bmatrix}, \quad (5.13)$$

$s$  is the along track distance, and  $e$  is the cross track error.  $\mathbf{R}_{p,z}(\alpha_k)$  is the rotation matrix from the path fixed frame to NED.  $s$  and  $e$  can be written out as

$$\begin{aligned} s(t) &= [x(t) - x_k] \cos(\alpha_k) + [y(t) - y_k] \sin(\alpha_k), \\ e(t) &= -[x(t) - x_k] \sin(\alpha_k) + [y(t) - y_k] \cos(\alpha_k). \end{aligned}$$

The look-ahead distance,  $\Delta$ , as seen in Figure (5.5), is set to a constant value or calculated as

$$\Delta(t) = \sqrt{R^2 - e(t)^2}, \quad (5.14)$$

where  $R$  is a constant radius. LOS with constant  $\Delta$  is called look-ahead-based steering and  $\Delta(t)$  for fixed  $R$  is called enclosure based steering. Decreasing the look-ahead distance, directly or via  $R$ , give a more aggressive response, but may also cause instability.

The angle  $\chi_r$  is given by (5.15) and is used to calculate the bearing,  $\chi_d$ , of the desired velocity vector as in (5.16).

$$\chi_r = \arctan\left(-\frac{e(t)}{\Delta(t)}\right), \quad (5.15)$$

$$\chi_d = \alpha_k + \chi_r. \quad (5.16)$$

$\dot{\mathbf{p}}_d$  is the desired translational velocity vector in the NED frame. This is given by the desired speed  $U_d$  and is expressed as

$$\dot{\mathbf{p}}_d = \mathbf{R}_{d,z}(\chi_d) \begin{bmatrix} 1 \\ 0 \end{bmatrix} U_d, \quad (5.17)$$

where  $\mathbf{R}_{d,z}(\chi_d)$  is the rotation matrix from the desired velocity fixed frame to the NED frame.

To get constant velocity parallel to the line between two way-points,  $U_d$  can be calculated as

$$U_d = U_{il} \frac{1}{\cos(|\chi_r|)}, \quad (5.18)$$

where  $U_{il}$  is the along track velocity. Note that this can result in an oscillating vehicle speed if the cross track error varies a lot.

The output of the LOS algorithm is the desired surge and sway velocities of the ROV;  $u_d$  and  $v_d$ . These are found by combining (5.17) and (5.19) to get the desired velocity in (5.20).

$$\dot{\mathbf{p}}_d = \mathbf{R}_b^n(\Theta_{nb}) \mathbf{v}_d, \quad (5.19)$$

$$\mathbf{v}_d = \mathbf{R}_b^n(\Theta_{nb})^T \dot{\mathbf{p}}_d = \mathbf{R}_b^n(\Theta_{nb})^T \mathbf{R}_{d,z}(\chi_d) \begin{bmatrix} 1 \\ 0 \end{bmatrix} U_d, \quad (5.20)$$

where  $\Theta_{nb} = [\phi \ \theta \ \psi]^T$  is the ROV attitude vector,  $\mathbf{R}_b^n$  is the rotation matrix from body to NED reference frame and  $\mathbf{v}_d = [u_d \ v_d]^T$  is the desired velocity vector in the body frame.

### Speed control

The desired velocity  $U_d$  can be controlled manually by an operator as the ROV moves between way-points or it can be assigned as a function of covered along track distance,  $U_d(s)$ . In the latter case,  $U_d(s)$  will be produced by a reference model based on desired cruise speed and transient behavior, which should reflect the ROV capabilities. The proposed constant jerk reference model can be used to generate a desired speed trajectory for LOS guidance.

### Way-point switching

A law for switching between way-points is proposed. The switching will occur when the covered along track distance is a length  $r_s$  from the way-point  $\mathbf{p}_{k+1}$ . The length of the line between way-point  $\mathbf{p}_k$  and  $\mathbf{p}_{k+1}$  is

$$l_k = \sqrt{(x_{k+1} - x_k)^2 + (y_{k+1} - y_k)^2}. \quad (5.21)$$

If  $s > (l_k - r_s)$  then  $k = k + 1$ .  $r_s$  is the radius of acceptance before switch to the next way-point, see Figure 5.5.

### Rotational DOFs

A benefit with the proposed LOS for fully actuated vehicles is that the heading can be controlled independently of the path tracking. This enables many modes of operations that are useful for survey missions. Some possible modes are given next.

**Parallel to line** The reference heading is the same as the bearing between way-points  $\mathbf{p}_k$  and  $\mathbf{p}_{k+1}$ ,  $\psi_{ref} = \alpha_k$ .  $\psi_{ref}$  is fed into a reference model, e.g. constant jerk, to give a continuous desired heading  $\psi_d$  after switching to the next way-point.

**Free heading** In this mode the heading can be controlled by the operator via an input to a reference model. The heading is completely separate from the LOS algorithm in this case. The user interface can be a knob or the reference heading can be assigned with a keyboard.

**Towards next way-point** By setting the desired heading to  $\psi_d = \chi_d$ , the LOS scheme is reduced to the steering law of the regular LOS for underactuated vehicles. This can be useful if the side thruster breaks down or if the cross flow for high surge velocity is so strong that the side thrust is severely reduced. To compensate for ocean currents in this case, the desired heading may be modified by including an integrator in  $\chi_r$ , proposed by [13] as

$$\chi_r = \arctan\left(-\frac{e(t) + \sigma_e e_{int}}{\Delta(t)}\right), \quad (5.22)$$

$$\dot{e}_{int} = \frac{\Delta e}{(e + \sigma_e e_{int})^2 + \Delta^2}. \quad (5.23)$$

where the integral gain  $\sigma_e > 0$  is a design parameter for the integrator  $e_{int}$ .

**Towards current** If the ocean current is considerable, it may not be possible to hold an arbitrary heading while tracking a line between way-points. This will be a problem if the current is greater than the maximum ROV directional velocity capability. The desired heading must be changed so that it is possible to track the line in presence of current, but not more if the heading is also of interest. E.g. during a search along a lawnmower pattern, it is desirable to look in the direction of the line between way-points. However, with strong side current it is necessary to head towards the current if the surge velocity capability is the strongest. Perhaps a small change in heading will be sufficient to maintain tracking of the line while still being able to look ahead.

### Depth

In the 2-D LOS scheme, the depth is controlled independently. This gives flexibility in the operation. A position controller is used to regulate depth, as opposed to velocity control in LOS for the horizontal motion. Some possible modes of depth control that are complementary to horizontal LOS are given next.

**Separate depth guidance** The way-points in the guidance block can also include a z coordinate,  $\mathbf{p}_k = [x_k \ y_k \ z_k]^T$ . The vertical motion is guided with a separate reference model which runs without further inputs from the operator.

**Adjustable depth** In this mode, the operator can control the depth as the ROV moves automatically in the horizontal plane. The operator sets a reference depth which is input to a reference model that generates a desired depth. This mode is useful during a search where an area is efficiently covered in a systematic way with the automatic x, y control. The operator can adjust the depth in order to get a close view of interesting features or a good overview.

**Altitude control** Altitude control is achieved by generating a desired depth. Automatic x, y control combined with altitude control is a nice feature for search and inspections. The reference altitude can be set in the mission plan or changed by the operator during tracking.

### 5.2.2 3-D LOS

Although, as seen for 2-D LOS, there are good reasons to keep the vertical motion separate from the horizontal guidance scheme. One of the reasons that this works well, is that the sea floor is often a flat surface with some irregularities. When close to vertical walls or overhangs, things are different. It is no longer possible to avoid impact by only controlling the depth. The mission must be planned in 3-D where all directions are equally important. For this, a 3-D LOS method is proposed.

The LOS algorithm for 3-D is mostly an extension of the 2-D version. The details of the extension are given in the following.

#### The 3-D LOS algorithm

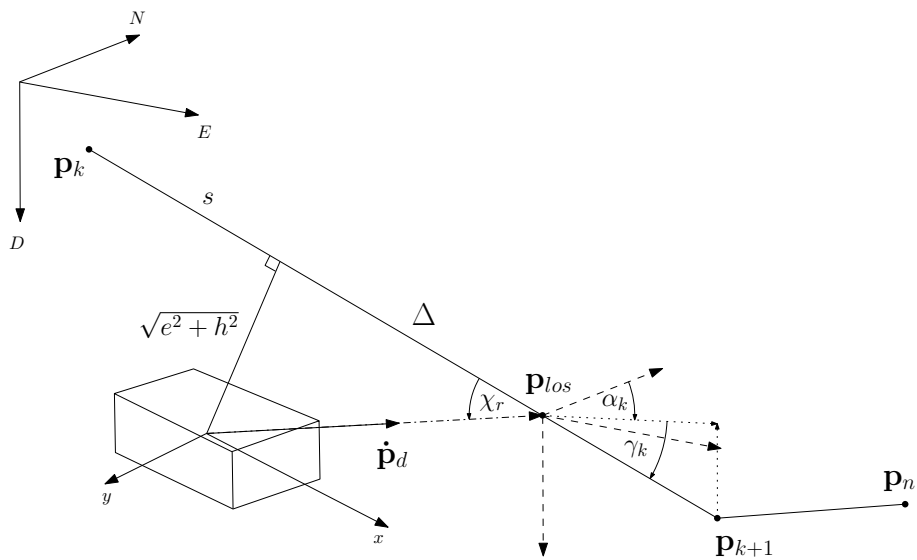


Figure 5.6: 3-D LOS parameters.

The horizontal bearing between two way-points  $p_k$  and  $p_{k+1}$  is given by  $\alpha_k$ . The angle

from the horizontal plane to the line between two way-points is  $\gamma_k$  as seen in Figure 5.6.  $\alpha_k$  and  $\gamma_k$  are calculated from the elements in way-points  $\mathbf{p}_k$  and  $\mathbf{p}_{k+1}$  as

$$\alpha_k = \text{atan}2(y_{k+1} - y_k, x_{k+1} - x_k), \quad (5.24)$$

$$\gamma_k = \arctan\left(\frac{-(z_{k+1} - z_k)}{\sqrt{(x_{k+1} - x_k)^2 + (y_{k+1} - y_k)^2}}\right). \quad (5.25)$$

The ROV position in the NED frame is  $\mathbf{p} = [x \ y \ z]^T$ . The position in the path fixed frame between way-points  $\mathbf{p}_k$  and  $\mathbf{p}_{k+1}$  is given as

$$\boldsymbol{\varepsilon}(t) = \begin{bmatrix} s(t) \\ e(t) \\ h(t) \end{bmatrix} = \mathbf{R}_p^T(\mathbf{p}(t) - \mathbf{p}_k), \quad (5.26)$$

where  $s$  is the along track distance,  $e$  is the cross track error in the path fixed x, y plane and  $h$  is the cross track error in the path fixed x, z plane.  $\mathbf{R}_p$  is the rotation matrix from the path fixed frame to NED and is calculated as

$$\mathbf{R}_p = \mathbf{R}_{p,z}(\alpha_k) \mathbf{R}_{p,y}(\gamma_k), \quad (5.27)$$

where

$$\mathbf{R}_{p,z}(\alpha_k) = \begin{bmatrix} \cos \alpha_k & -\sin \alpha_k & 0 \\ \sin \alpha_k & \cos \alpha_k & 0 \\ 0 & 0 & 1 \end{bmatrix}, \quad (5.28)$$

$$\mathbf{R}_{p,y}(\gamma_k) = \begin{bmatrix} \cos \gamma_k & 0 & \sin \gamma_k \\ 0 & 1 & 0 \\ -\sin \gamma_k & 0 & \cos \gamma_k \end{bmatrix}. \quad (5.29)$$

The look-ahead distance,  $\Delta$ , is set to a constant value or calculated as

$$\Delta(t) = \sqrt{R^2 - e(t)^2 - h(t)^2}, \quad (5.30)$$

where  $R$  is a constant radius. LOS with constant  $\Delta$  is called look-ahead-based steering and  $\Delta(t)$  for fixed  $R$  is called enclosure-based steering. Decreasing the look-ahead distance, directly or via  $R$ , give a more aggressive response.

The direction of the desired velocity vector in the NED frame is given by the angles  $\chi_d$  and  $\Gamma_d$  in (5.31) and (5.32), respectively. These angles are the rotations about the z and y-axis, respectively.

$$\chi_d = \alpha_k + \arctan\left(-\frac{e(t)}{\Delta(t)}\right), \quad (5.31)$$

$$\Gamma_d = \gamma_k + \arctan\left(\frac{h(t)}{\Delta(t)}\right), \quad (5.32)$$

$$\chi_r = \arctan\left(\frac{\sqrt{e(t)^2 + h(t)^2}}{\Delta(t)}\right), \quad (5.33)$$

where  $\chi_r$  is the angle between the desired velocity vector and the line between two way-points, see Figure 5.6.

$\dot{\mathbf{p}}_d$  is the desired translational velocity vector in the NED frame. This is given by the desired speed  $U_d$  and desired velocity direction as

$$\dot{\mathbf{p}}_d = \mathbf{R}_{d,z}(\chi_d) \mathbf{R}_{d,y}(\Gamma_d) \begin{bmatrix} 1 \\ 0 \\ 0 \end{bmatrix} U_d, \quad (5.34)$$

where  $\mathbf{R}_{d,z}(\chi_d)$  and  $\mathbf{R}_{d,y}(\Gamma_d)$  multiplied is the rotation matrix from the desired velocity fixed frame to the NED frame.

To get constant velocity parallel to the line between way-points,  $U_d$  can be calculated as

$$U_d = U_{il} \frac{1}{\cos(\chi_r)}, \quad (5.35)$$

where  $U_{il}$  is the along track velocity.

The output of the LOS algorithm is the desired surge, sway and heave velocities of the ROV;  $u_d$ ,  $v_d$  and  $w_d$ . These are found by combining (5.34) and (5.36) to get the desired velocity in (5.37).

$$\dot{\mathbf{p}}_d = \mathbf{R}_b^n(\Theta_{nb}) \mathbf{v}_d, \quad (5.36)$$

$$\mathbf{v}_d = \mathbf{R}_b^n(\Theta_{nb})^T \dot{\mathbf{p}}_d = \mathbf{R}_b^n(\Theta_{nb})^T \mathbf{R}_{d,z}(\chi_d) \mathbf{R}_{d,y}(\Gamma_d) \begin{bmatrix} 1 \\ 0 \\ 0 \end{bmatrix} U_d, \quad (5.37)$$

where  $\Theta_{nb} = [\phi \ \theta \ \psi]^T$  is the ROV attitude vector,  $\mathbf{R}_b^n$  is the rotation matrix from body to NED reference frame and  $\mathbf{v}_d = [u_d \ v_d \ w_d]^T$  is the desired velocity vector in the body frame.

The speed control for  $U_d$  is identical as for the 2-D case. The way-point switching is done as in 2-D, except the radius of a sphere is used as the switching criterion, instead of a circle. The attitude, or heading for 4-DOF workspace ROVs, is controlled independently as described for the 2-D LOS case.

## 5.3 Joystick in Closed-loop Control

Some ROV tasks, such as station keeping and trajectory tracking, can be automated by a closed-loop positioning control system. However, for tasks such as inspection of an unknown object or complex manipulation work, the desired trajectory is not known in advance, and must be decided by a pilot based on view from ROV cameras or other sensor data. In that case, the pilot should have an easy way of guiding the ROV without spending a lot of effort on the positioning control itself. The low level position control should be automated by a controller that compensates for the ROV dynamics and environmental loads.

Most ROVs are controlled by joysticks which are used to command the thrust. Automatic set-point control of heading and depth is the industry standard. Such basic use of the joystick means that the pilot spend a lot of effort on controlling the position and orientation of the ROV. He must compensate for the ROV dynamics, currents and other environmental loads. The joystick should merely be used to guide the ROV. This can be achieved by joystick in closed-loop control for all DOFs where joystick commands result in reference signals to a closed-loop controller. The result is improved performance of the ROV positioning and reduced stress on the pilot.

Previous work on joystick in closed-loop control of ROVs is found in [106], where the idea of relating joystick commands to different reference frames is introduced. The pilot can switch between body-fixed, earth-fixed, boundary-fixed and cylindrical reference frames to enhance performance and easiness of operation for various tasks.

Other fields where joysticks are used for direct or supervisory control are in flight control; [104], [34], ships; [40], heavy duty hydraulics; [77], bipeds; [15], [15], wheelchairs; [37], [20], surgery; [90] and cranes; [92], to mention some. As a human enters the control loop, it is necessary to model the operator as well as the real system. How the human works as a controller is a mature field of research. See e.g. [97], for early work in this field and [51] for more recent work on human adaptive mechatronics (HAM). To the knowledge of the author, except for the work of [106], there is little work on joystick for supervisory control for underwater vehicles in the literature.

The main contributions are

- a method for describing how joystick commands can be related to ROV motions and reference frames with coupled velocity constraints.
- Modifications to standard reference models to take into account that a human operator is in the control loop.
- Full scale experimental data from tests with NTNU's ROV Minerva.

### 5.3.1 The Joystick and ROV

A joystick with 4 axes is used for control of a ROV with actuation in 4 DOFs. Figure 5.7 shows the joystick and the ROV body-frames. The joystick has axes  $x$ ,  $y$ ,  $z$ , and  $w$ . The  $z$ -axis is fixed to the stick and the  $w$ -axis to a lever.  $\phi^{js}$ ,  $\theta^{js}$ ,  $\psi^{js}$  are the rotations

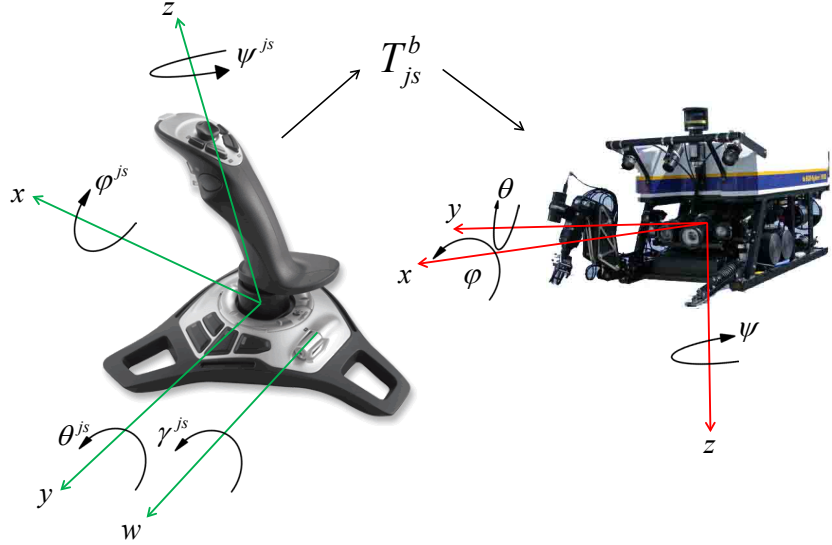


Figure 5.7: Transformation between the joystick and ROV axes.

of the stick about the  $x$ ,  $y$  and  $z$ -axis, respectively.  $\gamma^{js}$  is the rotation of the lever about the  $w$ -axis. Positive directions are given by the arrows and are according to a right hand coordinate system. Thus, the joystick commands are given by the vector

$$\Theta^{js} = [\phi^{js} \quad \theta^{js} \quad \psi^{js} \quad \gamma^{js}]^T. \quad (5.38)$$

It is more practical to work with normalized joystick commands than angles. The vector with normalized joystick commands is

$$\bar{\Theta}^{js} = [\bar{\phi}^{js} \quad \bar{\theta}^{js} \quad \bar{\psi}^{js} \quad \bar{\gamma}^{js}]^T, \quad (5.39)$$

where  $\bar{\phi}^{js}, \bar{\theta}^{js}, \bar{\psi}^{js}, \bar{\gamma}^{js} \in \mathbb{R} \subseteq [-1, 1]$ .

The ROV body-fixed frame is seen to the right in Figure 5.7.  $x, y, z$  is positive forward, starboard and down. The rotations  $\phi, \theta, \psi$  are roll, pitch and yaw, respectively. The generalized 4 DOF position of the ROV and the velocity in the body-frame is given as

$$\boldsymbol{\eta} = [x \quad y \quad z \quad \psi]^T, \quad \boldsymbol{\nu} = [u \quad v \quad w \quad r]^T, \quad (5.40)$$

respectively.  $x, y, z$  is the position in NED, and  $\psi$  is the heading angle.  $u, v, w, r$  are the surge, sway, heave and yaw velocities.

The 4 DOF resultant of the actuator forces are given by the vector

$$\boldsymbol{\tau} = [X \quad Y \quad Z \quad N]^T, \quad (5.41)$$

where  $X, Y, Z$  are the forces in  $x, y, z$  direction, and  $N$  is the torque about the  $z$ -axis.

The joystick command vector must be related to a reference frame and the ROV dynamics. Some possible reference frames are the body-fixed frame, an earth-fixed frame (NED or a rotated frame), cylinder frame and boundary-fixed frame. The magnitude of joystick commands can be related to properties such as position, speed or thrust.

In the body fixed-frame, pushing the stick forward will increase the surge velocity, and pushing it sideways will control the sway velocity. This mode is intuitive for a pilot who has the ROV point of view from cameras during an operation. The body frame mode is the preferred mode for observation tasks when controlling the ROV in an unknown and unstructured environment. In the NED frame mode, stick forward will make the ROV go North while automatically maintaining its heading. Push the stick to the right and the ROV will go East. This mode is used when the pilot controls the ROV while looking at the position and heading on a chart plotter. In cylinder mode, the joystick commands relate to parameters in a cylindrical coordinate system. The origin is set by the pilot to be a given distance ahead of the ROV. Stick forward will make the ROV go towards the origin. Push the stick sideways and the ROV will move on a circle about the origin while the heading is controlled to point towards the center. This mode is very useful and efficient for inspection of an object of interest from all angles. A boundary-fixed frame is defined such that when the joystick is moved sideways, the ROV follows a trajectory parallel to the boundary while heading towards it. The stick can be moved forward to get closer to the boundary or backwards to increase the distance to the boundary. The boundary could for instance be a ship hull or a coral reef.

Relating joystick commands directly to position is not practical for translational DOFs as the possible space to move in becomes too constrained. It is more practical and intuitive to relate the commands to speed, thrust or a combination of these. By making the desired joystick speed,  $\nu^{js}$ , or thrust,  $\tau^{js}$ , proportional to joystick commands, it is possible to scale the proportion constants in order to do fine or coarse maneuvering. Alternatively, a quadratic mapping between joystick commands and velocity or thrust can be used for fine adjustments at low speed or thrust and course adjustments for higher values. The desired joystick velocity is noted  $\nu^{js}$ . This is to separate it from the desired velocity,  $\nu_d$ , which is input to the closed-loop controller. The relationship between the desired joystick velocity,  $\nu^{js}$ , and the joystick commands for the body-fixed frame is expressed as

$$\nu^{js} = \mathbf{K}_{js}^\nu \mathbf{T}_{js}^b \bar{\Theta}^{js}, \quad (5.42)$$

where  $\mathbf{K}_{js}^\nu \in \mathbb{R}^{4x4}$  is a diagonal scaling matrix for velocity,  $\mathbf{T}_{js}^b \in \mathbb{R}^{4x4}$  is the transformation matrix from the joystick reference frame to the ROV body-fixed frame. The elements of these matrices are seen in (5.43) as

$$\mathbf{K}_{js}^\nu = \begin{bmatrix} K_u & 0 & 0 & 0 \\ 0 & K_v & 0 & 0 \\ 0 & 0 & K_w & 0 \\ 0 & 0 & 0 & K_r \end{bmatrix}, \quad \mathbf{T}_{js}^b = \begin{bmatrix} 0 & 1 & 0 & 0 \\ 1 & 0 & 0 & 0 \\ 0 & 0 & 0 & -1 \\ 0 & 0 & -1 & 0 \end{bmatrix}. \quad (5.43)$$

Note that  $\mathbf{T}_{js}^b(3, 4)$  is negative for the joystick in Figure 5.7. It is more intuitive for the pilot that rotating the lever upwards makes the ROV rise towards the surface and not downwards which is the positive z-direction for the ROV.

A similar expression for relating joystick commands to thrust for the body-fixed frame is given as

$$\boldsymbol{\tau}^{js} = \mathbf{K}_{js}^\tau \mathbf{T}_{js}^b \bar{\boldsymbol{\Theta}}^{js} \quad (5.44)$$

where  $\mathbf{K}_{js}^\tau \in \mathbb{R}^{4 \times 4}$  is a diagonal scaling matrix for thrust.

A quadratic mapping between joystick commands and desired joystick speed is obtained by using

$$\mathbf{K}_{js}^{\nu^2} = \begin{bmatrix} K_u |\bar{\phi}^{js}| & 0 & 0 & 0 \\ 0 & K_v |\bar{\theta}^{js}| & 0 & 0 \\ 0 & 0 & K_w |\bar{\psi}^{js}| & 0 \\ 0 & 0 & 0 & K_r |\bar{\gamma}^{js}| \end{bmatrix}, \quad (5.45)$$

instead of  $\mathbf{K}_{js}^\nu$  in (5.42). Quadratic thrust mapping is obtained likewise.

The joystick commands must be within the capabilities of the vehicle according to

$$\boldsymbol{\nu}^{js} \leq \boldsymbol{\nu}_{lim}, \quad (5.46)$$

where  $\boldsymbol{\nu}_{lim}$  is the maximum velocity of the vehicle and depends on the direction of  $\boldsymbol{\nu}$  due to hydrodynamical coupling effects. Figure 5.8 shows an example of surge and sway velocity capability plot for zero heave and yaw rate.  $\boldsymbol{\nu}_{lim}$  is seen as the closed curve. The enclosed area corresponds to the set of admissible velocity combinations,  $\boldsymbol{\nu}_{admissible}$ .

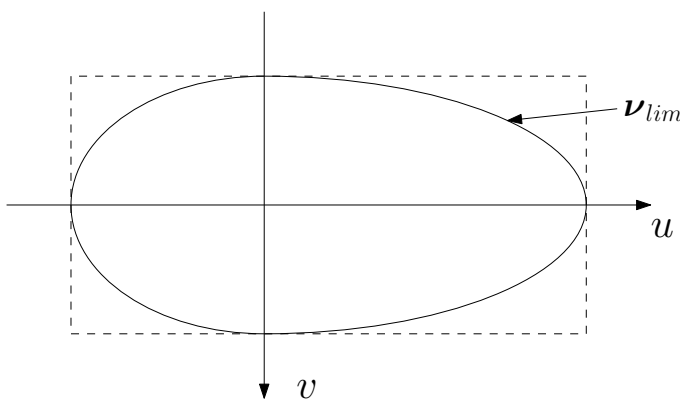


Figure 5.8:  $u, v$  capability plot for  $w, r = 0$ .

The scaling matrix  $\mathbf{K}_{js}^\nu$  may be a function of the velocity vector to assure that the given commands correspond to admissible velocities.

### 5.3.2 Human-in-the-Loop

The overall goal of the joystick in closed-loop control is to provide an easy way of guiding the ROV in presence of environmental loads and ROV dynamics. A human in a outer feedback loop, as seen in Figure 5.9, can be difficult to analyze in a quantitative way. However, the interactions between the inner and outer feedback loop are important for the performance of the system. Whereas the inner control loop uses feedback from measurements of position and velocity, the operator mostly rely on visual feedback of position and velocity from cameras. The thrust calculated by the inner loop is a number based on quantitative measurements. Joystick commands are given based on the visual feedback. Note that the operator does not know what velocity or thrust a certain stick position corresponds to. But he expects the vehicle to go faster or slower for changes in joystick commands.

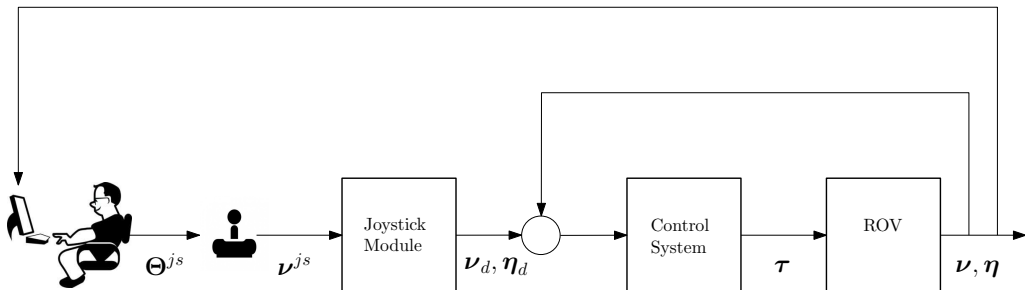


Figure 5.9: Block diagram of control system with pilot and joystick in the control loop.

It is important that the vehicle responds quickly to the joystick commands. Too much lag, and the operator feels out of control and keeps giving commands that the vehicle can not follow. This can cause pilot induced oscillations (PIO). PIO resulting from the complex interaction between the pilot behavior and vehicle dynamics has been a problem for aircraft since the Wright Brothers [73]. The topic has been studied for several decades, but it is still a problem that has caused aircraft crashes in modern times. A JAS 39 Gripen fighter crashed due to PIO during landing in Linkoping, Sweden in 1989. Aspects of PIO and human behavior is covered in [73]. Consequences are less severe for ROVs, and the problem is different from aircraft PIO in many ways. As the ROV pilot is not on-board the vehicle, acceleration cues do not affect PIO for ROVs. The ROV moves slowly and is stationary for large parts of many operations. Thus, it is important that the vehicle starts and stops quickly on the pilot command. If the pilot let go of the stick and the ROV keeps moving, he feels to be out of control.

For an operation mode where stick position corresponds to a desired velocity, the rate of change of stick position corresponds to vehicle acceleration. The vehicle acceleration is limited. An operator who is not aware of the ROV dynamics and limitations, may use fast changes in the joystick commands. That is, the joystick commanded velocity  $\nu^{js}(t)$  in Figure 5.9 may not feasible. However, the desired trajectory output from the joystick module should be feasible to track for the closed-loop controller. But to limit PIO, the joystick module should exploit the bandwidth of the ROV and control system. It

is observed that new pilots use the stick in an on-off manner, either full speed or no speed. The slower dynamics of the ROV, the more severe on-off joystick use.

As the pilot is not on-board the vehicle, the lack of acceleration cues can be compensated by force feedback to the joystick. This is a method to teach the pilot about the vehicle dynamics and capabilities. The pilot will feel a resistive force when trying to give too quick commands. The goal is that the pilot shall only produce joystick commands that are feasible for the vehicle. This is a subject for further research and it has not been studied in the work with this thesis. Only methods as in Figure 5.9 are proposed here.

### 5.3.3 Joystick Reference Models and Control

Reference models and controller types for joystick without force feedback are presented next. The main objective of the joystick reference model is to produce a feasible trajectory for the ROV while minimizing PIO. The proposed filters are based on reference models presented in [40]. The filter-based reference model used in the joystick guidance system was also presented in Chapter 5.1, where its performance was compared with the proposed constant jerk reference model. However, the filter-based reference model is chosen here as joystick commands are changing continuously. The constant jerk reference model works for fixed reference inputs.

The input signal to the reference model,  $\nu^{js}$ , may be of an oscillating and unpredictable character depending on the pilot. With few assumptions on the behavior of  $\nu^{js}$ , a filter based reference model for position and velocity is proposed as a basis in (5.47) and (5.48) as

$$\dot{\eta}_d = \mathbf{R}(\psi)\nu_d, \quad (5.47)$$

$$\ddot{\nu}_d + 2\Delta\Omega\dot{\nu}_d + \Omega^2\nu_d = \Omega^2\nu^{js}, \quad (5.48)$$

where  $\Delta > 0$  and  $\Omega > 0$  are diagonal design matrices of relative damping ratios and natural frequencies:

$$\Delta = \text{diag}\{\zeta_1, \zeta_2, \zeta_3, \zeta_4\} \quad (5.49)$$

$$\Omega = \text{diag}\{\omega_{n1}, \omega_{n2}, \omega_{n3}, \omega_{n4}\}. \quad (5.50)$$

In the following, three methods of combining reference models and control types are presented. The main concept of the different methods are

1. Speed reference model with position control of all DOFs.
2. Speed reference model with velocity control of surge and sway and position control of heave and yaw.
3. Thrust allocation for all DOFs with position set-point control of DOFs not activated by the joystick.

### Speed Reference, Position Control of all 4 DOFs

In this method, the joystick commands correspond to speed references. The joystick commands go through the filter in (5.52) to give a desired trajectory from (5.51). The trajectory is tracked using a position controller.

#### Reference Model

$$\begin{aligned} \dot{\eta}_d &= \mathbf{R}(\psi)\boldsymbol{\nu}_d, \\ \boldsymbol{\nu}_d &\Leftarrow \begin{cases} \ddot{\nu}_{d_i} + 2\zeta_i\omega_{n_i}\dot{\nu}_{d_i} + \omega_{n_i}^2\nu_{d_i} = \omega_{n_i}^2\nu_i^{js} & \text{if } \nu_i^{js} \neq 0, \\ \nu_{d_i} = \nu_{o_i}e^{-a_i(t-t_0)} & \text{if } \nu_i^{js} = 0, \quad |\nu_i| > \nu_i^{tol}, \\ \nu_{d_i} = 0 & \text{if } \nu_i^{js} = 0, \quad |\nu_i| \leq \nu_i^{tol}. \end{cases} \end{aligned} \quad (5.51)$$

where  $\nu_{o_i}$  is the velocity of DOF number  $i$  when the corresponding joystick command becomes zero.  $a_i$  sets the rate of deceleration.  $t_0$  is the time when the joystick command is set to zero.  $\nu_i^{tol}$  is a tolerance limit telling that the velocity is sufficiently close to zero to switch to set point regulation (DP).

The modification in (5.52) compared to (5.48) is that when the joystick command becomes zero, the desired velocity should go to zero as fast as feasible. This will give the pilot the sense that the ROV stops moving when he wants it to. This modification was done after sea trials when the standard reference model was first tested. The ROV typically kept on moving for several seconds after the stick was released. This was due to slow convergence towards zero (for all DOFs) for desired velocities from the reference model in (5.48). The convergence rates depend on the parameters in  $\Delta$  and  $\Omega$ . The parameters were set to  $\zeta_i = 1$  for  $i = 1, 2, 3, 4$  to yield critical damping while  $0.6 \leq \omega_{n_i} \leq 0.8$  for  $i = 1, 2, 3, 4$  to give a quick response to joystick commands. A note is that even though the reference model behaves the same from zero to a desired velocity as from that desired velocity to zero, the pilot's perception is not the same. If a forward joystick command is given, the pilot expects the ROV to start moving in that direction immediately. This is satisfied by the standard reference model as the desired velocity increases quickly to start with and the pilot sees the ROV moving. Assuming the joystick command is kept constant, it still takes a while before the desired velocity is reached. This is not a big problem as the pilot does not know exactly what velocity he commanded, and he can not really tell (from visual feedback) if the velocity is somewhat off the desired value. The problem occurs when he releases the stick. Then he expects the ROV to stop quickly. This is not the case if (5.48) is used. The ROV slows down considerably to begin with, but it keeps on moving for a while before the pilot perceives the ROV as standing still. This was the motivation for modifying the reference model for stops.

**Position Controller** The desired trajectories are tracked by a position controller. This is denoted as  $\tau^{pos}$ . In this case all DOFs are subject to position control, i.e.

$$\tau_i = \tau_i^{pos}, \quad i = 1, 2, 3, 4. \quad (5.53)$$

Position control compensates for currents and environmental forces in all directions. However, using position control to achieve a desired velocity can result in unnecessary oscillations, especially in surge and sway as acoustic positioning in these DOFs has slow update rates and possible high noise levels. An alternative method is needed as described next.

### Speed Reference, Speed/Position Control

This method also uses the speed reference model in (5.52). The difference is that a speed controller is used on surge or sway joystick commands and for the deceleration stage after the stick is released. This is expressed in (5.54) for  $i = 1, 2$  (surge and sway) as

$$\tau_i = \begin{cases} \tau_i^{\text{speed}} & \text{if } \nu_1^{js} \text{ or } \nu_2^{js} \neq 0, \\ \tau_i^{\text{speed}} & \text{if } \nu_1^{js} \text{ and } \nu_2^{js} = 0, \quad U > U^{\text{tol}}, \\ \tau_i^{\text{pos}} & \text{if } \nu_1^{js} \text{ and } \nu_2^{js} = 0, \quad U \leq U^{\text{tol}}, \end{cases} \quad (5.54)$$

where  $U = \sqrt{u^2 + v^2}$  and  $\tau^{\text{speed}}$  indicates that a speed controller is used. Position control is still in use when the stick is passive to ensure station keeping in presence of currents.

Position control is used for heave and yaw, i.e.

$$\tau_i = \tau_i^{\text{pos}} \quad \text{if } i = 3, 4. \quad (5.55)$$

This method is better than the speed reference with position control, especially due to increased performance of desired velocity tracking in surge and sway. If e.g. a forward joystick command is given, it still compensates for sideways drifting as sway velocity is controlled to zero. However, there is no spring pushing it back on the desired track.

It is possible to use speed control in the commanded direction in combination with position cross-track error control. Guidance laws for parameterized paths can be found in [8]. The problem with joystick is that the desired path in the future is unknown to the control system. In that respect, one could argue that joystick in closed-loop control is similar to tracking of a moving target.

After some testing with this method, the conclusion is that the response is too slow to be satisfactory. Especially if the joystick commands are changing rapidly. The ROV has limited bandwidth, but the reference model used is not able to fully exploit this and the effective bandwidth becomes lower than necessary. A proposed solution to this is given in the following. Alternatively, other reference models may be considered.

### Thrust Reference, Thrust and Speed/Position Control

The easiest way to get quick response and utilize the entire bandwidth of the ROV is to control the thrust directly. A very efficient and user friendly method is to use a joystick and thrust allocation. However, the pilot must compensate for vehicle dynamics and external forces. The proposed method is to use thrust allocation when a joystick command is given

while the other DOFs are set-point regulated. When a joystick command is set to zero, a reference model is used to stop movement faster than by natural damping. As the ROV comes to a stop for the given DOF, a new desired value is set for set-point regulation. Again, surge and sway are treated differently than heave and yaw.

For  $i = 1, 2$ , the control strategy is given by (5.56). The control system goes into thrust allocation for horizontal motions if a surge or sway joystick command is given. For a passive stick, the reference model for deceleration is used in combination with a speed controller to stop the ROV quickly. The ROV goes into DP mode when the horizontal velocity is sufficiently close to zero.

$$\tau_i = \begin{cases} \tau_i^{js} & \text{if } \nu_1^{js} \text{ or } \nu_2^{js} \neq 0, \\ \tau_i^{\text{speed}} & \text{if } \nu_1^{js} \text{ and } \nu_2^{js} = 0, \quad U > U^{\text{tol}}, \\ \tau_i^{\text{pos}} & \text{if } \nu_1^{js} \text{ and } \nu_2^{js} = 0, \quad U \leq U^{\text{tol}}. \end{cases} \quad (5.56)$$

The same strategy is used for heave and yaw except there is no coupling and a position controller is used during the deceleration stage when the joystick command is set to zero. This is seen in (5.57) for  $i = 3, 4$  as

$$\tau_i = \begin{cases} \tau_i^{js} & \text{if } \nu_i^{js} \neq 0, \\ \tau_i^{\text{pos}} & \text{if } \nu_i^{js} = 0, \quad |\nu_i| > \nu_i^{\text{tol}}, \\ \tau_i^{\text{pos}} & \text{if } \nu_i^{js} = 0, \quad |\nu_i| \leq \nu_i^{\text{tol}}. \end{cases} \quad (5.57)$$

The main advantage with this method is that it gives direct control of the ROV while also being able to do station keeping in closed-loop control without further instructions from the pilot. The disadvantage is that there is no compensation for currents when surge or sway joystick commands are given. This issue could be solved by including position cross-track error control in combination with direct thrust in the commanded direction. This is a subject for future studies.

### 5.3.4 Joystick Experimental Results

Full scale experimental results from sea trials with the ROV Minerva are given. A Logitech Freedom 2.4 wireless joystick, as seen in Figure 5.7, is used in the experiments. The experiment was conducted to show the performance and to compare the proposed methods. Sea trials are very important as the human operator depends on visual feedback, which is challenging to reproduce in simulations. Other effects such as delays, coupled dynamics and nonlinear thruster characteristics affects the pilot's perception of control. These are also difficult to model accurately in simulations.

#### Comparison and Performance of Joystick Control Methods

The three proposed methods are compared from tests where the wreck of a barge is inspected. The barge is about 20 m long with 4.5 m beam and is located East of Munkholmen in the Trondheimsfjord at ca. 32 m below the surface. The task in the tests is to swim

the ROV approximately 1.5 m above the contour of the wreck while heading tangentially to the wreck contour. Estimated states are obtained with the default model-based Kalman filter described in Chapter 4.

**Speed Reference, Position Control (1):** Figure 5.10a shows the ROV estimated, measured and desired positions and snapshots of the ROV outline for every 5<sup>th</sup> second during the test with speed reference and position control. The desired velocity and estimated velocity for surge during the test are seen in Figure 5.10b. Note that the surge velocity is oscillating about the desired velocity because position control, with feedback from the HiPAP system, is used to track the generated trajectory.

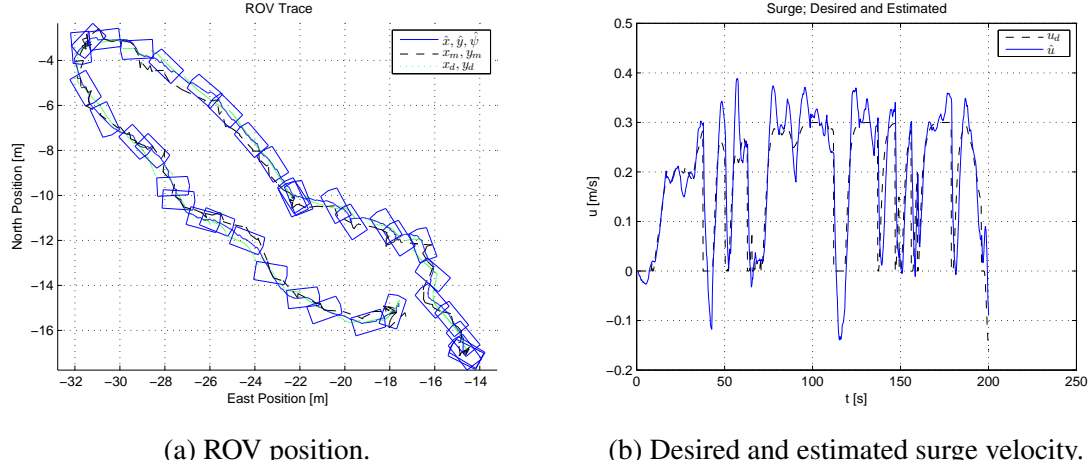


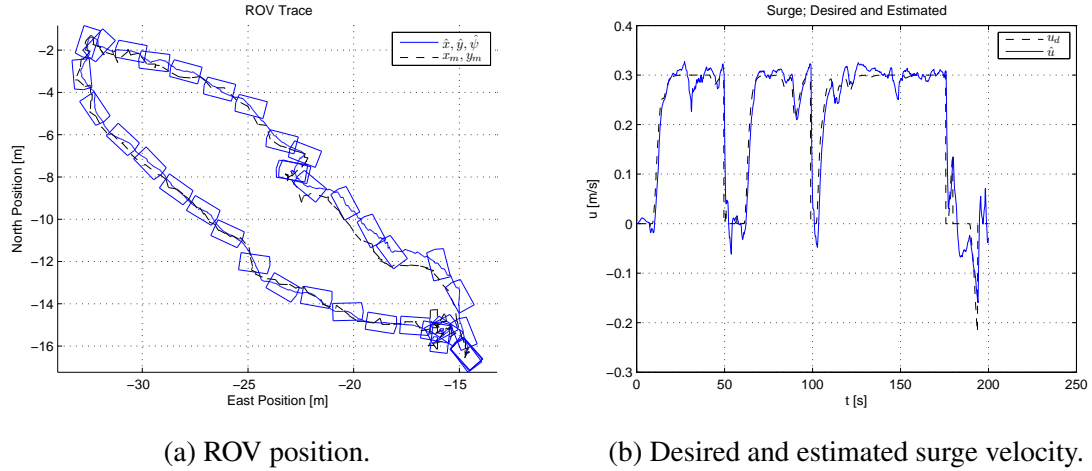
Figure 5.10: Joystick in closed-loop control with position mode (1).

**Speed Reference, Velocity Control (2):** Figure 5.11a shows the ROV estimated and measured positions during the test with speed reference and velocity control of surge and sway. The desired and estimated surge velocity are seen in Figure 5.11b. Note that the performance of the velocity control is much better than when position control is used, as expected.

**Thrust Allocation, Set-point Control (3):** Figure 5.12a shows the ROV estimated and measured positions during the test with thrust allocation for commanded DOFs. The estimated velocity is seen in Figure 5.12b. Note that the surge velocity is more oscillating compared to case (1) and (2) as the pilot must compensate for ROV dynamics and currents. The performance of case (3) depends highly on the pilot as well.

### Joystick Remarks

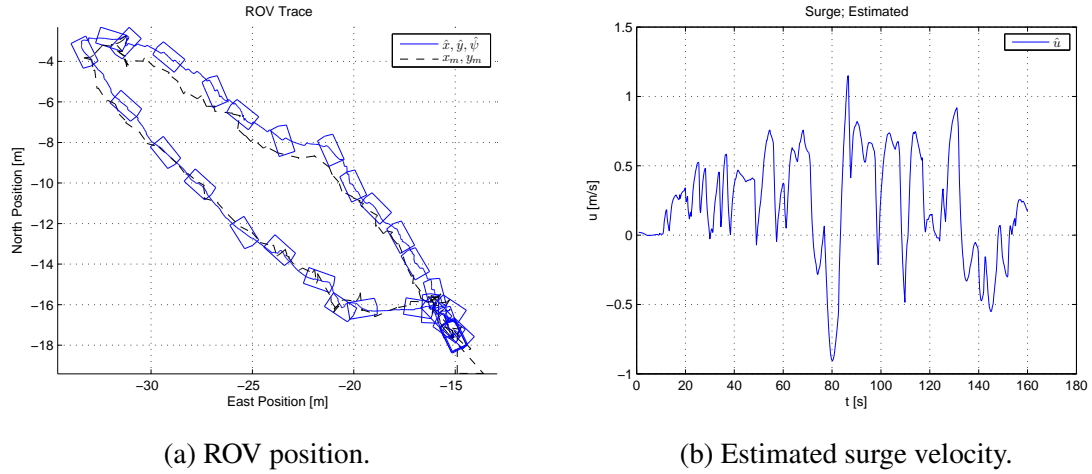
The method with speed reference and speed control in surge and sway gave the best results of the tests presented in the paper. However, the thrust mode is the preferred method in moderate currents as it gives more direct control of the ROV. This is important if the



(a) ROV position.

(b) Desired and estimated surge velocity.

Figure 5.11: Joystick in closed-loop control with speed mode (2).



(a) ROV position.

(b) Estimated surge velocity.

Figure 5.12: Joystick in closed-loop control with thrust allocation mode (3).

joystick commands are changing rapidly. These effects and the pilot's perception are difficult to show with plots and figures.



# Chapter 6

## Altitude Control and Terrain Following

The altitude, which is the vertical distance from the ROV to the sea floor, should be automatically controlled in order to follow the terrain for survey tasks close to the sea floor. This requires that the sea floor is sensed by the control system, which again takes the appropriate actions to maintain a desired distance from the sea floor.

A method for sea floor geometry approximation in a local region beneath a ROV for use in altitude control is proposed. The method is based on DVL altitude measurements and ROV state estimates. The vehicle estimates are obtained by methods proposed in Chapter 4. The ROV altitude and sea floor gradient, which is obtained from the sea floor approximation, is used in a proposed guidance law for altitude control. The altitude control is executed via depth control.

This work on altitude control and terrain following contains two main scientific contributions, which contains several partial contributions as listed below.

- A method to locally approximate the sea floor geometry based on DVL measurements.
  - The derivation of the altitude rate of change.
  - A least squares approximation method of the sea floor geometry.
  - A proposed altitude observer which runs in cascade with the vehicle observer.
  - Definitions of errors norms to asses the performance of the proposed sea floor approximation method.
- A guidance law to control a desired altitude via depth control.
  - A feedforward term that gives the vertical velocity for altitude control.
  - A feedback law to regulate the horizontal speed during altitude control.
  - A method to follow a coarse contour of the sea floor (platforming).

Another contribution is that the proposed methods have been implemented in the control system described in Chapter 3 and experimental results, demonstrating the performance of the proposed methods, are given. The work in this Chapter has been presented in [28] and [29].

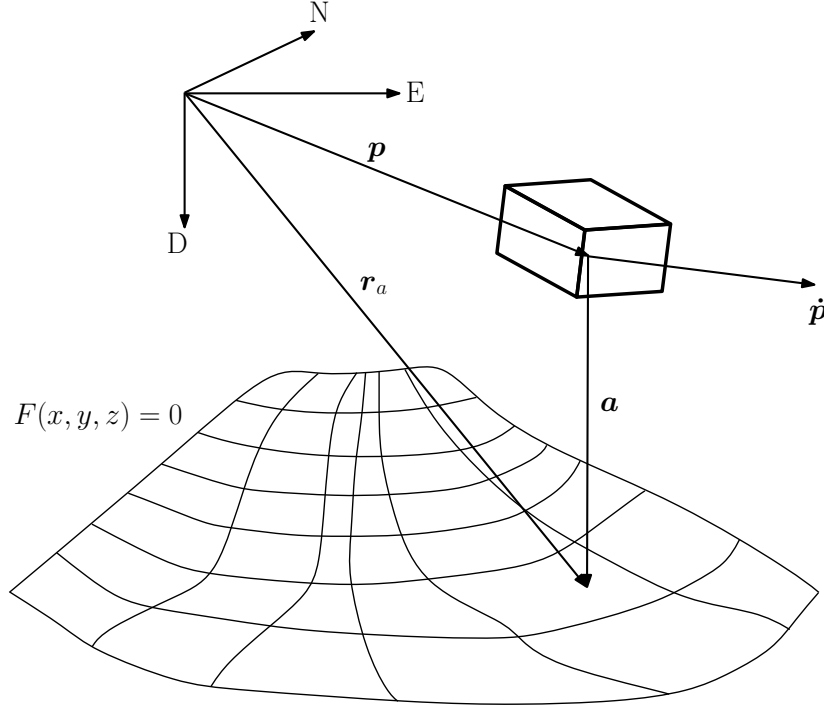


Figure 6.1: The ROV above the sea floor in the NED frame.

The proposed gradient based altitude estimation is inspired by the work of [12]. Other work on altitude control for ROVs can be found in e.g. [10], [11], and for AUVs in [81] and [105]. The close to sea floor altitude control problem is described in [69], and more results on the use of DVL for terrain navigation can be found in [1].

## 6.1 Altitude and the Sea floor Gradient

Figure 6.1 shows the ROV above the sea floor. The ROV position in the  $\{n\}$  frame, is  $\mathbf{p} = [x_p, y_p, z_p]^T$ . The NED velocity vector is  $\dot{\mathbf{p}}$  and can be expressed as

$$\dot{\mathbf{p}} = \mathbf{R}_b^n(\Theta_{nb})\mathbf{v}, \quad (6.1)$$

where  $\Theta_{nb} = [\phi, \theta, \psi]^T$  is the attitude vector,  $\mathbf{R}_b^n(\Theta_{nb})$  is the rotation matrix from  $\{b\}$  to  $\{n\}$ , and  $\mathbf{v} = [u, v, w]^T$  is the velocity vector in  $\{b\}$ .

It is assumed that the sea floor can be expressed as the surface given by the following equation:

$$F(x, y, z) = f(x, y) - z = 0, \quad \frac{\partial F}{\partial t} = 0, \quad (6.2)$$

where  $F$  is a time invariant function with continuous first-order partial derivatives. That the sea floor is time invariant is normally satisfied unless there are underwater

avalanches or volcanic activity. The assumption on continuous first-order partial derivatives will be violated if there are sharp edges, e.g. underwater rocks and cliffs. Effects of these violations are discussed later.  $F$  is an unknown function, but only the structure of  $F$  (as in (6.2)) is important to be known for the method of altitude estimation proposed in this paper.

### 6.1.1 Altitude

The altitude of the ROV is given by the following definition.

**Definition 6.1.1.** The altitude is the length of the vector from the center of origin (CO) of the ROV to the point on the sea floor with the same horizontal coordinates as the CO.

The ROV depth,  $z_p$ , is the vertical distance from the sea surface to the CO of the ROV. This should not be confused with the water depth or altitude. The altitude vector is expressed as

$$\mathbf{a} = \mathbf{r}_a - \mathbf{p} = \begin{bmatrix} x_p \\ y_p \\ f(x_p, y_p) \end{bmatrix} - \begin{bmatrix} x_p \\ y_p \\ z_p \end{bmatrix} = \begin{bmatrix} 0 \\ 0 \\ f(x_p, y_p) - z_p \end{bmatrix}, \quad (6.3)$$

where  $\mathbf{r}_a$  is the NED position of the point on the sea floor below the CO of the ROV, see Figure 6.1. According to the proposed Definition 6.1.1, the altitude is the length of (6.3) and is written as

$$a = f(x_p, y_p) - z_p = F(x_p, y_p, z_p). \quad (6.4)$$

It is seen from (6.4) that the altitude can be expressed by the same function  $F$  as the sea floor, when  $F$  is evaluated at the ROV position. Note that the altitude is completely given by the ROV position as the sea floor is time-invariant. These facts are used to find an expression for the altitude rate of change.

### 6.1.2 Altitude Rate of Change

The altitude rate of change is given in Proposition 6.1.1 and is valid for motions in 6 DOFs.

**Proposition 6.1.1.**

$$\dot{a} = \nabla F(\mathbf{p}) \cdot \dot{\mathbf{p}}, \quad (6.5)$$

where  $\nabla F(\mathbf{p}) = \left[ \frac{\partial f}{\partial x} \Big|_{x_p, y_p}, \frac{\partial f}{\partial y} \Big|_{x_p, y_p}, -1 \right]$  is the gradient vector of (6.2) evaluated at the horizontal position  $(x_p, y_p)$  of the ROV. The proof of (6.5) is given in the following.

**Proof 6.1.1.** An expression for the altitude rate of change is given in (6.7) using partial derivatives of  $a$  and the chain rule.

$$\dot{a} = D_t a(\mathbf{p}(t)) = D_t[a(x_p(t), y_p(t), z_p(t))] \quad (6.6)$$

$$= \frac{\partial a}{\partial x_p} \cdot \frac{dx_p}{dt} + \frac{\partial a}{\partial y_p} \cdot \frac{dy_p}{dt} + \frac{\partial a}{\partial z_p} \cdot \frac{dz_p}{dt}. \quad (6.7)$$

By using (6.4) in (6.7), the altitude rate of change becomes

$$\dot{a} = \frac{\partial f}{\partial x_p} \cdot \frac{dx_p}{dt} + \frac{\partial f}{\partial y_p} \cdot \frac{dy_p}{dt} - \frac{dz_p}{dt}. \quad (6.8)$$

According to Definition 6.1.1,  $x = x_p$  and  $y = y_p$  in the function  $f$  in (6.2) and (6.4). Then  $\frac{\partial f}{\partial x_p} = \frac{\partial f}{\partial x}\Big|_{x_p, y_p}$  and  $\frac{\partial f}{\partial y_p} = \frac{\partial f}{\partial y}\Big|_{x_p, y_p}$ , indicating that the partial derivatives are evaluated at  $x = x_p$ ,  $y = y_p$ . Using this, the altitude rate of change in (6.8) becomes

$$\dot{a} = \left[ \frac{\partial f}{\partial x}\Big|_{x_p, y_p}, \frac{\partial f}{\partial y}\Big|_{x_p, y_p}, -1 \right] \cdot \begin{bmatrix} \dot{x}_p \\ \dot{y}_p \\ \dot{z}_p \end{bmatrix} = \nabla F(\mathbf{p}) \cdot \dot{\mathbf{p}}, \quad (6.9)$$

where it was used that  $\nabla F = \left[ \frac{\partial f}{\partial x}, \frac{\partial f}{\partial y}, -1 \right]$  if  $F = F(x, y, z) = f(x, y) - z = 0$ , [33]. This completes the proof of (6.5).

Eq. (6.5) written out as in (6.10) shows how the altitude rate of change is related to the sea floor from the gradient vector, and to the ROV attitude and velocity vector.

$$\dot{a} = \left[ \frac{\partial f}{\partial x}\Big|_{x_p, y_p}, \frac{\partial f}{\partial y}\Big|_{x_p, y_p}, -1 \right] \mathbf{R}_b^n(\Theta_{nb}) \begin{bmatrix} u \\ v \\ w \end{bmatrix}, \quad (6.10)$$

where  $\Theta_{nb}$  and  $\mathbf{v}$  are measured or estimated from a vehicle observer as  $\hat{\Theta}_{nb}$  and  $\hat{\mathbf{v}}$  as shown in Chapter 4. The gradient vector,  $\nabla F(\mathbf{p}) = \left[ \frac{\partial f}{\partial x}\Big|_{x_p, y_p}, \frac{\partial f}{\partial y}\Big|_{x_p, y_p}, -1 \right]$  is approximated from the DVL altitude measurements as shown in Chapter 6.3.

## 6.2 DVL Measurements

The DVL is used to measure the ROV velocity through water or over the sea floor and to measure the altitude. This section explains the geometry of the DVL's acoustic beams in a Janus configuration and the transformation from the DVL fixed frame,  $\{d\}$ , to  $\{b\}$  and  $\{n\}$  for use in the sea floor approximation method.

### 6.2.1 DVL Beams and Kinematics

A typical DVL has 4 acoustic beams in a Janus configuration. The  $j^{\text{th}}$  DVL beam with its parameters is shown in Figure 6.2a. The  $j^{\text{th}}$  beam is represented by the vector  $\mathbf{r}_j^d$  in (6.11) and goes from the DVL to the sea floor.

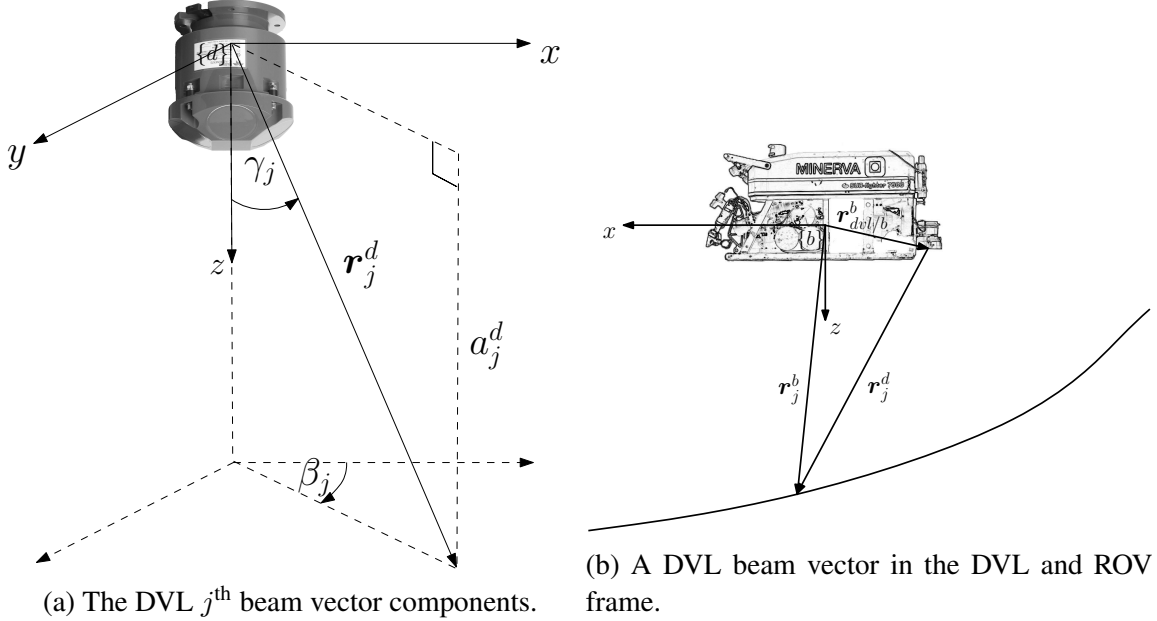


Figure 6.2: The DVL beam components and beam vectors in the DVL and vehicle frame.

$$\mathbf{r}_j^d = \begin{bmatrix} x_j^d \\ y_j^d \\ a_j^d \end{bmatrix} = a_j^d \begin{bmatrix} \tan(\gamma_j)\cos(\beta_j) \\ \tan(\gamma_j)\sin(\beta_j) \\ 1 \end{bmatrix}, \quad (6.11)$$

where  $\gamma_j$  is the angle of the  $j^{\text{th}}$  beam from the DVL z-axis, and  $\beta_j$  is the angle from the x-axis.  $a_j^d$  is the vertical component of  $\mathbf{r}_j^d$ .  $\mathbf{r}_j^d$  is expressed in terms of  $a_j^d$  and the constant angles  $\beta_j$  and  $\gamma_j$ .  $a_j^d$  is an output measurement from the DVL, and the vector with all 4 altitude measurements is noted  $\mathbf{a}^d$ .

### 6.2.2 Transformation of Beams

$\mathbf{r}_j^d$  is transformed and shifted to  $\{b\}$  in (6.12) and transformed to  $\{n\}$  in (6.13). The first transformation and shift are illustrated in Figure 6.2b.

$$\mathbf{r}_j^b = \mathbf{R}_d^b(\Theta_{bd})\mathbf{r}_j^d + \mathbf{r}_{dvl/b}^b, \quad (6.12)$$

$$\mathbf{r}_j^n = \mathbf{R}_b^n(\Theta_{nb})\mathbf{r}_j^b, \quad (6.13)$$

where  $\Theta_{bd}$  is the orientation of  $\{d\}$  relative to  $\{b\}$ .  $\mathbf{r}_{dvl/b}^b$  is the vector from the CO of the ROV to the center of the DVL expressed in  $\{b\}$ .

The result of this section is the 4 vectors from the ROV CO to the sea floor given in  $\{n\}$  as

$$\mathbf{r}_j^n = \begin{bmatrix} x_j^n \\ y_j^n \\ a_j^n \end{bmatrix}, \quad j = 1, 2, 3, 4. \quad (6.14)$$

This is used to approximate the sea floor geometry locally under the ROV.

### 6.3 Sea Floor Approximation by Use of a DVL

Information about the sea floor is needed in order to follow the terrain. This section presents methods for approximation of the sea floor geometry beneath the ROV by use of a DVL's altitude measurements. The most important result is an approximation of the ROV altitude and the sea floor gradient. The idea is to find a local approximation of the sea floor, as a function  $F(x, y, z) = f(x, y) - z = 0$ , based on the 4 points where the DVL beams intersect the sea floor as seen in Figure 6.3.

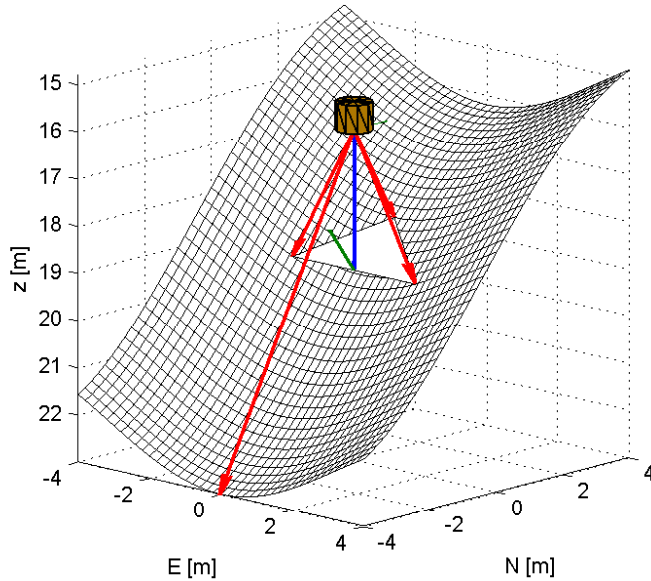


Figure 6.3: The DVL beams (red) and the linear sea floor approximation (white) using 3 of 4 beams. Approximated altitude (blue) and gradient vector (green).

#### 6.3.1 Basic Linear Approximation

A linear approximation of the sea floor requires 3 points. The linear sea floor function is  $f(x, y) = a + bx + cy$ , where the coefficients are found from 3 of the DVL altitude

measurements. When 4 measurements are available, 4 different approximations can be calculated by different combinations of 3 of 4 beams. However, one of the approximations must be selected for use. It is advised to use the combination which gives the most preview while going forward as the forward looking beam will give some collision avoidance feature. In the following, the origin is at the CO of the ROV. The intersection point between a DVL beam and the sea floor is  $\mathbf{r}_j^n$ . The sea floor approximation using 3 beams is found by solving the system (6.15) to obtain the coefficients  $a_j, b_j, c_j$ .

$$\begin{bmatrix} 1 & x_j^n & y_j^n \\ 1 & x_{j+1}^n & y_{j+1}^n \\ 1 & x_{j+2}^n & y_{j+2}^n \end{bmatrix} \begin{bmatrix} a_j \\ b_j \\ c_j \end{bmatrix} = \begin{bmatrix} a_j^n \\ a_{j+1}^n \\ a_{j+2}^n \end{bmatrix}. \quad (6.15)$$

From a combination of 3 beams, the  $j^{th}$  approximation of the sea floor is  $z_j^{CO} = a_j + b_j x + c_j y$ , where  $z_j^{CO}$  is the sea floor geometry in a frame parallel to  $\{n\}$  with origin in the CO of the ROV. Note that the approximated altitude of the ROV is  $a_j$  and the corresponding approximated sea floor gradient vector is

$$\hat{\nabla} F \Big|_j = \left[ \frac{\partial f}{\partial x} \Big|_j, \frac{\partial f}{\partial y} \Big|_j, -1 \right], \quad (6.16)$$

$$\frac{\partial f}{\partial x} \Big|_j = b_j, \quad \frac{\partial f}{\partial y} \Big|_j = c_j, \quad (6.17)$$

where  $(\hat{\phantom{x}})$  is used to denote the approximated gradient vector. Figure 6.3 shows the DVL beams (red arrows), and the white plane is one of the 4 basic linear approximations of the sea floor. The green arrow is the approximated gradient vector, and the blue arrow is the approximated altitude.

### 6.3.2 Least Squares Approximation

A least squares approximation of the sea floor is proposed to use all information provided by the DVL's 4 altitude measurements. As before,  $f(x, y) = a + bx + cy$ , but the object function

$$\sum_{j=1}^4 [a_j^n - (a + bx_j^n + cy_j^n)]^2, \quad (6.18)$$

is minimized. The system  $\mathbf{Ax} = \mathbf{b}$  is

$$\begin{bmatrix} 1 & x_1^n & y_1^n \\ 1 & x_2^n & y_2^n \\ 1 & x_3^n & y_3^n \\ 1 & x_4^n & y_4^n \end{bmatrix} \begin{bmatrix} a \\ b \\ c \end{bmatrix} = \begin{bmatrix} a_1^n \\ a_2^n \\ a_3^n \\ a_4^n \end{bmatrix}, \quad (6.19)$$

where  $\mathbf{x} = [a, b, c]^T$ , and is found by solving the normal system  $\mathbf{A}^T \mathbf{A} \mathbf{x} = \mathbf{A}^T \mathbf{b}$  in order to minimize (6.18), [32]. The least squares approximation of the sea floor geometry is given by (6.20) as

$$\hat{z}_{sf}^{CO} = a + bx + cy, \quad (6.20)$$

where  $\hat{z}_{sf}^{CO}$  is the approximated geometry of the sea floor in a frame parallel to  $\{n\}$  with origin in the CO of the ROV. As in Section 6.3.1, the ROV altitude and sea floor gradient vector directly under it is found from the coefficients  $a, b$  and  $c$ .

### 6.3.3 Combination Methods for Sea Floor Approximation

Although the least squares method provides the best linear approximation in the sense that (6.18) is minimized, it should be noted that the main reason for the sea floor approximation is to enable altitude control and terrain following. That is judgment of the different approximation methods must take into account that an approximated altitude greater than the true altitude is worse than vice versa as the ROV could risk to collide with the sea floor. With this in mind, a third method of linear approximation is proposed. The idea is to use the lowest DVL altitude measurement as a conservative approximation of the ROV altitude and use the gradient from the least squares method. That is the approximated sea floor geometry in a frame parallel to  $\{n\}$  with origin in the CO of the ROV is given by (6.21) as

$$\hat{z}_{sf}^{CO} = a_{min}^n + bx + cy, \quad (6.21)$$

where  $a_{min}^n$  is the lowest DVL altitude measurement.

### 6.3.4 Higher Order Methods for Sea Floor Approximation

A higher order approximation of the sea floor requires more measurement points than provided by the DVL's 4 beams. This can be achieved by e.g. a multibeam sonar or by windowing several DVL altitude measurements as the ROV moves over the sea floor. The windowing method requires position measurement of the ROV as the sea floor can no longer be expressed in a local ROV coordinate system. That means the errors associated with the positioning system will enter the sea floor approximation as well. This is a subject for further research.

## 6.4 Sea Floor Roughness and Approximation Validity

The DVL beam angles are constant so the footprint of the DVL increases with altitude. Hence, the validity of the linear approximation of the sea floor depends on both the sea floor roughness and the ROV altitude. It is difficult to characterize the sea floor roughness

by a simple metric and find a tolerance on the approximation error that is acceptable for use in altitude control. However, a generalization using error norms will provide information about what kind of terrain the method is suitable for. The roughness of the sea floor can be described in terms of amplitude and periods of dominating terrain features. Rugosity is used as a measure for the sea floor roughness. If a chain is laid in a straight line on the sea floor, the ratio of the chain length,  $L_{chain}$ , to the euclidean distance between the two end links,  $D_{chain}$ , is the rugosity,  $r_{chain}$ , of that transect, [43]. The rugosity of a surface, e.g. a sea floor, is the ratio of the area of a carpet draped over the sea floor,  $A_{carpet}$ , to the carpet's orthogonal footprint  $A'_{carpet}$ .  $r_{chain}$  and  $r_{carpet}$  are given in (6.22) as

$$r_{chain} = \frac{L_{chain}}{D_{chain}}, \quad r_{carpet} = \frac{A_{carpet}}{A'_{carpet}}. \quad (6.22)$$

The DVL altitude measurements are sensitive to the steepness of the sea floor. If the slope of the sea floor is larger than the angle between the horizontal plane and the DVL beams, 1 or 2 DVL altitude measurements will drop out depending on the DVL heading. Figure 6.4 shows a DVL with a 4 beam Janus configuration where  $\gamma_j = 30$  deg for all beams above a sea floor with slope of 80 degrees where 1 beam does not intersect with the sea floor. Note that the remaining 3 beams give a good approximation of the very steep sea floor. If the sea floor is discontinuous or has sharp edges, i.e. the assumption of continuous first-order partial derivatives is violated, the approximated sea floor will be filtered with the proposed method given in Section 6.3.2. Cliffs will look more like ramps and edges will be smoothed. Thus, the approximation method as proposed here, can be used for altitude control over rough terrain as well.

#### 6.4.1 Errors and Norms for Validation of the Sea Floor Approximation Method

The following errors and norms are defined in order to asses the performance of the sea floor approximation methods.

The instantaneous absolute altitude and gradient approximation errors are defined as

$$\tilde{a}_e = a - \hat{a}, \quad (6.23)$$

$$\tilde{\nabla}F = \|\nabla F - \hat{\nabla}F\|, \quad (6.24)$$

$$\cos \theta = \frac{\nabla F \hat{\nabla}F^T}{\|\nabla F\| \|\hat{\nabla}F\|}, \quad (6.25)$$

where  $\tilde{a}_e$  is the altitude approximation error,  $a$  is the true altitude and  $\hat{a}$  is the approximated altitude.  $\tilde{\nabla}F$  is the gradient error and  $\|\cdot\|$  is a vector length.  $\theta$  is the angle between the approximated and true gradient vector. The standard deviation of a series of absolute errors are noted  $\sigma_{\tilde{a}_e}$ ,  $\sigma_{\tilde{\nabla}F}$  and  $\sigma_\theta$ .

The instantaneous relative altitude and gradient approximation errors are defined as

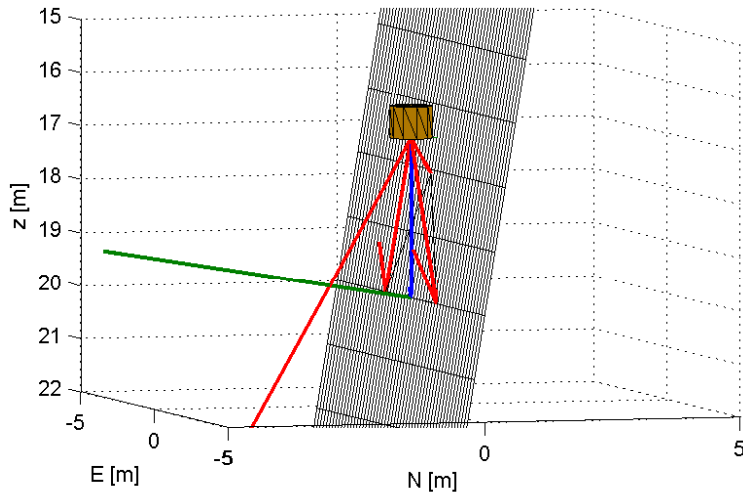


Figure 6.4: Too steep terrain for all DVL beams. One of the beams does not intersect with the sea floor but the remaining 3 beams give a good sea floor approximation.

$$\tilde{a}_{er} = \frac{a - \hat{a}}{a}, \quad (6.26)$$

$$\nabla \tilde{F}_r = \frac{\|\nabla F - \hat{\nabla F}\|}{\|\nabla F\|}. \quad (6.27)$$

The standard deviation of a series of relative errors are noted  $\sigma_{\tilde{a}_{er}}$  and  $\sigma_{\nabla \tilde{F}_r}$ .

The total absolute  $L^2$  error norms are

$$\|\tilde{a}_e\|_2 = \sqrt{\frac{1}{t_f - t_0} \int_{t_0}^{t_f} \tilde{a}_e^2 d\tau}, \quad (6.28)$$

$$\|\nabla \tilde{F}\|_2 = \sqrt{\frac{1}{t_f - t_0} \int_{t_0}^{t_f} \nabla \tilde{F}^2 d\tau}, \quad (6.29)$$

$$\|\theta\|_2 = \sqrt{\frac{1}{t_f - t_0} \int_{t_0}^{t_f} \theta^2 d\tau}, \quad (6.30)$$

where  $t_0$  and  $t_f$  are the start and end time respectively.

The total relative error norms are similarly

$$\|\tilde{a}_{er}\|_2 = \sqrt{\frac{1}{t_f - t_0} \int_{t_0}^{t_f} \tilde{a}_{er}^2 d\tau}, \quad (6.31)$$

$$\|\nabla \tilde{F}_r\|_2 = \sqrt{\frac{1}{t_f - t_0} \int_{t_0}^{t_f} \nabla \tilde{F}_r^2 d\tau}. \quad (6.32)$$

The reason for using both absolute and relative errors is that as the altitude increases, a higher tolerance on the absolute approximation error is acceptable for use in altitude control. Thus the absolute errors and norms show how the approximation accuracy deteriorates with increased altitude due to a larger DVL footprint. The relative error is useful to indicate if the sea floor approximation is sufficiently accurate to be used in altitude control. It should be noted that the true altitude and gradient must be known in order to calculate these errors. Hence, this is for use in simulations only, but it gives indications about what terrain and which altitudes the sea floor approximation methods are suitable for use in altitude control.

### 6.4.2 Approximation Modes

The performance of the approximation methods can be evaluated in three different modes of operation. These are (i) constant depth, (ii) exact constant altitude, and (iii) altitude control from a guidance law based on the approximated sea floor geometry. The first method has varying performance as the altitude can vary a lot over rugged terrain when the depth is constant. The second is of theoretical importance only as the sea floor geometry must be known and its contour followed exactly. However, this mode gives a good indication of the accuracy of the sea floor approximation for different altitudes over rugged terrain. In the third mode, the true altitude may vary as the altitude control is influenced by the approximation errors, dynamics of the guidance law and the depth controller. The ROV dynamics and bandwidth limitations are not considered in this analysis, but will complicate the problem further in a real implementation as the desired trajectory is obtained through closed-loop control.

#### Example: Exact Altitude over Rugged Terrain

This example shows the performance of the least squares linear approximation method by use of a DVL with 4 beams in a Janus configuration where  $\gamma_j = 30$  degs for all beams and  $\beta_j = 0, 90, 180, 270$  degs for  $j = 1, 2, 3, 4$ . The ROV moves horizontally 40 m straight forward while the altitude is exactly 2 m as seen in Figure 6.5. The red arrows shows a snapshot of the DVL beams, the green arrows are the true gradient vectors along the transect, and the blue arrows are the approximated gradient vectors. The area-based rugosity of the sea floor in Figure 6.5 is  $r_{carpet} = 1.42$ , and the chain tape rugosity along the transect is  $r_{chain} = 1.22$ . This indicates a fairly rugged terrain. The sea floor profile ( $z_{sf}$ ) of the transect is seen in the top plot in Figure 6.6a together with the profile of the approximated sea floor ( $\hat{z}_{sf} = \hat{z} + \hat{a}$ ) and the ROV trace ( $z$ ). The lower plot shows

Table 6.1: Altitude and gradient approximation  $L^2$  error norms with altitude, 1-5 m.

$a$ [m]	1	2	3	4	5
$\ \tilde{a}_e\ _2[m]$	0.0636	0.2040	0.5982	0.9301	1.1617
$\ \tilde{a}_{er}\ _2[-]$	0.0636	0.1020	0.1994	0.2325	0.2323
$\ \tilde{\nabla F}\ _2[-]$	0.1962	0.2884	0.3790	0.4863	0.6069
$\ \tilde{\nabla F}_r\ _2[-]$	0.0886	0.1361	0.1822	0.2380	0.3005
$\ \theta\ _2[rads]$	0.0736	0.1156	0.1466	0.1830	0.2333

the approximation error,  $\tilde{a}_e$ , and the tracking error  $\tilde{a}$ , which is zero as the approximation mode for constant altitude (ii) is used. Note that the largest approximation error of the sea floor occurs as the ROV goes over the ridge (ca. N=2 m) and one of the DVL beams does a jump in magnitude. The approximated sea floor gets a spike even though the sea floor is smooth. This can happen if the terrain has slope larger than the angle between the horizontal plane and the DVL beams (60 degrees) or if the sea floor is discontinuous, e.g. for cliffs.

The true and approximated sea floor slopes are seen in the top plot in Figure 6.6b. The gradient approximation error is seen in the lower plot.

The simulated altitude run is done over the same transect as seen in Figure 6.5 with altitudes of 1, 2, 3, 4 and 5 m as well. The expected increase in the  $L^2$  approximation error norms with altitude is seen in Table 6.1, which shows the error norms as calculated from 6.28, 6.29, 6.30, 6.31, and 6.32 for exact constant altitudes from 1 to 5 m. Note that the absolute altitude norms increase faster than the relative altitude error norms with altitude. However, an increase in the approximation errors with increased altitude is less critical since the risk of collision is reduced at higher altitudes. Increasing the altitude gives a form of low-pass filter effect on the approximated sea floor geometry. The gradient error also increases with altitude in this case. Most of the increase in the error norms is from the part where the ROV moves over the center ridge.

## 6.5 Altitude Estimation

The previous sections considered how to use the DVL to approximate the sea floor based on the DVL beams and geometry. As these are acoustic beams, the measurements are affected by noise. Although the noise is reduced by the proposed least squares approximation method, the approximated altitude can be discontinuous. This is the case if the ROV runs off a cliff. To assure a continuous and smooth estimated altitude suited for feedback to the depth guidance law, an altitude observer is proposed.

This section propose an observer for altitude estimation where the approximated altitude and altitude rate of change obtained from the DVL beam measurements are inputs. As the expression for altitude rate of change also involves the estimated states of the vehicle, this observer runs in cascade with the vehicle observer. The vehicle observers are

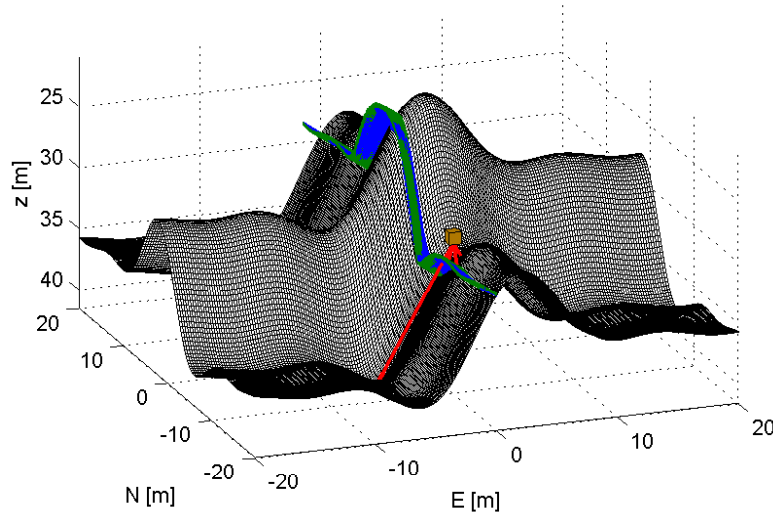
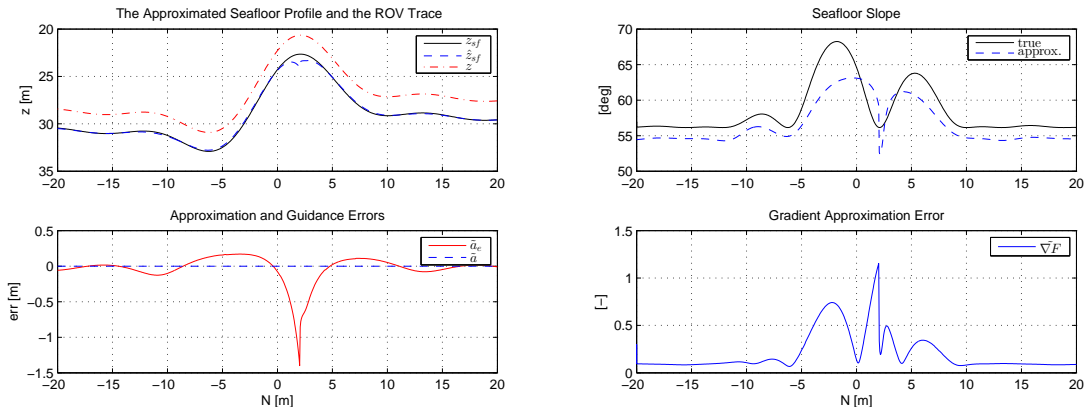


Figure 6.5: ROV over rugged terrain; sea floor approximation along a transect. Snapshot of DVL beams (red), approximated gradient vectors (blue) and true gradient vectors (green).



(a) ROV over rugged terrain; sea floor profile, sea floor approximation and errors. (b) ROV over rugged terrain; sea floor gradient approximation (upper) and errors (lower).

Figure 6.6: ROV over rugged terrain. Sea floor geometry approximation.

given in Chapter 4. However, the altitude observer itself is a pure kinematic observer with position and velocity as inputs. Figure 6.7 shows the signal flow to the kinematic altitude observer. The vehicle observer outputs the estimated generalized position and velocity,  $\hat{\eta} = [\hat{p} \ \hat{\Theta}]^T$ ,  $\hat{\nu} = [\hat{v} \ \hat{\omega}]^T$ , where  $\hat{\omega} = [p \ q \ r]^T$  is the turn rate vector for roll, sway and yaw respectively.  $a^d$  is the vector with the 4 DVL beam altitude measurements as given in Section 6.2,  $a_m$  is the approximated altitude obtained from one of the sea floor

approximation methods, or an altimeter.  $\dot{a}_m$  is the altitude rate of change obtained from (6.10) with the estimated vehicle states.  $\hat{a}$  is the estimated altitude.

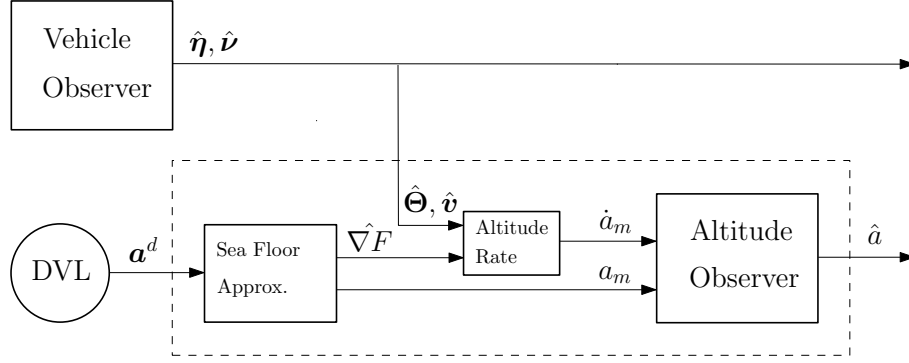


Figure 6.7: The altitude observer in cascade with the vehicle observer.

The measurement equations for the altitude observer are given as

$$a_m(k) = a(k) + v(k), \quad (6.33)$$

$$\dot{a}_m(k) = \dot{a}(k) + w(k), \quad (6.34)$$

where  $w(k)$  and  $v(k)$  are noise processes.

Using the Euler integration method, the discrete time control plant model (CPM) equations are given as

$$a(k+1) = a(k) + \dot{a}(k)h \quad (6.35)$$

$$= a(k) + \dot{a}_m(k)h - w(k)h, \quad (6.36)$$

$$y(k) = a_m(k) \quad (6.37)$$

$$= a(k) + v(k), \quad (6.38)$$

where  $h$  is the time step.

The CPM equations are reformulated to the notation used in [40] in (6.39) and (6.40) as

$$x(k+1) = \Phi x(k) + \Delta u(k) + \Gamma w(k), \quad (6.39)$$

$$y(k) = Hx(k) + v(k), \quad (6.40)$$

where  $x = a_m, u = \dot{a}_m, \Phi = 1, \Delta = h, \Gamma = -h, H = 1$ . An observer made by copying the dynamics in (6.39) and (6.40) should be used to estimate the altitude. A Kalman filter is used in the implementation of the altitude observer in the control system described in Chapter 3.

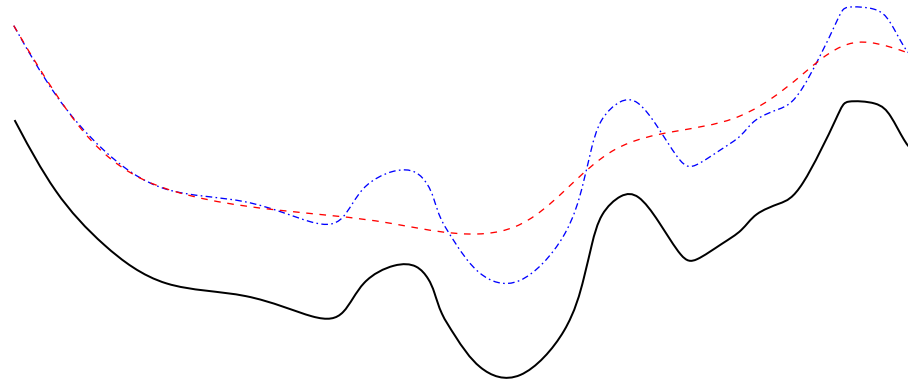


Figure 6.8: Fine contouring (blue) and platforming (red) trajectories over a rugged sea floor.

## 6.6 Guidance Laws for Altitude Control

Guidance laws for altitude control are proposed in the following. These guidance laws are part of the guidance system for the motion control system in Chapter 3, together with the guidance methods proposed in Chapter 5. First, definitions of altitude control are given, and control objectives are formulated.

**Definition 6.6.1.** In altitude control, the vehicle depth is controlled to obtain a desired altitude while the horizontal trajectories are controlled independently.

### 6.6.1 Control Objectives for Altitude Control

The main control objective during altitude control is to follow a fine or coarse contour of the sea floor. It is also important to avoid collision with the sea floor. As the vehicle has limited bandwidth in heave, it is not possible to follow any sea floor contour at any speed. This leads to two different ways of approaching the altitude control problem. (i) Fine contouring is achieved by regulation of the horizontal velocities so the desired heave velocity is within the vehicle's capabilities. (ii) Coarse contouring or platforming is achieved by filtering the sea floor contour to be tracked so the vehicle can run at constant horizontal velocity without exceeding the vehicle's limitation for vertical motions. Figure 6.8 shows the two approaches. The black line is the rugged sea floor profile, the blue and red lines are the ROV vertical trajectories during altitude control based on objective (i) fine contouring (blue) and (ii) platforming (red).

### 6.6.2 Guidance Law for Altitude Control

Depth measurements are usually more reliable than altitude measurements. As depth is a state of the ROV, altitude control should be obtained via a depth reference to a depth controller. This choice is also a stability concern as the depth of the ROV is always continuous but the altitude can be discontinuous. Therefore, the altitude should not be directly input to a feedback position controller. A general guidance law for the depth

reference to obtain a desired altitude is presented in this section. Modifications needed to satisfy the control objectives (i) and (ii) for altitude control are then proposed.

The relationship between the ROV motions, the sea floor gradient and the altitude rate of change is given in (6.10). This can be exploited in a feedforward term in the guidance law by setting (6.10) equal to the desired altitude rate of change as seen in (6.41). The desired heave velocity,  $w_{d,ff}$ , corresponding to the desired altitude rate is found by solving (6.41) for  $w$ .

$$\begin{aligned}\dot{a} &= \nabla F(\mathbf{p}) \cdot \mathbf{R}_b^n(\Theta_{nb}) \mathbf{v} \\ &= \left[ \frac{\partial f}{\partial x} \Big|_{x_p, y_p}, \frac{\partial f}{\partial y} \Big|_{x_p, y_p}, -1 \right] \mathbf{R}_b^n(\Theta_{nb}) \begin{bmatrix} u \\ v \\ w \end{bmatrix} = \dot{a}_d.\end{aligned}\quad (6.41)$$

The desired depth velocity is simplified in the case for zero roll and pitch according to

$$w_{d,ff} = \left[ \frac{\partial f}{\partial x} \Big|_{x_p, y_p}, \frac{\partial f}{\partial y} \Big|_{x_p, y_p} \right] \mathbf{R}_b^n(\psi)(3; 3) \begin{bmatrix} u \\ v \end{bmatrix} - \dot{a}_d, \quad (6.42)$$

where  $\mathbf{R}_b^n(\psi)(3; 3) \in \mathbb{R}^{2 \times 2}$  denotes the submatrix formed by deleting the 3<sup>rd</sup> row and column of  $\mathbf{R}_b^n(\psi)$ . Eq. (6.42) may be used for a ROV which has only small deviations from zero roll and pitch. This leads to a new guidance law in (6.43) and (6.44) for desired depth as

$$\begin{aligned}w_d &= \left[ \frac{\partial f}{\partial x} \Big|_{x_p, y_p}, \frac{\partial f}{\partial y} \Big|_{x_p, y_p} \right] \mathbf{R}_b^n(\psi)(3; 3) \begin{bmatrix} u \\ v \end{bmatrix} - \dot{a}_d \\ &\quad + k_p(a - a_d) + k_i \int_0^t (a - a_d) d\tau,\end{aligned}\quad (6.43)$$

$$z_d = \int_0^t w_d d\tau + z_{ic}, \quad (6.44)$$

where  $a_d$  is the desired altitude,  $\dot{a}_d$  is the desired altitude rate, and  $z_{ic}$  is the initial depth when altitude control is enabled. The exact tracking error is  $\tilde{a} = a - a_d$ , and the approximated tracking error is  $\tilde{a}_t = \hat{a} - a_d$ .  $\tilde{a}_t$  is used in the guidance law in real implementations as  $a$  is unknown. The altitude guidance error  $\tilde{a}_g = z_{sf} - z_d - a_d$  is introduced to separate the altitude error caused by the guidance law from that caused by the depth controller. This is only useful for simulations as the exact sea floor geometry must be known.

For cases including roll and pitch, the desired heave velocity must be transformed to NED before (6.44) is applied. The proportional and integral feedback terms in (6.43) is from [12], and the feedforward term is a new result. The feedback terms are needed to compensate for inaccuracies in the sea floor gradient estimation and vehicle state estimates, initial altitude errors and tidal water. The feedforward term is very important

as it assures a sufficient desired heave velocity for any horizontal velocity, heading and steepness of the sea floor.

Without the feedforward term, the tracking performance is reduced, and the ROV can collide with the sea floor while going uphill or overshoot downhill. The feedforward term's main advantage over the integral term is that it responds instantly to any changes in vehicle velocity or changes in the terrain. The integral term has dynamics and needs time to charge and empty.

Take for example the case where the vehicle comes to a stop after moving at constant desired altitude over a slope. If only the integral term is used to remove steady state altitude errors, then the desired heave velocity will not go to zero immediately, and an altitude error occurs. The magnitude and duration of the poor performance after the stop depends on the integrator time constant. If the feedforward term is used, then the desired heave velocity will be zero just as the vehicle stops and the desired altitude is maintained. If both feedforward and integral action are used, the integral term will be small as most of the error is taken care of by the feedforward term. Thus, the integrator wind-out effects are less profound on the desired depth. Similar effects are observed for changes in velocity or changes in the sea floor geometry.

It is difficult to determine the performance and obtain stability results for the closed-loop system from desired altitude to actual altitude that are general for all types of sea floor geometry, ROV altitude and horizontal velocity. However, it is possible to assess the performance and stability of the inner depth control loop and the interconnections to the outer altitude guidance loop for special cases of known sea floor geometry. This is done in Appendix D. For linearized ROV dynamics and a plane sea floor, it is trivial to find the closed-loop transfer function from desired altitude to actual altitude. Such analysis will show that the stability is most sensitive to the altitude guidance law gains  $k_i$  and  $k_p$ . Two poles of the closed-loop transfer function will move over to the right half-plane if  $k_i$  and/or  $k_p$  are too high, and the system becomes unstable.

A comparison of the tracking performance of the guidance law in (6.44), with and without the feedforward term, is seen in Figure 6.9 for a case with  $k_p = 0.5$  and no integral term. The ROV moves in surge at 0.5 m/s straight North, and the desired altitude is 2 m. The top plot shows the sea floor profile together with the desired ROV depths with and without the feedforward term for perfect depth control ( $z = z_d$ ).  $z^0$  is without feedforward, and  $z^{ff}$  is with. It is seen that the  $z^0$  trace almost collides with the sea floor at N=-1 m. This would have been a collision for higher surge speed, steeper terrain or lower  $k_p$  in the no feedforward case. The  $z^{ff}$  trace goes smoothly over the ridge with only small altitude tracking errors. The middle plot shows the approximation error for the two cases. The approximation error is less for the  $z^0$  case because it gets very close to the sea floor in the roughest part of the terrain. The lower the altitude, the better the sea floor approximation will be due to the smaller footprint of the DVL beams. However, as seen in the lower plot, the tracking error of the guidance law is much better with the feedforward term.

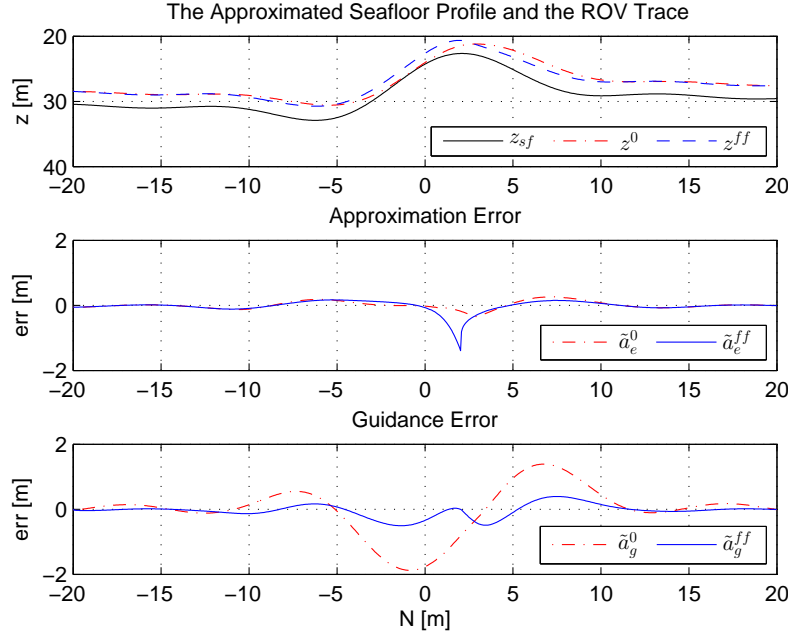


Figure 6.9: Effect of the feedforward term on the desired trajectory at 0.5 m/s and 2 m desired altitude.  $z_{sf}$  is the sea floor,  $z^0$  is the ROV depth for the case without feedforward term and  $z^{ff}$  is the ROV depth with the proposed feedforward term (upper).  $\tilde{a}_e^0$  and  $\tilde{a}_e^{ff}$  are the approximation errors for the cases without and with the feedforward term, respectively (middle).  $\tilde{a}_g^0$  and  $\tilde{a}_g^{ff}$  are the altitude guidance errors without and with the feedforward term, respectively (lower).

### 6.6.3 Sea Floor Collision Avoidance

Some interesting collision avoidance properties are obtained if the feedforward term in the guidance law (6.43) gets the gradient from the proposed sea floor approximation method. Although the main objective of altitude control is to maintain a desired altitude, it is more important to avoid collision with the sea floor, i.e. keep  $z_d < z_{sf}$ . Because of the DVL beam geometry, the DVL beam footprint on the sea floor decreases for lower altitudes. Hence, the local sea floor approximation improves with lower altitude as seen in (6.45) and (6.46).

$$\lim_{a \rightarrow 0} \hat{\nabla} F \rightarrow \nabla F, \quad (6.45)$$

$$\lim_{a \rightarrow 0} \hat{a} \rightarrow a. \quad (6.46)$$

E.g. if the actual altitude becomes lower than the desired altitude due to altitude approximation errors or poor depth control, the following desired depth trajectory will always be above or on the sea floor when the feedforward term is used alone or with the proportional term. This is because the sea floor gradient underneath the DVL is perfectly approximated as the DVL is just above the sea floor. Then, the desired heave velocity

feedforward term in (6.43) inserted in (6.10) gives zero altitude rate of change and the desired depth will stick to the sea floor if only the feedforward term is used. With the addition of the proportional term, the desired depth will move towards the depth corresponding to the desired altitude again. Note that  $z_d \leq z_{sf}$  does not hold if the integral term is used due to wind-up effects. It should be noted that these considerations do not apply directly to real implementations as a DVL does not give altitude measurements below its minimum range, typically 0.25 to 1 m. Also note that the ROV has volume so parts of it may collide with the sea floor even though  $a > 0$  when the altitude definition 6.1.1 is used. However, the important message is that the improvement of the sea floor approximation with lower altitude greatly reduces the risk of collision with the sea floor. In addition, the desired trajectory from the feedforward term converges to the sea floor tangentially. The latter may reduce the consequences in case of a collision.

### 6.6.4 Speed Reduction, Contouring and Platforming

It should be noted that if the ROV moves fast over a steep or rugged sea floor with altitude control, the ROV may not be able to follow the desired depth generated by (6.44). In that case a feedback to the horizontal speed guidance law will assure that the desired depth reference is within the ROV capabilities. A solution to this is proposed next.

#### Fine Contouring

During fine contouring, the horizontal velocities may have to be adjusted according to the sea floor and the vehicle's heave dynamics. The speed correction law presented here is based on a tracking supervisor which monitors the vertical motion errors. This is best used in combination with a guidance law where the desired speed is an input, e.g. line of sight (LOS). For a position feedback controller, the resulting desired position must also be corrected. Figure 6.10 shows the control loop during altitude control when LOS is used for horizontal guidance. The output of the LOS block is the desired surge and sway velocities and heading. These desired states are input to the controller together with the desired depth and heave velocity from the altitude guidance block. The vehicle states  $\eta$  and  $\nu$  are estimated by the vehicle observer. The altitude and sea floor gradient are estimated by the altitude observer. Note the multiplicative feedback to the desired speed,  $U_d$ , where  $\Gamma \in [0, 1]$  is a reduction function that reduces the speed if the ROV can not follow the desired depth trajectory.

#### Tracking Supervisor and Speed Reduction

A tracking supervisor monitors the vertical tracking errors and calculates a speed reduction function in order to adjust the horizontal velocity if needed. The heave velocity and depth monitoring errors are

$$\tilde{w} = w - w_d, \quad (6.47)$$

$$\tilde{z} = z - z_d. \quad (6.48)$$

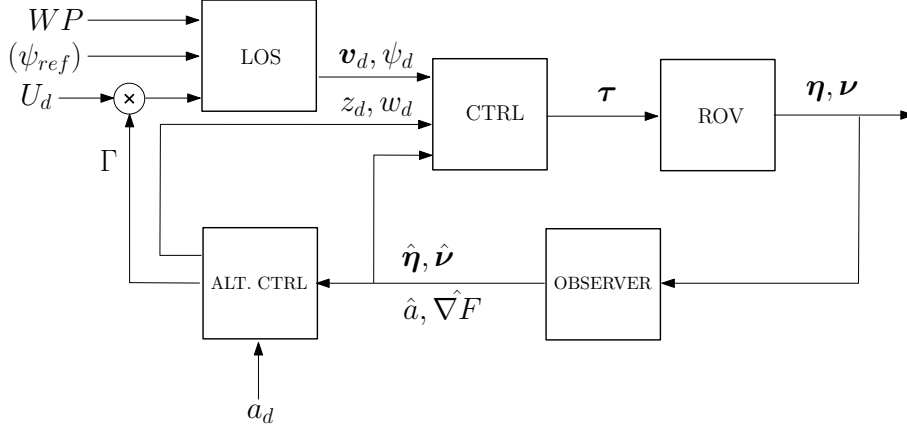


Figure 6.10: Feedback to the horizontal guidance system during altitude control.

Thus, the tracking error vector is  $\mathbf{e} = [\tilde{w}, \tilde{z}]^T$  and the speed reduction function is given as

$$\Gamma = \begin{cases} 1 & \text{if } e < e_{tol}, \\ \frac{1}{e_{max}-e_{tol}}(e_{max} - e) & \text{if } e_{tol} \leq e \leq e_{max}, \\ 0 & \text{if } e > e_{max}, \end{cases} \quad (6.49)$$

where  $e = \sqrt{\mathbf{e}^T \mathbf{Q} \mathbf{e}}$  is the weighted tracking error, and  $\mathbf{Q} \in \mathbb{R}^{2 \times 2}$  is a diagonal weight matrix with diagonal elements  $q_1, q_2 \in [0, 1]$ .  $e_{tol}$  and  $e_{max}$  are the error tolerance and maximum error, respectively. The error tolerance before the speed is reduced is introduced to avoid continuous speed variations for small errors. Smaller  $e_{max}$  will give a more aggressive speed reduction.

An example of the effect of the speed reduction function is seen in Figure 6.11. The top plot shows the sea floor, desired depth and actual depth trajectories when closed-loop control in heave is used. The bottom plot shows the desired and actual heave velocity in addition to the surge velocity with speed reduction. The desired surge speed is  $u_d = 0.5$  m/s,  $e_{tol} = 0.05$ ,  $e_{max} = 0.5$  and  $\mathbf{Q} = \mathbf{I}_{2 \times 2}$ . The simulated heave dynamics are from the model of ROV Minerva, given in Chapter 2. The maximum vertical thrust is set to 360 N, which gives a maximum heave velocity of about 0.6 m/s. The ROV moves straight North over the same transect as in the previous simulation examples. As the sea floor becomes steeper at ca. N=-4 m, the ROV is unable to follow the desired heave velocity. The tracking error increases and the surge speed is reduced. The surge speed reduction will reduce the desired heave velocity as well, and the ROV is again able to follow the desired trajectory over the sea floor. The ROV would have collided into the sea floor without the speed reduction function in this case.

### Coarse Contouring/Platforming

If constant horizontal velocity is of greater importance than accurate altitude tracking, the contour to be tracked should be filtered so the ROV can follow the trace at the desired

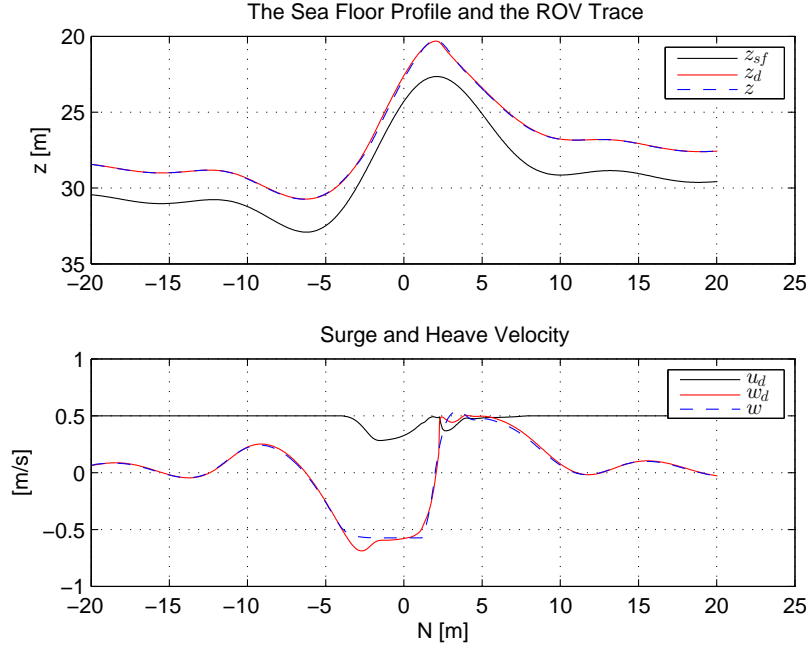


Figure 6.11: The sea floor profile ( $z_{sf}$ ), desired ( $z_d$ ) and actual depth ( $z$ ) trajectories (upper). The surge ( $u$ ) and desired ( $w_d$ ) and actual ( $w$ ) heave velocities with speed reduction (lower).

horizontal velocity. It is desirable to use information about the sea floor ahead of the ROV in order to take advantage of preview control. This has been explored for AUVs in e.g. [81]. However, the methods described in this paper are restricted to DVL measurements with limited preview capability especially for low altitudes. The proposed method to enable coarse contouring or platforming is to modify the depth guidance law in (6.43) and (6.44). The desired heave velocity is filtered by a first order low pass filter,  $h_{lp}(s)$ , before the integration in (6.44). The modification of the desired heave velocity is seen in (6.50).

$$w_{d_{lp}} = h_{lp}(s)w_d, \quad (6.50)$$

where  $s = i\omega$  is the Laplace variable. The low-pass filter can be designed as

$$h_{lp}(s) = \frac{1}{1 + T_w s}, \quad \omega_b < \frac{1}{T_w}, \quad (6.51)$$

where the time constant  $T_w$  should be set so the desired heave velocity is within the bandwidth of the ROV heave controller,  $\omega_b$ .

The speed reduction feedback should still be enabled during platforming to avoid collisions with the sea floor in steep terrain. However, it will be less active as the ROV should be able to track the low-pass filtered depth trajectory over rugged terrain. Care

should be taken as the filtered desired trajectory may cause the ROV to collide with the sea floor.

## 6.7 Experimental Results with Altitude Control

Full scale test results demonstrating the performance of the proposed altitude estimation and guidance methods are presented in this section. The tests were conducted in the Trondheimsfjord, Norway with the ROV Minerva. The developed control system from Chapter 3 was used in the sea trials. A Teledyne RDI Workhorse Navigator DVL (1200 kHz) mounted in the stern at 45 degrees in yaw was used and the ROV was positioned by a HiPAP 500 system on board the RV Gunnerus. During the tests, the ROV moved back and forth over a 100 m transect going straight from West to East under closed-loop control of all DOFs. Figure 6.12 shows the ROV positions for a test run. The top plot shows the ROV’s estimated, measured and desired positions on the transect and snapshots of the ROV outline taken every 11<sup>th</sup> second. The bottom plot shows the ROV depth trace as it moves uphill from East to West over the approximated sea floor profile,  $\hat{z}_{sf}$ , with a desired altitude of 2 m. The top plot in Figure 6.13 shows the DVL altitude measurements,  $a^d$ , during the test run with Teledyne RDI beam numbering. The bottom plot shows the corresponding approximated sea floor gradient vector obtained by the least squares approximation method.

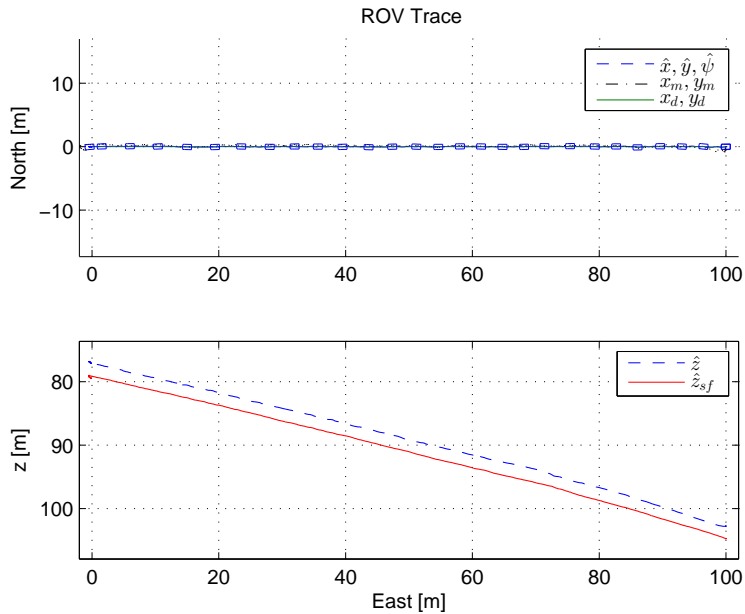


Figure 6.12: The ROV horizontal trace where  $(\hat{x}, \hat{y}, \hat{\psi})$  is the estimated position and heading,  $(x_m, y_m)$  is the measured position, and  $(x_d, y_d)$  is the desired position (upper).  $z_{sf}$  is the approximated sea floor profile, and  $\hat{z}$  is the estimated depth trajectory while going uphill, East to West (lower).

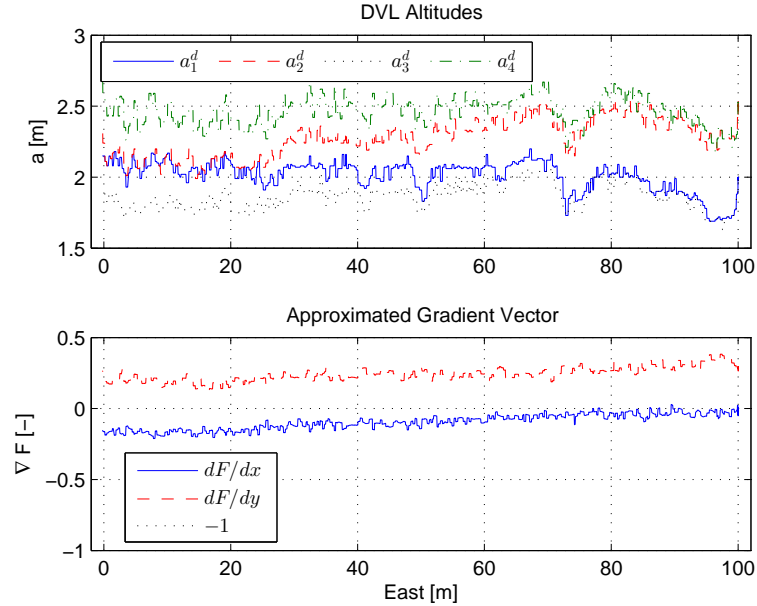
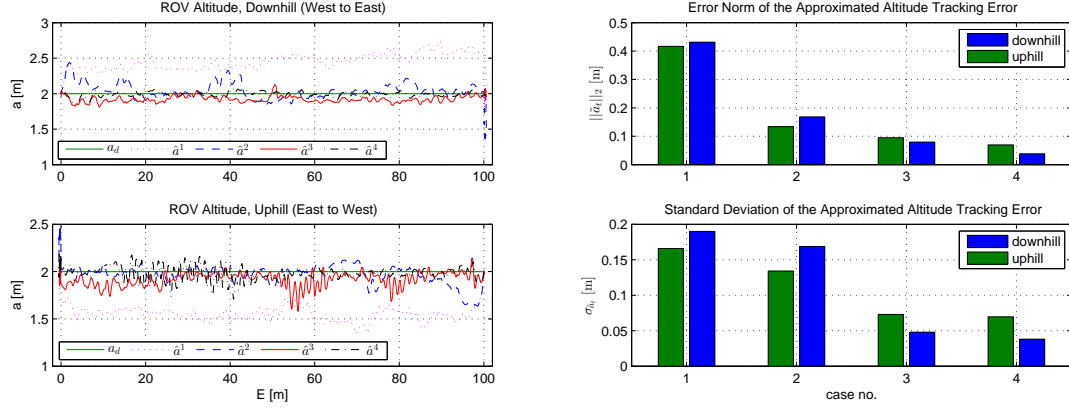


Figure 6.13: The DVL altitude measurements for beam no. 1, 2, 3, 4 (upper), and the components of the approximated gradient vector (lower).

Two tests are presented. In the first test, the altitude tracking performance is compared for different settings of the proposed guidance law. The desired altitude is 2 m and the surge speed is 0.3 m/s for all cases and each case is tested both downhill and uphill (West-East-West). 4 cases are run where case 1 is with proportional term only,  $k_p = 0.2$ , case 2 is with proportional and integral terms,  $k_p = 0.2, k_i = 0.01$ , case 3 is with proportional and feedforward terms,  $k_p = 0.2, ff$ , and case 4 is with all terms,  $k_p = 0.2, k_i = 0.01, ff$ .  $ff$  means that the proposed feedforward term is used. The main objective of this test is to show the effect of the proposed feedforward term. The selected  $k_p$  and  $k_i$  gains are obtained from a trial and error tuning procedure performed prior to the presented experiments. A tip for the tuning is to start with  $k_p$  as half of the maximum heave velocity of the underwater vehicle. This is assuming that the depth error can be maintained less than ca. 0.1-0.2 m.  $k_i$  should be small, and the better the sea floor approximation is, the smaller  $k_i$  and  $k_p$  should be.

In the second test, the altitude tracking performance is compared for desired altitudes from 1 to 5 m with the guidance law settings from case 4 in test no. 1. The surge speed is 0.3 m/s for all desired altitudes. The main objective of this test is to compare the tracking performance for lower and higher desired altitudes. Results from test no. 1 are shown in Figures 6.14a and 6.14b and results from test no. 2 are in Figures 6.15a and 6.15b.

The top plot in Figure 6.14a shows the estimated altitude vs. East position for case 1-4 as the ROV moves over the transect from West to East while going downhill. Note that the altitude is ca. 0.5 m greater than the desired altitude in case 1. With only the proportional term, an altitude tracking error is needed to produce a desired heave velocity. Hence, there will be a steady state offset in the altitude that depends on the horizontal speed of



(a) Altitude trajectories.  $a_d$  is the desired altitude and  $\hat{a}^1$ ,  $\hat{a}^2$ ,  $\hat{a}^3$ ,  $\hat{a}^4$  are the estimated altitudes for case no. 1-4.  
(b) The  $L^2$  error norm and standard deviation of the approximated altitude tracking error for 4 different guidance law settings.

Figure 6.14: Comparison of the altitude tracking performance for 4 different settings of the guidance law. Constant desired altitude of 2 m.

the ROV, the sea floor steepness and gain  $k_p$ . With the addition of an integral term in case 2, the steady state altitude tracking error is reduced shortly after start. However, as the ROV stops, it takes time to empty the integrator to reduce the desired heave velocity. This results in an altitude tracking error. The integrator term can produce altitude tracking errors in case of horizontal speed changes or variations in the terrain. There is little terrain variation over the test transect, so these effects are difficult to see in the test results. However, the tracking error around 40 m East in case 2 (downhill) could be a result of the integral term and terrain variation.

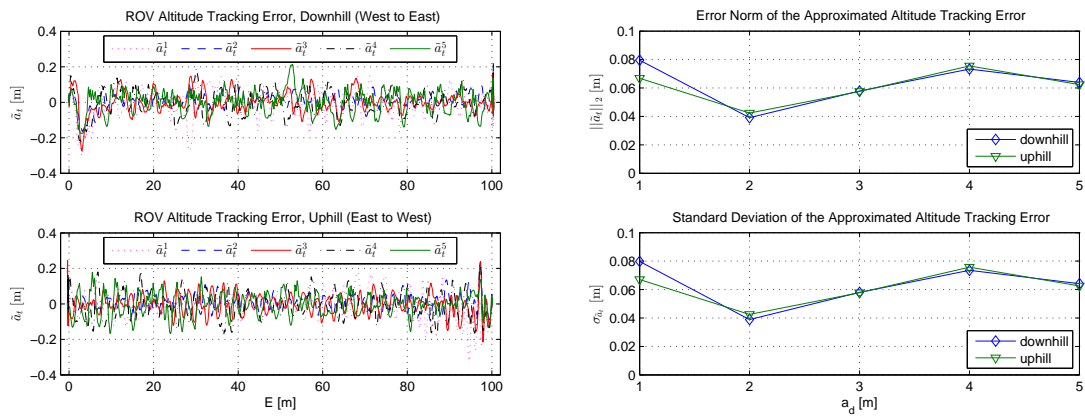
The addition of the proposed feedforward term gives good results as seen in case 3. Note that the altitude tracking performance is good during all stages from start to constant surge velocity to stop at the end of the transect. This is the strength of the feedforward term over the integral term; it produces the right desired heave velocity also for speed changes and terrain variation if the approximated gradient is accurate. The integral term is added again in case 4, but its effects are less profound as the altitude tracking errors are greatly reduced by the feedforward term.

The bottom plot in Figure 6.14a shows the same type of results as the top plot, but the ROV is going uphill from East to West. Similar behavior for the 4 cases are observed as for going downhill. However, the steady state offset in case 1 is negative because a negative desired heave velocity is needed to maintain a constant altitude while going uphill. It should also be noted that the DVL altitudes are greater uphill than downhill as the DVL is mounted in the stern. It is seen that in case 3 some oscillations in the altitude occurs between 50 and 70 m East and around 80 m East. Such oscillations have been observed when an initial error in the depth tracking occurs due to e.g. a taut cable. As this also causes an altitude error, the following desired depth can be quite oscillating if the vehicle is unable to follow it. The depth controller starts chasing the guidance law which

responds by making a more oscillatory desired depth if the vehicle is unable to follow the desired depth trajectory. The effects of this instability can be reduced by the use of speed reduction as proposed in Section 7.4. However, the speed reduction mode was not used during the sea trials.

The  $L^2$  error norm and the standard deviation of the altitude tracking error  $\tilde{a}_t$  are shown in Figure 6.14b for the 4 cases. Note that the error norm over the transect is greatly reduced by the feedforward term in case 3. Although the error norm for case 3 (feedforward) is lower than case 2 (integral), the difference would have been even greater for a shorter move on the transect as the tracking performance for case 3 is superior during the start and stop stages. It is seen from the standard deviation in the lower plot that the variance in the tracking performance is reduced by the feedforward term as well in case 3 and 4. Case 4 gives the best altitude tracking performance using the  $L^2$  norm and the standard deviation as performance indices. However, for a run over a transect with more terrain variation and speed changes, case 3 is likely to give better performance.

The altitude tracking errors for test no. 2 with desired altitudes from 1 to 5 m are seen in Figure 6.15a. The top plot shows errors for the downhill runs and the bottom plot shows uphill runs. For this transect there is not a clear relationship between the desired altitude and the tracking performance as seen in Figure 6.15b where the  $L^2$  error norm and the standard deviation of the altitude tracking error  $\tilde{a}_t$  are shown vs. the desired altitude. The small terrain variation can be an explanation. As the altitude is increased, so is the DVL footprint and the sea floor approximation accuracy is expected to decrease. However, for a linear sea floor, altitude does not affect the approximation accuracy. At least when differences in the acoustic properties in the water column are neglected. Note that the  $L^2$  error norm and the standard deviations are almost identical for all altitudes. It is seen that the altitude tracking performance is fairly good and consistent, both up- and downhill, for all altitudes.



(a) Altitude tracking error for desired altitudes from 1 to 5 m ( $\tilde{a}_t^1$ - $\tilde{a}_t^5$ ). (b) The  $L^2$  error norm and standard deviation of the approximated altitude tracking errors.

Figure 6.15: Comparison of the altitude tracking performance for altitudes from 1 to 5 m.

## 6.8 Conclusion and Further Work on Terrain Following

The work on altitude control and terrain following in this thesis has focused on sea floor geometry approximation and a guidance law for depth control to obtain a desired altitude.

The altitude control can be improved by enabling better preview. This requires that the sea floor ahead of the vehicle is observed.

More advanced terrain following features can be obtained by coupling information about the sea floor geometry to the horizontal motion guidance system of the ROV. E.g. the ROV can automatically follow the steepest decent or track a contour line. Pipeline tracking is another practical application where altitude control is needed.

# **Chapter 7**

## **Ocean Science Research Campaigns**

Field trials, implementation and practical experiments with ROVs have been important in the work with this thesis. The purpose of this Chapter is (i) to show how the experiments affect and contribute to the scientific work in the thesis. (ii) show how the results, when implemented in the control system, contribute to other ocean sciences and (iii) give insight to how the experiments were conducted.

The first field trial with the ROV Minerva and RV Gunnerus was done in the spring of 2010. Since then, there have been several cruises for testing of the motion control system and for using the ROV as a tool for researchers in ocean sciences. In the period from the spring of 2010 to fall 2013, there have been about 6 short cruises every year of 2 days duration, and 2 long annual 5 day cruises. The short cruises have been used for testing of the motion control system and to study coral reefs, kelp forests, wreck sites, etc. in the vicinity of the Trondheim harbor. The long cruises have had a specific research objective where several surface and underwater vehicles have been involved. Some of the experiments in these cruises are described in more detail in this Chapter. In addition, the ROV 30 k, with the developed motion control system, has been used in an inspection job for Shell outside the Nyhamna gas terminal. Experimental data from this survey is shown as well.

### **7.1 The Value of Experimental Testing**

An important aspect of doing experiments with ROVs is to get experimental data that are used to validate the proposed theories for guidance, navigation and control. However, this is not a open-loop process that ends with experimental data to be shared with the scientific community. Much of scientific work in this thesis come from, and are inspired by problems discovered in sea trials and research campaigns for marine biology, archeology and geology. This is shown in the following.

#### **7.1.1 Research Motivated by Sea Trials**

Some examples of research topics in this thesis that are directly inspired from experiences from sea trials are listed below.

- The work on sensor-based observers in Chapter 4 was initiated because of the poor performance of the model-based Kalman filter during manipulation tasks.
- The joystick in closed-loop control proposed in Chapter 5 was inspired by observing the differences in the performance of ROV operations depending on the pilot. Specific features, such as the cylinder mode, was added based on experience with ROV tasks needed in the real missions.
- The work with altitude control and terrain following in Chapter 6 was initiated because of the need to maintain a constant distance to the sea floor during video and photomosaic surveys. The solutions came from knowledge of ROV sensors and their practical use.

Having the ability to do experiments, and to make the ROV move like you want it to, is a great motivation for doing the scientific work. The feedback from how other researchers use the ROV and their needs is also valuable when it comes to finding real problems that needs to be solved. Without user feedback, the pure engineer or scientist may come up with a good solution, but there is no problem.

### 7.1.2 Lessons Learned

In addition to inspiration and motivation, several lessons have been learned from the sea trials. Some important lessons are

- It is necessary to have a plan B when minor surprises and faults make the first plan impossible to execute. Time is scarce while on the ship, and it takes a lot of people and resources to run the ROV operations. Therefore, if something fails, you still need to be able to use the time on the vessel to produce results.
- Thorough preparations are key for a successful cruise. Before testing of new features in the control system, they must have passed the HIL test before use in sea trials. If new sensors are required, they must be installed on the ROV and calibrated on shore before the cruise.
- Cruises for testing of new technology related to guidance, navigation and control of the ROV should be separated from the ocean science cruises. It is never a good idea to test out a new feature of the motion control system in a mission where a biologist or archeologist is using the ROV as a tool. Even though the new feature worked great in the HIL test, there is always something unexpected happening in the first sea trail. It is better to test out new features without others depending on it to work the same day.
- It is important to test the control system in different locations and under varying environmental conditions. In the beginning, we mostly tested the motion control system at the same location close to the harbor to save steaming time, as we did

not need a special location to study for the tests. This was a location with shallow water, fairly smooth sea floor, low ocean current and good conditions for the acoustic positioning system. The ROV could track the desired patterns with great accuracy, over and over again. When the system was to be used in science missions for studying coral reefs, vertical walls or deep water wrecks, the performance of the control system was not the same as for the well known test location. Strong ocean currents over coral reefs would lead to thruster saturation, DVL out of range for vertical wall surveys degraded the performance of the motion control system, and cable forces for deep water mission altered the dynamics and degraded the performance as well. However, new topics for further research, in order to develop a robust motion control system for the entire ocean space, are discovered from these experiments.

- The search for perfection can hinder progress. This applies especially to the tuning of observers and controllers. You can only spend so much time on tuning as you are using valuable time for the actual tests or missions. At some point the tuning must be accepted as sufficient, and the planned tests must be conducted. The same goes for modeling. There is no point in spending days finding the perfect model coefficients as they will be off once the ROV is equipped with new instruments or other pay loads. Go for robustness in the control design instead.

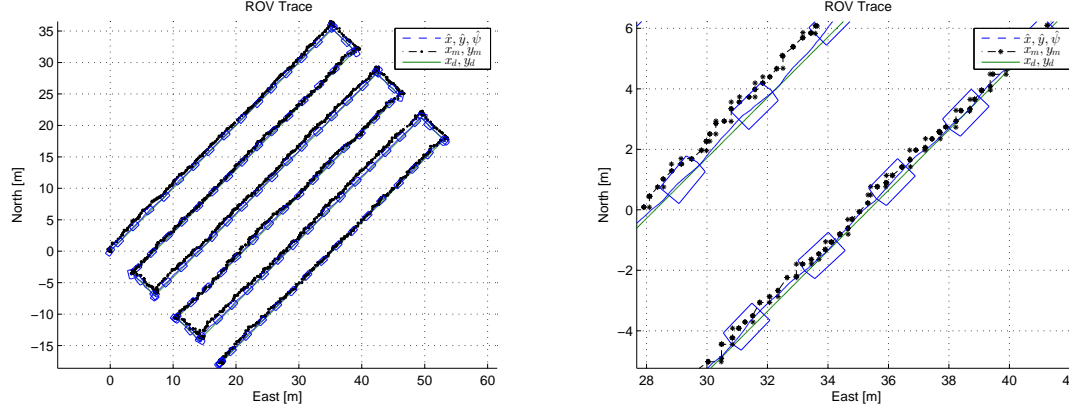
## 7.2 AUR-Lab Cruises with RV Gunnerus

Some of the experimental data from cruises are presented in more detail. This is in order to demonstrate what the developed motion control system has been used for and to show how the scientific contributions in this thesis has enabled these missions.

### 7.2.1 Lawn Mower Pattern with Altitude Control

This example is a demonstration of several of the contributions in this thesis. Figure 7.1a shows the ROV Minerva tracking a lawn mower pattern with 50 m lines with spacing of 5 m while maintaining a distance to the sea floor of 2 m. A zoom-in is seen in Figure 7.1b. The constant jerk reference model in Chapter 5.1 is used to generate the desired trajectory (green line) from a list of way-points. The blue line is the estimated position from the sector Kalman filter in Chapter 4.2. The black dots are the position measurements from the HiPAP system on board RV Gunnerus.

Figure 7.2a shows the altitudes in the upper plot and the depth in the lower plot during the lawn mower pattern in Figure 7.1a. The desired altitude and depth are green lines and the estimated altitude and depth are blue. The desired altitude is maintained using the proposed guidance law for desired depth in Chapter 6.6. Note that there is a steady state offset of about 0.1 m in the altitude. This is most likely due to small errors in the sea floor gradient approximation and the integral term in the guidance law was not used. Note that the sea floor in this example is fairly flat as the difference in depth is only about 2 m over

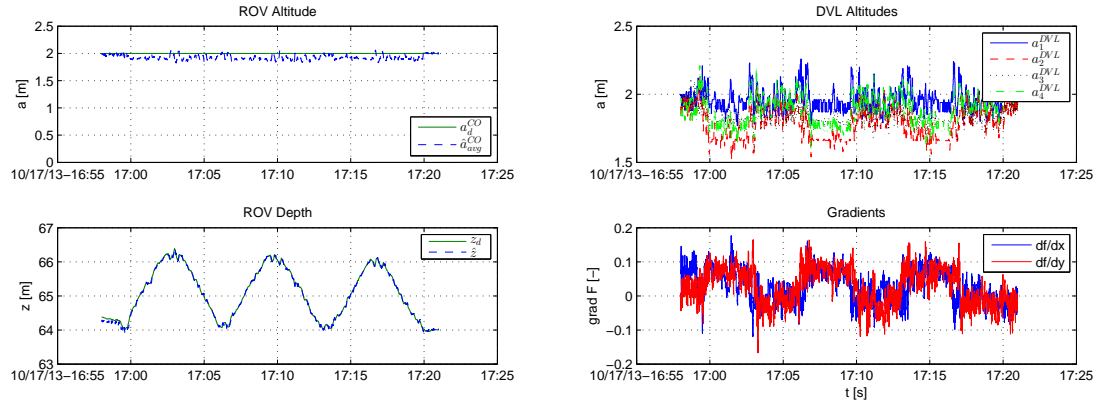


(a) ROV trace and snapshots of its outline during tracking.  
(b) Zoom-in of the ROV trace and snapshots of the ROV outline.

Figure 7.1: Lawn mower example: ROV trace and snapshots of the ROV outline during lawn mower tracking with altitude control.

a 50 m horizontal distance. However, for tasks like photomosaicking, it is still important to maintain a precise altitude.

Figure 7.2b shows the 4 DVL altitude measurements vs. time in the upper plot and the approximated gradient from the least squares approximation method proposed in Chapter 6.3 in the lower plot. Note that there is a consistent difference in the DVL measurements, and hence the sea floor gradient approximation, depending on whether the ROV is going uphill or downhill. It should be noted that the DVL is mounted at the stern of the ROV. Thus, it is closer to the sea floor for the same ROV altitude while going downhill than uphill.



(a) ROV altitude and depth vs. time.

(b) Approximated sea floor gradient vs. time.

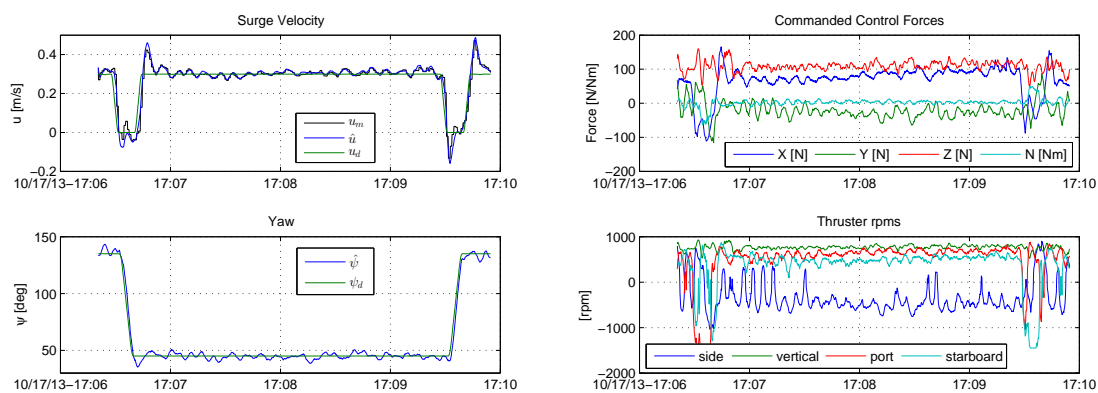
Figure 7.2: Lawn mower example: altitude control and sea floor approximation.

The desired, measured and estimated surge velocity for the third line is seen in the top plot in Figure 7.3a. The lower plot shows the desired and estimated heading. The

desired surge velocity and heading are produced by the constant jerk reference model and the estimated heading is from the explicit complementary filter in Chapter 4.3. There are some oscillations in the surge velocity as position control is used in the tracking. For the third tracking line from 17:07 to 17:09, the standard deviation for the estimated surge velocity is 0.01 m/s with a range of 0.06 m/s. In the same period, the estimated heading standard deviation is 2.4 degrees with a range of 12.2 degrees. That is decent performance, but the heading should ideally be more accurate. The heading control tends to be more accurate when less side forces are acting on the vehicle.

It should be noted that the thruster configuration for the ROV Minerva, as seen in Appendix A, is not ideal for use in automatic motion control systems. The forward thrusters are the thrusters that control the heading. At high surge speeds or in strong currents, little capacity is left for heading control. However, if thruster saturation becomes a problem, it is the heading that should have priority. Also, the thruster configuration for ROV Minerva results in great thrust losses in reverse as the jet goes into the vehicle. The sensible thruster configuration, for use in automatic motion control systems, are thrusters mounted at 45 degrees in each corner of the vehicle. This gives similar thrust capacity in surge and sway, forward and backwards and better heading control. The forward thruster are also located below the CG and attack point of the hydrodynamical forces. Thus, pitch motions are induced when the forward thrusters are used and there are no available thrusters to compensate for this on the ROV Minerva.

Figure 7.3b shows the commanded forces and yaw moment in the upper plot and the corresponding propeller revolution speeds in revolutions per minute (rpm) in the lower plot as calculated from the thruster model in Chapter 2. It is seen that the side thrusters are working against a sideways force from the ocean current and/or the cable in order to stay on the desired trajectory. The fairly smooth vertical thrust is working against the ROV buoyancy and the drag forces as it is going downwards. Thruster saturation is not an issue during the straight line segment as the maximum rpm is 1500 for all thrusters.



(a) Surge velocity and heading during the third survey line. (b) Commanded thrust and revolution speed during the third survey line.

Figure 7.3: Lawn mower example: surge velocity, heading and thrust.

### 7.2.2 Falstad Cruise and Search for Wreck

In this cruise the mission was to search for the wreck of a ship loaded with the bodies of executed prisoners from the Falstad concentration camp from the second world war. According to Falstadsenteret, the Nazi-Germans had loaded the bodies in an old fishing vessel about 70 feet long. The boat is believed to have been sunk somewhere between Levanger and Ytterøya in the Trondheims fjord.

In the cruise, the HUGIN AUV from Kongsberg Maritime was used to search an area with a HiSAS (High Resolution Interferometric Synthetic Aperture Sonar). Special sites of interest, based on the sonar images from the AUV, were inspected by the ROV Minerva in more detail. Data from one of these sites where the object of interest turned out to be a boat is shown next. Unfortunately, the wreck of interest was not found. The same methods of trajectory tracking and altitude control was used as in the previous example. However, the operation is at much deeper water and the ship wreck in the search pattern clearly violates the assumptions on the sea floor geometry smoothness and continuity for the sea floor approximation method from Chapter 6.3. The effect on the performance of the ROV mission despite these violations is shown here.

A similar type of plot as in Figure 7.1 is seen in Figure 7.4. Figure 7.4a shows the ROV search pattern over the wreck site and a zoom-in is seen in Figure 7.4b. The depth of the ROV is about 415 m and note that the variance of the HiPAP measurements are considerably larger than in the previous example where the ROV depth was about 65 m. However, the estimated position from the sector Kalman filter seems to produce smooth and accurate outputs well suited for closed-loop control. Although, no ground truth is available.

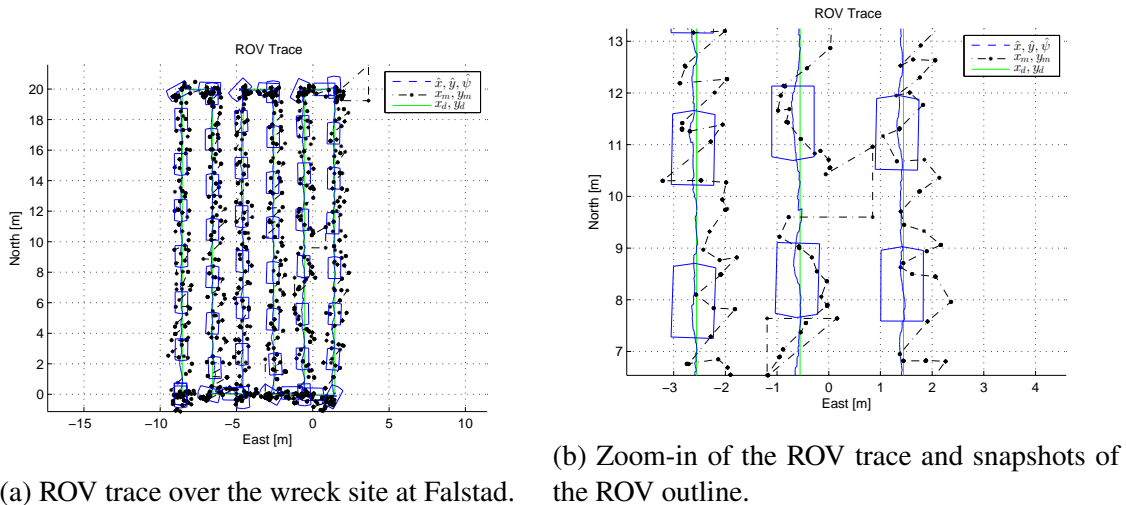
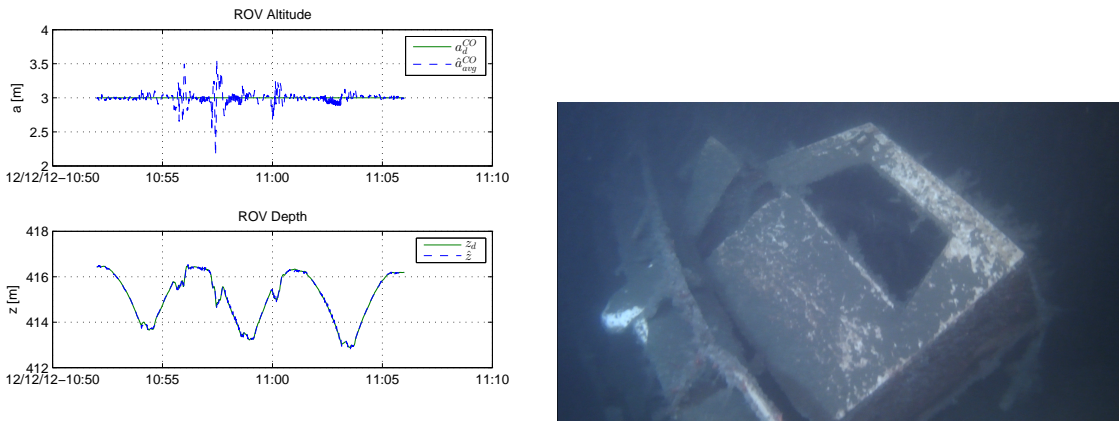


Figure 7.4: ROV trace and snapshots of the ROV outline during search for the Falstad ship wreck.

The ROV altitude and depth are seen in Figure 7.5a. Figure 7.5b shows the wheel house of the wreck which the ROV was inspecting during the lawn mower pattern. The picture was taken from the ROV just before the spike in the altitude at ca. 10:57 in Figure

7.5a. When the ROV approaches the wheelhouse, some of the DVL altitude measurements does a jump and the sea floor approximation will not be correct. However, the generated depth trajectory from the guidance law in (6.44) is smooth and feasible for the ROV. The surge speed was 0.3 m/s. Based on the DVL altitude measurements and the proposed sea floor approximation method and guidance law, the ROV is able to detect and safely fly over the wheelhouse without pilot interaction. Note that sudden altitude tracking errors are not necessarily the same as poor tracking performance. It is not possible for the vehicle to change depth instantaneously. When a sudden change in the sea floor geometry occurs, the ROV must still follow a smooth and continuous path.



(a) ROV altitude and depth over wreck site at Falstad. (b) Picture of the wheel house of a wreck at Falstad.

Figure 7.5: ROV altitude during search for Falstad wreck.

### 7.2.3 Ormen Lange

The previous examples in this thesis have shown experimental data for the ROV Minerva. The motion control system described in Chapter 3 has also been implemented on the larger ROV 30 k. See Appendix A for details. ROV 30 k was used in a cruise close to the gas terminal at Nyhamna for inspection of parts of the Langeled pipeline. The control system and altitude control was used in the mission.

Figure 7.6a shows the ROV trace during part of a pipeline survey. A zoom-in is seen in Figure 7.6b. Note that the drop-out in position measurement at about 103.5 m East causes the estimated position to go off track when a new measurement is available. These intermittent position drop outs occurred several times during the survey for unknown reasons. The drag towards port during drop-out of position measurements is most likely due to the cable forces. The cable forces on the ROV 30 k are much greater than on the ROV Minerva. Especially in this case as the ROV is going down a steep slope and the cable is payed out manually. If the winch operator pays out cable too slowly, the cable tension will rise quickly and pull the ROV towards the vessel. This shows the need for an automatic winch and cable control system that collaborates with the ROV motion control

system. The bias estimator in the Kalman filter in Chapter 4 will adapt to slowly varying cable forces, but quick changes cause errors in the estimated position, especially during dead-reckoning. Although there was no ground truth available, the sideways motion was confirmed from visual feedback of the pipeline as seen from the ROV cameras.

Figure 7.6a shows the desired and estimated altitude in the top plot and the desired and estimated depth in the lower plot vs. time. The desired altitude was set to 3 m. Note that the DVL was mounted with an orientation of 45 degrees on the ROV so that all acoustic beams measured the range to the sea floor on each side of the pipeline. Thus, the altitude over the pipeline was about 1.5-2 m. This worked fine except for segments with large free span of the pipeline. For these segments, the depth was controlled manually from visual feedback of the pipeline while the horizontal motion was automatically controlled.

Figure 7.6b shows the DVL altitude measurements in the top plot and the approximated sea floor gradient vector components from the least squares method in Chapter 6.3 in the lower plot. Note that the sea floor is fairly steep in the first part of the shown segment. For steep terrain, the gradient approximation is very important for the performance of the depth guidance law in (6.43) and (6.44) as the feedforward term will give a considerable contribution.

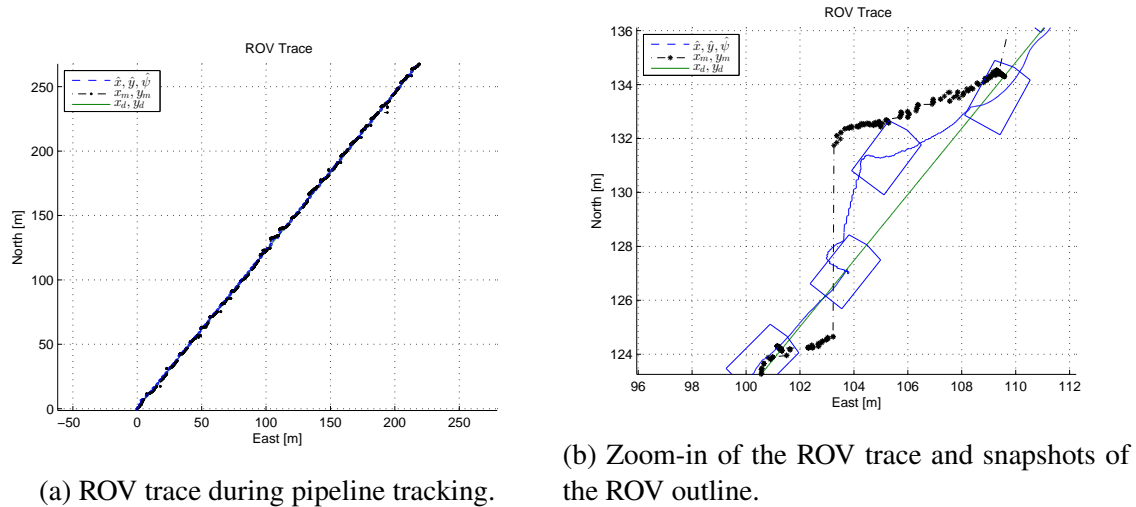
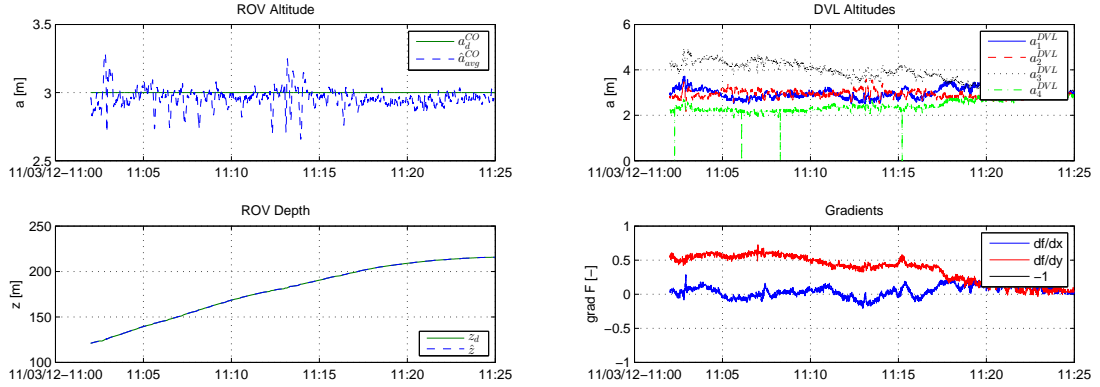


Figure 7.6: ROV trace and snapshots of the ROV outline during tracking of a pipeline.

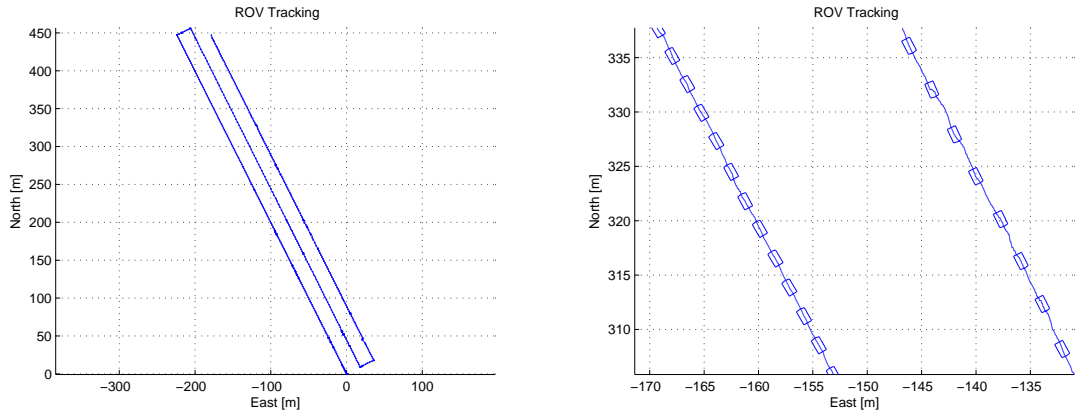
#### 7.2.4 Video Survey of a Coral Reef at Tautra

The ROV Minerva was used to do a video survey of a coral reef at Tautra in the Trondheimsfjord. The developed motion control system with altitude control was again used. In order to cover a larger area, the RV Gunnerus was put in follow target mode. In this mode the RV Gunnerus follows the ROV Minerva automatically using its DP system. Figure 7.8a shows the ROV trace for 3 survey lines of 500 m each. A zoom-in of the trace with snapshots of the ROV outline is shown in Figure 7.8b. Due to strong ocean currents, the speed was reduced while going towards North to avoid thruster saturation.



(a) ROV altitude and depth during pipeline track- (b) DVL measurements and sea floor gradient approximation.

Figure 7.7: ROV altitude and sea floor gradient approximation from DVL measurements during pipeline tracking.



(a) ROV trace over coral reef at Tautra. 500 m (b) Zoom-in of the ROV trace and snapshots of survey lines with 20 m spacing.

Figure 7.8: ROV trace with RV Gunnerus in target following.

Figure 7.9 shows the ROV depth trajectory and the estimated sea floor profile for the first survey line while maintaining a desired altitude of 2 m. This demonstrates the capability of the proposed sea floor approximation method and altitude control over rugged terrain.

### 7.2.5 Barge Wreck Survey at Munkholmen

A wrecked barge of about 20 m in length and 4 m beam was found at ca. 35 m depth just East of Munkholmen in the Trondheimsfjord. A lawn mower pattern with line spacing of 1 m was set up over it in order to make a photomosaic of the wreck site. The desired depth was set to 32.25 m. This is the same wreck used for the joystick tests in Chapter 5.

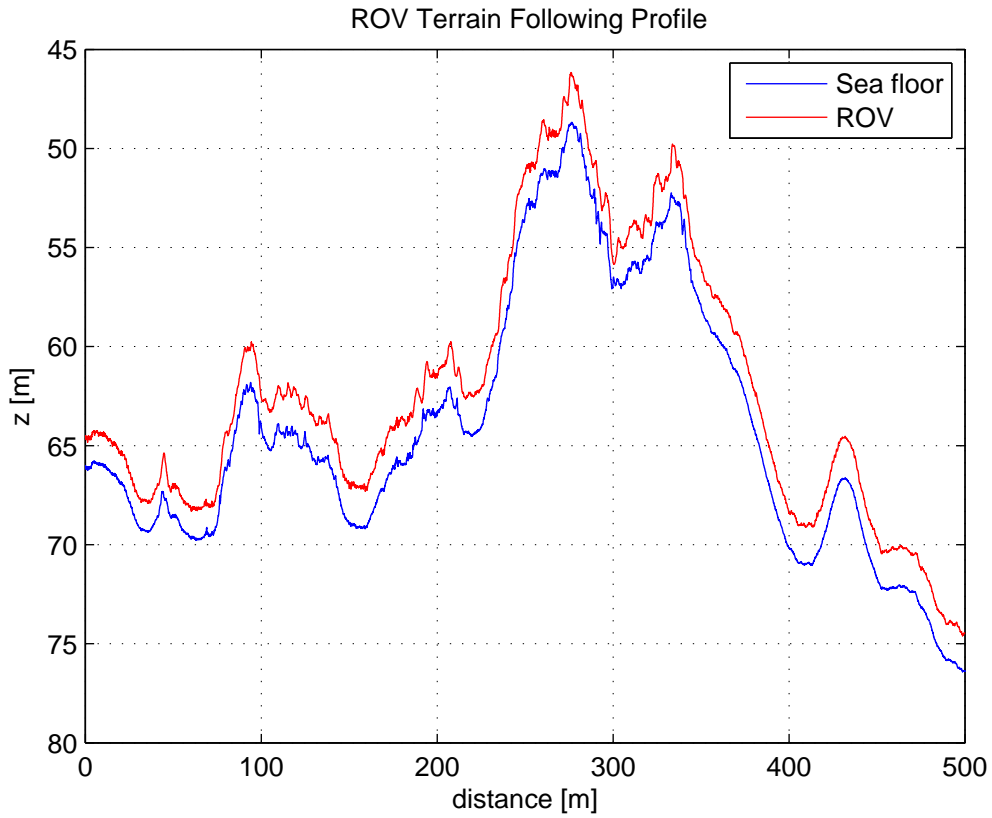


Figure 7.9: ROV depth trace and the estimated terrain profile from the DVL measurements for the first survey line at the coral reef at Tautra.

Figure 7.10a shows the ROV trace and snapshots of the outline during the lawn mower pattern. In this experiment, the original fluxgate compass was used as the heading reference in the motion control system. This resulted in poor tracking performance of all horizontal DOFs and heading compared to when the Xsens MTi-100 or the MRU-6 has been used for heading reference. Figure 7.10b shows a HiSAS sonar image of the barge taken from the HUGIN AUV.

Figure 7.11a demonstrates what the barge looks like from the least squares sea floor approximation method in Chapter 6.3. This is another case where the theoretical assumption on a smooth and continuous sea floor is clearly violated. However, the sea floor approximation method still provides useful data about the barge geometry. Each sidewall is detected as two peaks as the DVL beams sees the outside and inside of the barge when the DVL is directly above a sidewall. Figure 7.11b shows the result when the average of the basic linear approximation method from Chapter 6.3 is applied. This is an example that shows how the sea floor geometry and objects can be detected using only DVL measurements in combination with the navigation system.

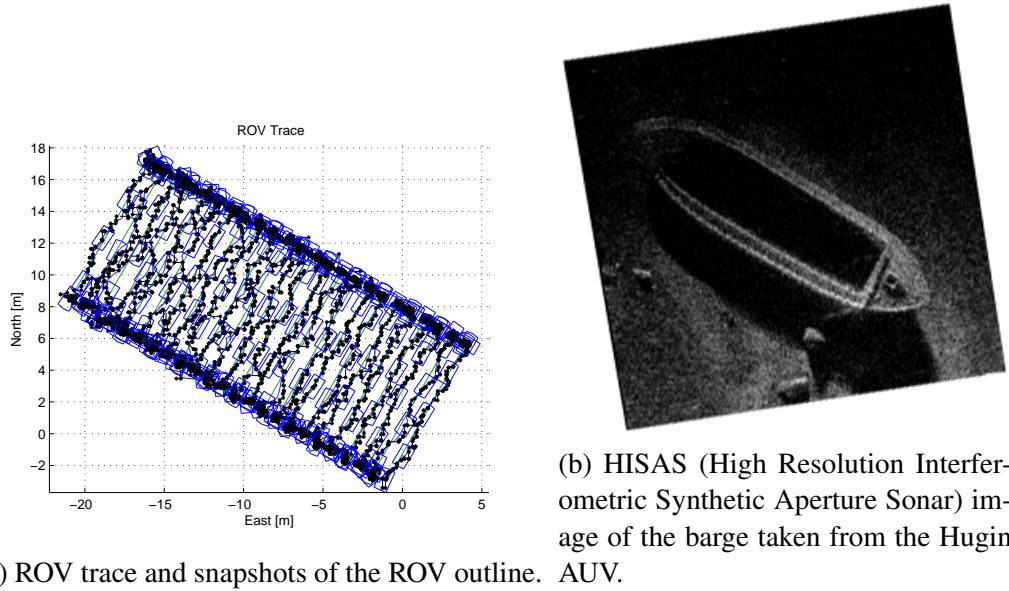
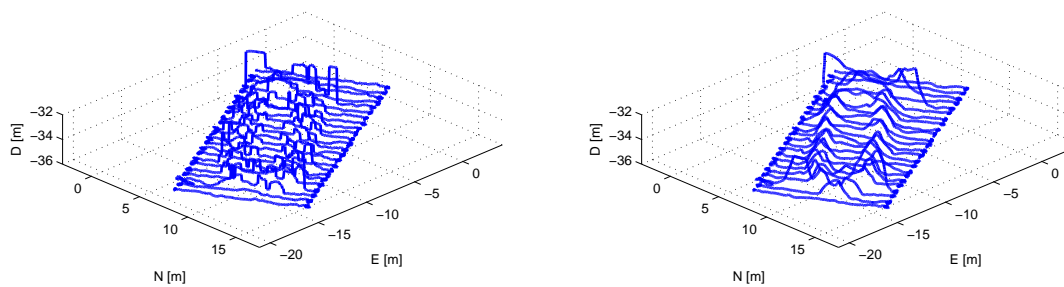


Figure 7.10: Barge wreck site East of Munkholmen, Trondheim.



(a) Sea floor geometry, least squares approximation method.  
(b) Sea floor geometry, average of 4 basic linear approximation methods.

Figure 7.11: Barge and sea floor geometry approximation from DVL altitude measurements and ROV position estimates.

## 7.2.6 Photomosaic

Figure 7.12 shows an example result of a photomosaic obtained from using the ROV Minerva and motion control system with altitude control in a cruise in April 2012. An area of 20 by 10 m of the coral reef at Tautra in the Trondheimsfjord was covered with desired altitude of 2 m. The selected area was found from the video survey described previously in this Chapter. PhD candidate Mauro Candeloro did the camera setup, operation and post processing of the raw pictures in order to make the mosaic.

With this high resolution image of the coral reef section, the biologist can identify the

species and evaluate the condition of the habitat. Since the ROV motion control system was used, it is easy to go back and re-run the motion pattern over the same location in order to monitor changes over time. Some of the species recognized and highlighted in Figure 7.12 are a sea urchin, a Norway redfish (*Sebastes viviparus*), a starfish (*Henricia*) and another sea urchin (*Echinus esculentus*), which is edible.

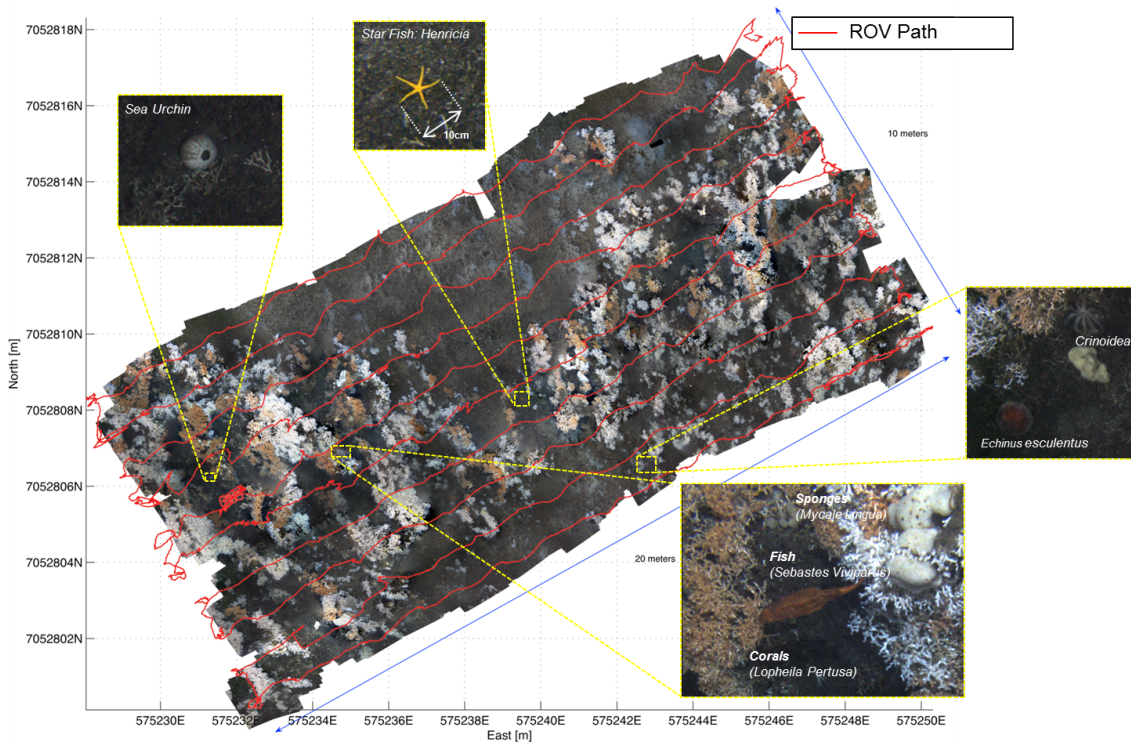


Figure 7.12: Photomosaic of part of the coral reef at Tautra in the Trondheimsfjord (Courtesy of Mauro Candeloro).

# Chapter 8

## Conclusion and Future Work

This thesis was about automatic motion control systems for ROVs. The main scientific contributions have been related to guidance strategies, in addition to underwater navigation and state estimation. The proposed methods have been implemented on NTNU's ROVs, tested in sea trials and experimental results have been presented.

### 8.1 Concluding Remarks

The most important scientific contributions in guidance related topics for ROVs have been

- Altitude control and terrain following.
- Joystick in closed-loop control.
- Constant jerk reference model.

The altitude control problem contained two main contributions; a method for sea floor geometry approximation from DVL measurements and a guidance law for desired depth to control a reference altitude, where a proposed feedforward term assured proper heave velocity. The method was implemented in the developed motion control system and has been successfully used on both ROV Minerva and ROV 30k.

The proposed method for joystick in closed-loop control was developed in order to enable the pilot to easily guide the ROV without having to compensate for dynamical and environmental forces. The main idea was to generate a desired trajectory based on joystick commands which were fed to a closed-loop controller for execution. A filter-based reference model based on the ROV dynamics was used to generate the desired states. Modifications to this reference model were proposed in order to reduce pilot induced oscillations. The methods have been implemented and tested on the ROV Minerva.

The work with the constant jerk reference model was done because a simple and intuitive reference model for a fully actuated vehicle was needed in the motion control system. The main idea was to integrate a constant jerk, that is on or off, in order to produce desired velocities and positions for all DOFs. The constant jerk reference model has

been implemented as the default reference model for A to B moves in the motion control system.

The work with underwater navigation and state estimation has been important in order to have a working motion control system. The main contributions here have been in two areas;

- Model-based Kalman filter.
- Sensor-based integration filter.

Model-based Kalman filters, both linearized and extended, were made based on a mathematical model of the ROV. These observers were adapted from model-based Kalman filters designed for ships. The linearized Kalman-filter has been implemented as the default observer in the motion control system and is used on both ROVs.

The work with sensor-based attitude estimation and integration filters was based on a new type of explicit complementary filters. The main new contribution was a proposed method for using the DVL velocity measurements in order to approximate the proper acceleration. This improved both the attitude estimation and thus the performance of the integration filter in simulations. The explicit complementary filter for attitude estimation was implemented in the motion control system as the default attitude observer. The sensor-based integration filter worked very well in simulations, but the performance was not satisfactory when used on actual ROV mission data. This was most likely due to sensitivity to noise and other uncertainties in sensor positions and calibration.

As part of work with the thesis and teaching assistant duties, a motion control system has been developed in collaboration with other PhD candidates and MSc students under the supervision of postdoc Martin Ludvigsen and prof. Asgeir J. Sørensen. The motion control software runs on a compactRIO, which is a real-time controller, and a GUI runs on a host computer. The motion control system has been tested and used on both NTNU ROVs. The motion control system has also been used in cruises for ocean science researchers in marine biology and archeology.

## 8.2 Future Work

There are some areas that require more work in order to improve the performance of a motion control system for ROVs. The most important are;

- Underwater navigation.
- Combined manipulator and vehicle control.
- Thruster allocation and fault handling.
- Umbilical control and estimation.

The main challenge with underwater motion control systems is finding the position with sufficient accuracy and smoothness for use in closed-loop control. More work is needed on sensor-based navigation system that can use small and inexpensive sensors, and still provide good position estimates in the entire water column. The systems today rely too much on acoustic positioning systems and DVL. Alternative navigation solutions, such as SLAM and other terrain-based navigation methods, should be investigated further and new types of sensors should be considered to give more complementary data. Also, a closer integration of different navigation solutions, such as sensor-based, model-based and terrain navigation, can produce a better overall navigation system as long as the underwater GPS is not available.

For the ROV to do automated intervention work, the problem of combined manipulator and vehicle control must be studied further. In manipulator work tasks, the objective is usually to control the end point of the manipulator arm. The finger position is set by the arm joint angles and/or the ROV position for better leverage or access. Finding a control strategy that handles this is of importance and a challenge as the manipulator forces also affects the ROV motions.

Thruster allocation methods that account for saturation and thruster failures are needed in order to increase the operation time and robustness to environmental forces. This is an interesting field which should be investigated further.

Manual payout of the umbilical is a limitation for a fully automatic and autonomous operations. An umbilical control system that minimize the forces on the ROV is desirable to both ease and improve the performance of ROV operations. Ideally, the system should know the position of the umbilical in order to not get entangled or to untangle the ROV when performing task in complex environments. Work in this field of ROV motion control systems is needed.



# Bibliography

- [1] K.B. Anonsen and O.K. Hagen. An analysis of real-time terrain aided navigation results from a HUGIN AUV. *OCEANS 2010*, pages 1–9, 2010.
- [2] T. Bailey and H. Durrant-Whyte. Simultaneous localization and mapping (SLAM): Part II. *IEEE Robotics & Automation Magazine*, 13(3):108–117, 2006.
- [3] V. Berg. Development and Commissioning of a DP system for ROV SF 30k. Master's thesis, Norwegian University of Science and Technology, Department of Marine Technology, 2012.
- [4] J.C. Blankenburgh, B.A. Fossum, P.A. Østerholt, and H.O. Torsen. Norwegian marine geodetic projects. *Marine Geodesy*, 1(2):125–145, 1977.
- [5] Naval Studies Board et al. *Autonomous vehicles in support of naval operations*. National Academies Press, 2005.
- [6] E. Børhaug and K.Y. Pettersen. Cross-track control for underactuated autonomous vehicles. In *Decision and Control, 2005 and 2005 European Control Conference. CDC-ECC'05. 44th IEEE Conference on*, pages 602–608. IEEE, 2005.
- [7] E. Børhaug, K.Y. Pettersen, and A. Pavlov. An optimal guidance scheme for cross-track control of underactuated underwater vehicles. In *Control and Automation, 2006. MED'06. 14th Mediterranean Conference on*, pages 1–5. IEEE, 2006.
- [8] M. Breivik and T.I. Fossen. Principles of Guidance-Based Path Following in 2D and 3D. In *Decision and Control, 2005 and 2005 European Control Conference. CDC-ECC '05. 44th IEEE Conference on*, pages 627 – 634, dec. 2005.
- [9] M. Breivik and T.I. Fossen. Guidance laws for planar motion control. In *Decision and Control, 2008. CDC 2008. 47th IEEE Conference on*, pages 570 –577, dec. 2008.
- [10] M. Caccia, R. Bono, G. Bruzzone, and G. Veruggio. Bottom-following for remotely operated vehicles. *Control engineering practice*, 11(4):461–470, 2003.
- [11] M. Caccia, G. Bruzzone, and G. Veruggio. Active sonar-based bottom-following for unmanned underwater vehicles. *Control Engineering Practice*, 7(4):459–468, 1999.

- [12] M. Caccia, G. Bruzzone, and G. Veruggio. Bottom-following for remotely operated vehicles: algorithms and experiments. *Autonomous Robots*, 14(1):17–32, 2003.
- [13] W. Caharija, Kristin Y. Pettersen, Jan Tommy Gravdahl, and Asgeir Johan Sørensen. Topics on Current Compensation for Path Following Applications of Underactuated Underwater Vehicles. In *NGCUV, 2012 IFAC - Portugal*, april 2012.
- [14] W. Caharija, K.Y. Pettersen, J.T. Gravdahl, and E. Børhaug. Path following of underactuated autonomous underwater vehicles in the presence of ocean currents. In *Decision and Control (CDC), 2012 IEEE 51st Annual Conference on*, pages 528–535. IEEE, 2012.
- [15] J. Chestnutt, P. Michel, K. Nishiwaki, J. Kuffner, and S. Kagami. An intelligent joystick for biped control. In *Robotics and Automation, 2006. ICRA 2006. Proceedings 2006 IEEE International Conference on*, pages 860 –865, may 2006.
- [16] J.C.K. Chou. Quaternion kinematic and dynamic differential equations. *Robotics and Automation, IEEE Transactions on*, 8(1):53–64, 1992.
- [17] R.D. Christ and R.L. Wernli Sr. Observation class rovs come of age. In *Sixth International Symposium on Underwater Technology*, 2009.
- [18] R.D. Christ and R.L. Wernli Sr. *The ROV manual: A User Guide for Remotely Operated Vehicles*. Butterworth-Heinemann, 2013.
- [19] Robert D. Christ and Robert L. Wernli sr. *The ROV Manual: A User Guide for Observation-Class Remotely Operated Vehicles*. Butterworth-Heinemann, 2007.
- [20] R.A. Cooper, D.M. Spaeth, D.K. Jones, M.L. Boninger, S.G. Fitzgerald, and S. Guo. Comparison of virtual and real electric powered wheelchair driving using a position sensing joystick and an isometric joystick. *Medical Engineering and Physics*, 24(10):703 – 708, 2002.
- [21] J.L. Crassidis, F.L. Markley, and Y. Cheng. Survey of nonlinear attitude estimation methods. *Journal of Guidance, Control, and Dynamics*, 30(1):12–28, 2007.
- [22] Ø. Ødegård, M. Ludvigsen, G. Johnsen, A.J. Sørensen, S. Ekehaug, F. Dukan, and M. Moline. Managing Data from Multiple Sensors in an Interdisciplinary Research Cruise AUR-Lab Integrated Marine Environmental Monitoring and Mapping Cruise December 2011. In *Archaeology in the Digital Era. Papers from the 40th Annual Conference of Computer Applications and Quantitative Methods in Archaeology (CAA)*, volume 40. Amsterdam University Press, 2013.
- [23] M.W.M. Gamini Dissanayake, P. Newman, S. Clark, H.F. Durrant-Whyte, and M. Csorba. A solution to the simultaneous localization and map building (SLAM) problem. *Robotics and Automation, IEEE Transactions on*, 17(3):229–241, 2001.

- [24] F.R. Driscoll, R.G. Lueck, and M. Nahon. Development and validation of a lumped-mass dynamics model of a deep-sea ROV system. *Applied Ocean Research*, 22(3):169–182, 2000.
- [25] F. Dukan, M. Ludvigsen, and A.J. Sørensen. Dynamic Positioning System for a Small Size ROV with Experimental Results. In *OCEANS, 2011 IEEE - Spain*, pages 1 –10, june 2011.
- [26] F. Dukan and A.J. Sørensen. Altitude Estimation and Control of ROV by use of DVL. In *MCMC 2012, 9th IFAC Conference on Manoeuvring and Control of Marine Craft - Italy*, pages 1 –6, september 2012.
- [27] F. Dukan and A.J. Sørensen. Joystick in Closed-loop Control of ROVs with Experimental Results. In *Navigation, Guidance and Control of Underwater Vehicles*, volume 3, pages 293–300, 2012.
- [28] F. Dukan and A.J. Sørensen. Integration Filter for APS, DVL, IMU and Pressure Gauge for Underwater Vehicles. In *CAMS 2013, The 9th IFAC Conference on Control Applications in Marine Systems 2013 - Japan*, pages 1 –6, september 2013.
- [29] F. Dukan and A.J. Sørensen. Nonlinear Observer for Underwater Vehicles with IMU and Velocity Measurements in the Body Frame. *Submitted to IEEE Transactions on Control Systems Technology*, 2014.
- [30] F. Dukan and A.J. Sørensen. Sea Floor Geometry Approximation and Altitude Control of ROVs. *Control Engineering Practice*, 29:135–146, 2014.
- [31] H. Durrant-Whyte and T. Bailey. Simultaneous localization and mapping: part I. *Robotics & Automation Magazine, IEEE*, 13(2):99–110, 2006.
- [32] C.H. Edwards and D.E. Penney. *Elementary Linear Algebra*. Prentice-Hall, 1988.
- [33] C.H. Edwards and E.D. Penney. *Edwards & Penney fifth edition Calculus with Analytical Geometry*. Prentice Hall, 1997.
- [34] J. Elliott. Nasa’s advanced control law program for the f-8 digital fly-by-wire aircraft. *Automatic Control, IEEE Transactions on*, 22(5):753 – 757, oct 1977.
- [35] R.M. Eustice, H. Singh, J.J. Leonard, and M.R. Walter. Visually mapping the RMS Titanic: Conservative covariance estimates for SLAM information filters. *The international journal of robotics research*, 25(12):1223–1242, 2006.
- [36] O.M. Faltinsen. *Sea Loads on Ships and Offshore Structures*. Cambridge University Press, 1990.
- [37] A. Fattouh, M. Sahnoun, and G. Bourhis. Force feedback joystick control of a powered wheelchair: preliminary study. In *Systems, Man and Cybernetics, 2004 IEEE International Conference on*, volume 3, pages 2640 – 2645 vol.3, oct. 2004.

- [38] D. de A. Fernandes, F. Dukan, and A.J. Sørensen. Reference Model for High Performance and Low Energy Consumption Motions. In *Navigation, Guidance and Control of Underwater Vehicles*, volume 3, pages 217–222, 2012.
- [39] N.P. Fofonoff and R.C. Millard. *Algorithms for Computation of Fundamental Properties of Seawater*. Unesco, 1983.
- [40] T.I. Fossen. *Handbook of Marine Craft Hydrodynamics and Motion Control*. John Wiley and Sons Ltd., 2011.
- [41] T.I. Fossen and J.P. Strand. Passive nonlinear observer design for ships using lyapunov methods: full-scale experiments with a supply vessel. *Automatica*, 35(1):3–16, 1999.
- [42] C.C. Foster and G.H. Elkaim. Extension of a two-step calibration methodology to include nonorthogonal sensor axes. *Aerospace and Electronic Systems, IEEE Transactions on*, 44(3):1070–1078, 2008.
- [43] A. Friedman, O. Pizarro, S.B. Williams, and M. Johnson-Roberson. Multi-scale measures of rugosity, slope and aspect from benthic stereo image reconstructions. *PLoS ONE*, 7(12):e50440, 2012.
- [44] R.B. Fugitt. Design and operation of two remotely manned undersea vehicles. In *OCEAN 75 Conference*, pages 870–876, Sept 1975.
- [45] D. Gebre-Egziabher, G.H. Elkaim, J.D. Powell, and B.W. Parkinson. Calibration of strapdown magnetometers in magnetic field domain. *Journal of Aerospace Engineering*, 19(2):87–102, 2006.
- [46] R.L. Gordon. Principles of Operation a Practical Primer. *RD Instruments, San Diego*, 1996.
- [47] H.F. Grip, T.I. Fossen, T.A. Johansen, and A. Saberi. A nonlinear observer for integration of GNSS and IMU measurements with gyro bias estimation. In *American Control Conference (ACC), 2012*, pages 4607–4612. IEEE, 2012.
- [48] H.F. Grip, T.I. Fossen, T.A. Johansen, and A. Saberi. Attitude estimation using biased gyro and vector measurements with time-varying reference vectors. *Automatic Control, IEEE Transactions on*, 57(5):1332–1338, 2012.
- [49] H.F. Grip, T.I. Fossen, T.A. Johansen, and A. Saberi. Nonlinear observer for gnss-aided inertial navigation with quaternion-based attitude estimation. In *American Control Conference (ACC), 2013*, pages 272–279. IEEE, 2013.
- [50] P.D. Groves. *Principles of GNSS, inertial, and multisensor integrated navigation systems*. Artech House, 2013.

- [51] F. Harashima and S. Suzuki. Human adaptive mechatronics - interaction and intelligence. In *Advanced Motion Control, 2006. 9th IEEE International Workshop on*, pages 1 –8, 0-0 2006.
- [52] D. Hiranandani, C. White, C. Clark, T. Gamin, and K. Buhagiar. Underwater robots with sonar and smart tether for underground cistern mapping and exploration. In *The 10th International Symposium on Virtual Reality, Archaeology and Cultural Heritage VAST*, 2009.
- [53] M.-D. Hua. Attitude estimation for accelerated vehicles using GPS/INS measurements. *Control Engineering Practice*, 18(7):723–732, 2010.
- [54] M.-D. Hua, K. Rudin, G. Ducard, T. Hamel, and R. Mahony. Nonlinear attitude estimation with measurement decoupling and anti-windup gyro-bias compensation. In *Proceedings of the 18th IFAC World Congress, Milano, Italia*, 2011.
- [55] H.-M. Huang, K. Pavek, B. Novak, J. Albus, and E. Messin. A framework for autonomy levels for unmanned systems (ALFUS). *Proceedings of AUVSI Unmanned Systems 2005*, 2005.
- [56] J.C. Kinsey, R.M. Eustice, and L.L. Whitcomb. *A survey of underwater vehicle navigation: Recent advances and new challenges*. Citeseer, 2006.
- [57] J.C. Kinsey and L.L. Whitcomb. In situ alignment calibration of attitude and doppler sensors for precision underwater vehicle navigation: Theory and experiment. *IEEE Journal of Oceanic Engineering*, 32(2), 2007.
- [58] M. Kirkeby. Comparison of Controllers for Dynamic Positioning and Tracking of ROV Minerva. Master’s thesis, Norwegian University of Science and Technology, Department of Marine Technology, 2010.
- [59] S.Ø. Kørte. Guidance & control strategies for UUVs. Master’s thesis, Norwegian University of Science and Technology, Department of Marine Technology, 2011.
- [60] H. Lie, B. Sortland, and W. Lian. Design of ROV umbilical configurations to improve ROV operability. In *Proc. 8th Intn. Conference, Offshore Mechanics and Arctic Engineering*, volume 7, 1989.
- [61] M. Ludvigsen and Ø.T. Ødegaard. Slebeforsøk av modell for å bestemme Cd - koeffisient. *Norwegian University of Science and Technology, Department of Marine Technology*, 2003.
- [62] M. Ludvigsen and Ø.T. Ødegaard. Slebeforsøk modell Cd-koeffisient i alle vinkler. *Norwegian University of Science and Technology, Department of Marine Technology*, 2003.
- [63] M. Ludvigsen and Ø.T. Ødegaard. Fullskala thrust-test av Minerva. *Norwegian University of Science and Technology, Department of Marine Technology*, 2004.

- [64] M. Ludvigsen and Ø.T. Ødegaard. Friprøveforsøk med ROV-thruster. *Norwegian University of Science and Technology, Department of Marine Technology*, 2005.
- [65] M. Ludvigsen and Ø.T. Ødegaard. Sammenfatning av hydrodynamiske forsøk med ROV-en Minerva. *Norwegian University of Science and Technology, Department of Marine Technology*, 2006.
- [66] C.C. Lysdahl. Design of Dynamic Positioning System for ROV Minerva. Master's thesis, Norwegian University of Science and Technology, Department of Marine Technology, 2010.
- [67] R. Mahony, T. Hamel, and J.-M. Pflimlin. Nonlinear complementary filters on the special orthogonal group. *Automatic Control, IEEE Transactions on*, 53(5):1203–1218, 2008.
- [68] R. Mahony, T. Hamel, J. Trumpf, and C. Lageman. Nonlinear attitude observers on SO (3) for complementary and compatible measurements: A theoretical study. In *Decision and Control, 2009 held jointly with the 2009 28th Chinese Control Conference. CDC/CCC 2009. Proceedings of the 48th IEEE Conference on*, pages 6407–6412. IEEE, 2009.
- [69] T. Maki, T. Ura, H. Mizushima, H. Kondo, T. Sakamaki, and M. Yanagisawa. Low altitude tracking of rugged seafloors for autonomous visual observation. In *Underwater Technology and Workshop on Scientific Use of Submarine Cables and Related Technologies, 2007. Symposium on*, pages 488–494. IEEE, 2007.
- [70] P. Martin and E. Salaün. Design and implementation of a low-cost observer-based attitude and heading reference system. *Control Engineering Practice*, 18(7):712–722, 2010.
- [71] G.I. Matsumoto and T.A. Potts. Two ways of researching the underwater world. *Brooks/Cole Enrichment Module*, 2011.
- [72] T.W. McLain and S.M. Rock. Experimental measurement of ROV tether tension. *Proceedings of Intervention/ROV*, 92, 1992.
- [73] D.T. McRuer. *Pilot-induced oscillations and human dynamic behavior*, volume 4683. NASA, 1995.
- [74] J.M.G. Merayo, F. Brauer, P. and Primdahl, J.R. Petersen, and O.V. Nielsen. Scalar calibration of vector magnetometers. *Measurement science and technology*, 11(2):120, 2000.
- [75] P.H. Milne. *Underwater Acoustic Positioning Systems*. Gulf Publishing Co., Houston, TX, 1983.
- [76] H. Nijmeijer and T.I. Fossen. *New directions in nonlinear observer design*, volume 244. Springer, 1999.

- [77] N.R. Parker, S.E. Salcudean, and P.D. Lawrence. Application of force feedback to heavy duty hydraulic machines. In *Robotics and Automation, 1993. Proceedings., 1993 IEEE International Conference on*, pages 375 –381 vol.1, may 1993.
- [78] E. Ruth. *Propulsion control and thrust allocation on marine vessels*. PhD thesis, Norwegian University of Science and Technology, Department of Marine Technology, 2008.
- [79] I. Schjølberg, O. Egeland, et al. Lateral Motion Control of an Underwater Thruster System Suspended to a Ship by a Slender Marine Structure. *International Journal of Offshore and Polar Engineering*, 6(04), 1996.
- [80] N.A. Shneydor. *Missile guidance and pursuit: kinematics, dynamics and control*. Elsevier, 1998.
- [81] C. Silvestre, R. Cunha, N. Paulino, and A. Pascoal. A bottom-following preview controller for autonomous underwater vehicles. *Control Systems Technology, IEEE Transactions on*, 17(2):257–266, 2009.
- [82] R. Skjetne, Ø. Kjerstad, et al. Recursive nullspace-based control allocation with strict prioritization for marine craft. In *Control Applications in Marine Systems*, volume 9, pages 49–54, 2013.
- [83] D.A. Smallwood and L.L. Whitcomb. Model-based dynamic positioning of underwater robotic vehicles: theory and experiment. *Oceanic Engineering, IEEE Journal of*, 29(1):169–186, 2004.
- [84] Ø.N. Smogeli. *Control of marine propellers: From normal to extreme conditions*. PhD thesis, Norwegian University of Science and Technology, Department of Marine Technology, 2006.
- [85] A.J. Sørensen, S.I. Sagatun, and T.I. Fossen. Design of a dynamic positioning system using model-based control. *Control Engineering Practice*, 4(3):359–368, 1996.
- [86] A.J. Sørensen. Structural issues in the design and operation of marine control systems. *Annual Reviews in Control*, 29(1):125–149, 2005.
- [87] A.J. Sørensen. *Propulsion and Motion Control of Ships and Ocean Structures. Lecture Notes, UK-11-76*. Department of Marine Technology, NTNU, January 2011.
- [88] A.J. Sørensen, F. Dukan, M. Ludvigsen, D. de A. Fernandes, and M. Candeloro. Development of Dynamic Positioning and Tracking System for the ROV Minerva. In *Further Advances in Unmanned Marine Vehicles. G. Roberts and B. Sutton*, pages 113 –128, 2012.

- [89] L. Standardi. Signal Processing and Change Detection Applied to ROV in a DP System. Master's thesis, Norwegian University of Science and Technology, Department of Marine Technology, 2011.
- [90] D. Stoianovici, L.L. Whitcomb, J. Anderson, R. Taylor, and L. Kavoussi. A modular surgical robotic system for image guided percutaneous procedures. In *Medical Image Computing and Computer-Assisted Intervention—MICCAI'98*, pages 404–410. Springer, 1998.
- [91] E. Svendby. Robust control of ROV/AUVs. Master's thesis, Norwegian University of Science and Technology, Department of Engineering Cybernetics, 2007.
- [92] K. Tervo, M. Bocca, L.M. Eriksson, and A. Manninen. Wireless joystick control for human adaptive mechatronics applications: Case trolley crane. In *Networking, Sensing and Control, 2009. ICNSC '09. International Conference on*, pages 19–24, march 2009.
- [93] D. Titterton and J. Weston. Strapdown Inertial Navigation Technology. 2-nd Edition. *The Institution of Electronic Engineers, Reston USA*, 2004.
- [94] E. Tolpinrud. Development and Implementation of Computer-Based Control System for ROV with Experimental Results. Master's thesis, Norwegian University of Science and Technology, Department of Marine Technology, 2012.
- [95] G. Troni and L.L. Whitcomb. New methods for in-situ calibration of attitude and doppler sensors for underwater vehicle navigation: Preliminary results. In *OCEANS 2010*, pages 1–8. IEEE, 2010.
- [96] G. Troni and L.L. Whitcomb. Preliminary experimental evaluation of a doppler-aided attitude estimator for improved doppler navigation of underwater vehicles. In *Robotics and Automation (ICRA), 2013 IEEE International Conference on*, pages 4134–4140. IEEE, 2013.
- [97] A. Tustin. The nature of the operator's response in manual control, and its implications for controller design. *Electrical Engineers - Part IIA: Automatic Regulators and Servo Mechanisms, Journal of the Institution of*, 94(2):190 –206, may 1947.
- [98] J.F. Vasconcelos, G. Elkaim, C. Silvestre, P. Oliveira, and B. Cardeira. Geometric approach to strapdown magnetometer calibration in sensor frame. *Aerospace and Electronic Systems, IEEE Transactions on*, 47(2):1293–1306, 2011.
- [99] K. Vickery. Acoustic positioning systems. A practical overview of current systems. In *Autonomous Underwater Vehicles, 1998. AUV'98. Proceedings Of The 1998 Workshop on*, pages 5–17. IEEE, 1998.
- [100] R. Video. Autonomous mini rov control for offshore survey, target id, and reacquisition. *Ocean News & Technology*, 18(11):10–11, december 2012.

- [101] T.I. Vik, B.and Fossen. A nonlinear observer for GPS and INS integration. In *Decision and Control, 2001. Proceedings of the 40th IEEE Conference on*, volume 3, pages 2956–2961. IEEE, 2001.
- [102] M. Whitworth and S. Cohan. Advances in rov automation. *Ocean News & Technology*, 17(6):22–23, july 2011.
- [103] H.K. Woud and D. Stapersma. *Design of propulsion and electric power generation systems*. IMarEST, 2002.
- [104] Y.C. Yeh. Design considerations in boeing 777 fly-by-wire computers. In *High-Assurance Systems Engineering Symposium, 1998. Proceedings. Third IEEE International*, pages 64 –72, nov 1998.
- [105] D.R. Yoerger, A.M. Bradley, B.B. Walden, M.-H. Cormier, and W.B.F. Ryan. Fine-scale seafloor survey in rugged deep-ocean terrain with an autonomous robot. In *Robotics and Automation, 2000. Proceedings. ICRA'00. IEEE International Conference on*, volume 2, pages 1787–1792. IEEE, 2000.
- [106] D.R. Yoerger, J. Newman, and J.-J. Slotine. Supervisory control system for the JASON ROV. *Oceanic Engineering, IEEE Journal of*, 11(3):392 – 400, jul 1986.
- [107] B. Zhao, R. Skjetne, M. Blanke, and F. Dukan. Particle Filter for Fault Diagnosis and Robust Navigation of Underwater Robot. *Control Systems Technology, IEEE Transactions on*, 1(1):1–16, 2014.



# Appendix A

## NTNU Vehicles

### A.1 ROVs

The developed motion control system from Chapter 3 has been implemented and tested on the NTNU owned ROVs Minerva and 30 k. A description of these ROVs is given here. Figure A.1a shows the ROV Minerva at the quay of Trondheim Biological Station. The ROV 30 k is seen in Figure A.1b. The thruster configurations are seen in Figure A.2a and A.2b for the ROV Minerva and 30 k respectively.



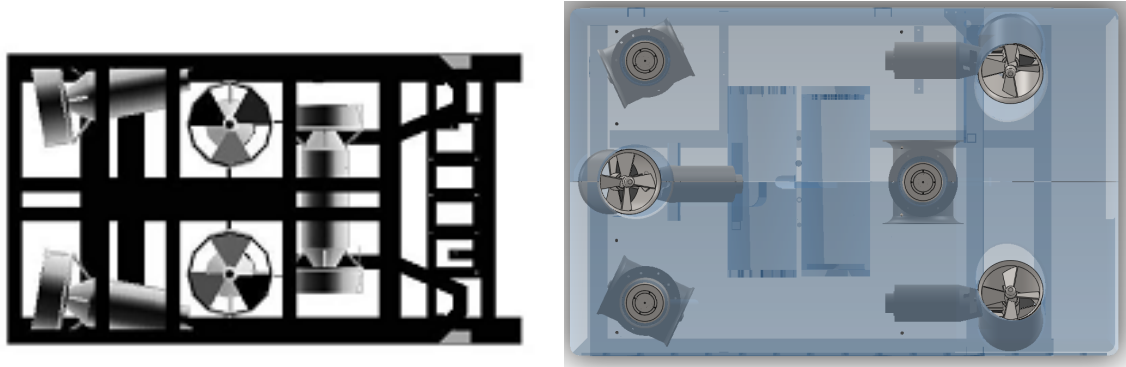
Figure A.1: ROV Minerva and 30 k.

#### A.1.1 Specifications

The key specifications for ROV Minerva and 30 k are given in Table A.1. Both ROVs are made by Sperre AS in Notodden, Norway.

#### A.1.2 Mathematical Properties

The values of the mathematical properties, according to the model in Chapter 2, are given next for the ROV Minerva and 30 k. These values are used in the simulation models and



(a) ROV Minerva: Overview of thruster configu- (b) ROV 30k: Overview of thruster configura-  
ration.  
tion.

Figure A.2: Thruster configurations, ROV Minerva and 30 k.

Table A.1: Comparison of Minerva and 30 k specs.

	ROV Minerva	ROV 30 k
Make	Sperre AS	Sperre AS
Model	SUB-fighter 7500	SUB-fighter 30K
Year	2003	2004
Dimensions (LWH)	144 x 82 x 81 cm	260 x 150 x 160 cm
Weight (air)	485 kg	1800 kg
Payload	20 kg	60 kg
Max depth	700 m	1000 m
Power input	230 VAC, 1 phase, 7.5 kW	230 VAC, 3 phase, 40 kW, 125 A
Thrusters	Horizontal: 2 x 2000 W	Horizontal: 2 x 3000 W
	Vertical: 2 x 2000 W	Vertical: 3 x 3000 W
	Lateral: 1 x 2000 W	Lateral: 1 x 3000 W
	(electrical asynchronous motors)	(electrical asynchronous motors)
Manipulators	5-function hydraulic arm Hydro-Lek (HLK-HD5)	7-function hydraulic arm Kraft Telerobotics (Raptor)
Umbilical	Diameter: 15.5 mm 0.18 kg/m	Diameter: 27 mm - kg/m
Lights	4 x 250 W halogen lights 2 x 400 W HMI lights	6 x 250 W halogen lights 2 x 400 W HMI lights

in the controller and observer designs.

## Minerva

The values for mass, added mass, linear and quadratic damping of ROV Minerva are given by (A.1), (A.2), (A.3) and (A.4) as calculated in [58].

$$\mathbf{M}_{RG}^{CG} = \begin{bmatrix} 460 & 0 & 0 & 0 & 0 & 0 \\ 0 & 460 & 0 & 0 & 0 & 0 \\ 0 & 0 & 460 & 0 & 0 & 0 \\ 0 & 0 & 0 & 105 & 0 & 0 \\ 0 & 0 & 0 & 0 & 104 & 0 \\ 0 & 0 & 0 & 0 & 0 & 50 \end{bmatrix}, \quad (\text{A.1})$$

$$\mathbf{M}_A = \begin{bmatrix} 293 & 0 & 0 & 0 & 0 & 0 \\ 0 & 302 & 0 & 0 & 0 & 0 \\ 0 & 0 & 326 & 0 & 0 & 0 \\ 0 & 0 & 0 & 52 & 0 & 0 \\ 0 & 0 & 0 & 0 & 52 & 0 \\ 0 & 0 & 0 & 0 & 0 & 57 \end{bmatrix}, \quad (\text{A.2})$$

$$\mathbf{D} = \begin{bmatrix} 29 & 0 & 0 & 0 & 0 & 0 \\ 0 & 41 & 0 & 0 & 0 & 0 \\ 0 & 0 & 254 & 0 & 0 & 0 \\ 0 & 0 & 0 & 34 & 0 & 0 \\ 0 & 0 & 0 & 0 & 59 & 0 \\ 0 & 0 & 0 & 0 & 0 & 45 \end{bmatrix}, \quad (\text{A.3})$$

$$\mathbf{D}_n = \begin{bmatrix} 292 & 0 & 0 & 0 & 0 & 0 \\ 0 & 584 & 0 & 0 & 0 & 0 \\ 0 & 0 & 635 & 0 & 0 & 0 \\ 0 & 0 & 0 & 84 & 0 & 0 \\ 0 & 0 & 0 & 0 & 148 & 0 \\ 0 & 0 & 0 & 0 & 0 & 100 \end{bmatrix}. \quad (\text{A.4})$$

### ROV 30 k

The values for mass, added mass, linear and quadratic damping of ROV 30 k are given by (A.5), (A.6), (A.7) and (A.8) as calculated in [3]. The values are calculated in WAMIT from a CAD drawing of the ROV provided by the manufacturer.

$$\mathbf{M}_{RG}^{CG} = \begin{bmatrix} 1862.9 & 0 & 0 & 0 & 0 & 0 \\ 0 & 1862.9 & 0 & 0 & 0 & 0 \\ 0 & 0 & 1862.9 & 0 & 0 & 0 \\ 0 & 0 & 0 & 525.4 & 1.4 & 33.4 \\ 0 & 0 & 0 & 1.4 & 794.2 & 2.6 \\ 0 & 0 & 0 & 33.4 & 2.6 & 691.2 \end{bmatrix}, \quad (\text{A.5})$$

$$\mathbf{M}_A = \begin{bmatrix} 779.8 & -6.9 & -103.3 & 8.5 & -165.5 & -7.8 \\ -6.9 & 1222 & 51.3 & 409.4 & -5.8 & 62.7 \\ -103.3 & 51.3 & 3659.9 & 6.1 & -386.4 & 10.7 \\ 8.5 & 409.4 & 6.1 & 534.9 & -10.0 & 21.0 \\ -165.5 & -5.8 & -386.4 & -10.0 & 2.69 & -1.1 \\ -7.8 & 62.7 & 10.7 & 21.0 & -1.1 & 224.3 \end{bmatrix}, \quad (\text{A.6})$$

$$\mathbf{D} = \begin{bmatrix} 74.82 & 0 & 0 & 0 & 0 & 0 \\ 0 & 69.48 & 0 & 0 & 0 & 0 \\ 0 & 0 & 728.40 & 0 & 0 & 0 \\ 0 & 0 & 0 & 268.80 & 0 & 0 \\ 0 & 0 & 0 & 0 & 309.77 & 0 \\ 0 & 0 & 0 & 0 & 0 & 105 \end{bmatrix}, \quad (\text{A.7})$$

$$\mathbf{D}_n = \begin{bmatrix} 748.2 & 0 & 0 & 0 & 0 & 0 \\ 0 & 992.5 & 0 & 0 & 0 & 0 \\ 0 & 0 & 1821 & 0 & 0 & 0 \\ 0 & 0 & 0 & 672 & 0 & 0 \\ 0 & 0 & 0 & 0 & 774.4 & 0 \\ 0 & 0 & 0 & 0 & 0 & 523.3 \end{bmatrix}. \quad (\text{A.8})$$

## A.2 Research Vessel Gunnerus

The Research Vessel (RV) Gunnerus has been used as the support vessel during ROV operations. The topside control system is installed in the control container on the deck of RV Gunnerus. Figure A.3 shows RV Gunnerus about to launch the ROV Minerva from the deck crane. RV Gunnerus is equipped with a DP system from Kongsberg Maritime and provide the ROV position through the hull mounted acoustic positioning system HiPAP 500, also delivered by Kongsberg Maritime.

The key specifications for RV Gunnerus are given in Table A.2.



Figure A.3: RV Gunnerus. (Courtesy of Fredrik Skoglund).

Table A.2: RV Gunnerus specifications.

RV Gunnerus	
Yard	Larsnes Mekaniske Verksted, Norway
Design	Polarkonsult AS, Norway
Year	2006
Dimensions	Loa: 31.25 m
	Lpp: 28.9 m
	Lwl: 29.9 m
	Beam: 9.6 m
	Depth mld: 4.2 m
	Draught mld: 2.7 m
	Dwt: 107 tonnes
Propulsion	Main electric propulsion: 1000 kW (Siemens 2 x 500 kW)
	Main generators: 3 x Nogva-Scania 450 kW
	Bow tunnel thruster: 1 x Brunvoll 200 kW
	Speed at 100% MCR: 12.6 kn
	Cruising speed: 9.4 kn
	Gear: 2 x Finnøy
	Rudder: 2 x Ulstein Hinze Rudder FB-H 1200
	Steering gear: 2 x Tenfjord SR562-FCPX2



## Appendix B

# Position & Velocity Control

The default control algorithm in the motion control system is the nonlinear PID. This is run in two modes, position and speed control. In speed control, the surge and sway motions are controlled to a desired speed while heading and depth are under position control.

The control force vector calculated by the PID control law is given as

$$\boldsymbol{\tau}_{PID} = -\mathbf{J}^T(\boldsymbol{\eta})(\mathbf{K}_p \tilde{\boldsymbol{\eta}} + \mathbf{K}_d \mathbf{J}(\boldsymbol{\eta}) \boldsymbol{\nu} + \mathbf{K}_i \int_0^t \tilde{\boldsymbol{\eta}}(t) d\tau), \quad (\text{B.1})$$

where  $\tilde{\boldsymbol{\eta}} = \boldsymbol{\eta} - \boldsymbol{\eta}_d$  is the tracking error, and  $\mathbf{K}_p$ ,  $\mathbf{K}_d$  and  $\mathbf{K}_i \in \mathbb{R}^{4 \times 4}$  are the PID gain matrices.

During tracking, a feedforward term given by (B.2) is added to the control force.

$$\boldsymbol{\tau}_{FF} = \mathbf{M}\boldsymbol{a}_d + \mathbf{C}(\boldsymbol{\nu}_d)\boldsymbol{\nu}_d + \mathbf{D}(\boldsymbol{\nu}_d)\boldsymbol{\nu}_d, \quad (\text{B.2})$$

The total control vector becomes

$$\boldsymbol{\tau} = \boldsymbol{\tau}_{PID} + \boldsymbol{\tau}_{FF}. \quad (\text{B.3})$$

In speed control, the elements for surge and sway in the control force vector are calculated as

$$\begin{aligned} \tau_1 &= -K_{p,u}(u - u_d) - K_{i,u} \int_0^t (u - u_d) d\tau, \\ \tau_2 &= -K_{p,v}(v - v_d) - K_{i,v} \int_0^t (v - v_d) d\tau, \end{aligned} \quad (\text{B.4})$$

where  $K_{p,u}$ ,  $K_{i,u}$ ,  $K_{p,v}$  and  $K_{i,v} \in \mathbb{R}$  are the PI gains for surge and sway, respectively. The other DOFs, yaw and heave, are calculated as in (B.3).

An anti-windup strategy is implemented in the controller. The elements in the integral term are calculated as

$$\tau_i = (K_i - K_{\text{anti},i}(\text{sat}(\tau_i) - \tau_i)) \int_0^T \tilde{\boldsymbol{\eta}}(t) d\tau, \quad (\text{B.5})$$

where  $K_{anti,i}$  is an anti-windup gain for DOF no. i. The integral term is saturated at 80% of the available thrust in the corresponding DOF.

# Appendix C

## Mathematical Toolbox

### C.1 Rotation Matrix

The rotation between two rigid bodies or reference frames  $\{b\}$  and  $\{n\}$  can be produced by a simple rotation  $\beta$  of  $\{b\}$  in  $\{n\}$  about a unit vector  $\boldsymbol{\lambda} = [\lambda_1, \lambda_2, \lambda_3]^T$ . That is,

$$\mathbf{R}_b^n := \mathbf{R}_{\lambda,\beta}, \quad (\text{C.1})$$

where

$$\mathbf{R}_{\lambda,\beta} = \mathbf{I}_{3 \times 3} + \sin \beta \mathbf{S}(\boldsymbol{\lambda}) + [1 - \cos \beta] \mathbf{S}^2(\boldsymbol{\lambda}). \quad (\text{C.2})$$

### C.2 Quaternions

The unit quaternion is an alternative to Euler angles for representation of attitude. This complex 4 parameter attitude representation avoids the singularity of the Euler angle representation.

The quaternion is defined by [16] as a complex number with one real part  $\eta$  and a vector with three imaginary elements given by

$$\boldsymbol{\epsilon} = [\epsilon_1, \epsilon_2, \epsilon_3]^T. \quad (\text{C.3})$$

The unit quaternion satisfies  $\mathbf{q}^T \mathbf{q} = 1$ . The set  $Q$  of unit quaternions is

$$Q := \{\mathbf{q} | \mathbf{q}^T \mathbf{q} = 1, \mathbf{q} = [\eta, \boldsymbol{\epsilon}]^T, \boldsymbol{\epsilon} \in \mathbb{R}^3, \eta \in \mathbb{R}\}. \quad (\text{C.4})$$

The real and imaginary part of the unit quaternion are defined as

$$\boldsymbol{\eta} := \cos \frac{\beta}{2}. \quad (\text{C.5})$$

$$\boldsymbol{\epsilon} = [\epsilon_1, \epsilon_2, \epsilon_3]^T := \boldsymbol{\lambda} \sin \frac{\beta}{2}. \quad (\text{C.6})$$

## Appendix D

# Altitude Control Dynamics and Stability

The closed-loop dynamics of the vertical motion during altitude control is complex. It is difficult to obtain stability results that are general for all types of sea floor geometry, ROV altitude and horizontal velocity. The complexity is illustrated in Figure D.1 which shows the block diagram of the heave dynamics from the desired altitude to actual altitude during closed-loop altitude control.  $\tau_z$  is the vertical control force on the ROV. It is especially the sea floor geometry, the corresponding DVL measurements and the approximation method that are difficult to analyze w.r.t. stability.

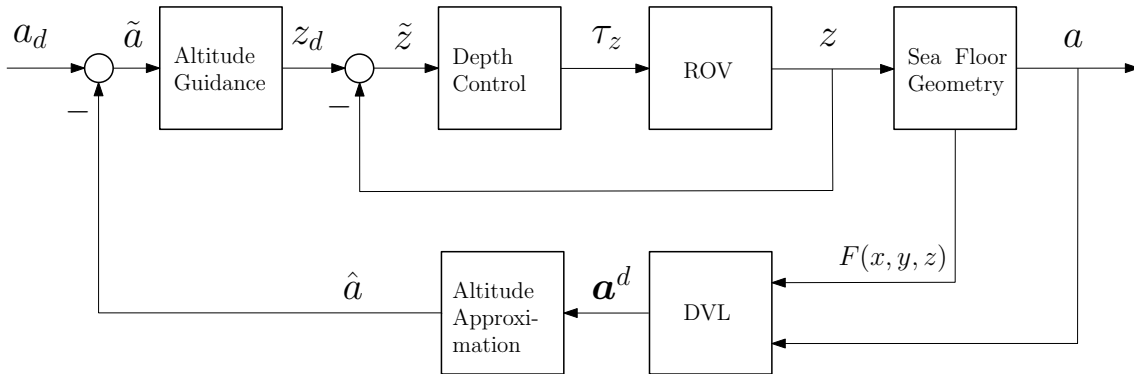


Figure D.1: Block diagram of the closed-loop altitude control system.

A simplified block diagram which is valid for a level sea floor and linear ROV heave dynamics is shown in Figure D.2.  $A(s)$  is the transfer function from altitude error to desired depth,  $C(s)$  is the transfer function for the PID depth controller and  $G(s)$  is the transfer function for the ROV heave dynamics.  $H(s)$  is the transfer function for the closed-loop depth control. The transfer functions  $A(s)$ ,  $C(s)$ , and  $G(s)$  are given by (D.1), (D.2), and (D.3), respectively.

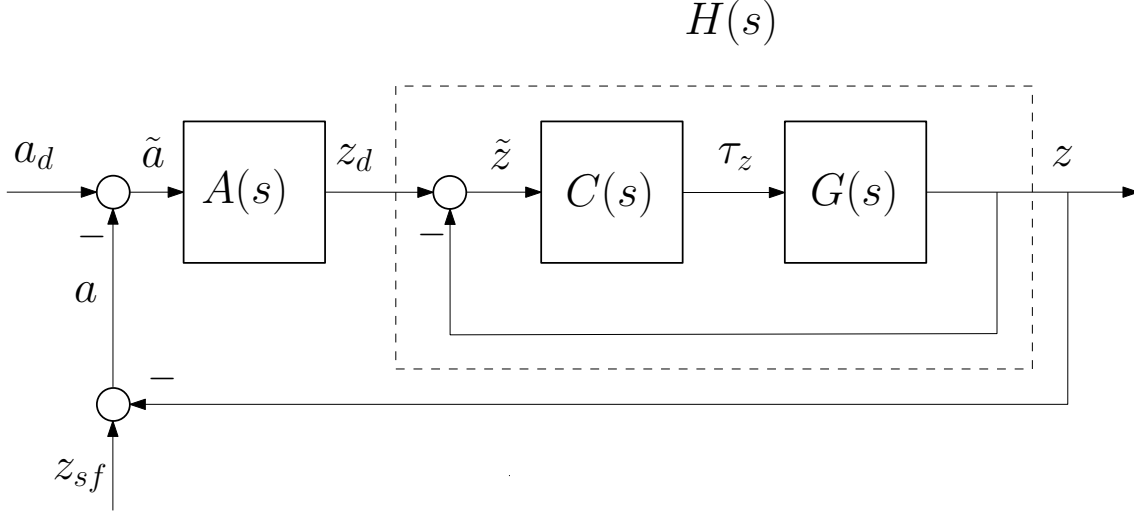


Figure D.2: Block diagram of the simplified closed-loop altitude control system.

$$A(s) = \frac{-(sk_p + k_i)}{s^2}, \quad (\text{D.1})$$

$$C(s) = s\sigma_d + \sigma_p + \frac{\sigma_i}{s}, \quad (\text{D.2})$$

$$G(s) = \frac{1}{s^2m_z + sd_z}, \quad (\text{D.3})$$

where  $A(s)$  contains the proportional and integral terms from (6.43) and (6.44).  $\sigma_p$ ,  $\sigma_i$ , and  $\sigma_d$  are the PID gains for the depth controller.  $m_z$  is the effective mass in heave for the ROV and  $d_z$  is the linear heave damping.

The closed-loop depth and altitude control dynamics are given by  $H(s)$  and  $R(s)$  in (D.4) and (D.5), respectively.

$$H(s) = \frac{C(s)G(s)}{1 + C(s)G(s)}, \quad (\text{D.4})$$

$$R(s) = \frac{A(s)H(s)}{1 - A(s)H(s)}. \quad (\text{D.5})$$

The transfer function  $R(s)$  from desired altitude,  $a_d$  to ROV depth,  $z$ , is written out in (D.6) as

$$R(s) = \frac{-(sk_p + k_i)(s^2\sigma_d + s\sigma_p + \sigma_i)}{s^2(s^3m_z + s^2(\sigma_d + d_z) + s\sigma_p + \sigma_i) + (sk_p + k_i)(s^2\sigma_d + s\sigma_p + \sigma_i)}. \quad (\text{D.6})$$

Stability is achieved for the simplified system by selecting the depth controller and altitude guidance law parameters so all poles of (D.6) are in the left half-plane. Note that the stability is most sensitive to the altitude guidance law parameters  $k_i$  and  $k_p$ . Increasing

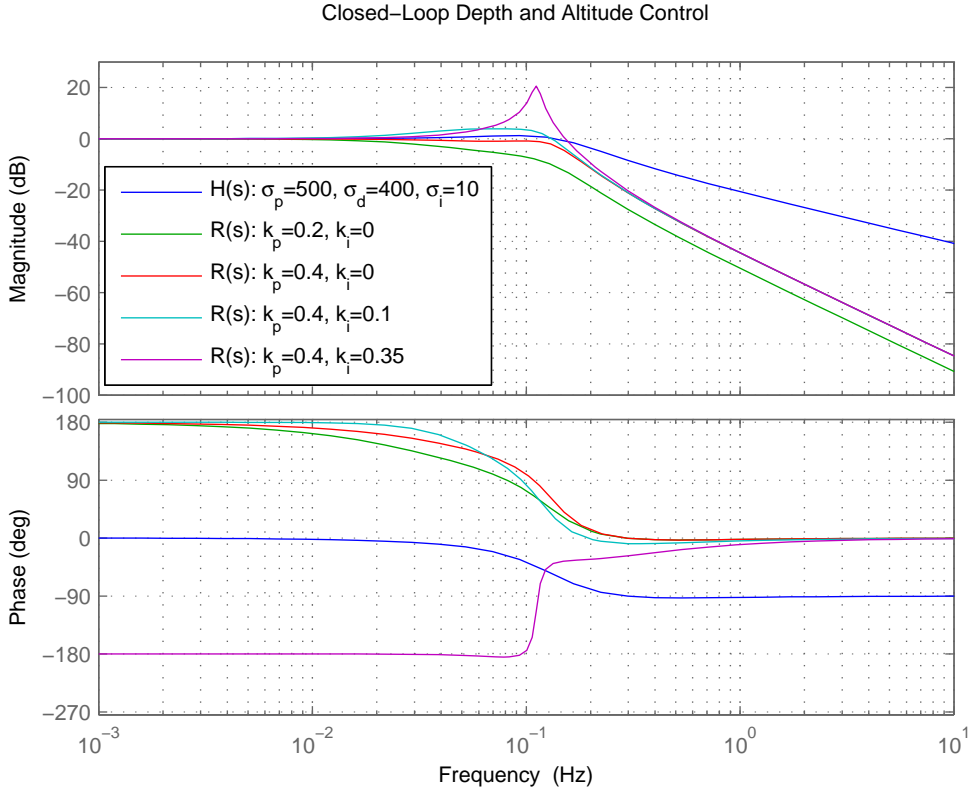


Figure D.3: Bode plot of depth and altitude control dynamics.

$k_i$  and/or  $k_p$  too much will move two of the poles in (D.6) over to the right half-plane and the system becomes unstable.

Bode plots for  $H(s)$  and  $R(s)$  with variation in the altitude guidance law parameters  $k_p$  and  $k_i$  are compared in Figure D.3. The ROV heave dynamics are given by  $G(s)$  with  $m_z = 700$  [kg] and  $d_z = 300$  [kg/s]. The PID gains for the depth controller are the same for all plots;  $\sigma_p = 500$ ,  $\sigma_d = 400$  and  $\sigma_i = 10$ . With  $k_p = 0.4$ , the system becomes unstable for  $k_i > 0.3$ . Note that the phase starts at 180 degrees for  $R(s)$  as this is the transfer function from desired altitude to depth. Low  $k_p$  gives poor bandwidth of the closed-loop altitude control compared to depth control. A large integrator gain,  $k_i$ , causes a peak in the magnitude plot, but delays the phase-shift. The phase-shift starts at lower frequencies for closed-loop altitude control,  $R(s)$ , than for the closed-loop depth control,  $H(s)$ .

The performance of the altitude control, based on the guidance law with feedback terms only, is considerably worse than of the depth control. If it is known that the sea floor is level, it is better to use  $z_d = z_{sf} - a_d$  instead of  $A(s)$ . Then the performance of the depth and altitude control is equal. However, this is not possible in the general case with varying terrain. This shows the importance of the proposed feedforward term in the altitude guidance law in (6.43). With a perfect feedforward term, the performance of the closed-loop altitude control will be equal to that of the closed-loop depth control even

for varying terrain and horizontal velocity. Although this is not feasible, the goal of the feedforward term is to bring the performance of the closed-loop altitude control as close as possible to that of the depth control.

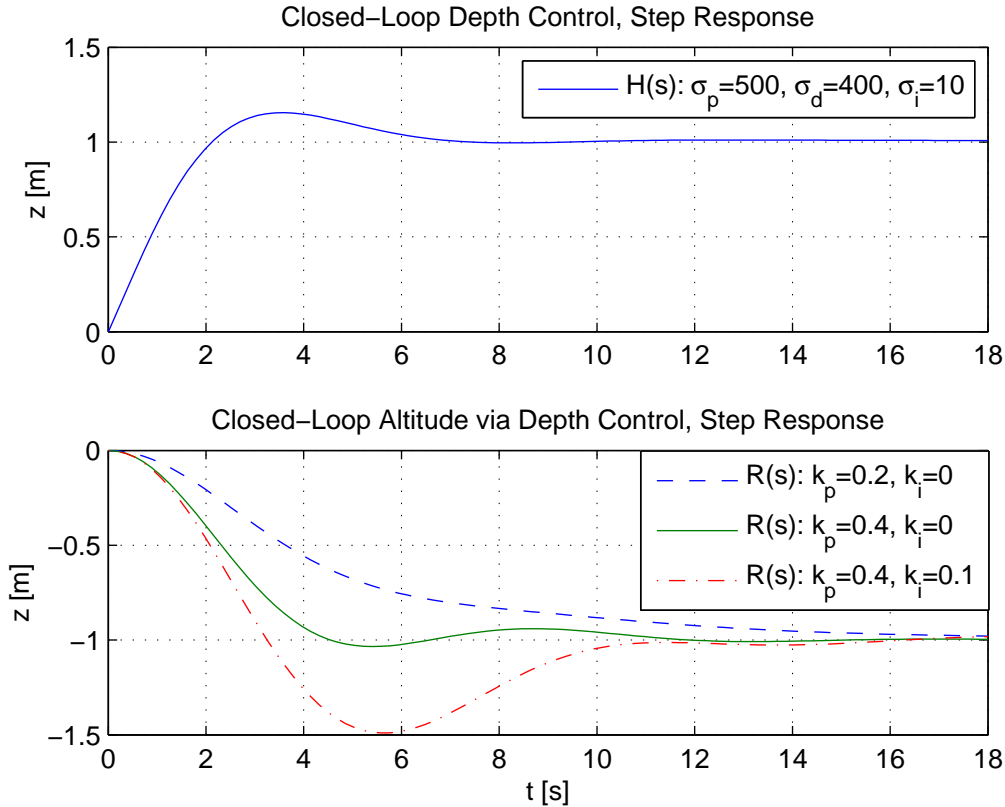


Figure D.4: Step response of the closed-loop depth and altitude system.

The step response of  $H(s)$  and  $R(s)$  with variation in the parameters are seen in Figure D.4. The upper plot shows the ROV depth for the step response of  $H(s)$ . The lower plot shows the ROV depth for the step response of  $R(s)$  with variation in parameters. Note the overshoot caused by the integral action in the altitude guidance law.

**Previous PhD theses published at the Departement of Marine Technology  
(earlier: Faculty of Marine Technology)  
NORWEGIAN UNIVERSITY OF SCIENCE AND TECHNOLOGY**

<b>Report No.</b>	<b>Author</b>	<b>Title</b>
	Kavlie, Dag	Optimization of Plane Elastic Grillages, 1967
	Hansen, Hans R.	Man-Machine Communication and Data-Storage Methods in Ship Structural Design, 1971
	Gisvold, Kaare M.	A Method for non-linear mixed -integer programming and its Application to Design Problems, 1971
	Lund, Sverre	Tanker Frame Optimization by means of SUMT-Transformation and Behaviour Models, 1971
	Vinje, Tor	On Vibration of Spherical Shells Interacting with Fluid, 1972
	Lorentz, Jan D.	Tank Arrangement for Crude Oil Carriers in Accordance with the new Anti-Pollution Regulations, 1975
	Carlsen, Carl A.	Computer-Aided Design of Tanker Structures, 1975
	Larsen, Carl M.	Static and Dynamic Analysis of Offshore Pipelines during Installation, 1976
UR-79-01	Brigt Hatlestad, MK	The finite element method used in a fatigue evaluation of fixed offshore platforms. (Dr.Ing. Thesis)
UR-79-02	Erik Pettersen, MK	Analysis and design of cellular structures. (Dr.Ing. Thesis)
UR-79-03	Sverre Valsgård, MK	Finite difference and finite element methods applied to nonlinear analysis of plated structures. (Dr.Ing. Thesis)
UR-79-04	Nils T. Nordsve, MK	Finite element collapse analysis of structural members considering imperfections and stresses due to fabrication. (Dr.Ing. Thesis)
UR-79-05	Ivar J. Fylling, MK	Analysis of towline forces in ocean towing systems. (Dr.Ing. Thesis)
UR-80-06	Nils Sandmark, MM	Analysis of Stationary and Transient Heat Conduction by the Use of the Finite Element Method. (Dr.Ing. Thesis)
UR-80-09	Sverre Haver, MK	Analysis of uncertainties related to the stochastic modeling of ocean waves. (Dr.Ing. Thesis)
UR-81-15	Odland, Jonas	On the Strength of welded Ring stiffened cylindrical Shells primarily subjected to axial Compression
UR-82-17	Engesvik, Knut	Analysis of Uncertainties in the fatigue Capacity of

Welded Joints		
UR-82-18	Rye, Henrik	Ocean wave groups
UR-83-30	Eide, Oddvar Inge	On Cumulative Fatigue Damage in Steel Welded Joints
UR-83-33	Mo, Olav	Stochastic Time Domain Analysis of Slender Offshore Structures
UR-83-34	Amdahl, Jørgen	Energy absorption in Ship-platform impacts
UR-84-37	Mørch, Morten	Motions and mooring forces of semi submersibles as determined by full-scale measurements and theoretical analysis
UR-84-38	Soares, C. Guedes	Probabilistic models for load effects in ship structures
UR-84-39	Aarsnes, Jan V.	Current forces on ships
UR-84-40	Czujko, Jerzy	Collapse Analysis of Plates subjected to Biaxial Compression and Lateral Load
UR-85-46	Alf G. Engseth, MK	Finite element collapse analysis of tubular steel offshore structures. (Dr.Ing. Thesis)
UR-86-47	Dengody Sheshappa, MP	A Computer Design Model for Optimizing Fishing Vessel Designs Based on Techno-Economic Analysis. (Dr.Ing. Thesis)
UR-86-48	Vidar Aanesland, MH	A Theoretical and Numerical Study of Ship Wave Resistance. (Dr.Ing. Thesis)
UR-86-49	Heinz-Joachim Wessel, MK	Fracture Mechanics Analysis of Crack Growth in Plate Girders. (Dr.Ing. Thesis)
UR-86-50	Jon Taby, MK	Ultimate and Post-ultimate Strength of Dented Tubular Members. (Dr.Ing. Thesis)
UR-86-51	Walter Lian, MH	A Numerical Study of Two-Dimensional Separated Flow Past Bluff Bodies at Moderate KC-Numbers. (Dr.Ing. Thesis)
UR-86-52	Bjørn Sortland, MH	Force Measurements in Oscillating Flow on Ship Sections and Circular Cylinders in a U-Tube Water Tank. (Dr.Ing. Thesis)
UR-86-53	Kurt Strand, MM	A System Dynamic Approach to One-dimensional Fluid Flow. (Dr.Ing. Thesis)
UR-86-54	Arne Edvin Løken, MH	Three Dimensional Second Order Hydrodynamic Effects on Ocean Structures in Waves. (Dr.Ing. Thesis)
UR-86-55	Sigurd Falch, MH	A Numerical Study of Slamming of Two-Dimensional Bodies. (Dr.Ing. Thesis)
UR-87-56	Arne Braathen, MH	Application of a Vortex Tracking Method to the Prediction of Roll Damping of a Two-Dimension Floating Body. (Dr.Ing. Thesis)

UR-87-57	Bernt Leira, MK	Gaussian Vector Processes for Reliability Analysis involving Wave-Induced Load Effects. (Dr.Ing. Thesis)
UR-87-58	Magnus Småvik, MM	Thermal Load and Process Characteristics in a Two-Stroke Diesel Engine with Thermal Barriers (in Norwegian). (Dr.Ing. Thesis)
MTA-88-59	Bernt Arild Bremsdal, MP	An Investigation of Marine Installation Processes – A Knowledge - Based Planning Approach. (Dr.Ing. Thesis)
MTA-88-60	Xu Jun, MK	Non-linear Dynamic Analysis of Space-framed Offshore Structures. (Dr.Ing. Thesis)
MTA-89-61	Gang Miao, MH	Hydrodynamic Forces and Dynamic Responses of Circular Cylinders in Wave Zones. (Dr.Ing. Thesis)
MTA-89-62	Martin Greenhow, MH	Linear and Non-Linear Studies of Waves and Floating Bodies. Part I and Part II. (Dr.Techn. Thesis)
MTA-89-63	Chang Li, MH	Force Coefficients of Spheres and Cubes in Oscillatory Flow with and without Current. (Dr.Ing. Thesis)
MTA-89-64	Hu Ying, MP	A Study of Marketing and Design in Development of Marine Transport Systems. (Dr.Ing. Thesis)
MTA-89-65	Arild Jæger, MH	Seakeeping, Dynamic Stability and Performance of a Wedge Shaped Planing Hull. (Dr.Ing. Thesis)
MTA-89-66	Chan Siu Hung, MM	The dynamic characteristics of tilting-pad bearings
MTA-89-67	Kim Wikstrøm, MP	Analysis av projekteringen for ett offshore projekt. (Licentiat-avhandling)
MTA-89-68	Jiao Guoyang, MK	Reliability Analysis of Crack Growth under Random Loading, considering Model Updating. (Dr.Ing. Thesis)
MTA-89-69	Arnt Olufsen, MK	Uncertainty and Reliability Analysis of Fixed Offshore Structures. (Dr.Ing. Thesis)
MTA-89-70	Wu Yu-Lin, MR	System Reliability Analyses of Offshore Structures using improved Truss and Beam Models. (Dr.Ing. Thesis)
MTA-90-71	Jan Roger Hoff, MH	Three-dimensional Green function of a vessel with forward speed in waves. (Dr.Ing. Thesis)
MTA-90-72	Rong Zhao, MH	Slow-Drift Motions of a Moored Two-Dimensional Body in Irregular Waves. (Dr.Ing. Thesis)
MTA-90-73	Atle Minsaas, MP	Economical Risk Analysis. (Dr.Ing. Thesis)
MTA-90-74	Knut-Aril Farnes, MK	Long-term Statistics of Response in Non-linear Marine Structures. (Dr.Ing. Thesis)
MTA-90-75	Torbjørn Sotberg, MK	Application of Reliability Methods for Safety Assessment of Submarine Pipelines. (Dr.Ing.

		Thesis)
MTA-90-76	Zeuthen, Steffen, MP	SEAMAIL. A computational model of the design process in a constraint-based logic programming environment. An example from the offshore domain. (Dr.Ing. Thesis)
MTA-91-77	Haagensen, Sven, MM	Fuel Dependant Cyclic Variability in a Spark Ignition Engine - An Optical Approach. (Dr.Ing. Thesis)
MTA-91-78	Løland, Geir, MH	Current forces on and flow through fish farms. (Dr.Ing. Thesis)
MTA-91-79	Hoen, Christopher, MK	System Identification of Structures Excited by Stochastic Load Processes. (Dr.Ing. Thesis)
MTA-91-80	Haugen, Stein, MK	Probabilistic Evaluation of Frequency of Collision between Ships and Offshore Platforms. (Dr.Ing. Thesis)
MTA-91-81	Sødahl, Nils, MK	Methods for Design and Analysis of Flexible Risers. (Dr.Ing. Thesis)
MTA-91-82	Ormberg, Harald, MK	Non-linear Response Analysis of Floating Fish Farm Systems. (Dr.Ing. Thesis)
MTA-91-83	Marley, Mark J., MK	Time Variant Reliability under Fatigue Degradation. (Dr.Ing. Thesis)
MTA-91-84	Krokstad, Jørgen R., MH	Second-order Loads in Multidirectional Seas. (Dr.Ing. Thesis)
MTA-91-85	Molteberg, Gunnar A., MM	The Application of System Identification Techniques to Performance Monitoring of Four Stroke Turbocharged Diesel Engines. (Dr.Ing. Thesis)
MTA-92-86	Mørch, Hans Jørgen Bjelke, MH	Aspects of Hydrofoil Design: with Emphasis on Hydrofoil Interaction in Calm Water. (Dr.Ing. Thesis)
MTA-92-87	Chan Siu Hung, MM	Nonlinear Analysis of Rotordynamic Instabilities in Highspeed Turbomachinery. (Dr.Ing. Thesis)
MTA-92-88	Bessason, Bjarni, MK	Assessment of Earthquake Loading and Response of Seismically Isolated Bridges. (Dr.Ing. Thesis)
MTA-92-89	Langli, Geir, MP	Improving Operational Safety through exploitation of Design Knowledge - an investigation of offshore platform safety. (Dr.Ing. Thesis)
MTA-92-90	Sævik, Svein, MK	On Stresses and Fatigue in Flexible Pipes. (Dr.Ing. Thesis)
MTA-92-91	Ask, Tor Ø., MM	Ignition and Flame Growth in Lean Gas-Air Mixtures. An Experimental Study with a Schlieren System. (Dr.Ing. Thesis)
MTA-86-92	Hessen, Gunnar, MK	Fracture Mechanics Analysis of Stiffened Tubular Members. (Dr.Ing. Thesis)

MTA-93-93	Steinebach, Christian, MM	Knowledge Based Systems for Diagnosis of Rotating Machinery. (Dr.Ing. Thesis)
MTA-93-94	Dalane, Jan Inge, MK	System Reliability in Design and Maintenance of Fixed Offshore Structures. (Dr.Ing. Thesis)
MTA-93-95	Steen, Sverre, MH	Cobblestone Effect on SES. (Dr.Ing. Thesis)
MTA-93-96	Karunakaran, Daniel, MK	Nonlinear Dynamic Response and Reliability Analysis of Drag-dominated Offshore Platforms. (Dr.Ing. Thesis)
MTA-93-97	Hagen, Arnulf, MP	The Framework of a Design Process Language. (Dr.Ing. Thesis)
MTA-93-98	Nordrik, Rune, MM	Investigation of Spark Ignition and Autoignition in Methane and Air Using Computational Fluid Dynamics and Chemical Reaction Kinetics. A Numerical Study of Ignition Processes in Internal Combustion Engines. (Dr.Ing. Thesis)
MTA-94-99	Passano, Elizabeth, MK	Efficient Analysis of Nonlinear Slender Marine Structures. (Dr.Ing. Thesis)
MTA-94-100	Kvålvold, Jan, MH	Hydroelastic Modelling of Wetdeck Slamming on Multihull Vessels. (Dr.Ing. Thesis)
MTA-94-102	Bech, Sidsel M., MK	Experimental and Numerical Determination of Stiffness and Strength of GRP/PVC Sandwich Structures. (Dr.Ing. Thesis)
MTA-95-103	Paulsen, Hallvard, MM	A Study of Transient Jet and Spray using a Schlieren Method and Digital Image Processing. (Dr.Ing. Thesis)
MTA-95-104	Hovde, Geir Olav, MK	Fatigue and Overload Reliability of Offshore Structural Systems, Considering the Effect of Inspection and Repair. (Dr.Ing. Thesis)
MTA-95-105	Wang, Xiaozhi, MK	Reliability Analysis of Production Ships with Emphasis on Load Combination and Ultimate Strength. (Dr.Ing. Thesis)
MTA-95-106	Ulstein, Tore, MH	Nonlinear Effects of a Flexible Stern Seal Bag on Cobblestone Oscillations of an SES. (Dr.Ing. Thesis)
MTA-95-107	Solaas, Frøydís, MH	Analytical and Numerical Studies of Sloshing in Tanks. (Dr.Ing. Thesis)
MTA-95-108	Hellan, Øyvind, MK	Nonlinear Pushover and Cyclic Analyses in Ultimate Limit State Design and Reassessment of Tubular Steel Offshore Structures. (Dr.Ing. Thesis)
MTA-95-109	Hermundstad, Ole A., MK	Theoretical and Experimental Hydroelastic Analysis of High Speed Vessels. (Dr.Ing. Thesis)
MTA-96-110	Bratland, Anne K., MH	Wave-Current Interaction Effects on Large-Volume Bodies in Water of Finite Depth. (Dr.Ing. Thesis)
MTA-96-111	Herfjord, Kjell, MH	A Study of Two-dimensional Separated Flow by a Combination of the Finite Element Method and

		Navier-Stokes Equations. (Dr.Ing. Thesis)
MTA-96-112	Æsøy, Vilmar, MM	Hot Surface Assisted Compression Ignition in a Direct Injection Natural Gas Engine. (Dr.Ing. Thesis)
MTA-96-113	Eknes, Monika L., MK	Escalation Scenarios Initiated by Gas Explosions on Offshore Installations. (Dr.Ing. Thesis)
MTA-96-114	Erikstad, Stein O., MP	A Decision Support Model for Preliminary Ship Design. (Dr.Ing. Thesis)
MTA-96-115	Pedersen, Egil, MH	A Nautical Study of Towed Marine Seismic Streamer Cable Configurations. (Dr.Ing. Thesis)
MTA-97-116	Moksnes, Paul O., MM	Modelling Two-Phase Thermo-Fluid Systems Using Bond Graphs. (Dr.Ing. Thesis)
MTA-97-117	Halse, Karl H., MK	On Vortex Shedding and Prediction of Vortex-Induced Vibrations of Circular Cylinders. (Dr.Ing. Thesis)
MTA-97-118	Igland, Ragnar T., MK	Reliability Analysis of Pipelines during Laying, considering Ultimate Strength under Combined Loads. (Dr.Ing. Thesis)
MTA-97-119	Pedersen, Hans-P., MP	Levendefiskteknologi for fiskefartøy. (Dr.Ing. Thesis)
MTA-98-120	Vikestad, Kyrre, MK	Multi-Frequency Response of a Cylinder Subjected to Vortex Shedding and Support Motions. (Dr.Ing. Thesis)
MTA-98-121	Azadi, Mohammad R. E., MK	Analysis of Static and Dynamic Pile-Soil-Jacket Behaviour. (Dr.Ing. Thesis)
MTA-98-122	Ulltang, Terje, MP	A Communication Model for Product Information. (Dr.Ing. Thesis)
MTA-98-123	Torbergsen, Erik, MM	Impeller/Diffuser Interaction Forces in Centrifugal Pumps. (Dr.Ing. Thesis)
MTA-98-124	Hansen, Edmond, MH	A Discrete Element Model to Study Marginal Ice Zone Dynamics and the Behaviour of Vessels Moored in Broken Ice. (Dr.Ing. Thesis)
MTA-98-125	Videiro, Paulo M., MK	Reliability Based Design of Marine Structures. (Dr.Ing. Thesis)
MTA-99-126	Mainçon, Philippe, MK	Fatigue Reliability of Long Welds Application to Titanium Risers. (Dr.Ing. Thesis)
MTA-99-127	Haugen, Elin M., MH	Hydroelastic Analysis of Slamming on Stiffened Plates with Application to Catamaran Wetdecks. (Dr.Ing. Thesis)
MTA-99-128	Langhelle, Nina K., MK	Experimental Validation and Calibration of Nonlinear Finite Element Models for Use in Design of Aluminium Structures Exposed to Fire. (Dr.Ing. Thesis)
MTA-99-	Berstad, Are J., MK	Calculation of Fatigue Damage in Ship Structures.

129		(Dr.Ing. Thesis)
MTA-99-130	Andersen, Trond M., MM	Short Term Maintenance Planning. (Dr.Ing. Thesis)
MTA-99-131	Tveiten, Bård Wathne, MK	Fatigue Assessment of Welded Aluminium Ship Details. (Dr.Ing. Thesis)
MTA-99-132	Søreide, Fredrik, MP	Applications of underwater technology in deep water archaeology. Principles and practice. (Dr.Ing. Thesis)
MTA-99-133	Tønnessen, Rune, MH	A Finite Element Method Applied to Unsteady Viscous Flow Around 2D Blunt Bodies With Sharp Corners. (Dr.Ing. Thesis)
MTA-99-134	Elvekrok, Dag R., MP	Engineering Integration in Field Development Projects in the Norwegian Oil and Gas Industry. The Supplier Management of Norne. (Dr.Ing. Thesis)
MTA-99-135	Fagerholt, Kjetil, MP	Optimizeringsbaserte Metoder for Ruteplanlegging innen skipsfart. (Dr.Ing. Thesis)
MTA-99-136	Bysveen, Marie, MM	Visualization in Two Directions on a Dynamic Combustion Rig for Studies of Fuel Quality. (Dr.Ing. Thesis)
MTA-2000-137	Storteig, Eskild, MM	Dynamic characteristics and leakage performance of liquid annular seals in centrifugal pumps. (Dr.Ing. Thesis)
MTA-2000-138	Sagli, Gro, MK	Model uncertainty and simplified estimates of long term extremes of hull girder loads in ships. (Dr.Ing. Thesis)
MTA-2000-139	Tronstad, Harald, MK	Nonlinear analysis and design of cable net structures like fishing gear based on the finite element method. (Dr.Ing. Thesis)
MTA-2000-140	Kroneberg, André, MP	Innovation in shipping by using scenarios. (Dr.Ing. Thesis)
MTA-2000-141	Haslum, Herbjørn Alf, MH	Simplified methods applied to nonlinear motion of spar platforms. (Dr.Ing. Thesis)
MTA-2001-142	Samdal, Ole Johan, MM	Modelling of Degradation Mechanisms and Stressor Interaction on Static Mechanical Equipment Residual Lifetime. (Dr.Ing. Thesis)
MTA-2001-143	Baarholm, Rolf Jarle, MH	Theoretical and experimental studies of wave impact underneath decks of offshore platforms. (Dr.Ing. Thesis)
MTA-2001-144	Wang, Lihua, MK	Probabilistic Analysis of Nonlinear Wave-induced Loads on Ships. (Dr.Ing. Thesis)
MTA-2001-145	Kristensen, Odd H. Holt, MK	Ultimate Capacity of Aluminium Plates under Multiple Loads, Considering HAZ Properties. (Dr.Ing. Thesis)
MTA-2001-146	Greco, Marilena, MH	A Two-Dimensional Study of Green-Water Loading. (Dr.Ing. Thesis)

MTA-2001-147	Heggelund, Svein E., MK	Calculation of Global Design Loads and Load Effects in Large High Speed Catamarans. (Dr.Ing. Thesis)
MTA-2001-148	Babalola, Olusegun T., MK	Fatigue Strength of Titanium Risers – Defect Sensitivity. (Dr.Ing. Thesis)
MTA-2001-149	Mohammed, Abuu K., MK	Nonlinear Shell Finite Elements for Ultimate Strength and Collapse Analysis of Ship Structures. (Dr.Ing. Thesis)
MTA-2002-150	Holmedal, Lars E., MH	Wave-current interactions in the vicinity of the sea bed. (Dr.Ing. Thesis)
MTA-2002-151	Rognebakke, Olav F., MH	Sloshing in rectangular tanks and interaction with ship motions. (Dr.Ing. Thesis)
MTA-2002-152	Lader, Pål Furset, MH	Geometry and Kinematics of Breaking Waves. (Dr.Ing. Thesis)
MTA-2002-153	Yang, Qinzheng, MH	Wash and wave resistance of ships in finite water depth. (Dr.Ing. Thesis)
MTA-2002-154	Melhus, Øyvin, MM	Utilization of VOC in Diesel Engines. Ignition and combustion of VOC released by crude oil tankers. (Dr.Ing. Thesis)
MTA-2002-155	Ronæss, Marit, MH	Wave Induced Motions of Two Ships Advancing on Parallel Course. (Dr.Ing. Thesis)
MTA-2002-156	Økland, Ole D., MK	Numerical and experimental investigation of whipping in twin hull vessels exposed to severe wet deck slamming. (Dr.Ing. Thesis)
MTA-2002-157	Ge, Chunhua, MK	Global Hydroelastic Response of Catamarans due to Wet Deck Slamming. (Dr.Ing. Thesis)
MTA-2002-158	Byklum, Eirik, MK	Nonlinear Shell Finite Elements for Ultimate Strength and Collapse Analysis of Ship Structures. (Dr.Ing. Thesis)
IMT-2003-1	Chen, Haibo, MK	Probabilistic Evaluation of FPSO-Tanker Collision in Tandem Offloading Operation. (Dr.Ing. Thesis)
IMT-2003-2	Skaugset, Kjetil Bjørn, MK	On the Suppression of Vortex Induced Vibrations of Circular Cylinders by Radial Water Jets. (Dr.Ing. Thesis)
IMT-2003-3	Chezhian, Muthu	Three-Dimensional Analysis of Slamming. (Dr.Ing. Thesis)
IMT-2003-4	Buhaug, Øyvind	Deposit Formation on Cylinder Liner Surfaces in Medium Speed Engines. (Dr.Ing. Thesis)
IMT-2003-5	Tregde, Vidar	Aspects of Ship Design: Optimization of Aft Hull with Inverse Geometry Design. (Dr.Ing. Thesis)
IMT-2003-6	Wist, Hanne Therese	Statistical Properties of Successive Ocean Wave Parameters. (Dr.Ing. Thesis)

IMT-2004-7	Ransau, Samuel	Numerical Methods for Flows with Evolving Interfaces. (Dr.Ing. Thesis)
IMT-2004-8	Soma, Torkel	Blue-Chip or Sub-Standard. A data interrogation approach of identity safety characteristics of shipping organization. (Dr.Ing. Thesis)
IMT-2004-9	Ersdal, Svein	An experimental study of hydrodynamic forces on cylinders and cables in near axial flow. (Dr.Ing. Thesis)
IMT-2005-10	Brodkorb, Per Andreas	The Probability of Occurrence of Dangerous Wave Situations at Sea. (Dr.Ing. Thesis)
IMT-2005-11	Yttervik, Rune	Ocean current variability in relation to offshore engineering. (Dr.Ing. Thesis)
IMT-2005-12	Fredheim, Arne	Current Forces on Net-Structures. (Dr.Ing. Thesis)
IMT-2005-13	Heggernes, Kjetil	Flow around marine structures. (Dr.Ing. Thesis)
IMT-2005-14	Fouques, Sebastien	Lagrangian Modelling of Ocean Surface Waves and Synthetic Aperture Radar Wave Measurements. (Dr.Ing. Thesis)
IMT-2006-15	Holm, Håvard	Numerical calculation of viscous free surface flow around marine structures. (Dr.Ing. Thesis)
IMT-2006-16	Bjørheim, Lars G.	Failure Assessment of Long Through Thickness Fatigue Cracks in Ship Hulls. (Dr.Ing. Thesis)
IMT-2006-17	Hansson, Lisbeth	Safety Management for Prevention of Occupational Accidents. (Dr.Ing. Thesis)
IMT-2006-18	Zhu, Xinying	Application of the CIP Method to Strongly Nonlinear Wave-Body Interaction Problems. (Dr.Ing. Thesis)
IMT-2006-19	Reite, Karl Johan	Modelling and Control of Trawl Systems. (Dr.Ing. Thesis)
IMT-2006-20	Smogeli, Øyvind Notland	Control of Marine Propellers. From Normal to Extreme Conditions. (Dr.Ing. Thesis)
IMT-2007-21	Storhaug, Gaute	Experimental Investigation of Wave Induced Vibrations and Their Effect on the Fatigue Loading of Ships. (Dr.Ing. Thesis)
IMT-2007-22	Sun, Hui	A Boundary Element Method Applied to Strongly Nonlinear Wave-Body Interaction Problems. (PhD Thesis, CeSOS)
IMT-2007-23	Rustad, Anne Marthine	Modelling and Control of Top Tensioned Risers. (PhD Thesis, CeSOS)
IMT-2007-24	Johansen, Vegar	Modelling flexible slender system for real-time simulations and control applications
IMT-2007-25	Wroldsen, Anders Sunde	Modelling and control of tensegrity structures. (PhD Thesis, CeSOS)
IMT-	Aronsen, Kristoffer Høy	An experimental investigation of in-line and

2007-26		combined inline and cross flow vortex induced vibrations. (Dr. avhandling, IMT)
IMT-2007-27	Gao, Zhen	Stochastic Response Analysis of Mooring Systems with Emphasis on Frequency-domain Analysis of Fatigue due to Wide-band Response Processes (PhD Thesis, CeSOS)
IMT-2007-28	Thorstensen, Tom Anders	Lifetime Profit Modelling of Ageing Systems Utilizing Information about Technical Condition. (Dr.ing. thesis, IMT)
IMT-2008-29	Berntsen, Per Ivar B.	Structural Reliability Based Position Mooring. (PhD-Thesis, IMT)
IMT-2008-30	Ye, Naiquan	Fatigue Assessment of Aluminium Welded Box-stiffener Joints in Ships (Dr.ing. thesis, IMT)
IMT-2008-31	Radan, Damir	Integrated Control of Marine Electrical Power Systems. (PhD-Thesis, IMT)
IMT-2008-32	Thomassen, Paul	Methods for Dynamic Response Analysis and Fatigue Life Estimation of Floating Fish Cages. (Dr.ing. thesis, IMT)
IMT-2008-33	Pákozdi, Csaba	A Smoothed Particle Hydrodynamics Study of Two-dimensional Nonlinear Sloshing in Rectangular Tanks. (Dr.ing.thesis, IMT/ CeSOS)
IMT-2007-34	Grytøy, Guttorm	A Higher-Order Boundary Element Method and Applications to Marine Hydrodynamics. (Dr.ing.thesis, IMT)
IMT-2008-35	Drummen, Ingo	Experimental and Numerical Investigation of Nonlinear Wave-Induced Load Effects in Containerships considering Hydroelasticity. (PhD thesis, CeSOS)
IMT-2008-36	Skejic, Renato	Maneuvering and Seakeeping of a Singel Ship and of Two Ships in Interaction. (PhD-Thesis, CeSOS)
IMT-2008-37	Harlem, Alf	An Age-Based Replacement Model for Repairable Systems with Attention to High-Speed Marine Diesel Engines. (PhD-Thesis, IMT)
IMT-2008-38	Alsos, Hagbart S.	Ship Grounding. Analysis of Ductile Fracture, Bottom Damage and Hull Girder Response. (PhD-thesis, IMT)
IMT-2008-39	Graczyk, Mateusz	Experimental Investigation of Sloshing Loading and Load Effects in Membrane LNG Tanks Subjected to Random Excitation. (PhD-thesis, CeSOS)
IMT-2008-40	Taghipour, Reza	Efficient Prediction of Dynamic Response for Flexible and Multi-body Marine Structures. (PhD-thesis, CeSOS)
IMT-2008-41	Ruth, Eivind	Propulsion control and thrust allocation on marine vessels. (PhD thesis, CeSOS)
IMT-2008-42	Nystad, Bent Helge	Technical Condition Indexes and Remaining Useful Life of Aggregated Systems. PhD thesis, IMT

IMT-2008-43	Soni, Prashant Kumar	Hydrodynamic Coefficients for Vortex Induced Vibrations of Flexible Beams, PhD thesis, CeSOS
IMT-2009-43	Amlashi, Hadi K.K.	Ultimate Strength and Reliability-based Design of Ship Hulls with Emphasis on Combined Global and Local Loads. PhD Thesis, IMT
IMT-2009-44	Pedersen, Tom Arne	Bond Graph Modelling of Marine Power Systems. PhD Thesis, IMT
IMT-2009-45	Kristiansen, Trygve	Two-Dimensional Numerical and Experimental Studies of Piston-Mode Resonance. PhD-Thesis, CeSOS
IMT-2009-46	Ong, Muk Chen	Applications of a Standard High Reynolds Number Model and a Stochastic Scour Prediction Model for Marine Structures. PhD-thesis, IMT
IMT-2009-47	Hong, Lin	Simplified Analysis and Design of Ships subjected to Collision and Grounding. PhD-thesis, IMT
IMT-2009-48	Koushan, Kamran	Vortex Induced Vibrations of Free Span Pipelines, PhD thesis, IMT
IMT-2009-49	Korsvik, Jarl Eirik	Heuristic Methods for Ship Routing and Scheduling. PhD-thesis, IMT
IMT-2009-50	Lee, Jihoon	Experimental Investigation and Numerical in Analyzing the Ocean Current Displacement of Longlines. Ph.d.-Thesis, IMT.
IMT-2009-51	Vestbøstad, Tone Gran	A Numerical Study of Wave-in-Deck Impact usin a Two-Dimensional Constrained Interpolation Profile Method, Ph.d.thesis, CeSOS.
IMT-2009-52	Bruun, Kristine	Bond Graph Modelling of Fuel Cells for Marine Power Plants. Ph.d.-thesis, IMT
IMT-2009-53	Holstad, Anders	Numerical Investigation of Turbulence in a Sekwed Three-Dimensional Channel Flow, Ph.d.-thesis, IMT.
IMT-2009-54	Ayala-Uraga, Efren	Reliability-Based Assessment of Deteriorating Ship-shaped Offshore Structures, Ph.d.-thesis, IMT
IMT-2009-55	Kong, Xiangjun	A Numerical Study of a Damaged Ship in Beam Sea Waves. Ph.d.-thesis, IMT/CeSOS.
IMT-2010-56	Kristiansen, David	Wave Induced Effects on Floaters of Aquaculture Plants, Ph.d.-thesis, CeSOS.
IMT-2010-57	Ludvigsen, Martin	An ROV-Toolbox for Optical and Acoustic Scientific Seabed Investigation. Ph.d.-thesis IMT.
IMT-2010-58	Hals, Jørgen	Modelling and Phase Control of Wave-Energy Converters. Ph.d.thesis, CeSOS.
IMT-2010-59	Shu, Zhi	Uncertainty Assessment of Wave Loads and Ultimate Strength of Tankers and Bulk Carriers in a

IMT 2010-60	Shao, Yanlin	Reliability Framework. Ph.d. Thesis, IMT/ CeSOS Numerical Potential-Flow Studies on Weakly- Nonlinear Wave-Body Interactions with/without Small Forward Speed, Ph.d.thesis,CeSOS.
IMT 2010-61	Califano, Andrea	Dynamic Loads on Marine Propellers due to Intermittent Ventilation. Ph.d.thesis, IMT.
IMT 2010-62	El Khoury, George	Numerical Simulations of Massively Separated Turbulent Flows, Ph.d.-thesis, IMT
IMT 2010-63	Seim, Knut Sponheim	Mixing Process in Dense Overflows with Emphasis on the Faroe Bank Channel Overflow. Ph.d.thesis, IMT
IMT 2010-64	Jia, Huirong	Structural Analysis of Insect and Damaged Ships in a Collision Risk Analysis Perspective. Ph.d.thesis CeSoS.
IMT 2010-65	Jiao, Linlin	Wave-Induced Effects on a Pontoon-type Very Large Floating Structures (VLFS). Ph.D.-thesis, CeSOS.
IMT 2010-66	Abrahamsen, Bjørn Christian	Sloshing Induced Tank Roof with Entrapped Air Pocket. Ph.d.thesis, CeSOS.
IMT 2011-67	Karimirad, Madjid	Stochastic Dynamic Response Analysis of Spar- Type Wind Turbines with Catenary or Taut Mooring Systems. Ph.d.-thesis, CeSOS.
IMT - 2011-68	Erlend Meland	Condition Monitoring of Safety Critical Valves. Ph.d.-thesis, IMT.
IMT - 2011-69	Yang, Limin	Stochastic Dynamic System Analysis of Wave Energy Converter with Hydraulic Power Take-Off, with Particular Reference to Wear Damage Analysis, Ph.d. Thesis, CeSOS.
IMT – 2011-70	Visscher, Jan	Application of Particle Image Velocimetry on Turbulent Marine Flows, Ph.d.Thesis, IMT.
IMT – 2011-71	Su, Biao	Numerical Predictions of Global and Local Ice Loads on Ships. Ph.d.Thesis, CeSOS.
IMT – 2011-72	Liu, Zhenhui	Analytical and Numerical Analysis of Iceberg Collision with Ship Structures. Ph.d.Thesis, IMT.
IMT – 2011-73	Aarsæther, Karl Gunnar	Modeling and Analysis of Ship Traffic by Observation and Numerical Simulation. Ph.d.Thesis, IMT.
Imt – 2011-74	Wu, Jie	Hydrodynamic Force Identification from Stochastic Vortex Induced Vibration Experiments with Slender Beams. Ph.d.Thesis, IMT.
Imt – 2011-75	Amini, Hamid	Azimuth Propulsors in Off-design Conditions. Ph.d.Thesis, IMT.
IMT – 2011-76	Nguyen, Tan-Hoi	Toward a System of Real-Time Prediction and Monitoring of Bottom Damage Conditions During

		Ship Grounding. Ph.d.thesis, IMT.
IMT-2011-77	Tavakoli, Mohammad T.	Assessment of Oil Spill in Ship Collision and Grounding, Ph.d.thesis, IMT.
IMT-2011-78	Guo, Bingjie	Numerical and Experimental Investigation of Added Resistance in Waves. Ph.d.Thesis, IMT.
IMT-2011-79	Chen, Qiaofeng	Ultimate Strength of Aluminium Panels, considering HAZ Effects, IMT
IMT-2012-80	Kota, Ravikiran S.	Wave Loads on Decks of Offshore Structures in Random Seas, CeSOS.
IMT-2012-81	Sten, Ronny	Dynamic Simulation of Deep Water Drilling Risers with Heave Compensating System, IMT.
IMT-2012-82	Berle, Øyvind	Risk and resilience in global maritime supply chains, IMT.
IMT-2012-83	Fang, Shaoji	Fault Tolerant Position Mooring Control Based on Structural Reliability, CeSOS.
IMT-2012-84	You, Jikun	Numerical studies on wave forces and moored ship motions in intermediate and shallow water, CeSOS.
IMT-2012-85	Xiang ,Xu	Maneuvering of two interacting ships in waves, CeSOS
IMT-2012-86	Dong, Wenbin	Time-domain fatigue response and reliability analysis of offshore wind turbines with emphasis on welded tubular joints and gear components, CeSOS
IMT-2012-87	Zhu, Suji	Investigation of Wave-Induced Nonlinear Load Effects in Open Ships considering Hull Girder Vibrations in Bending and Torsion, CeSOS
IMT-2012-88	Zhou, Li	Numerical and Experimental Investigation of Station-keeping in Level Ice, CeSOS
IMT-2012-90	Ushakov, Sergey	Particulate matter emission characteristics from diesel engines operating on conventional and alternative marine fuels, IMT
IMT-2013-1	Yin, Decao	Experimental and Numerical Analysis of Combined In-line and Cross-flow Vortex Induced Vibrations, CeSOS
IMT-2013-2	Kurniawan, Adi	Modelling and geometry optimisation of wave energy converters, CeSOS
IMT-2013-3	Al Ryati, Nabil	Technical condition indexes doe auxiliary marine diesel engines, IMT
IMT-2013-4	Firoozkohi, Reza	Experimental, numerical and analytical investigation of the effect of screens on sloshing, CeSOS
IMT-2013-5	Ommani, Babak	Potential-Flow Predictions of a Semi-Displacement Vessel Including Applications to Calm Water Broaching, CeSOS

IMT-6-2013	Xing, Yihan	Modelling and analysis of the gearbox in a floating spar-type wind turbine, CeSOS
IMT-7-2013	Balland, Océane	Optimization models for reducing air emissions from ships, IMT
IMT-8-2013	Yang, Dan	Transitional wake flow behind an inclined flat plate----Computation and analysis, IMT
IMT-9-2013	Abdillah, Suyuthi	Prediction of Extreme Loads and Fatigue Damage for a Ship Hull due to Ice Action, IMT
IMT-10-2013	Ramirez, Pedro Agustín Pérez	Ageing management and life extension of technical systems- Concepts and methods applied to oil and gas facilities, IMT
IMT-11-2013	Chuang, Zhenju	Experimental and Numerical Investigation of Speed Loss due to Seakeeping and Maneuvering, IMT
IMT-12-2013	Etemaddar, Mahmoud	Load and Response Analysis of Wind Turbines under Atmospheric Icing and Controller System Faults with Emphasis on Spar Type Floating Wind Turbines, IMT
IMT-13-2013	Lindstad, Haakon	Strategies and measures for reducing maritime CO2 emissions, IMT
IMT-14-2013	Haris, Sabril	Damage interaction analysis of ship collisions, IMT
IMT-15-2013	Shainee, Mohamed	Conceptual Design, Numerical and Experimental Investigation of a SPM Cage Concept for Offshore Mariculture, IMT
IMT-16-2013	Gansel, Lars	Flow past porous cylinders and effects of biofouling and fish behavior on the flow in and around Atlantic salmon net cages, IMT
IMT-17-2013	Gaspar, Henrique	Handling Aspects of Complexity in Conceptual Ship Design, IMT
IMT-18-2013	Thys, Maxime	Theoretical and Experimental Investigation of a Free Running Fishing Vessel at Small Frequency of Encounter, CeSOS
IMT-19-2013	Aglen, Ida	VIV in Free Spanning Pipelines, CeSOS
IMT-1-2014	Song, An	Theoretical and experimental studies of wave diffraction and radiation loads on a horizontally submerged perforated plate, CeSOS
IMT-2-2014	Rogne, Øyvind Ygre	Numerical and Experimental Investigation of a Hinged 5-body Wave Energy Converter, CeSOS
IMT-3-2014	Dai, Lijuan	Safe and efficient operation and maintenance of offshore wind farms ,IMT
IMT-4-2014	Bachynski, Erin Elizabeth	Design and Dynamic Analysis of Tension Leg Platform Wind Turbines, CeSOS
IMT-5-2014	Wang, Jingbo	Water Entry of Freefall Wedged – Wedge motions

and Cavity Dynamics, CeSOS

IMT-6- 2014	Kim, Ekaterina	Experimental and numerical studies related to the coupled behavior of ice mass and steel structures during accidental collisions, IMT
IMT-7- 2014	Tan, Xiang	Numerical investigation of ship's continuous- mode icebreaking in leverl ice, CeSOS
IMT-8- 2014	Muliawan, Made Jaya	Design and Analysis of Combined Floating Wave and Wind Power Facilities, with Emphasis on Extreme Load Effects of the Mooring System, CeSOS
IMT-9- 2014	Jiang, Zhiyu	Long-term response analysis of wind turbines with an emphasis on fault and shutdown conditions, IMT
IMT-10- 2014	Dukan, Fredrik	ROV Motion Control Systems, IMT



GODKJENNING  
FRA  
OPPNEVNT SENSURKOMITE  
av avhandling for graden

## PERSONALOPPLYSNINGER

Kandidat: **Fredrik Dukan**

Institutt: **Department of Marine  
Technology**

## AVHANDLING

Tittel på avhandlingen:

**ROV Motion Control Systems**

K O R R E K T U R

## SENSURKOMITEENS VURDERING

Avhandlingen er bedømt og godkjent for graden philosophiae doctor

Avhandlingen er bedømt og godkjent for graden doctor philosophiae

Trondheim, den

.....  
navn

.....  
underskrift

.....  
navn

.....  
underskrift

.....  
navn

.....  
underskrift

.....  
navn

.....  
underskrift